UNIVERSITEIT VAN PRETORIA
UNIVERSITY OF PRETORIA
YUNIBESITHI YA PRETORIA

Computational study of cryogenic jet impingement boiling on concave and singular needle surfaces

by

Daiman Somerville

Submitted in partial fulfilment of the requirements for the degree
Master of Engineering
(Mechanical Engineering)

in the

Department of Mechanical and Aeronautical Engineering

Faculty of Engineering, Built Environment and Information Technology

University of Pretoria

February 13, 2025

Abstract

Computational study of cryogenic jet impingement boiling on concave and singular needle surfaces

by

Daiman Somerville

Supervisor:	Prof. K. Craig (University of Pretoria)
Co-Supervisor:	Prof. P. Valluri (The University of Edinburgh)
Department:	Mechanical and Aeronautical Engineering
University:	University of Pretoria
Degree:	Master of Engineering (Mechanical Engineering)
Keywords:	Jet impingement, Boiling, Curved surface, Singular needle, RPI Boiling model, Cryogenic fluids, Computational Fluid Dynamics (CFD), Multiphase Eulerian

Jet impingement boiling is a highly effective method of surface cooling and is particularly suited to high heat-flux applications such as microprocessor cooling and cryogenic probe cooling. In the present study, we computationally explore the effect that the geometric parameters of surface curvature, needle height and impingement height have on the boiling curve. The multiphase Eulerian model coupled with the Rensselaer Polytechnic Institute (RPI) wall boiling model is employed in tandem with an axisymmetric steady-state assumption. The RPI wall boiling model decomposes the wall heat flux into three components: quenching, convective and evaporative. Each of these components comprise of multiple closing models. A focus is placed on selecting RPI closing models that are suitable for cryogenic fluids. Moreover, a new empirical correlation is proposed for the non-dimensional area of influence (A_b) which determines the ratio of quenching to convective heat flux. Based on results of a Monte Carlo experiment aimed at mimicking the distribution of nucleation sites and their overlapping area of influence, this model is given as: $A_b = 1 - e^{-1.5\beta^{1.2}}$. The bubble waiting time coefficient (C_{wt}) can be described as the quenching heat flux pre-multiplicative coefficient and is responsible for adjusting the quenching heat flux independent of the evaporative and convective components. The range for which the bubble waiting time coefficient (C_{wt}) can vary is likewise computed using the results of the Monte Carlo method with the inclusion of the reduction of area of influence due to bubble growth ($1 \leq C_{wt} \leq 1.2$). These findings are incorporated into a CFD model. Additionally, a computational fluid dynamics (CFD) model based on RPI closing models developed for water and modified by increasing the bubble waiting time coefficient well beyond the applicable range (to a value of $C_{wt} = 3$) is also developed for comparative purposes.

The CFD models are validated against experimental findings from literature concerning a jet of liquid nitrogen (2mm in diameter) impinging onto a heated surface (5mm in diameter) of various shapes (flat, hemispherical and singular needle) in a radially confined domain. The Reynolds numbers range from 3 700 to 12 200. The steady-state solver used was found to have a maximum deviation of 2.4% near the experimental critical heat flux when compared to a transient solution. The experimental parameters of subcooling, jet velocity and pressure had large ranges of uncertainty or were ill-defined. As such their impact on the CFD models was explored. It was revealed that increased subcooling increased the quenching and convective heat fluxes resulting in the nucleate boiling curve shifting to the left. Increased pressure displayed a similar shift of the boiling curve to the left for the cryogenic model due to the increase in nucleation site density (as a result of the change in the fluid saturation properties). However, as the nucleation site density was not dependent on fluid properties for the water based model, there was minimal impact of pressure on wall superheat. Increased jet velocity resulted in a marginal increase in boiling heat transfer coefficient (BHTC) for all models. The settings of the cryogenic CFD model selected for use in the subsequent parametric study were finalised based on the parameter combination (velocity, subcooling and nucleation site density) that resulted in the lowest root mean squared deviation across

all three experimental surfaces.

A parametric study was then conducted to determine the influence of surface curvature ($k = 0 - 0.42$) on confined cryogenic jet impingement boiling. It is revealed that increased curvature resulted in approximately quadratic growth of the BHTC. The main mechanism behind this was revealed to be the growth in surface area resulting from increased curvature. Additionally, the parametric study explored the impact of needle height ($h_{needle}0 - 5$ mm) on the BHTC when using both flat and curved surfaces. The BHTC was found to grow approximately linearly with increased needle height. This was again attributed largely to the increase in surface area with increased needle height. Lastly, the parametric study explored the effect of jet impingement height ($a = 0.5 - 5.5$ mm) on both curved, needled and combined curved-needled surfaces. It was revealed that there exists an optimum impingement height of approximately $a = 1.5 - 2.5$ mm for most of the tested surfaces (with slight variation depending on curvature and needle height). The optimum parameter combination was found to be [$a = 1.5$ mm, $k = 0.42$ and $h_{needle} = 4$ mm] with a BHTC of 3.66 W/(cm^2·K).

Declaration of Originality

The **Department of Mechanical and Aeronautical Engineering** places great emphasis upon integrity and ethical conduct in the preparation of all written work submitted for academic evaluation.

The following declaration is required by the **Department of Mechanical and Aeronautical Engineering**:

Full names of Student:	Daiman Athony Hugh Somerville
Student Number:	u18108352
Topic of Work:	Computational study of cryogenic jet impingement boiling on concave and singular needle surfaces

Declaration:

1. I understand what plagiarism is and am aware of the University's policy in this regard.
2. I declare that this dissertation is my own original work. Where other people's work has been used (either from a printed source, Internet, or any other source), this has been properly acknowledged and referenced in accordance with departmental requirements.
3. I have not used work previously produced by another student or any other person to hand in as my own.
4. I have not allowed and will not allow anyone to copy my work with the intention of passing it off as his or her own work.

SIGNATURE _____

Acknowledgments

I would like to express deep gratitude and thanks to my supervisors, Prof. K. Craig and Prof. P. Valluri for their invaluable insight and guidance throughout this project. I would also thank the ThermaSMART project, funded by the European Commission under Grant EC-H2020-RISE-ThermaSMART-778104, for their invaluable financial support. Additionally, I would like to acknowledge the Centre for High-Performance Computing (CHPC) in South Africa for providing the computational resources essential to this research endeavor.

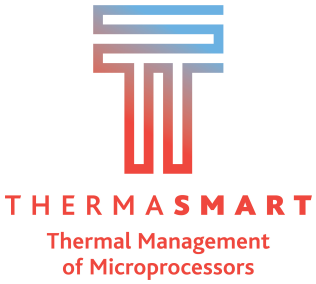

UNIVERSITEIT VAN PRETORIA
UNIVERSITY OF PRETORIA
YUNIBESITHI YA PRETORIA

THE UNIVERSITY *of* EDINBURGH

Contents

List of Figures

Nomenclature

Acronyms

	Description	Dimensions	Units
$N1$	RPI framework for water		
$N2$	RPI framework for cryogenic fluids		
BHTC	Boiling Heat Transfer Coefficient		
BWTC	Bubble Waiting Time Coefficient		
CFD	Computational Fluid Dynamics		
DNS	Direct Numerical Simulation		
LBM	Lattice Boltzman Method		
LS	Level Set		
MD	Molecular Dynamics		
NS	Navier Stokes		
ONB	Onset of Nucleate Boiling		
RPI	Rensselaer Polytechnic Institute		

Greek Symbols

	Description	Dimensions	Units
α	Volume fraction	–	–
β	Cumulative non-dimensional area of influence	–	–
$\boldsymbol{\tau_{\bar{\bar{eff}},q}}$	Effective viscous stress tensor	$\mathrm{ML^{-1}T^{-2}}$	Pa
$\bar{\bar{\boldsymbol{\tau}}}$	Viscous stress tensor	$\mathrm{ML^{-1}T^{-2}}$	Pa
λ	Diffusivity	L^2T^{-1}	$\mathrm{m^2/s}$
Λ_q	Bulk viscosity of phase q	$\mathrm{ML^1T^1}$	$\mathrm{Pa \cdot s}$
μ	Dynamic viscosity	$ML^{-1}T^{-1}$	$\mathrm{Pa \cdot s}$
ρ	Density	ML^{-3}	$\mathrm{kg/m^3}$
σ	Surface tension	MT^{-2}	N/m
θ	Contact angle	–	–

Roman Symbols

	Description	Dimensions	Units
$\bar{\bar{\boldsymbol{I}}}$	Identity matrix	–	–
$\boldsymbol{F_{\vec{lift},q}}$	Lift force	$\mathrm{MLT^{-2}}$	N
$\boldsymbol{\vec{F_q}}$	External body force	$\mathrm{MLT^{-2}}$	N
$\boldsymbol{F_{\vec{td},q}}$	Turbulent dispersion force	$\mathrm{MLT^{-2}}$	N

$\vec{\boldsymbol{F_{vm,q}}}$	Virtual mass force	MLT^{-2}	N
$\vec{\boldsymbol{F_{wall,q}}}$	Wall lubrication force	MLT^{-2}	N
$\vec{\boldsymbol{g}}$	Gravitational acceleration vector	MT^{-2}	$\mathrm{m/s^2}$
$\vec{\boldsymbol{R_{pq}}}$	Interaction force between phases p and q	MLT^{-2}	N
$\vec{\boldsymbol{V_q}}$	Velocity vector of phase q	LT^{-1}	m/s
$\dot{m_{pq,q}}$	Rate of mass transfer from phase q to phase p from the perspective of phase q	MT^{-1}	kg/s
$\dot{q_C}$	Convective Heat Flux	MT^{-3}	$\mathrm{W/m^2}$
$\dot{q_E}$	Evaporative Heat Flux	MT^{-3}	$\mathrm{W/m^2}$
$\dot{q_Q}$	Quenching Heat Flux	MT^{-3}	$\mathrm{W/m^2}$
$\dot{q_W}$	Wall Heat Flux	MT^{-3}	$\mathrm{W/m^2}$
$\dot{q}$	Heat Flux	MT^{-3}	$\mathrm{W/m^2}$
$\cancel{V_b}$	Bubble volume	L^3	$\mathrm{m^3}$
$\cancel{V}$	Total volume	L^3	$\mathrm{m^3}$
$\cancel{V_q}$	Volume of phase q	L^3	$\mathrm{m^3}$
a or H	Impingement height	L	m
A_b	Non-dimensional Area of Influence	–	–
a_{nd}	Non-dimensional impingement height	–	–
$c_{p,l}$	Specific heat Liquid	$L^2T^{-2}\Theta^{-1}$	$\mathrm{J/(kg \cdot K)}$
C_{wt}	Bubble Waiting Time Coefficient	–	–
d	Diameter	L	m
D_w	Maximum Bubble Departure Diameter	L	m
$D_{surface}$	Surface diameter	L	m
e_q	Internal energy of phase q	$\mathrm{ML^2T^{-2}}$	J/kg
f	Frequency of Bubble Departure	T^{-1}	1/s
g	Gravitational acceleration constant	LT^{-2}	$\mathrm{m/s^2}$
h	Heat Transfer Coefficient	$MT^{-3}\Theta^{-1}$	$\mathrm{W/(m^2 \cdot K)}$
h_q	Enthalpy of phase q	$\mathrm{ML^2T^{-2}}$	J/kg
h_C	Heat Transfer Coefficient	$MT^{-3}\Theta^{-1}$	$\mathrm{W/(m^2 \cdot K)}$
$h_{boiling}$	Boiling heat transfer coefficient (BHTC)	$MT^{-3}\Theta^{-1}$	$\mathrm{W/(m \cdot K)}$
h_{pq}	Interphase enthalpy	$\mathrm{ML^2T^{-2}}$	J/kg
I	Turbulence intensity	–	–
K	Dimensionless Area of Influence Constant	–	–
k	Surface curvature	–	–
k_l	Liquid Thermal Conductivity	$MLT^{-3}\Theta^{-1}$	$\mathrm{W/(m \cdot K)}$
$k_{eff,q}$	Effective thermal conductivity of phase q	$MLT^{-3}\Theta^{-1}$	$\mathrm{W/(m \cdot K)}$
$k_{t,q}$	Turbulent thermal conductivity	$MLT^{-3}\Theta^{-1}$	$\mathrm{W/(m \cdot K)}$
N_w	Nucleation Site Density	M^{-2}	$\mathrm{1/m^2}$
Nu	Nusselt number	–	–
P	Pressure	$\mathrm{ML^{-1}T^{-2}}$	Pa
Pr	Prandtl number	–	–

Q_{pq}	Intensity of heat exchange between phase p and q		
r_j	Jet radius	L	m
$R_{surface}$	Surface radius	L	m
Re	Reynolds number	–	–
S_q	Additional source term		
T	Temperature	Θ	K
t	Time	T	s
T_l	Liquid Temperature	Θ	K
t_p	Bubble period	T	s
T_q	Temperature of phase q	Θ	K
T_s	Surface Temperature	Θ	K
T_w	Wall Temperature	Θ	K
T_{sat}	Fluid Saturation Temperature	Θ	K
U	Average velocity	LT^{-1}	m/s
u or v	Velocity component parallel to jet axis	LT^{-1}	m/s
V_d	Maximum Bubble volume	L^3	m^3
We	Weber number	–	–
x, y, z	Cartesian co-ordinates	L	m

Subscripts

	Description	**Dimensions**	**Units**
j	Jet nozzle exit		
l	Liquid		
m	Mean jet axis value		
p	Phase p		
q	Phase q		
v	Vapour		

Chapter 1

Introduction

1.1 Background

Jet impingement boiling is a highly effective method of surface cooling and is particularly suited to high heat-flux applications. One of the earliest known high heat-flux applications is the quenching of steel, a process that has been carried out for millennia [116] and is an integral part of historic and modern society. Industrial jet quenching has been used to enhance this process since at least the 1940's [24]. However, since the development of the transistor in 1947 [159] a new high heat-flux application has emerged; the cooling of microelectronic components. This has become a primary application of interest for jet impingement boiling (dating as far back as 1986 [115]). This stems from the fact that thermal limitations of microelectronic devices is one of the main performance limiting factors [65]. Due to the dogged pursuit of further performance and efficiency increases, through the increase of transistor densities and clock-speeds (the ramification of which is the production of smaller microprocessors that produce higher heat fluxes), it is expected that this issue will only become more prevalent in the future [30]. Having said this, other applications of jet impingement boiling do exist, including but not limited to, the cooling of nuclear reactor cores [115] and cryogenic probe cooling [205]. However, this text will focus primarily on the applications pertaining to microelectronic cooling and the suitability of jet impingement boiling for this application.

In general, microprocessor cooling systems are subject to restrictions in terms of size and fluid type. Furthermore, they have stringent surface temperature requirements that need to be timeously enforced to ensure optimum processor performance and protection. Jet impingement boiling promises to be an effective cooling solution as it meets the requirement of being compact, can utilize a variety of fluids (provided the necessary saturation pressure of the fluid can be maintained within the system) [193] and can remove high heat fluxes with minimal fluctuations in surface temperature. Furthermore, jet impingement boiling has the added benefit of suitability for low pressure drop applications [154] thus allowing for high system efficiencies. The capacity to extract large quantities of heat stems from the fact that jet impingement boiling exploits both sensible (heat absorbed leading up to a phase change) and latent (heat absorbed during a phase change) heat of cooling [195]. When compared to pool boiling, jet impingement boiling has the additional benefit of providing enhanced heat transfer coefficients and delaying dryout [154].

There exist many methods of improving the heat transfer characteristics of jet impingement boiling, including: increasing jet velocity, increasing subcooling and altering impingement surface shape. Two surface modifications of interest include the introduction of singular needles beneath the jet and concave impingement surfaces (see *fig. 1.1*). It was shown by Zhang et al. 2011 [205] that the introduction of single pin at the stagnation point increased the multiphase heat transfer coefficient and delayed dryout. The effect of needle height was not explored in this experiment. Concave impingement surfaces have experimentally been shown to improve the heat transfer coefficient of the surface in both single-phase (see *section 2.2.3*) and multiphase boiling (*section 2.4.6*) applications. Extensive analysis of this phenomenon has been conducted in the single-phase regime, both empirically and computationally. The same cannot be said, however, for the impact of curved surfaces in the multiphase regime. Current literature literature for axisymmetric jets have been restricted to the single curvature (hemispherical) studies of Zhang et al. 2011 [205] and Aihara et al. 1993 [8]. Thus, the impact of varying surface curvature, as well as other parametric variables such as impingement height and local surface modifications (such as the introduction of needles) in addition to curvature are not well understood.

This is in part due to the complex nature of the boiling process itself, for which no empirical solutions for such complex flow conditions are known. In order to better understand the characteristics of heat transfer in complex multiphase flow conditions, two main methods exist: experimental and computational. Experimental methods

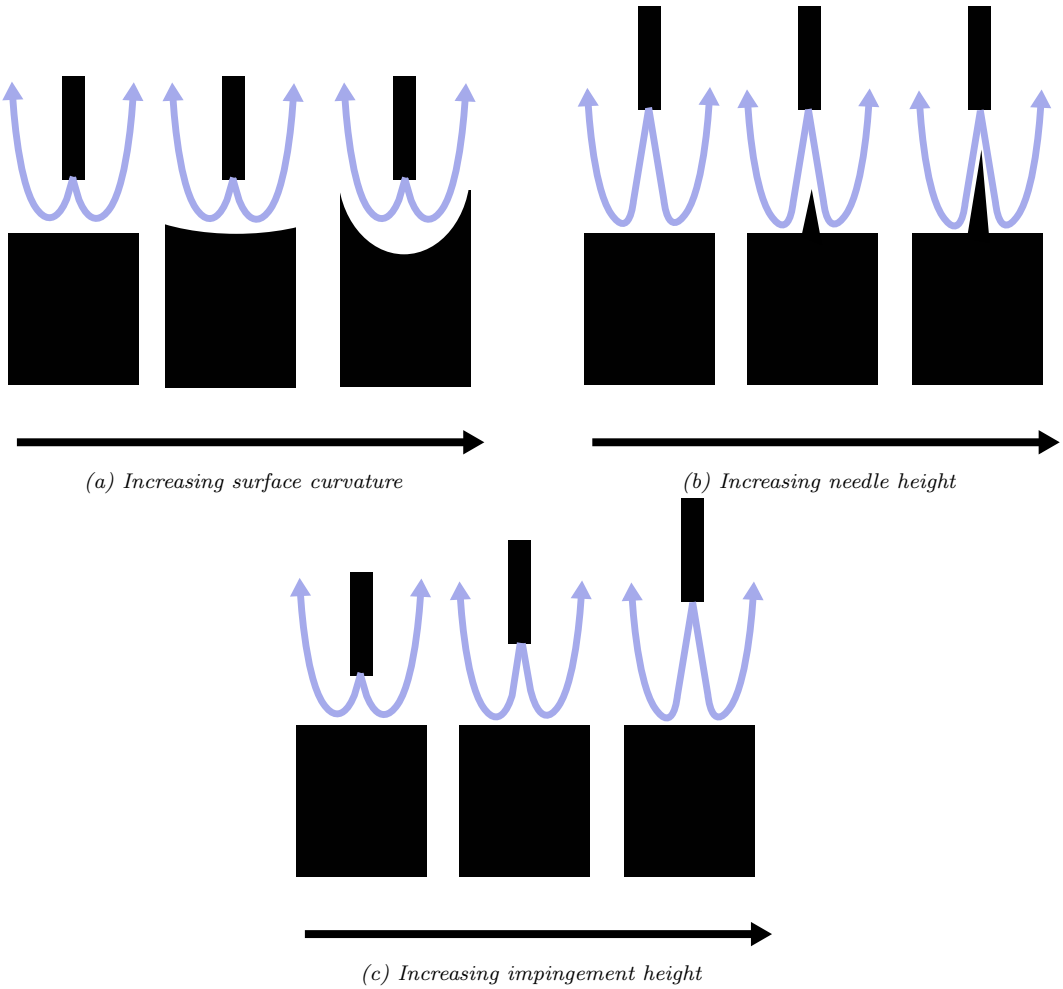

(a) Increasing surface curvature

(b) Increasing needle height

(c) Increasing impingement height

Figure 1.1: Cross sectional diagram of a) varying surface curvature, b) varying needle height and c) varying impingement height

provide data that are realistic, although usually somewhat limited due to the number and spatial limitations of the measurement probes utilized. The second is computational methods such as: Molecular Dynamics (MD), Lattice Boltzman Method (LBM), Direct Numerical Simulation (DNS) and multiphase Eulerian models. These provide the additional benefit of allowing one to analyse local flow variables such as velocity, vapour fraction, density etc... This allows for more rigorous analysis of the underlying enhancement mechanisms, however, more caution needs to be applied in the setup of these computational models in order to validate their performance against experimental observation. Recent literature has focused on employing the multiphase Eulerian model coupled with the Rensselaer Polytechnic Institute (RPI) wall boiling model [195] [114] to accurately predict the wall temperature under a variety of conditions. The multiphase Eulerian model is a Favre averaged approach to solving Navier Stokes (NS) equations and thus introduces additional variables to monitor the turbulence and vapour fraction. This allows for larger cell sizes and time steps resulting in reduced computational cost, making it an ideal model to perform large parametric studies of jet impingement boiling. However, this comes at the expense of requiring additional empirical relations that need to be carefully selected in order to form a closed solution of the NS equations.

In summary, concave surfaces and needles have been shown to independently improve heat transfer during jet impingement boiling. However, very little detail is known regarding the influence of varying surface curvature or the possible improvements that may be made by combining these geometric surfaces. The multiphase Eulerian coupled with the RPI model has shown promising results in the modelling of jet impingement boiling and may help shed light on the parametric influence of these variables. This research promises to be beneficial to the application of microelectronic cooling by exposing the underlying mechanisms behind surface curvature and needle height variation, thus allowing for a greater accuracy of wall temperature prediction at imposed heat fluxes.

1.2 Problem Statement

There exists a gap in known literature pertaining to jet impingement boiling on curved surfaces. In particular, as far as the author is aware, little to no research has been conducted with respect to the impact of varying surface curvature on heat transfer coefficient during multiphase jet impingement. In addition, the influence of varying jet impingement height and introduction of needles on curved surfaces has yet to be explored in detail.

1.3 Objectives

In order to address this problem statement, the following objectives have been formulated:

1. Survey of applicable literature in jet impingement and boiling to describe the extent of the gap in jet impingement boiling research for concave and needled surfaces.
2. Comparison of available empirical models used in the RPI wall boiling models and the development of new correlations if required.
3. Validation of two separate CFD models against the cryogenic application of Zhang et al. 2011 [205].
    - Development of a CFD model for water and evaluation of modifications necessary for extension to the current application.
    - Development of a second CFD model specifically for cryogenic fluids.
    - Execution of a mesh independence study and assessment of temporal and boundary location effects.
    - Full comparison of the performance of the CFD models across the entire range of experimental results reported by Zhang et al. 2011 [205].
    - Detailed comparison of the CFD models against one another and finalization of settings to be used in the parametric study.
4. Parametric study of the effects of varying the concavity and needle geometry on the heat transfer performance using model the best CFD model.
    - Evaluation of the effect of curvature on: boiling heat transfer coefficient, wall heat flux partitioning, liquid temperature, vapour fraction distribution, liquid velocity, solid temperature, area of influence, bubble departure diameter, nucleation site density and bubble departure frequency.
    - Evaluation of the effect of needle height using the same metrics mentioned above.
    - Evaluation of the effect of impingement height using the same metrics mentioned above.
    - Full parametric study investigating a broad array of possible combinations for curvature, needle height and impingement height and the resulting effect on the boiling heat transfer coefficient.

1.4 Dissertation Layout

The document begins with a literature review in *chapter 2* that presents a brief overview of single-phase jet impingement, boiling and multiphase jet impingement. Related heat transfer enhancement mechanisms are also addressed. Thereafter, in *chapter 3*, an extensive overview of the Rensselaer Polytechnic Institute (RPI) wall boiling model and its closing sub-models are discussed. Particular emphasis is placed on sub-model applicability to cryogenic fluids and the development of a new area of influence model in conjunction with these sub-models. *Chapter 4* describes the validation of the experimental results of Zhang et al. 2011 [205] using liquid nitrogen. This is done for a flat, single needle and hemispherical case using two separate CFD models. Both models employ a 2D axisymmetric domain coupled with the multiphase Eulerian model. However, the first CFD model ($N1$) employs commonly used RPI sub-models for water and attempts to extend applicability to the current application through substantial modification of the bubble waiting time coefficient. The second CFD model ($N2$) uses the aforementioned RPI sub-models (from *chapter 3*) tailored for cryogenic fluids. A parametric study considering the effect of varying curvature, needle height and jet impingement height on wall temperature is then presented in *chapter 5* alongside a detailed analysis of heat flux partitioning on the surface as well as volume fraction and other flow variable analysis using both models. The most favourable geometric configuration is then identified and presented. Finally, *chapter 6* concludes with a summary of the observed trends and identification of opportunities for future work.

Chapter 2

Literature Review

2.1 Introduction

The literature review begins with an overview of single-phase jet impingement, which, due to its relative simplicity and extensive research, lays the foundations for analyzing multiphase impingement phenomena in latter sections. Thereafter, the concept of boiling is introduced utilising pool boiling, with the effects of roughness, wettability and pressure being investigated. The concept of boiling is then extended to flow boiling in tubes with an overview of the energy and force balance on individual bubbles within this environment. Methods of understanding boiling through experimental and numerical approaches are then stated. Finally, multiphase jet impingement is addressed. A brief investigation of hysteresis effects and the impact of: velocity, subcooling, impingement height and cryogenic fluids on the boiling curve is given. Additionally, literature pertaining to boiling on curved surfaces, pinned surfaces and a summary of previous numerical work in jet impingement boiling using the multiphase Eulerian model coupled with the RPI wall boiling model is provided. This is followed by a synopsis of the key insights gained in each section.

Detail regarding the multiphase Eulerian model has been omitted from *chapter 2* as it has been extensively covered by the following : [137], [195], [114], [194] and [113]. However, an overview can be found in *appendix A*.

Literature pertaining to the RPI wall boiling model has been deferred to *chapter 3* as a more detailed analysis of the closing models is required. Specifically the applicability of these closing models for use in cryogenic fluid applications such as those of the selected validation case presented in *chapter 4*. In addition, analysis in *chapter 3* yields a new correlation for the area of influence, as well as, a deeper understanding of applicable ranges of the bubble waiting time coefficient for cryogenic fluids. Thus *chapter 3* forms a combination of literature and novel work that necessitates its own chapter.

2.2 Single-Phase Jet Impingement

Single-phase flow is a well-established field of study compared to multiphase flow. The understanding gained from single-phase studies provides a springboard for investigating the mechanisms of enhanced heat transfer in multiphase impingement flows. Detailed below are the various jet types of jet impingement, followed by a focus on the hydrodynamics of submerged turbulent axisymmetric jets and the parameters influencing their heat transfer performance.

Notable reviews covering this topic are contained in the following references: [44], [80], [145] and [167].

2.2.1 Jet Types

Single-jet impingement can be broadly classified into five categories:

1. **Free-Surface Jet Impingement** (*fig. 2.1a*) is defined by a jet of high density fluid (e.g. water) flowing through an immiscible low density fluid (e.g. air) before contacting a solid surface and spreading out along the surface [193] (or spraying up from the surface if sufficiently large jet nozzle exit Weber numbers ($We_j = \frac{\rho U_j d_j}{\sigma}$) and nozzle to surface distances are achieved [149]). The surrounding immiscible fluid often has a characteristically low viscosity such that the shear forces at the fluid-fluid boundary interface are negligible, allowing the jet to flow unimpeded towards the impingement surface.

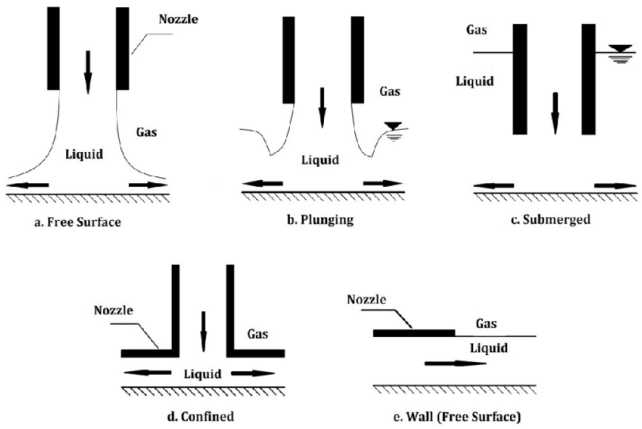

Figure 2.1: Types of jet impingement, reproduced from [131]

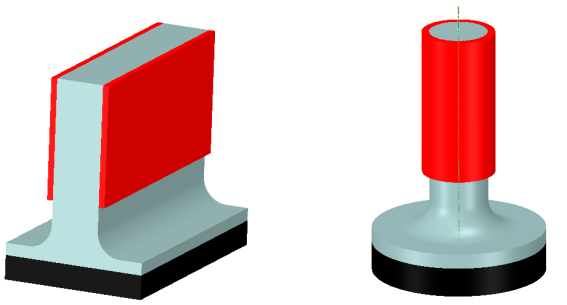

(a) Slot Jet *(b) Axisymmetric Jet*

Figure 2.2: Sub-classification of jet impingement types (shown for free-surface jet impingement)

2. **Plunging Jet Impingement** (*fig. 2.1b*) involves impingement into a pool of miscible fluid before contacting the surface. The pool height must be less than the nozzle to surface distance.[193]

3. **Submerged Jet Impingement** (*fig. 2.1c*) involves the fluid impinging onto a surface with the jet's complete trajectory being through a miscible fluid (usually of the same type as the impinging jet). This case is of particular interest due to the unique effects of turbulence induced by the surrounding fluid and their resulting impact on the heat transfer coefficient at the stagnation point and downstream.[193] Additionally, submerged jets lend themselves to applications in compact confined systems. Multiple studies have been conducted for this type of impingement to evaluate the effect of nozzle height, diameter, Reynolds number, turbulence level and nozzle angle (to name a few parameters) on heat transfer coefficient as will be elaborated on in *section 2.2.3*.

4. **Confined Jet Impingement** (*fig. 2.1d*). This is similar to submerged jet impingement, with the main distinguishing attribute being the non-negligible development of a boundary layer induced by a confining surface that influences the flow characteristics [193]. It is important to note that this may be applicable to submerged jets with sufficiently small nozzle heights such that the wall thickness at the lower edge of the nozzle can be viewed as a confining plate of finite distance.

5. **Wall Jet Impingement** (*fig. 2.1e*). Unlike the other categories, this is characterised by the average jet exit velocity being parallel to the wall as opposed to perpendicular. Shown in (*fig. 2.1e*) is a free-surface wall jet, although submerged applications could conceivably exist. It could be argued that wall jet impingement is simply an extension of either the submerged or free jet impingement in the extreme scenario where the impingement angle is zero.

Utilising nozzle shape, the first four categories can be further divided into three subcategories: **2D slot jets** (*fig. 2.2a*) (provided the slot is of sufficient length to enforce an approximate 2D flow far from the bounding edges), **round axisymmetric jets** (*fig. 2.2b*) and **arbitrary shaped jets**. Here, arbitrary shape jets are defined to include: square/rectangular jets [168], elliptical jets [161] and any other jet nozzle shapes that fail to fall into the first two subcategories.

Round and slot jets appear most often in literature and will be the focus of the following sections. They have the additional benefit of being able to be approximated, in the case of laminar or mean turbulent flow, using axisymmetric and symmetric planar model assumptions respectively. This greatly reduces the number of cells required in the numerical domain, thereby lowering computational costs. Submerged axisymmetric jets are the closest in application to the validation case considered in *chapter 4* and the subsequent parametric study (*chapter 4*).

2.2.2 Hydrodynamics of Submerged Turbulent Jets

Figure 2.3 displays the axial velocity, radial velocity and turbulence profiles of a fully developed submerged 2D free stream jet as it enters a body of fluid of the same composition of that issuing from the jet. Here, u_m denotes the time averaged mean velocity at the centreline in the axial direction which is a variable quantity. u_j is a constant and denotes the value of u_m at the precise instant that the fluid leaves the nozzle. u' is the root-mean-square of the turbulent velocity fluctuations. Turbulence intensity based on the local mean velocity is defined as $I_m = u'/u_m$, whilst the turbulence intensity based on the mean velocity at the exit of the nozzle is

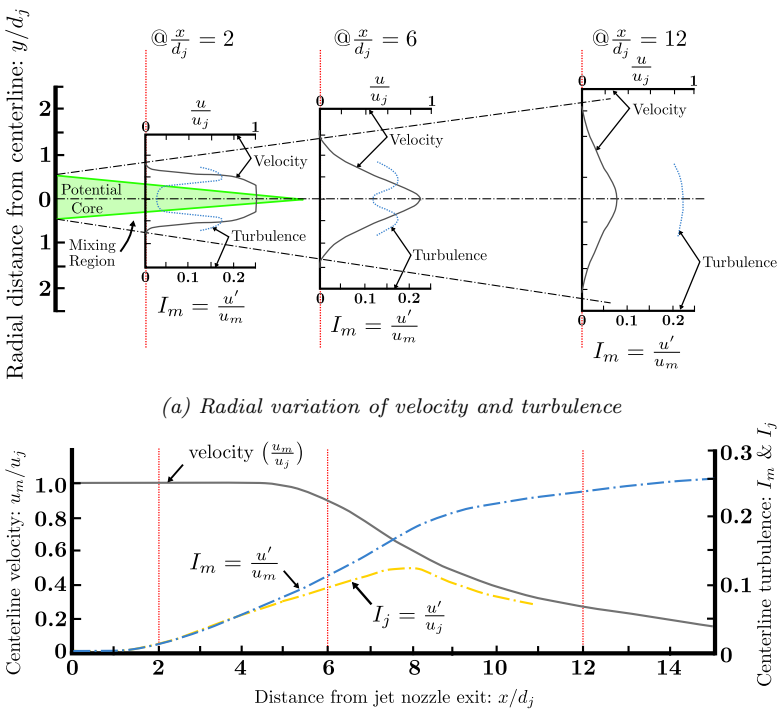

(a) Radial variation of velocity and turbulence

(b) Axial variation of velocity and turbulence

Figure 2.3: Schematic variation of velocity and turbulence, adapted from [55]

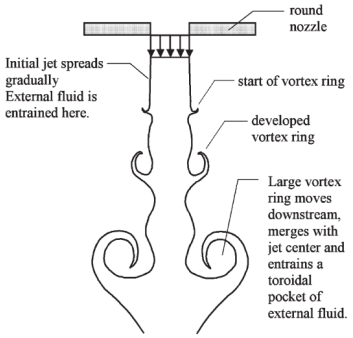

(a) Free stream jet

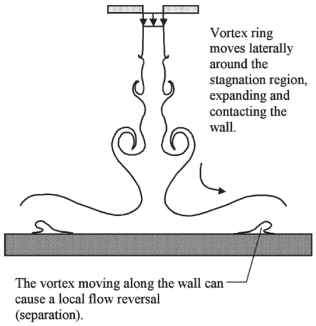

(b) Impinging jet

Figure 2.4: Development and propagation of vortices in axisymmetric turbulent jet, reproduced from [212]

defined as $I_j = u'/u_j$. As one can see from *fig. 2.3b*, the jet initially exits the nozzle with $I_m = I_j \approx 0$. However, as the distance from the nozzle increases, both turbulence intensities increase. This is due to the interaction of the outer fluid layer of the jet with the slower surrounding fluid resulting in Kelvin–Helmholtz like instability [212]. This causes vortex formation (see *fig. 2.4a*) and results in the entrainment of the surrounding fluid as well as the production of mixing-induced-turbulence at a variety of length scales in this outer jet region (see *fig. 2.3a*). The oscillations in velocity (caused by the turbulence) propagate temporally through the fluid towards the centreline. It is important to note that the increase in axial turbulence does not affect the mean velocity of the jet axis (u_m) until approximately five jet diameters from the exit. This denotes the end of the 'potential core' past which point, the axial velocity decreases monotonically due to the sharing of momentum with the entrained fluid. The precise termination point of the potential core is defined as the location along the jet centreline where the dynamic pressure decays to 95% of its original value at the nozzle exit [212]. I_j reaches a maximum at a length of approximately eight diameters at which point, the slowing mean velocity has a dampening effect on I_j. However, I_m continues to grow due to the value of u_m decaying faster than that of u' [55].

The addition of a perpendicular impingement surface in the path of the jet results in the formation of a stagnation point at the wall-jet-axis intersection (*fig. 2.5*). Leclerc 1950 [104] and Schrader 1961 [163] independently showed that the effect of a wall boundary condition (and resulting reduction in velocity) is only felt by circular jets emanating at roughly 1-2 jet diameters from the wall. Thus the development of the free stream characteristics of the jet leading up to impingement are expected to and have been proven to play a role in the velocity and thermal boundary layer development at impingement. The reduction in velocity as fluid approaches the stagnation point (*fig. 2.3b*) is accompanied with an increase in pressure due to Bernoulli's principle.

From the stagnation point, the flow turns through $\frac{\pi}{2}$ radians and accelerates radially outwards. The resulting pressure profile along the wall is shown in *fig. 2.6* and is relatively insensitive to Reynolds number. In axisymmetric jets, Schrader 1961 [163] showed empirically that the boundary layer thickness is expected to remain very thin and approximately constant within a radius of approximately 1.1 jet diameters of the stagnation point for laminar flows. However, a slightly contradictory result was found in an empirical solution by Kezios 1956 [90], who showed a slight thinning in the boundary layer at approximately 0.5 diameters from the stagnation point. This phenomenon is believed to manifest itself in turbulent flows as well and is is thought to result from the large negative pressure gradients surrounding the immediate vicinity of the stagnation zone (*fig. 2.6*) which serve to stabilize the flow in this region and prevent transition to turbulence, coupled with fluid acceleration at

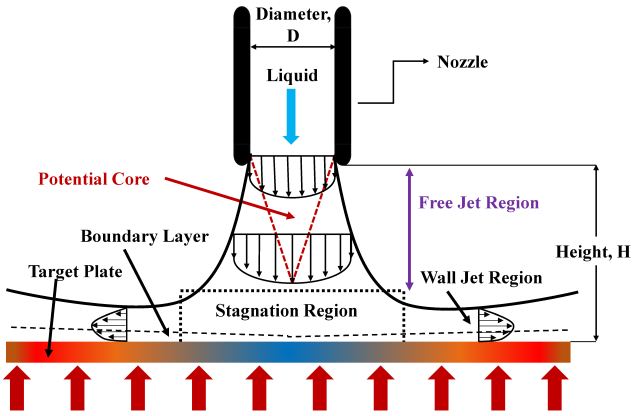

Figure 2.5: Free-surface jet impingement flow regions, reproduced from [81]

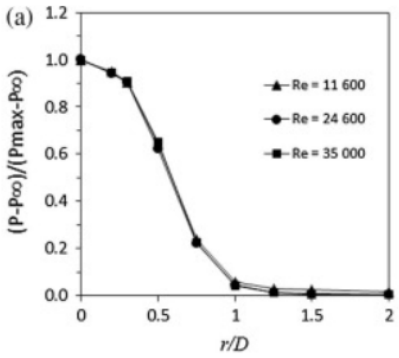

Figure 2.6: Pressure distribution along the wall of a free-surface axisymmetric jet (impingement height: $a = 2d_j$) , reproduced from [6]

the stagnation point due to the conservation of momentum [212]. Supporting evidence of this thinning is found in *section 2.2.3.*

Further away from the stagnation point, as the pressure gradient reduces, the boundary layer is expected to grow, transition to a turbulent and then continue growing as distance from the stagnation point increases and radial velocity decreases. This region is termed the "wall jet region" (*fig. 2.5*). Strong vortices (see *fig. 2.4b*) may result in flow reversal within the wall jet region, temporarily degrading the heat transfer coefficient in this region [212].

2.2.3 Parameters Influencing Heat Transfer Characteristics

In cooling applications, the surface of interest is heated by either a constant heat flux or constant surface temperature boundary condition (in excess of the incoming fluid temperature). The local single-phase heat transfer coefficient (h) is defined as [212]:

$$h = \frac{\dot{q}}{T_l - T_w} = \frac{-k_l \frac{\partial T}{\partial n}}{T_l - T_w} \tag{2.1}$$

where k_l is the local thermal conductivity of the fluid, n is the direction normal to the wall, T_l is the local temperature of the fluid and T_w is the wall temperature and $\dot{q_C}$ is the convective heat flux. In the case of high Mach number jets, where the associated reduction in velocity results in an appreciable increase in local fluid temperature, T_l is replaced with T_{l0}. Where T_{l0} is the calculated local liquid temperature in the case of an adiabatic wall [212].

Due to the unknown variation in fluid temperature along the surface, some authors may choose to compute the heat transfer coefficient based on properties defined at the jet exit:

$$h_j = \frac{q}{T_j - T_w} = \frac{-k_j \frac{\partial T}{\partial n}}{T_j - T_w} \tag{2.2}$$

where k_j and T_j are evaluated at the jet exit.

The non-dimensional Nusselt number is then defined as:

$$Nu = \frac{h_j d_j}{k_j} \tag{2.3}$$

Refer to *fig. 2.7* at a $Re_j = 30\ 000$. This is a characteristic plot of Nusselt number along the wall for an axisymmetric jet at small nozzle to jet surface spacing ($L/d_j \leq 4$ [within the potential core]) [85] and low inlet turbulence intensity. One should note the presence of two prominent peaks. The first peak is thought to be attributed to either the thinning of the boundary layer until $x/D = 0.5$ [55] or the increase in turbulent kinetic energy in this region due to turbulent mixing on the outer edge of the fluid flow [141]. However, local thermal boundary layer thinning, as a result of flow acceleration, is supported by a numerical study conducted by Rohlfs et al. 2014 [157]. The second peak is attributed to the transition from laminar to turbulent flow [55]

and its exact location has been found to be dependent on both Reynolds number and impingement height [139]. Following the second peak, the Nusselt number decreases monotonically with increasing radial distance. This is due to thermal and hydrodynamic boundary layer development as a result of local fluid temperature increase and reduced radial velocity. [139].

Several key parameters have been identified that influence the heat transfer coefficient of the jet, including: Reynolds number, jet impingement height, inlet turbulence intensity, swirl, pulsating jet inlets and impingement surface shape.

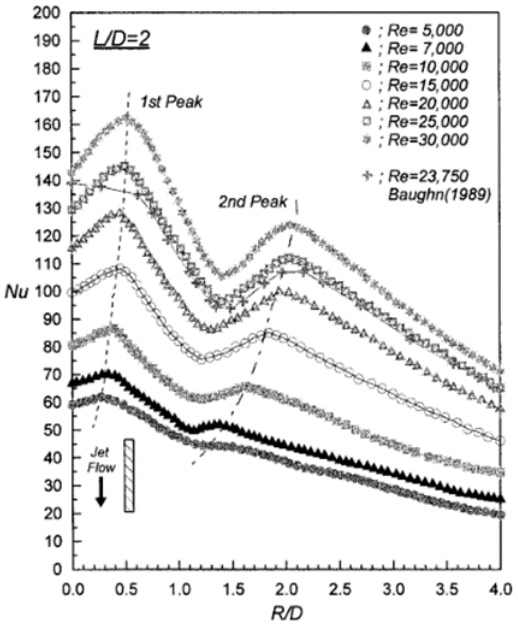

Figure 2.7: Variation of the heat transfer coefficient along the impingement wall for an axisymmetric jet at differing Reynolds numbers (L/D=2), reproduced from [85]

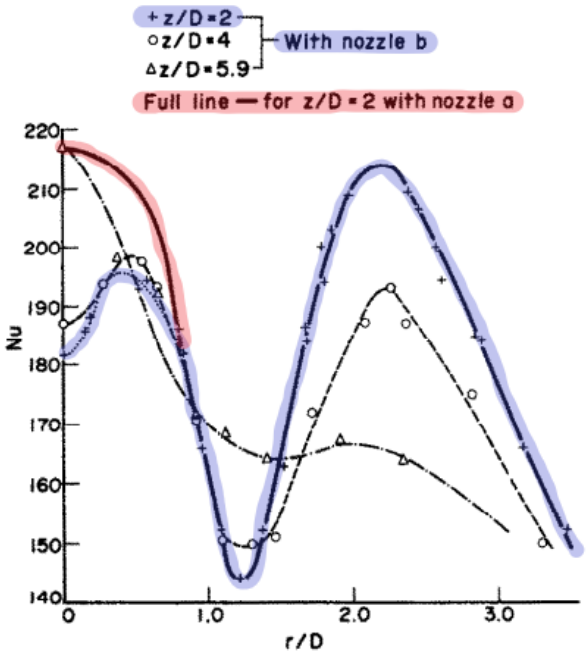

Figure 2.8: Radial distribution of Nu for an axisymmetric air jet ($Re = 66\ 000$, $I_{j(nozzle\ a)} \approx 3.2\%$, $I_{j(nozzle\ b)} \approx 0.5\%$), reproduced form [67]

Reynolds number

The jet Reynolds number is defined as:

$$Re_j = \frac{\rho_j u_j d_j}{\mu_j} \tag{2.4}$$

where the fluid properties of density (ρ_j) and viscosity (μ_j) are evaluated at the jet inlet temperature and pressure.

As shown in *fig. 2.7*, increasing the Reynolds number results in an increase in the Nusselt number due to a reduction in boundary layer thickness.

Inlet turbulence intensity

Increasing the inlet turbulent intensity at the nozzle exit (through use of rougher pipes or turbulence promoters within the nozzle (such as mesh grids)) results in a significant increase in heat transfer at the stagnation point. This shifts the maximum of the inner peak to the centre of the jet and overrides the effect of boundary thinning seen at lower inlet turbulence intensities (see *fig. 2.8*). This emphasizes that the initial turbulence level upon arrival at the stagnation point plays a critical role in determining the boundary layer formation and hence heat transfer characteristics in this region [55].

Jet impingement height

The dimensionless impingement height (a_{nd}) is defined as:

$$a_{nd} = \frac{H}{d_j} = \frac{a}{d_j} \tag{2.5}$$

$a = H$ is the height of the nozzle above the stagnation point.

Increasing impingement height results in increasing turbulence intensity of the jet at stagnation point arrival (see *section 2.2.2*). In addition, the diameter of the jet is expanded as it propagates through a larger free stream region [212]. This results in the "lip" of the jet expanding with increasing impingement height. This is evidenced by the broadening of the wall pressure profile shown in *fig. 2.10*. Recalling that large negative pressure gradients are attributed to suppressing the transition to turbulence [55], this results in the location of the outer peak in Nusselt number shifting to the right as the impingement height is increased (see *fig. 2.9*). The magnitude of the second peak is seen to decrease with a shift to the right as a result of a thicker thermal boundary layer (lower wall-fluid temperature differential) and reduced fluid velocity as the jet expands radially. At large impingement heights the second peak is seen to disappear entirely. Depending on the initial turbulence of the jet, the inner peak may be present at low impingement heights, but is seen to flatten and shift to the stagnation point with increased impingement height due to increased turbulence intensity upon arrival.

There is a large drop in peak stagnation point pressure as the impingement height is increased beyond the potential core length (illustrated by the transition from $H/d_j = 10$ to $H/d_j = 12$ in *fig. 2.10*). Increases in impingement height outside of the potential core serve to deteriorate the average Nusselt number [29] due to lower impingement velocity and decreased jet turbulence intensity (I_j).

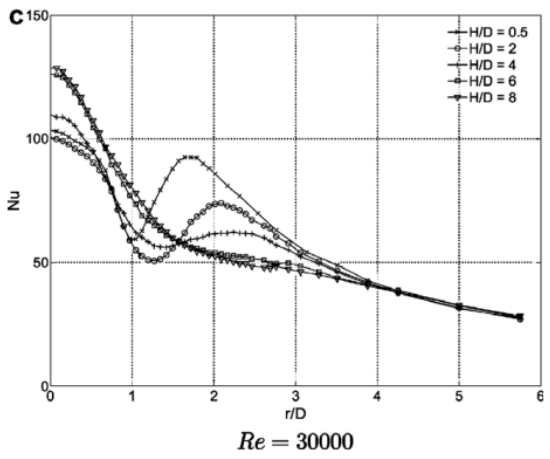

Figure 2.9: Variation of the heat transfer coefficient along the impingement wall for an axisymmetric air jet at differing impingement heights, reproduced from [139]

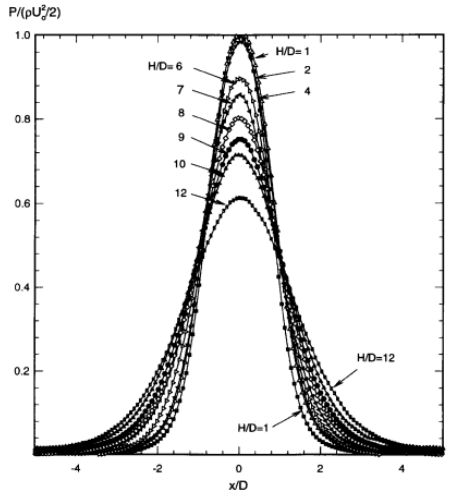

Figure 2.10: Wall pressure distribution for a planar air jet at $Re = 11\ 000$, reproduced from [182]

Concave impingement surfaces

Surface curvature (k) can be defined as:

$$k = \frac{d_j}{D_{surface}} = \frac{r_j}{R_{surface}} \tag{2.6}$$

where r_j is the radius of the jet and $R_{surface}$ is the radius of the surface (see *fig. 2.11*).

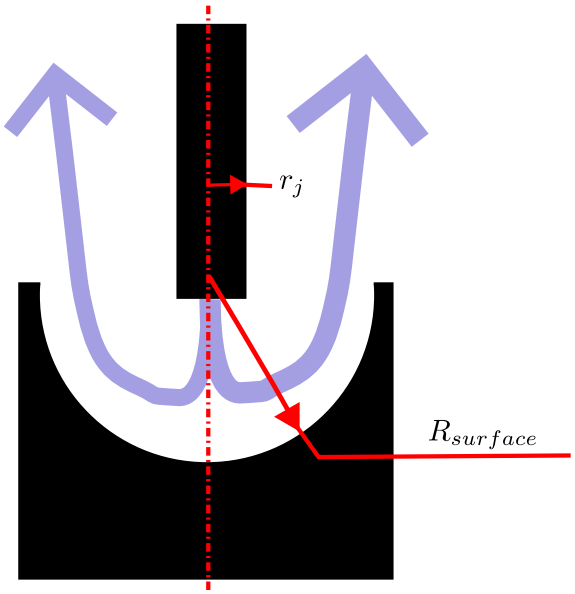

Figure 2.11: Visual representation of parameters presented in eq. (2.6)

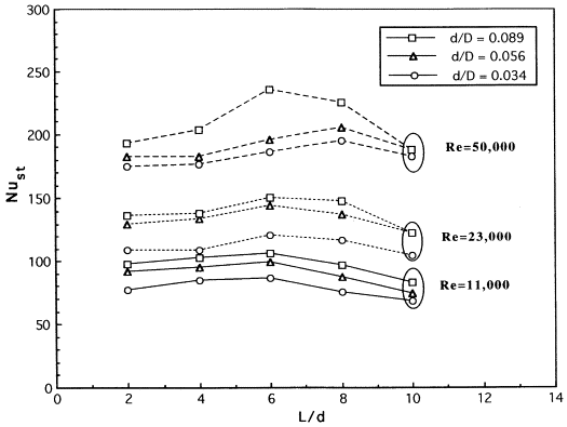

Figure 2.12: Stagnation point Nusselt number of an axisymmetric jet at varying surface curvatures, impingement heights and Reynolds numbers, reproduced from [106]

Lee, Chung, and Won 1999 [106] demonstrated that the stagnation point Nusselt number (*fig. 2.12*) and wall jet Nusselt number (*fig. 2.13*) increases consistently with increasing surface curvature over a range of impingement heights and Reynolds numbers. Similar results for enhancement on curved surfaces have been found by [198], [176], [68] and [56]. These have been attributed to:

- Increases in surface area (over that of a flat plate) [68].
- Increases in radial fluid acceleration at the stagnation point and hence enhanced boundary layer thinning [106]
- The formation of large scale Taylor-Görtler vortices during turbulent transition that enhance turbulent mixing. It is beleived that centrifugal forces create flow instability along the surface resulting in pairs of counter rotating vortices with axis of rotation in the streamwise direction (see *fig. 2.14*) [176], [56], [162], [188].

Erasmus, Lubkoll, and Backström 2021 [46] successfully used the transition SST RANS turbulence model to predict the heat transfer and pressure drop of a single axisymmetric air jet impinging on a concave hemispherical surface.

Ekkad and Kontrovitz 2002 [43] experimented with single-phase impingement of an array of air jets onto a dimpled surface with the varying dimple depths and dimple placement both inline and staggered. No manifold was utilized to reduce cross flow effects. It was found that dimples reduced the heat transfer coefficient compared to impingement on a flat plate. This was attributed to a bursting phenomenon that caused the turbulence generated in the dimple to break up the potential core and presumably lead to thicker thermal boundary layers particularly surrounding the stagnation pointy. It was found that the deeper inline dimples performed the best of the tested configurations. It is worthy to note that crossflow effects influence this study and that nozzle diameter and height was not varied in this study.

Jet impingement height and Reynolds number effects were found to behave in a similar manner to those presented in *section 2.2.3* and *section 2.2.3*.

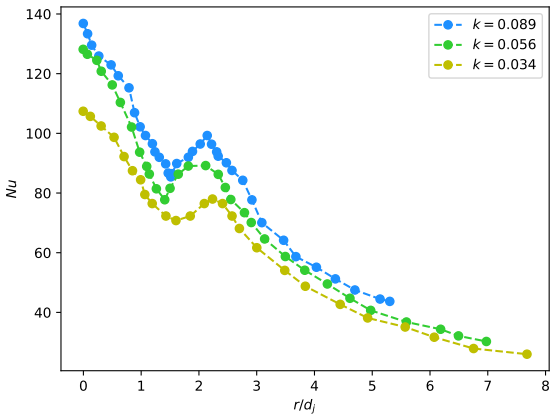

Figure 2.13: Local wall Nusselt number for axisymmetric jet at varying curvatures at $Re = 23\ 000$ and $a = H/d_j = 2$, adapted from [106]

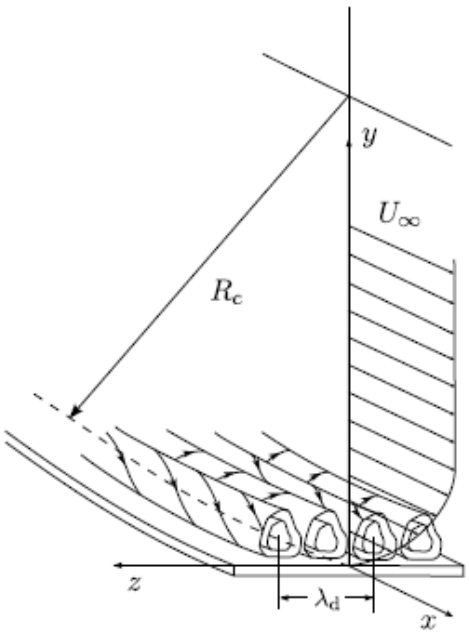

Figure 2.14: Illustration of Taylor-Görtler vortices, reproduced form [1]

Convex and Conical impingement surfaces

Lee, Chung, and Kim 1997 [105] also experimented with convex hemispherical surfaces ($k = 0.034 - 0.089$). It was shown that increased curvature resulted in higher heat transfer coefficients. The heat transfer coefficient exhibited similar trends to their concave impingement experiment [106] (see *fig. 2.12*) with regards to Reynolds number and impingement height. Comparable findings were later presented by [33] for round jets impinging onto semi-cylindrical convex surfaces with varying curvature ranging from $k = 0.18 - 0.38$.

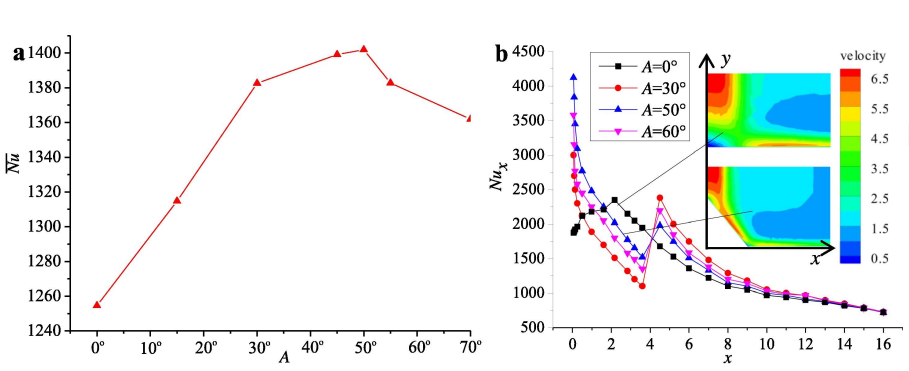

Figure 2.15: Local and average Nusselt number for varying cone angles at $u_j = 6$ m/s, $H/d_j = 4$, $d_1/d_j = 2$, $q = 80$ W/cm^2, reproduced from [174]

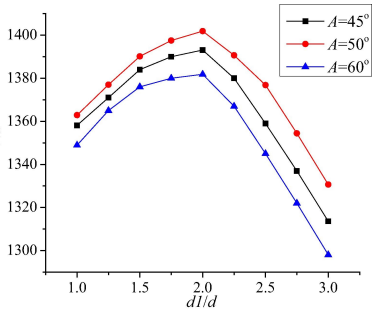

Figure 2.16: Average Nusselt number for varying cone base diameter ratios at $u_j = 6$ m/s, $H/d_j = 4$, $q = 80$ W/cm^2, reproduced from [174]

Tang et al. 2017 [174] investigated impingement onto convex conical surfaces. An experimental test was conducted utilising single-jet impinging onto a singular cone and the results were used to validate their computational study. They found a local maximum in cone angle ($A = 50°$) under set conditions (see *fig. 2.15*). The increase in performance of the cone over the flat plate was attributed to the presence of an additional impact region at the base of the cone that serves to thin the thermal boundary layer in that region. Increases in surface area were also discussed as an enhancement mechanism. The maximum is thought to result from a balance between the primary and secondary impingement zone heat transfer as a result of the change of dimensionless velocity and temperature gradient vector with cone angle. They also investigated the effect of cone base diameter ($d1$) to jet diameter ratio ($d1/d_j = 1 - 3$) and discovered another local maximum (see *fig. 2.16*). Initially there is an increase in heat transfer as the cone base diameter ratio is increased due to larger surface area but a decrease soon follows as a result of increased entrainment in the freestream jet.

Froissart et al. 2021 [52] expanded on the work of Tang et al. 2017 [174] and computationally investigated the

effect of adding a hump to the base of the cone so as to induce turbulence. Results for larger humps showed improved heat transfer over smooth cone solutions.

Again impingement height and Reynolds number effects were found to behave in a similar manner to those presented in *section 2.2.3* and *section 2.2.3* for all conical surfaces discussed.

2.3 Boiling

2.3.1 Pool boiling on Flat Surfaces

Boiling can be subdivided into pool boiling and flow boiling. Jet impingement typically falls into the latter category. However, because pool boiling is generally better understood (due to the relative ease with which experiments can be performed and the lack of flow specific parameters such as driving velocity and pressure gradients), an overview of pool boiling is presented. It should be noted that many of the same mechanisms of pool boiling translate to flow boiling and thus provide a necessary framework to understand flow boiling. Furthermore, in regions sufficiently far from the stagnation point, where the fluid velocity is near zero, pool boiling may be the dominant boiling mechanism in jet impingement boiling as noted by Ludick et al. 2023 [114].

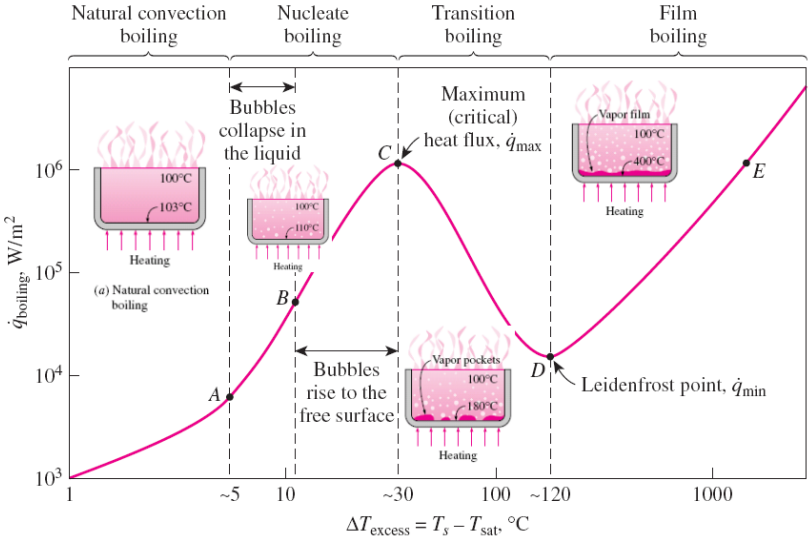

Figure 2.17: Boiling curve of water at 1 atmosphere, reproduced from [45]

The boiling heat transfer coefficient (BHTC) ($h_{boiling}$) is defined by *eq.* (2.7) [102] based on the surface temperature (T_s) and the saturation temperature of the fluid (T_{sat}).

$$q = h_{boiling}(T_s - T_{sat}) \tag{2.7}$$

Pool boiling comprises of 4 regimes (see *fig. 2.17*), described in order of monotonically increasing wall heat flux:

1. **Convective boiling** results from low wall superheats (approximately 5°C for water). This causes the fluid at the heater interface to become slightly superheated and rise by means of natural convection, resulting in an increase in vapour pressure, which translates to the formation of a vapour layer on the free-surface of the fluid. Low heat transfer coefficients are associated with this regime and there is an absence of bubble formation. Note, in flow boiling applications, forced convective heat transfer (enhanced by increasing natural convection) is dominant in this regime and free-surface vapour formation is unlikely due to the typically subcooled temperature of the surrounding fluid outside of the developed surface thermal boundary layer.

2. **Nucleate boiling** is the next regime. The onset of nucleate boiling (ONB) is defined by the formation of the first bubble at a nucleation site on the surface. The bubble then grows and detaches due to buoyancy forces. At the early stage of nucleate boiling, the bubbles shrink and collapse as they rise (due to heat exchange with the surrounding fluid). This is more pronounced in subcooled flow boiling applications. As greater heat fluxes are applied, more nucleation sites are activated and bubble formation occurs at a steadier rate. Bubble sizes also grow resulting in bubbles rising higher before collapse. Increasing the heat flux further results in the bubble coalescing on the surface or after departure and forming slugs that rise through the fluid. The formation of bubbles results in large amounts of turbulence in the near wall

region that encourages mixing. This disrupts the thermal boundary layer and results in high heat transfer coefficients associated with this regime (far greater than those of simple convection). Due to the fact that relatively low wall superheats are required to remove large quantities of heat (due to the large rate of change of heat flux with respect to increases in surface temperature), this is the predominant regime that most boiling applications are designed to operate in. [102] The presence of more nucleation sites (i.e. as a result of increased surface roughness) lowers the wall superheat required for ONB. If the heat flux is increased slightly further after slug formation, the critical heat flux is reached (CHF). This marks the end of nucleate boiling. The nucleate boiling regime has a large boiling heat transfer coefficient (BHTC). Therefore, large heat flux increases are associated with small wall temperature increases, making it the ideal regime for cooling applications [193].

3. **Film boiling**. Any additional heat flux past the CHF will cause a film of vapour to form on the wall surface. This forms an insulating barrier between the wall surface and the fluid above, resulting in the primary means of heat transfer transitioning from convection to radiation heat transfer. This necessitates a large increase in surface temperature in order to achieve the same heat flux and is commonly termed 'burnout' as the surface temperatures required are usually in excess of the melting point of the surface material (although this is dependent on the fluid and wall material utilized). Provided that the surface material can withstand the necessary superheat, the next regime of boiling is reached. This is termed film boiling and the radiation heat transfer increases with increasing surface temperature, although the value of the heat transfer coefficient in this regime is generally lower than that of nucleate boiling. [102]
4. **Transition boiling** exists between film boiling and nucleate boiling, and is achieved by lowering the heat flux (or by imposing the seldom encountered constant surface temperature boundary condition). This regime is of little interest in the current application as it is seldom encountered in practice, especially when utilizing applied heat flux boundary conditions coupled with low surface temperature requirements such as those imposed by microelectronic components.

Roughness

The prevailing theory in literature is that nucleation sites consist of cavities containing entrapped vapour [12]. It has been shown that only cavities of a certain shape [15] and within a certain size range [69] can serve as nucleation sites. Re-entrant cavities (that resist full re-wetting upon bubble departure) are thought to form more stable nucleation sites [60]. Thus surface cavity shape and size distribution play an important role in boiling and can result in large boiling heat transfer disparities between different wall surface finishes. Average roughness (R_a) has been used as a loose measure of a cavity size and distribution, although the validity of this assumption due to the inability of R_a to properly define cavity shape and size has been expressed [82] [103]. Nevertheless, it has been shown that increased surface roughness generally results in earlier incipience and increased nucleation site density that initially enhances the BHTC [82]. Discussion regarding the CHF and BHTC with further progression up the boiling curve is slightly more nuanced as wettability has been shown to play a large role. Hydrophilic surfaces have been reported to experience increases in BHTC further up the nucleate boiling curve as well as increases in CHF with increasing surface roughness. This has been attributed to increased capillary wicking. However, hydrophobic surfaces have been reported to experience a decline in BHTC with progression up the boiling curve and a decline in CHF with increasing roughness. This has been attributed to increased blanketing [92].

Jones, McHale, and Garimella 2009 [82] used both Fluorinert™ FC-77 (a highly wetting fluid with contact angle $\approx$ 49° [123]) and water (reported to be less wetting in [82]) for pool boiling on aluminium electric discharge machined (EDM) surfaces of varying average roughness (R_a values). They noted earlier incipience for both fluids as roughness increased as a result of larger cavity sizes, a theory supported by [60]. They found that the highly wetting FC-77 experienced a larger and continuous increase in heat transfer coefficient as shown in *fig. 2.18a* compared to water with a heat transfer coefficient that initially increased, stabilized and then again increased *fig. 2.18b*. This was attributed to FC-77 requiring smaller cavity sizes as a result of its higher wettability and hence a continuous increases in heat transfer with increased roughness and higher active nucleation site densities. On the other hand, water requires larger cavity sizes and it is thought that at some roughness values there is not an appreciable increase in the requisite number of applicable cavities [82]. This should serve as a cautionary tale that the size and shape of the cavities play an arguably more important role than the roughness.

Expanding on the work of [82], McHale and Garimella 2010 [123] illustrated that increasing roughness for a highly wetting fluid (FC-77) resulted in increased nucleation site density, increased bubble departure frequency and reduced bubble departure diameters at lower wall superheats. For hydrophilic surfaces, however, increased bubble departure diameters and reduced bubble departure frequency have been observed with increased roughness [136].

When examining the boiling of refrigerants and organic fluids on tubes, Kotthoff and Gorenflo 2009 [103] showed that small areas with enhanced microstructures can have a large influence on the surrounding heat transfer due to the influence bubbles emanating from such regions then sliding and coalescing with neighbouring bubbles.

Marto, Moulson, and Maynard 1968 [120] conducted experiments using pool boiling of liquid nitrogen. It was discovered that increased artificial cavity size and number increased the heat flux required for incipience and shifted the nucleate boiling curve to the left. Increased roughness had a similar effect.

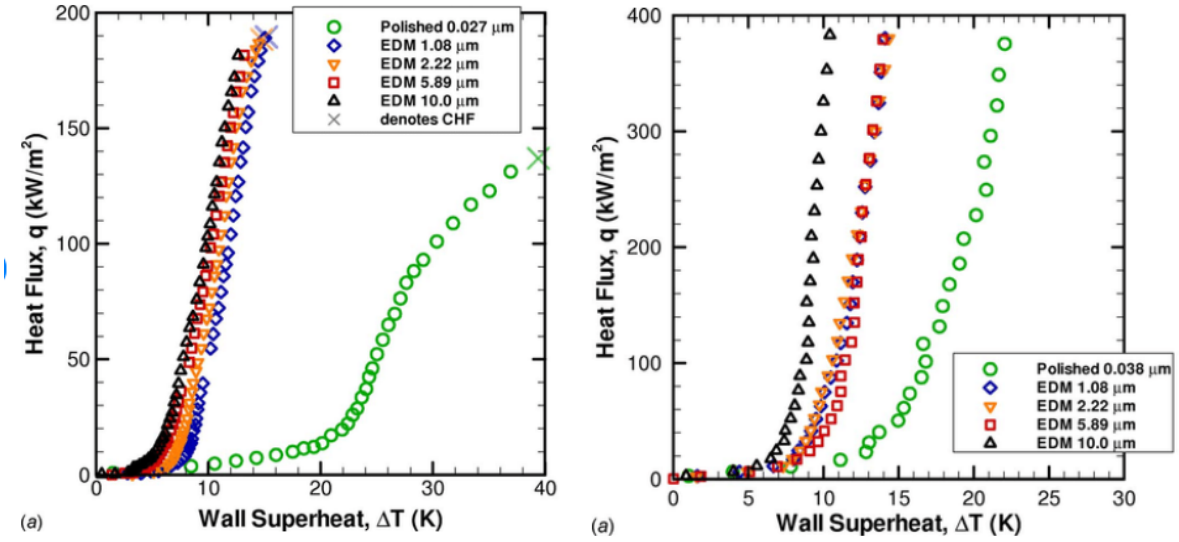

(a) FC-77 *(b) Water*

Figure 2.18: Boiling curves for FC-77 and water on EDM surfaces of varying average roughness, reproduced from [82]

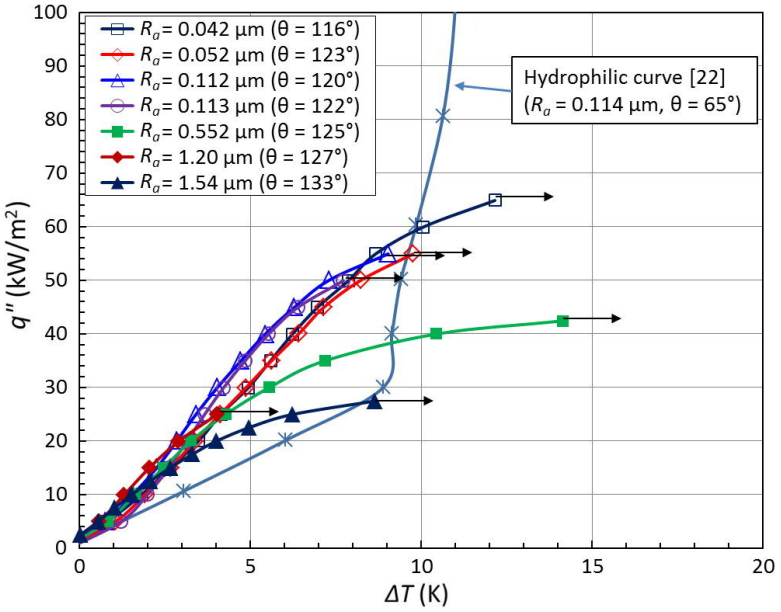

Figure 2.19: Effect of roughness on hydrophobic surface, reproduced from [92]

Wettability

Wettability is dependent on the fluid's surface tension and the wall surface energy. Low surface tension and high surface energy combinations result in hydrophilic surfaces, whereas high surface tension and low surface energy combinations result in hydrophobic surfaces (see *fig. 2.20*). Young's contact angle (θ_Y)is a measure of wettability and is defined as shown in *fig. 2.21 a* for a bubble and *fig. 2.21 b* for a droplet. $\theta_Y > 90$ indicates a hydrophobic surface and $\theta_Y < 90$ a hydrophilic surface.

Increased wettability results in improved CHF [130] [135] (see *fig. 2.22*) . Rahman, Ölçeroglu, and McCarthy 2014 [152] stated that wickability is the sole factor influencing CHF on hydrophilic surfaces. It has been reported

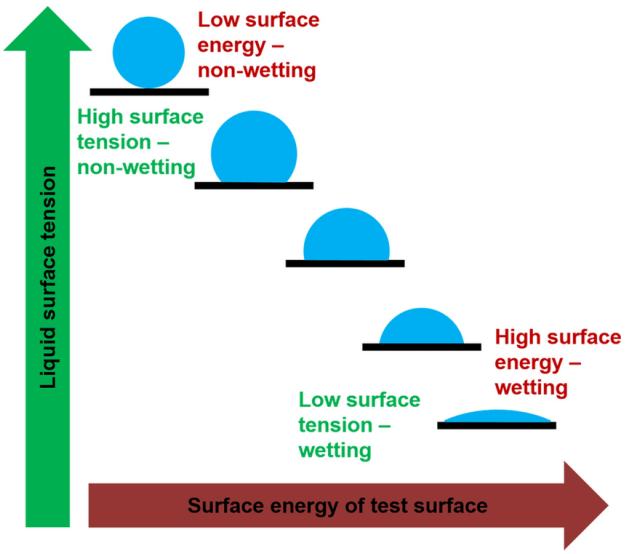

Figure 2.20: Effect of surface tension and surface energy on wettability of a droplet, reproduced from [147]

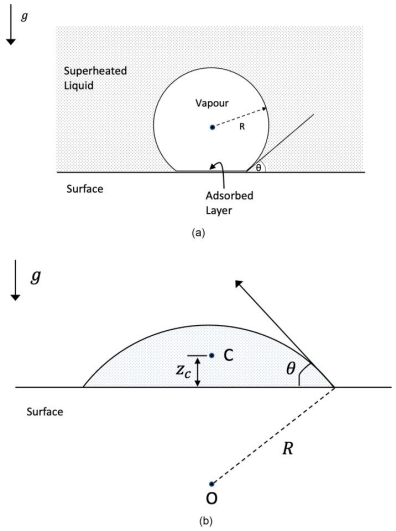

Figure 2.21: Contact angle, reproduced from [13]

that increased wettability can help shift the nucleate boiling curve to the left and increase the gradient of the boiling curve [130] [190]. At contact angles below 10° there is a large enhancement in CHF due to capillary wicking [7]. Kim and Kim 2021 [91] reported increased wetting velocity with increasing wettability, resulting in more rapid quenching following bubble departure. They also reported increased bubble growth rate with increased wettability as a result of larger microlayers beneath the bubble.

Earlier incipience has been reported on hydrophobic surfaces [93] [19] [119] [191], together with initially higher BHTCs [58] (compared to hydrophilic surfaces) that then degrade due to vapour blanketing.

Hydrophobic surfaces leave behind residual vapour bubbles that serve as nucleation sites for the next ebullition cycle, thus eliminating the bubble waiting period between cycles. Hydrophilic surfaces completely flood the nucleation site leading to longer waiting times. [58]

Gong and Cheng 2015 [58] reported increased bubble departure frequency with decreased wettability on hydrophilic surfaces and contact angle independence of frequency on hydrophobic surfaces.

Nucleation site density was reported to increase with increased wettability [130]. However, contradictory results were reported by [58].

Bubble departure diameter decreases with increased wettability [130] [58]. This is supported by the departure diameter equation proposed by Fritz [51].

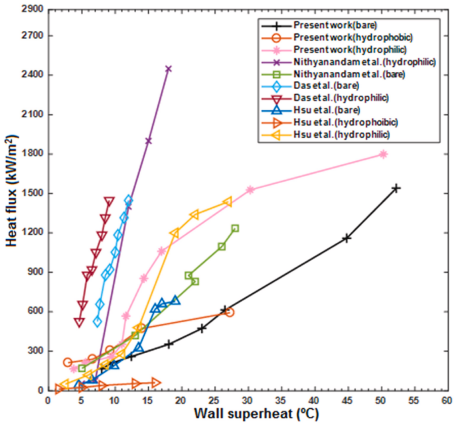

Figure 2.22: Effect of wettability on nucleate pool boiling, reproduced from [130]

$$D_w = 0.0146\theta\left[\frac{2\sigma}{g(\rho_l - \rho_v)}\right]^{1/2} \tag{2.8}$$

where *theta* is the fluid-surface contact angle.

Assuming that the fluid is operating in the Wenzel regime, wettability increases in tandem with increases in roughness for hydrophilic surfaces. However, wettability decreases with increased roughness for hydrophobic surfaces [49].

Ardron and Giustini 2021 [13] used Adamson's absorption theory [3] [4] in order to explain why water bubbles formed at high pressure and temperatures appear to have contact angles 30-50° lower than experimental measurements of sessile droplets. This theory relies on a nano-layer of water adhering to the wall (even in the "dry" area beneath the bubble). This serves to reduce the work required to form a new surface and thus reduces the contact angle as well as makes bubble contact angle less dependent on surface characteristics [13]. As sessile

droplet experiments are typically not performed in highly saturated environments, this effect is expected to be absent when performing such experiments.

Marto, Moulson, and Maynard 1968 [120] conducted experiments using pool boiling of liquid nitrogen and reported a significant shift of the nucleate boiling curve to the left when switching from a nickle surface to a copper one. This is somewhat counter intuitive as nickle has a higher surface energy than copper (1.77 J/m^2 compared to 1.36 J/m^2 [95]) and therefore one would expect a degradation in BHTC (considering operation in the hydrophilic regime for both surfaces), however, the increased performance was attributed the increased thermal conductivity of copper.

Pressure

Moreno, Montgomery, and Narumanchi 2014 [133] indicated the increasing the pressure shifts the nucleate pool boiling curve to the left (see *fig. 2.23*). This is thought to result from an increase in nucleation site density caused by a wider range of applicable cavity sizes. Dahariya and Betz 2019 [34] conducted experiments utilising water and reported increased nucleation site density and bubble departure frequency with increased pressure. The bubble departure diameter was reported to decrease with increased pressure. This resulted in an increase in BHTC (boiling curve shifted to the left and the slope increased) and CHF with increased pressure. Fariñas Alvariño et al. 2019 [48] used HFE-7100 (a very low contact angle fluid $\theta \approx 4°$) and obtained similar improvements to [34]. Both [133] and [34] found excellent boiling curve prediction utilising the correlation presented by Rohsenow 1952 [158]:

$$\frac{q}{A} = \mu_l h_{lv} \left[\frac{g(\rho_l - \rho_v)}{\sigma}\right]^{1/2} \left[\frac{c_{pl}(T_s - T_{sat})}{C_{sf} h_{lv} Pr_l^n}\right]^3 \tag{2.9}$$

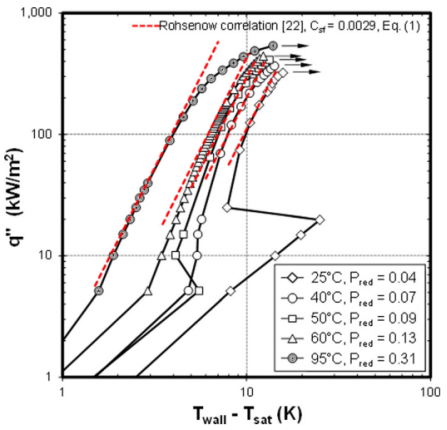

Figure 2.23: Effect of pressure on nucleate pool boiling of HFC-245fa, reproduced from [133]

2.3.2 Subcooled Flow boiling In Tubes

In flow boiling, there is a non-negligible, externally applied, parallel velocity profile along the surface on which boiling occurs. This has several advantages over pool boiling. First is the introduction of additional forces that assist in sweeping bubbles away from the surface and thus help in delaying dryout and increasing the critical heat flux. Secondly is the ability to increase the heat transfer coefficient through the addition of a forced convection heat flux component as well as a quenching component that results from supplying 'fresh' subcooled fluid to a region upon bubble departure (as opposed to near saturation temperature fluid as would be found in pool boiling).

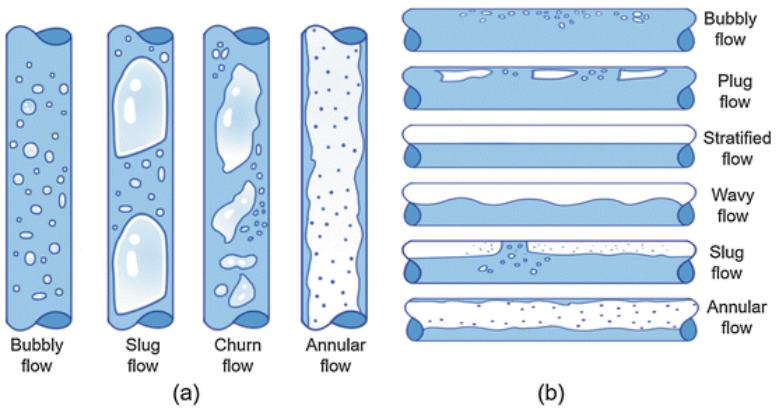

Figure 2.24: Isolated flow boiling regimes in vertical and horizontal tubes, reproduced from [111]

Extensive work has been done in understanding of boiling in vertically and horizontally aligned tubes. The resulting induced flow patterns that occur in a fixed location along a tube as a result of increasing heat flux/temperature boundary condition are: bubbly flow, slug flow , churn flow, annular flow and mist flow (see *fig. 2.24*). It should be noted that stratification occurs in horizontal tubes (due to buoyancy forces) that can lead to premature dryout on the upper surface [57].

Given a constant velocity and subcooled fluid inlet, the progression of the regimes in a vertical tube subject to a constant heat flux is given in *fig. 2.25*. *Figure 2.25 b* is consistent with the regimes seen in *fig. 2.24 a*, this results from low velocity and/or low subcooling temperature inlets that allow the bubbles to migrate to the centre of the tube without shrinking and collapsing due to condensation. This forms an annular core of vapour.

Lowering the subcooling or velocity will promote boiling incipience to occur sooner and shift the dryout location closer to the inlet [57]. However, high velocity and subcooling inlets can result in the formation of inverted annular flow form a blanket near the wall [128] (see *fig. 2.25 a*).

Similar to pool boiling, wall temperatures are reported to increase only slightly in the nucleate and convective heat transfer regime, with a large spike in temperature reported during dryout (see *fig. 2.26*).

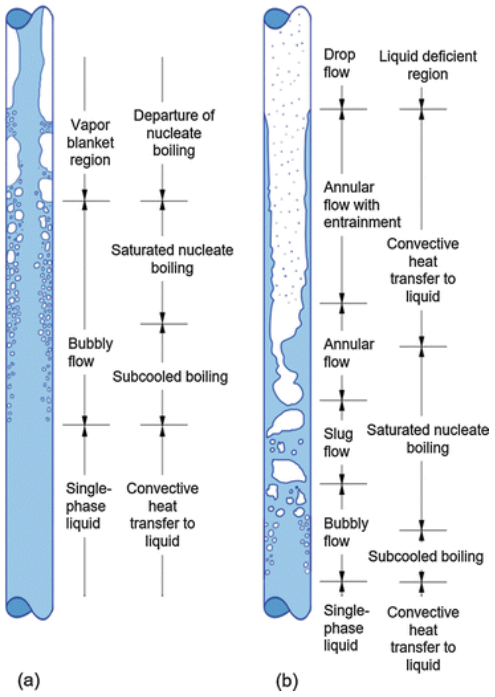

Figure 2.25: Progression of flow boiling regimes along a constant heat flux tube, reproduced from [111]

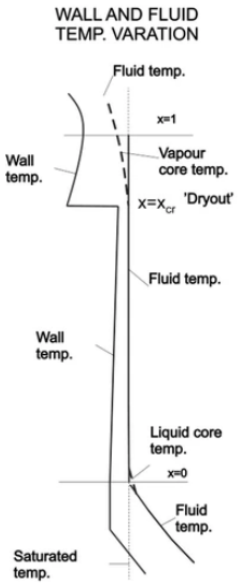

Figure 2.26: Wall and fluid temperature along the length of a constant heat flux tube subject to flow boiling, reproduced from [140]

2.3.3 Subcooled Flow Boiling Bubble Growth and Dynamics

Energy Balance model

First proposed by Ünal 1976 [183], the current energy balance model is primarily utilized to predict bubble growth rate by considering the flow of energy into (via evaporation), out of (via condensation) and stored (via latent heat storage) in a bubble during its lifetime [199].

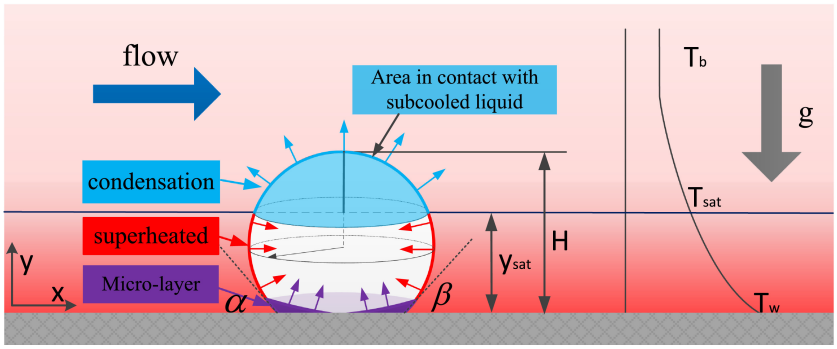

Figure 2.27: Diagram illustrating energy transfer during bubble growth in subcooled flow boiling conditions, reproduced from [211]

The resulting equation for the bubble energy model is:

$$\dot{E_{stored}} = \dot{E_{in}} - \dot{E_{out}} \tag{2.10}$$

The energy stored in a bubble can be represented by:

$$\dot{E_{stored}} = \rho_v h_{lv} \frac{d\cancel{V_b}}{dt} \tag{2.11}$$

where h_{lv} is the interphase enthalpy and $\cancel{V_b}$ is the volume of the bubble.

The energy into the bubble stems from evaporation that occurs in the micro-layer located beneath the bubble and the superheated layer that extends a small distance up the side of the bubble (refer to *fig. 2.27*).

$$\dot{E_{in}} = \dot{q_{ml}} A_{ml} + \dot{q_{sl}} A_{sl} \tag{2.12}$$

where $\dot{q_{ml}}$ is the heat flux from the micro-layer into the bubble, $\dot{q_{ml}}$ is the heat flux from the superheated layer into the bubble and A_{ml} and A_{sl} are the corresponding interfacial surface areas associated with the micro-layer and superheated layer respectively.

The energy out of the bubble occurs in the condensation layer where the liquid temperature is lower than that of T_{sat}.

$$\dot{E_{out}} = \dot{q_c} A_c \tag{2.13}$$

where $\dot{q_c}$ is the heat flux due to condensation and A_c is the area over which condensation occurs.

It is typical to model the bubble as spherical (not completely accurate in the event of wall contact) and then enforce *eq.* (2.10), which results in:

$$\rho_v h_{vl} \frac{d(\frac{4}{3}\pi R_b^3)}{dt} = \dot{q_{ml}} A_{ml} + \dot{q_{sl}} A_{sl} - \dot{q_c} A_c \tag{2.14}$$

This can be simplified to:

$$\frac{dR}{dt} = \frac{1}{\rho_v h_{lv}} \left(\dot{q_{ml}} \frac{A_{ml}}{4\pi R^2} + \dot{q_{sl}} \frac{A_{sl}}{4\pi R^2} - \dot{q_c} \frac{A_c}{4\pi R^2} \right) \tag{2.15}$$

where R is the radius of the bubble.

Equation (2.15) represents the growth rate of the bubble. Various solutions for $\dot{q_{ml}}$, $\dot{q_{sl}}$ and $\dot{q_c}$ are given in [199]. Due to the complex nature of the temperature field surrounding bubbles (as a result of turbulence induced mixing from bubble departures in close spatiotemporal proximity coupled with boundary layer development from the bulk subcooled flow), the general approach in experimental literature has been to provide empirical models. Note that some researchers have cited the micro-layer contribution as being negligible [36], [93], [64], [108] or very small $< 25\%$ of the total heat flux [202], [156].

In order to solve for the surface areas (A_{ml}, A_{sl} and A_c), one should be aware of the formation of a dry spot (A_{dry}) in the center of the micro-layer as the bubble grows [54], [170], however, the heat transfer to the bubble from this area is usually considered negligible as is the area itself (particularly if maximum bubble diameter is reached), although some researchers have accounted for it [39]. The areas are usually solved as proportional values relative to the total spherical bubble surface area, where:

$$\frac{A_{ml}}{4\pi R^2} + \frac{A_{sl}}{4\pi R^2} + \frac{A_c}{4\pi R^2} + \frac{A_{dry}}{4\pi R^2} = 1 \tag{2.16}$$

Again, proposed solutions are presented in [199].

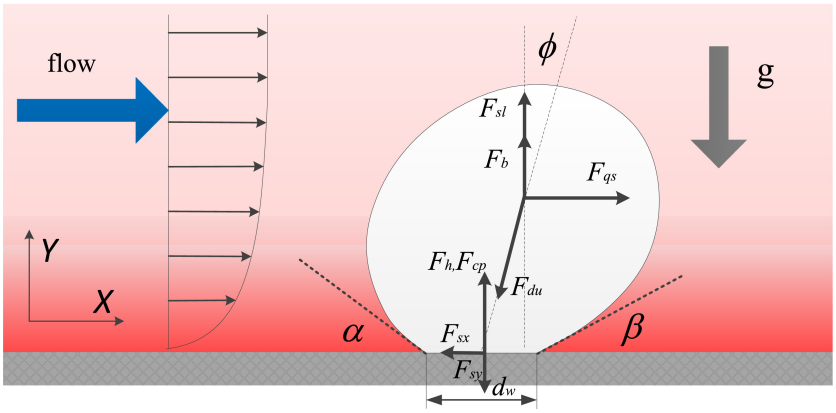

Figure 2.28: Diagram illustrating forces acting on bubbles on a horizontal flat plate subject to flow boiling conditions, reproduced from [211]

Force Balance model

First proposed by Klausner et al. 1993 [99], the force balance model is typically utilized to predict the bubble departure or sliding diameter.

The net force is typically decomposed into seven independent forces that act on a single bubble [199] (see *fig. 2.28*), these are:

$$\frac{dm_b\vec{V_b}}{dt} = \sum F = F_s + F_{qs} + F_{du} + F_b + F_{sl} + F_h + F_{cp} \tag{2.17}$$

1. **Surface tension force** (F_s): The surface tension force acts along the vapour-liquid interface. The force represented here acts along the micro-layer interface and serves to maintain bubble attachment to the wall by opposing sliding and lifting forces [199]. This is the largest force in both the tangential and normal flow directions during bubble growth. Solutions proposed by [99] are shown below.

$$F_{sx} = -d_w\sigma\frac{\pi(\alpha-\beta)}{\pi^2-(\alpha-\beta)^2}(\sin\alpha+\sin\beta) \tag{2.18}$$

$$F_{sy} = -1.25d_w\sigma\frac{\pi}{\alpha-\beta}(\cos\beta-\cos\alpha) \tag{2.19}$$

   where d_w is the diameter of bubble area in contact with the wall and α and β are the leading and receding contact angles respectively.

2. **Quasi-steady drag force** (F_{qs}): This force acts in the flow direction and results from the frictional and pressure drag forces. This, together with the surface tension, is the dominant force in the flow direction. Solutions can be found in [99] and [77].

3. **Unsteady drag force** (F_{du}): This force results from the unsteady resistance to bubble growth [99].

$$F_{dux} = -\rho_l\pi r_b^2\left(r_b\ddot{r}_b + \frac{3}{2}C_s\dot{r}_b{}^2\right)\sin\phi \tag{2.20}$$

$$F_{duy} = -\rho_l\pi r_b^2\left(r_b\ddot{r}_b + \frac{3}{2}C_s\dot{r}_b{}^2\right)\cos\phi \tag{2.21}$$

   where ϕ is the inclination angle between the wall normal line and the bubble symmetry line.

4. **Buoyancy force** (F_b): This results from the presence of a hydrostatic pressure gradient in the fluid.

$$F_b = \frac{4}{3}\pi r_b^3(\rho_l-\rho_v)g \tag{2.22}$$

5. **Shear lift force** (F_{sl}): This force acts to lift the bubble off the surface. Van Helden, Van Der Geld, and Boot 1995 [187] attributed Bernoulli suction and vorticity effects as major drivers behind this force.

$$F_{sl} = \frac{1}{2} C_l \pi u_r^2 r_b^2 \tag{2.23}$$

where C_l is a lift coefficient.

6. **Hydrodynamic force** (F_h): This force results from hydrodynamic pressure generated as a result of surrounding fluid velocity and bubble growth.

$$F_h = \frac{9}{8} \rho_l u_r^2 \frac{\pi d_w^2}{4} \tag{2.24}$$

where u_r is the relative velocity between the bubble centre and the local averaged fluid velocity at that bubble center.

$$u_r = u_l - u_b \tag{2.25}$$

7. **Contact pressure force** (F_{cp}):

$$F_{cp} = \frac{\pi d_w^2}{4} \frac{2\sigma}{r_c} \tag{2.26}$$

where r_c is the radius of curvature at the wall and can be approximated by $r_c = 5r_b$ [199].

Additionally, a virtual mass force can be added to *eq.* (2.17). This force serves to account for the inertial resistance of the surrounding fluid experienced by bubble as it attempts to move through the fluid [41] and thus acts in the opposite direction of bubble motion. Such a force has been found to be particularly relevant in pulsating flow conditions [204].

The force due to the Marangoni effect can also be added to *eq.* (2.17). The Marangoni effect is caused by a gradient in surface tension along the interphase between two phases that results in a net flow at the interphase in the direction of positive surface tension gradient (from low to high surface tension) [144]. In the case of subcooled flow boiling, there exists a temperature gradient from the wall to the bulk subcooled flow. As surface tension typically increases with decreasing temperature, this results in a flow along the interface (see *fig. 2.29*) that serves to increase the heat transfer around the bubble. This can result in a force that propagates the bubble away the heated surface, thus promoting bubble departure [143]. Additionally, the Marangoni effect can also promote bubble attraction and coalescence on a heated surface [206]. Opposite flow directions are observed for self-rewetting fluids (fluids that exhibit increases in surface tension with increases in temperature) [70].

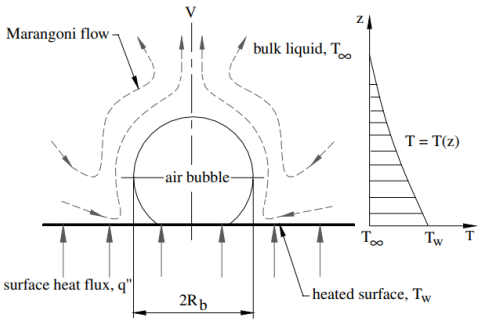

Figure 2.29: Marangoni flow around an air bubble submersed in distilled water with a thermal gradient, reproduced from [144]

2.3.4 Understanding Boiling through Experimental and Numerical Approaches

Experimental Approaches

Experimental observation of bubble nucleation, growth and dynamics is typically done via the post-processing of visual images obtained from high speed cameras. With thermocouples, mas flow meters and pressure gauges used to measure temperature, mass flow and pressure respectively [199]. Primary advances in the field include the development of algorithms capable of post-processing higher resolution images to more accurately keep track of nucleation [211] and bubble interface growth and deformation. Rainbow schlieren deflectometry is another promising method to achieve higher levels of detail with regards to bubble shape and temperature distribution [169].

Numerical Approaches

Numerical approaches have the additional benefit of providing detailed flow data (i.e. detailed force vectors, velocity vectors, vapour fraction, heat transfer etc...) that can be utilized for detailed analysis of bubble dynamics and growth. In general, the greater the numerical detail and accuracy, the larger the computational cost. These numerical costs can be greatly reduced by applying a series of assumptions to the underlying physical forces and interactions of the molecules/atoms that form the fluid. However, as the level of abstraction increases, one increasingly runs the risk that the applicability of one or more of the underlying assumptions falls out of scope for the modelling application of interest (something that may or may not be immediately obvious). This is only exacerbated if the inclusion of empirical sub-models is required to provide closing relations in the numerical model. Thus, careful consideration should be applied to numerical model selection in accordance with the required level of detail and accuracy for the problem at hand.

In general, numerical methods can be broken down into three distinct categories [199]:

1. **Microscale**: Molecular Dynamics (MD) simulations that model the interaction of individual molecules/atoms are typically employed at this scale in order to model bubble nucleation and optimise surface characteristics [121]. These simulation are, however, computationally expensive due to the fine grid and small timestep requirements. Examples can be found in the following references: [122], [110], [197] and [165].

2. **Mesoscale**: These simulations typically consider the modelling of collections/groups of particles whereby the statistical result of colliding particle groups is used to update neighbouring grid points. The Lattice Boltzman Method (LBM) and its variations are the main methods at this scale. This has the advantage of reducing the required grid size and therefore computational cost whilst still accurately modelling the average particle motion. It is often coupled with an interface tracking algorithm such as the Level Set (LS) method in order to keep track of bubble movement [199]. Examples can be found in the following references: [59], [173], [5], [142], [10] and [203].

3. **Macroscale**: Simulations at this scale make the assumption that the fluid is a continuum and therefore utilise the Navier-Stokes (NS) equations. Solution of the NS equations can be derived from either the Lagrangian or Eulerian viewpoint. The Lagrangian viewpoint tracks the motion of a parcel of fluid (of fixed mass) through the domain and is employed in methods such as the "smoothed particle hydrodynamics" method [153]. The advantage of such a method is that it is a mesh-less approach. The Eulerian viewpoint considers a fixed volume/grid (although adaptive meshing may be applied) in space and keeps track of quantities of the fluid as they flow past each grid point or through each volume, depending on weather a finite difference method (FDM) or finite volume method (FVM) is utilised (with FVM being favoured in CFD applications [153]). In order to capture the interface between two fluids, front-tracking or interface-capturing methods are used [175]. Front-tracking methods utilize Lagrangian tracking of markers attached to the interface and require adaptive meshing [124] whilst interface-capturing methods introduce the concept of a volume fraction within a fixed mesh (VOF method), with the introduction of an advection equation to keep track of the interface [175] such as the LS method. The methods described above have thus far been direct methods, in which small timesteps and/or grid sizes are required to directly resolve the smallest influencing turbulent fluctuations using DNS solvers. However, less computationally expensive Favre averaged or Reynolds averaged equations can be utilised to solve the NS equations in the turbulence regime. One such method is the Multiphase-Eulerian method. A disadvantage of such an approach is that phases are treated as interpenetrating continua and less emphasis placed on clearly defining the vapour-fluid interface. The Multiphase-Eulerian method is the least computationally expensive of all the numerical methods proposed (allowing for the largest grid and timestep sizes), however, it does require the highest number of assumptions and closing equations (often empirical in nature). Such a model has been coupled with the RPI wall boiling model to successfully model jet impingement boiling in the following references: [137], [2], [150], [47], [195] and [114].

That being said, if one were primarily concerned with the accurate prediction of the wall temperature in a flow boiling simulation across a large range of geometric parameters (and thus large number of simulations), the macroscale Multiphase-Eulerian model presents itself as an attractive option due to its low computational requirements whilst still providing some level of detailed that can be utilized to analyse results. The caveat being that any results and corresponding conclusions must be viewed , at least partially, through a lens of skepticism, so as to acknowledge the impact that assumptions may have caused on the potential delineation of said numerical results from reality.

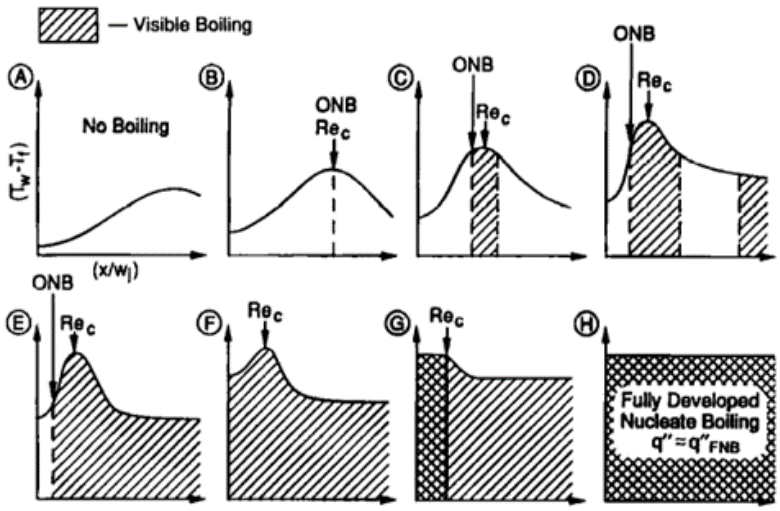

Figure 2.30: The progressive development of nucleate boiling in 2D planar free-surface jets, reproduced from [184]

2.4 Multiphase Jet impingement

A basic depiction of jet impingement boiling is given in *fig. 2.30* for a constant heat flux boundary condition. At *fig. 2.30 A*, the wall temperature is initially lowest at the stagnation point due to the thin boundary layer thickness. Further from the stagnation point, the boundary layer thickens resulting in an increase in wall temperature. The wall temperature then reaches a peak which marks the transition to turbulent flow, followed by a decrease in wall temperature. Note, this decrease extends for a finite region and eventually, far away from the peak, the turbulent boundary layer will thicken, resulting in increased wall temperatures (this is not indicated on *fig. 2.30 A*). Application of more heat results in a similar curve to that of *fig. 2.30 A* in *fig. 2.30 B*, except that the thermal boundary layer thickens more rapidly, resulting in a rise of the peak surface temperature to the critical Reynolds number (R_c). Application of a greater heat flux causes the surface temperature difference to be high enough above the saturation temperature of the fluid to initiate bubble formation and hence partial nucleation boiling (shown in *fig. 2.30 C*). This shifts the peak surface temperature closer to the stagnation point as the turbulence generated by the bubble departure promotes the earlier transition of the flow from laminar to turbulent. Further increasing the heat flux then causes this peak to shift progressively towards the left (shown by *fig. 2.30 C* to *fig. 2.30 E*). *fig. 2.30 F* and *G* illustrates that even if the entire surface then experiences nucleate boiling, the convective heat transfer component may still have a significant effect resulting in non uniform surface temperature. Fully developed nucleate boiling then develops at the stagnation point in G and propagates outwards towards the rest of the fluid where nucleation boiling becomes the primary means of heat dissipation and the temperature across the entire surface is approximately constant [193].

Notable reviews covering this topic are contained in the following references: [193], [151] and [37]. These have been used as primary sources of information in the following section.

2.4.1 Temperature Excursion/Overshoot and Hysteresis

When traversing up the boiling curve, one may notice a sudden decrease in wall temperature (usually near incipience) (see *fig. 2.31*). This temperature excursion is thought to be a result of insufficient nucleation site activation at a specified heat flux, resulting in excessive wall superheats. However, nucleation within a single cavity in a region can result in the vapour impregnating neighbouring flooded cavities, triggering a chain reaction of nucleation site activation that rapidly lowers the wall temperature. It is suggested that low contact angle fluids are most susceptible to this phenomenon [16]. Temperature excursion appears to decrease with increasing velocity, pressure and subcooling [16] [209] [208]. However, Cardenas and Narayanan 2012 [26] has suggested that temperature excursion occurs randomly and independent of jet velocity.

Hysteresis effects on wall temperature have been shown to occur when traversing up and down the boiling curve. This is evident in *fig. 2.32* where the increasing heat flux scenario has higher wall temperature around incipience. Again, this is thought to be a result of inadequate nucleation site activation, however, one may or may not experience a rapid decrease in wall temperature that is characteristic for temperature excursion over a small area. Jones, Evans, and Galvin 1999 [83] reported a reduction in hysteresis effects due to vapour cavity entrapment on subsequent boiling runs that lowers the wall superheat required for incipience. Experimentation

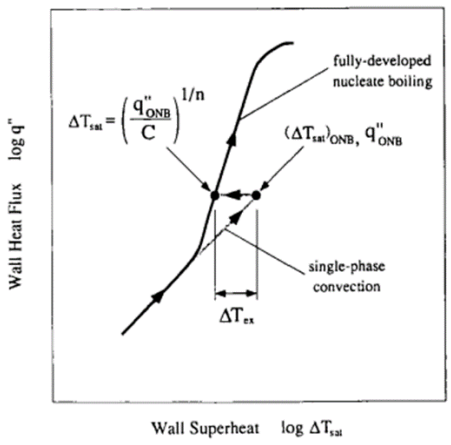

Figure 2.31: Temperature excursion at the point of incipience, adapted from [16]

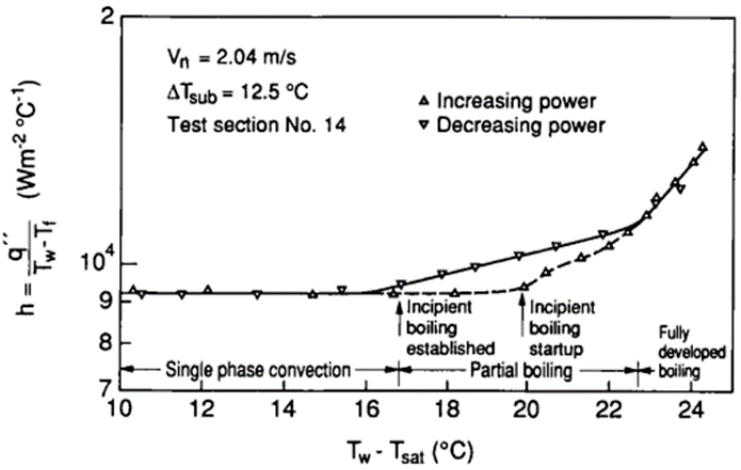

Figure 2.32: Transition between single-phase convection and fully developed nucleate boiling of an axisymmetric jet of R-113, reproduced from [115]

with the inclusion of biphilic surfaces has been reported to help reduce hysteresis [189].

2.4.2 Jet velocity

For submerged jets it has been shown by [17], [115], [88] and [26] that increasing the jet velocity simply extends the nucleate boiling regime (i.e. increases the CHF) by allowing the fluid to pierce the vapour layer and wet the surface [37]. No lateral shifting of the nucleate boiling curve nor change in gradient has been reported by these authors. Zhou and Ma 2004 [208] supported this observation for low jet velocities ($u_j < 10$ m/s) but reported a shift to the right in the boiling curve at higher velocities ($u_j > 10$ m/s) as a result of increased stagnation pressure and therefore increased saturation temperature.

However, Vader et al. 1995 [185] experimented with liquid nitrogen impingement and found increased BHTC with increased velocity. Zhang et al. 2011 [205] and Aihara et al. 1993 [8] experimented with confined impingement of liquid nitrogen and found improvements in heat transfer with increases in jet velocity. Most notably, a shift of the boiling curve to the left, an extension of the forced convection regime and an increase in the CHF with increases in velocity. Zhang et al. 2011 [205] attributed this to operation within the convective evaporative regime (where BHTC is primarily dependent on mass flux) as opposed to the nucleate boiling regime (where BHTC is dependent on heat flux and pressure [148]). However, Aihara et al. 1993 [8] and Vader et al. 1995 [185] assumed operation in the nucleate boiling regime.

Browne et al. 2010 [23] [22] showed delayed onset of nucleate boiling due to increased single-phase convection at higher velocities.

2.4.3 Subcooling

Wolf, Incropera, and Viskanta 1993 [193] and Qiu et al. 2015 [151] indicated that [32], [75], [184], [134], [207] reported no effect of subcooling in the nucleate boiling regime. [17] [115] reported a shift of the boiling curve to the left with an increase in moderate subcooling (around 20 K) for an impinging jet of R-113 and [210] reported lower wall superheats required for incipience with increased subcooling. However, Vader et al. 1995 [185] utilised liquid nitrogen and reported a shift to the right with increased subcooling (when operating in a low subcooling range 0.1-8.7 K) but observed a reduction in CHF and onset of nucleate boiling (ONB). The reduction in ONB in conjunction with reducing subcooling is supported by [23]. It is generally accepted that CHF increases with increasing subcooling as the surrounding liquid condenses vapour faster and allows more effective use of the fluids sensible heat to cool the wall [37].

2.4.4 Jet impingement height

Aihara et al. 1993 [8] found increasing BHTC with decreased impingement height for liquid nitrogen impingement in a tube-in-tube (radially) confined configuration. This was attributed to decreasing heights resulting in less momentum transfer to the returning fluid/vapour and therefore faster streamwise velocities along the surface. This caused thinner thermal boundary layers and promoted more effective sweeping of vapour from the surface,

thus delaying dryout. This finding was weakly supported by the data of Zhang et al. 2011 [205] using a similar configuration. Katto and Kunihiro 1973 [88] indicated increases in CHF with decreasing impingement heights.

Hong et al. 2014 [66] found that there was an optimum impingement height between $a/d_j = 1 - 3$. However, the jet Reynolds numbers were in the laminar regime ($Re_j = 200 - 600$) for this experiment and it is therefore likely that transition to turbulence in the freestream jet was a contributing factor.

Multiple authors report no effect on wall temperature in nucleate boiling regime [132] [87] [86]. Nonn, Dagan, and Jiji 1988 [138] supported this, but reported influence at very small impingement heights ($a = 0.1$ mm) where the confining effects of the nozzle served to enhance the heat transfer. Wright et al. 2023 [195] performed a numerical study using the RPI boiling model and reported an increase in heat transfer with increased impingement height for $Re_j = 10\ 000$ but a decrease in BHTC with decreased a for $Re_j > 10\ 000$. It is believed by Devahdhanush and Mudawar 2021 [37] that the impact of impingement height on CHF cannot be viewed in isolation, with other parameters such as velocity and subcooling having influence effects. They suggest that more research be done on the parameter to conclusively deduce its effects.

2.4.5 Cryogenic Applications

Li et al. 2009 [109] conducted a numerical flow boiling study of liquid nitrogen boiling in order to establish closing correlations for their wall heat flux partitioning model. They stated that due to liquid nitrogen's low surface tension and low contact angle, it has smaller departure diameters and higher nucleation site densities than one would typically encounter in fluids such as water. They identified active nucleation site density as the primary influencing factor that impacts wall temperature. Additionally they reported a decrease in bubble waiting time with decreased subcooling.

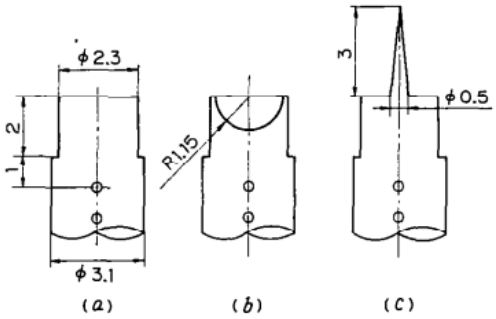

Figure 2.33: Flat, Hemispherical and single pin impingement surfaces, reproduced from [8]

Vader et al. 1995 [185] conducted an experiment using liquid nitrogen to cool a silicon chip. They explored both pool boiling and jet impingement boiling applications and pressurised the environment in order to increase the subcooling. They revealed a shift in the boiling curve to the right and increase in CHF with increased subcooling for pool boiling. Increasing jet velocities resulted in an increase in BHTC and a shift of the boiling curve to the left.

Zhang et al. 2011 [205] and Aihara et al. 1993 [8] explored radially confined jet impingement boiling within cryoprobes. They explored three surfaces: flat, single needle and hemispherical curved surfaces (*fig. 2.33*). Aihara et al. 1993 [8] focused primarily on impingement using a hemispherical surface. They found the resulting boiling curve to lie between the experimental results of pool boiling of liquid nitrogen [120] and jet impingement boiling of water in a restricted space [87]. They demonstrated that increased roughness resulted in improvements in the BHTC. Additionally, their smoothest mirror finish surface experienced a reduction in CHF over the other surfaces. These results are consistent with observations of pool boiling on hydrophilic surfaces as noted in *section 2.3.1* and *section 2.3.1*. Zhang et al. 2011 [205] showed that contaminating the surface with a layer of epoxy decreased the CHF, shifted the boiling curve to the right and lowered the heat flux required for incipience.

Findings pertaining specifically to the influence of hemispherical and singular needle cases are addressed in *section 2.4.6* and *section 2.4.7* respectively.

2.4.6 Curved Surfaces

Inoue et al. 1995 [74] experimentally investigated the impact of surface curvature ($R_{surface} = \infty, 62.1, 24.8$ mm), subcooling ($\Delta T_{sub} = 30, 60, 80$ K) and jet velocity ($u_j = 6.7 - 14.6$ m/s) on the nucleate boiling curve using free-surface slot jet impingement of water (see *fig. 2.34 a*). Their application of interest was the cooling of a divertor surface of a magnetic confinement fusion reactor. They proposed three main benefits of curved surfaces over flat surfaces. The first was the introduction of a centrifugal force that results in increased pressure along the surface, which in turn increases liquid subcooling and reduces sputtering caused by intense boiling further from the stagnation point. The second was an increase in normal pressure gradients that promoted earlier departure of bubbles, thus reducing the bubble departure diameter and delaying dryout. The third was application specific and related to the non-uniform heat flux (which reduced with distance from the stagnation point) that would be seen in practical operation, although all experiments were conducted using uniform heat fluxes. They indicated that increased velocity and subcooling resulted in large increases in CHF directly beneath the jet but degraded

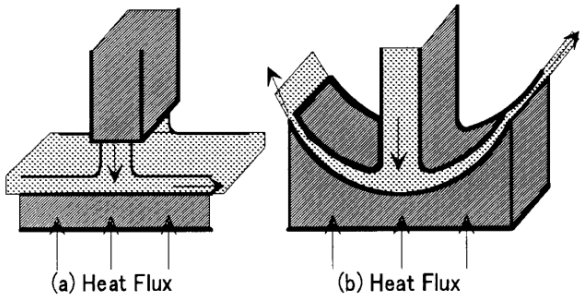

Figure 2.34: Experimental surfaces used by Inoue et al., reproduced from [72]

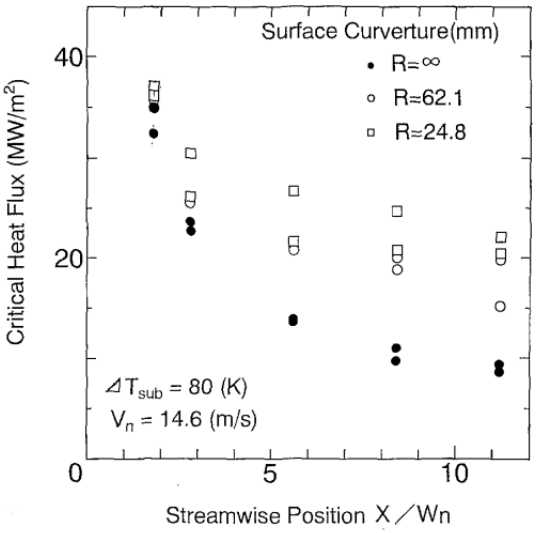

Figure 2.35: Local profile of critical heat flux along curved surfaces, reproduced from [74]

sharply with streamwise distance from the stagnation point for a flat plate. However, increasing curvature or increased velocity on curved surfaces resulted in reduced degradation of CHF with increased streamwise distance from the stagnation point, compared to a flat plate, provided that the Froude number exceeded 100. The CHF at the stagnation point was seen to remain largely unaffected. The Froude number (Fr_j) was defined as:

$$Fr_j = \frac{u_j^2}{gR_{surface}} \tag{2.27}$$

and represents the ratio of centrifugal force to gravitational force. The results of [74] indicate that increasing Froude number increases CHF at an equivalent streamwise distance provided $Fr_j \geq 100$, with the effects being more prominent as streamwise distance increases (see *fig. 2.35*).

As part of the same research group, Furuya, Inoue, and Tanno 1995 [53] explored the effect of lower jet velocities ($u_j = 1.3 - 3.2$ m/s), lower subcoolings ($\Delta T_{sub} = 1.1 - 60$ K) as well as the influence of adjusting the jet width ($w_j = 2.2 - 4.4$ mm), using the same experimental apparatus ($R_{surface} = \infty, 62.1, 24.8$ mm) and planar free-surface jet configuration as [74]. Their findings revealed reduced degradation in local Nusselt number with respect to the stagnation point Nusselt number as $R_{surface}$ increased, with the effects slightly less prominent possibly as a result of a lower Froude number.

Inoue et al. 2000 [72] then published another paper considering the effect of confined planar jet impingement (see *fig. 2.34 b*). The noted the following benefits of confinement: the reduction in splashing due to intense boiling (thus increasing fluid contact with the wall), the ability to tailor the velocity profile to the observed CHF profile (as is shown in *fig. 2.34 b* by reducing the channel height to increase the velocity towards the outer edge of the domain) and the notable compactness of the system. They noted an absence of CHF dependence on curvature due to confinement. It was therefore concluded that splashing as a result of intense boiling is the main degrading factor in the free-surface impingement configuration. Increased subcooling and velocity uniformly increased CHF along the entire surface.

The final paper by Inoue et al. 2000 [73] on confined planar curved surfaces reported no influence of curvature on the boiling curve prior to incipience. However, in the nucleate boiling regime, the BHTC improved (resulting in a steeper slope of the boiling curve) with increased curvature. This was attributed to the increased lift forces on bubbles as a result of larger normal pressure gradients with increased curvature. It was also discovered that rounding the inlet of the jet avoided excess pressure drop that results with sharp inlets directly outside of the stagnation point region. This prevented a drop in the local saturation temperature and premature dryout in the region near the stagnation point.

Aihara et al. 1993 [8] noted a substantial increase in CHF, as well as, boiling BHTC over both the flat and singular needled surface (see *fig. 2.36*) when using a tube-in-tube radially confined impinging jet of liquid nitrogen (see *fig. 2.33*). This was attributed to the substantially larger surface area of the hemispherical surface (approximately twice that of the flat surface) and the absence of stagnation points created by sharp corners where dryout is expected to initiate.

Zhang et al. 2011 [205] used a similar experimental setup to Aihara et al. 1993 [8] using slightly larger but geometrically similar impingement surfaces. They too observed an increase in BHTC and CHF on the hemispherical surface in comparison to the flat plate and needle surface (see *fig. 2.37*).

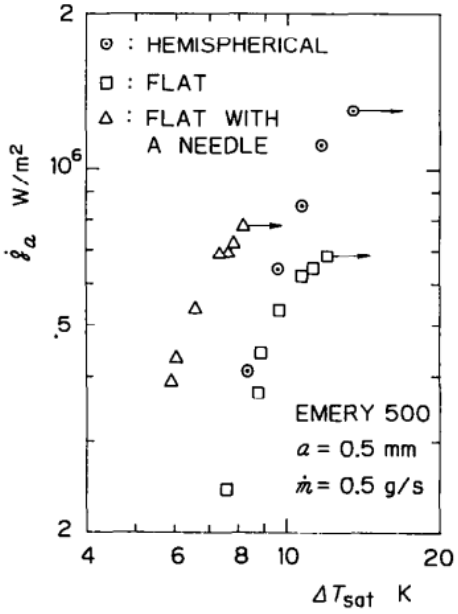

Figure 2.36: Boiling curves of hemispherical, singular needle and flat surface using liquid nitrogen, reproduced from [8]

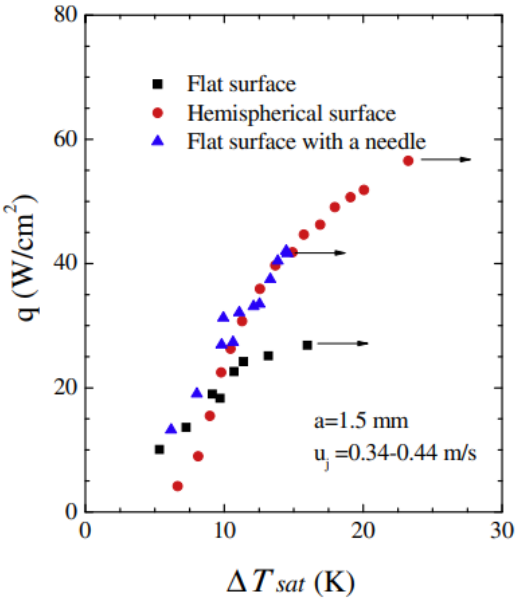

Figure 2.37: Boiling curves of hemispherical, singular needle and flat surface using liquid nitrogen, reproduced from [205]

2.4.7 Pinned Surfaces

Aihara et al. 1993 [8] noted a reduction in wall superheat using a singular needle surface (see *fig. 2.38 c)*), thus shifting the boiling curve to the left compared to their results using a flat surface (see *fig. 2.36*). They also noted a delay in boiling incipience to a higher heat flux. This was attributed to the larger surface area of the needled surface and an increased forced convection component. The CHF was between the hemispherical and flat surface. It is thought that the CHF is lower than the hemispherical case as a result of local dryout originating in the stagnation region at the root of the needle.

Zhang et al. 2011 [205] noted a similar pronounced shift of the boiling curve to the left only at the larger tested impingement height ($a = 3.5$ mm). The lower impingement height revealed a slight reduction in wall superheat and an increase in BHTC (see *fig. 2.37*). CHF values were between the hemispherical and flat surface.

Rau and Garimella 2014 [155] investigated single submerged jet impingement of HFE-7100 onto an enhanced surface consisting of a regular array of square pins arranged in a grid-like pattern. They indicated that, compared to a flat surface, there was significant enhancement in the single phase regime as a result of larger surface area

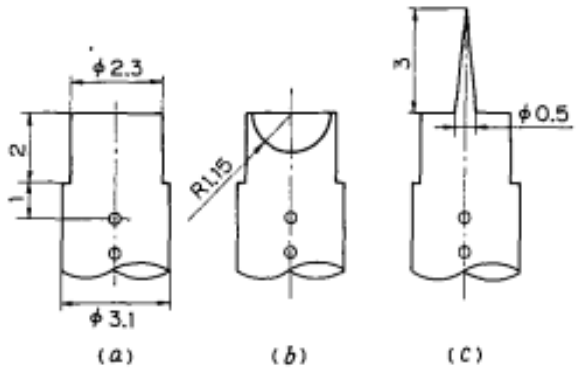

Figure 2.38: Cross sectional diagram of experimental impingement surfaces used by Aihara et al. 1993 [8], reproduced from [8]

and turbulence generated by the fins. In the two-phase regime, there was a reduction in temperature excursion, the wall superheat reduced by 6-8 K and the CHF increased. They also reported a slight reduction in BHTC (reduced slope) as a result of local dryout occurring at the base of the pins. Introduction of a rough micro structure coating on the pin fins resulted in a pronounced shift of the boiling curve to the left and increase in the BHTC and CHF. The effects on pressure drop as a result of the pins was reported to be insignificant.

2.4.8 Previous Numerical Work

Narumanchi et al. 2008 [137] was first to report use of the multiphase Eulerian model coupled with the Rensselaer Polytechnic Institute (RPI) boiling model in order to successfully model wall superheat during jet impingement boiling. They validated their model utilising the experimental observations of both Katto and Kunihiro 1973 [88] (unconfined axisymmetric water jet) and Zhou and Ma 2004 [208] (unconfined axisymmetric R-113 jet) with time averaged results within 20% of the measured stagnation point temperature (all quantaties experienced temporal fluctuation). Following validation, they modelled the cooling of a Insulated-Gate Bipolar Transistor package utilising R-134a in a submerged, radially confined configuration. Their results revealed that boiling is beneficial in increasing the BHTC of low velocity jets at low heat fluxes, but indicated that at high velocities and high heat fluxes, boiling may degrade the heat transfer performance. They also reported that their results were independent of jet orientation and diameter (although they neglected to present these results).

Abishek, Narayanaswamy, and Narayanan 2013 [2] investigated the effect of heater width to nozzle width ratios ($1 \leq w_H/w_N \leq 11$) and Reynolds number ($Re_j = 2\ 500$ and $3\ 750$) within a 2D parallel confinement case. They validated against the results of Mani, Cardenas, and Narayanan 2012 [118] (unconfined axisymmetric water jet) and Shin et al. 2009 [166] (confined 2D slot jet of PF-5060). Their CFD results of wall temperature were within 10% of experimental results. They utilised constant fluid properties. They reported monotonous increase of evaporative heat flux and decrease of convective heat flux with increasing wall temperature, whilst the quenching heat flux increased to a maximum and then decayed due to larger wall vapour volume fractions at increased superheat. The combined quenching and convective heat fluxes was dominant for small heaters with an exponential decay of quenching with increase in heater size. This resulted in lower wall temperatures for smaller heaters. Of the three heat fluxes, the convective heat flux was the only one to increase with increasing Reynolds number.

Qiu et al. 2015 [150] investigated the effect of conjugation (modelling of the solid through which heat transfer takes place) on axisymmetric jet impingement boiling. They validated their model against Katto and Kunihiro 1973 [88] (the same case that Narumanchi et al. 2008 [137] used, except better results were found when including conjugation) and Vader et al. 1995 [185] (axisymmetric nitrogen jet). The validation results for [185] seemed to grossly overpredict heat transfer in the lower portion of the boiling curve. By including conjugation, they were able to capture the advancing boiling front that one would theoretically expect. This was not captured when using an isoflux boundary condition. Therefore they highlighted the importance of including conjugation. They found relatively low influence of the thermal conductivity on the average wall temperature, however it did influence the local wall temperature distribution.

Esmailpour, Azizi, and Hosseinalipour 2019 [47] investigated the influence of Reynolds number ($2\ 500 \leq Re_j \leq 10\ 000$) and impingement height ($2 \leq a \leq 6$) on a 2D parallel confinement case. They validated their results to within 15% of the experimental data of Shin et al. 2009 [166].They noted an increase in heat transfer coefficient with decreased impingement height and increased Reynolds number.

Wright et al. 2023 [195] conducted two separate numerical experiments, one submerged single-jet impingement using water (validated against the results of Katto and Kunihiro 1973 [88]) and another confined 3D multi-jet impingement case utilising R134a (validated against the results of Devahdhanush and Mudawar 2021 [38]). They reiterated that conjugation heat transfer (through the modelling of the thermal mass of the surface) is a critical numerical component required to successfully replicate experimental results where the impingement surface had a significant thermal mass. They investigated the effect of subcooling and found reduced subcooling to lower the wall superheat required for the onset of nucleate boiling and thus shift the boiling curve to the left. They found increased Reynolds numbers resulted in higher convective heat fluxes and lower evaporative heat fluxes, resulting in increased CHF for both cases. They noted general increases in total heat flux with reduced impingement height and increased velocity for the single-jet, with the opposite being true of the multi-jet case.

Ludick et al. 2023 [114] focused on confined singular impingement onto an enhanced surface consisting of a regular array of pins (electing to conduct the study using a 3D computational domain). The working fluid was HFE-7100 and the validation case selected was that of Rau and Garimella 2014 [155]. A star pattern pin arrangement was proposed that reduced flow obstruction, thereby reducing the region of dryout further from the jet. This was also true of reduced pin height and increased pin spacing. Increased surface augmentation factor (defined as $A_{surface}/A_{flat\ plate}$) was identified as the primarily variable responsible for increases in heat

transfer.

To the best of the authors knowledge, no numerical studies addressing the influence of surface curvature, as well as, geometric parameters relating to single/conical surfaces in jet impingement boiling have been undertaken.

2.5 Summary

The Literature review covered three main sections, single phases jets, boiling and multiphase jets.

Literature concerning single phase jets focused primarily on the submerged axisymmetric jet impingement. In *section 2.2.2* the hydrodynamics of submerged single-phase jets was discussed, with the concept and mechanisms of jet turbulence propagation introduced alongside the definition of a potential core. The stagnation point, pressure profile along the impingement surface and boundary layer development was also covered. The single-phase heat transfer coefficient was defined with an explanation for the two peaks in single-phase Nusselt number profile. Increased jet Reynolds number was seen to increase the Nusselt number and shift the peaks further from the stagnation point. Increased turbulence intensity and height resulted in an increase in Nusselt number at the stagnation point (provided the the height remained within the potential core). Increased surface curvature on concave surfaces was seen to uniformly enhance the Nusselt number. This was attributed to, among other things, increases in surface area and radial fluid acceleration. Placing a cone centred at the stagnation point resulted in an additional impact region that is thought to result in a local thinning of the boundary layer and enhancement of the average Nusselt number. Increases in surface area were also cited as a reason for improvements in the average Nusselt number. A local maximum in average Nusselt number was reported for both cone angle and cone base to jet diameter ratio.

Literature concerning boiling began with the introduction of the boiling curve and defined the nucleate boiling heat transfer coefficient (BHTC) (*eq.* (2.7)). Increasing surface roughness, for highly wetting fluids, resulted in earlier incipience, increased nucleation site density, increased bubble departure frequency reduced bubble departure diameter, decreased wall superheat and increased BHTCs. Increased wettability on hydrophilic surfaces shifted the boiling curve to the left and increased the BHTC. Increased pressure was seen to reduce the wall superheat and shift the boiling curve to the left. A review of subcooled flow boiling introduced the idea of additional bubble forces and heat flux considerations as a result of fluid velocity and subcooling. The factors influencing growth and dynamics of bubbles were then covered in detail based on an energy and a force balance model.

Literature pertaining to multiphase jet impingement revealed the presence of hysteresis and temperature excursion effects in experimental boiling boiling curves. It was shown that increasing jet velocity resulted in minor increases in BHTC for liquid nitrogen jets with a noticeable increase in CHF. It was reported that decreased subcooling promoted earlier incipience and shifted the nucleate boiling curve to the left when operating in a low subcooling range (0-8K). Decreased impingement height was shown by multiple authors to increase BHTC. It was noted that cryogenic fluids (such as liquid nitrogen) have low surface tension resulting in low contact angles and high wettability. This resulted in small bubble departure diameters. Increased surface curvature was found to increase BHTC and CHF, with increased surface area, increased normal pressure gradients and pressure along the wall cited as possible reasons. The addition of a singular pin to the surface resulted in decreased wall superheat (shifting the boiling curve to the left) and increased CHF. Mixed results were obtained with respect the influence on BHTC.

It was discovered that the multiphase Eulerian model coupled with the RPI wall boiling model is a computationally inexpensive method of modeling jet impingement boiling and has been successfully implemented by multiple authors. Whilst many of the same settings and sub-models used by previous authors ([195], [114]) can be employed as closing relations in the multiphase Eulerian model, the RPI wall boiling model requires additional attention as the use of a cryogenic fluid (with high wettability) in the validation case presented in *chapter 4* necessitates differing RPI closing models. It is thus desirable to conduct an in-depth investigation into relevant RPI closing models in *chapter 3*, establishing new correlations where applicable.

Chapter 3

RPI Wall Boiling Model

3.1 Introduction

This chapter provides an overview of the RPI wall boiling model, followed by an investigation into the applicable cryogenic closing models of: maximum bubble departure diameter, nucleation site density, frequency of bubble departure, area of influence and bubble waiting time coefficient. Where literature is deemed to be sparse or inadequate, new correlations or applicable ranges are proposed. Comparisons are continually made with respect to commonly employed closing models for water.

3.2 RPI Heat Flux Partitioning

The Rensselaer Polytechnic Institute (RPI) boiling model has been derived in order to provide closing relations for the local heat transfer between the wall and the fluid in the multiphase Eulerian model (see *appendix A* for a detailed description of the multiphase Eulerian model or [137], [150], [195], [114] for a shorter summary). The RPI wall boiling model postulates that the heat flux at the wall can be decomposed into three components:

$$\dot{q_W} = \dot{q_C} + \dot{q_E} + \dot{q_Q} \tag{3.1}$$

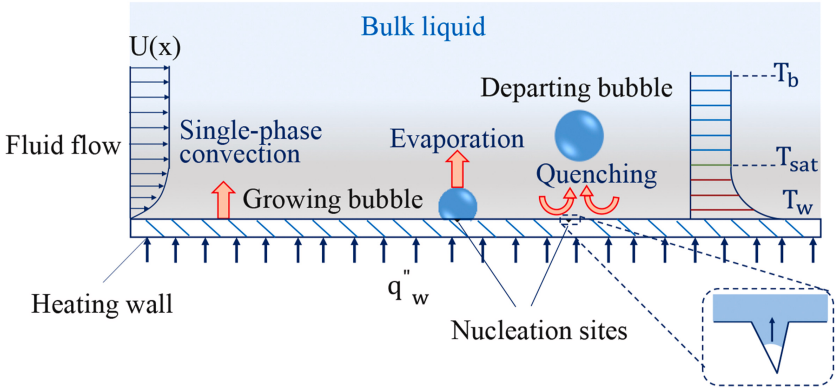

Figure 3.1: Heat flux partitioning in the RPI wall boiling model, reproduced from [164]

where: $\dot{q_W}$ is the net wall heat flux into the liquid, $\dot{q_C}$ is the liquid convective heat flux, $\dot{q_E}$ is the evaporative heat flux (responsible for bubble formation) and $\dot{q_Q}$ is the quenching heat flux.

3.2.1 Convective Heat Flux

$\dot{q_C}$ is derived based on Newton's law of cooling and is defined as:

$$\dot{q_C} = h_C(T_w - T_l)(1 - A_b) \tag{3.2}$$

where: h_C is the liquid phase convective heat transfer coefficient derived from the log law [150], T_w is the local wall temperature, T_l is the local liquid temperature and A_b is the non-dimensional area of influence.

The area of influence represents the area around all nucleation sites that repeatedly experience quenching at the bulk temperature (at the frequency of bubble departure).This area has typically been correlated with the bubble departure diameter in literature. For a single nucleation site it has been reported to range between 0.25 to 7.5 times the area occupied by the bubble at its departure diameter [9]. In CFD applications, the area of influence is non-dimensionalized with respect to the wall area in order to extend the applicability of the concept to a subdivided domain. The resulting non-dimensional area of influence A_b varies between 0 (no surface quenching) and 1 (complete surface quenching) and is typically defined as:

$$A_b = \min\left(1, K\frac{N_w \pi D_w^2}{4}\right) \tag{3.3}$$

where: N_w is the nucleation site density, K is dimensionless area of influence constant and D_w is the maximum bubble departure diameter.

Therefore, the non-dimensional area $(1 - A_b)$ in *eq.* (3.2) represents the portion of the wall over which convective heat transfer occurs, in other words $(1 - A_b = 1)$ implies convective heat transfer over the entire wall area and $(1 - A_b = 0)$ implies no convective heat transfer over the wall area (only quenching).

Note: A_b has been limited in order to avoid numerical errors that may arise due to the unbounded nature of the empirical nucleation site density formulas that will be proposed. The ramifications of this will be discussed in *section 3.3.4*, along with an alternate proposed formulation of *eq.* (3.3).

3.2.2 Quenching Heat Flux

The quenching heat flux $\dot{q_Q}$ is obtained from the following assumption:

Consider the departure of a single bubble from the surface. It is assumed that the bubble draws with it/disturbs the thermal boundary layer on the surface of the wall in an area of influence that is directly proportional the projected area of the maximum bubble departure diameter (i.e. departure diameter D_w). New fluid at the bulk temperature then replaces the displaced fluid. This fluid is assumed to be a semi-infinite static slab of fluid with thermodynamic properties at the bulk thermodynamic state. The generic one dimensional heat equation:

$$\frac{\partial^2 T}{\partial x^2} = \frac{1}{\lambda_l}\frac{\partial T}{\partial t} \tag{3.4}$$

is then solved using the following initial and boundary conditions:

$$(t = 0)\begin{cases} T = T_w \text{ at } x = 0 \\ T = T_l \text{ at } x > 0 \end{cases} \quad \text{and} \quad (t > 0)\begin{cases} T = T_w \text{ at } x = 0 \\ T = T_l \text{ at } x = \infty \end{cases} \tag{3.5}$$

The solution to this problem is [181] [27]:

$$T - T_l = (T_w - T_l)\text{erf}\left(\frac{x}{2\sqrt{\lambda_l t}}\right) \tag{3.6}$$

where $\text{erf}(x)$ is the Gaussian error function:

$$\text{erf}(x) = \frac{2}{\sqrt{\pi}}\int_0^x e^{-u^2} du \tag{3.7}$$

Taking the partial derivative of *eq.* (3.6) with respect to x results in:

$$\frac{\partial T}{\partial x} = -\frac{(T_w - T_l)}{\sqrt{\pi \lambda_l t}} e^{\left(-\frac{x^2}{4\lambda_l t}\right)} \tag{3.8}$$

Evaluating *eq.* (3.8) at the wall $(x = 0)$ yields:

$$\left(\frac{\partial T}{\partial x}\right)_{x=0} = -\frac{(T_w - T_l)}{\sqrt{\pi \lambda_l t}} \tag{3.9}$$

The instantaneous quenching heat flux $\dot{q_q}(t)$ at the wall is then defined as:

$$\dot{q_q}(t) = \frac{k_l(T_w - T_l)}{\sqrt{\pi\lambda_l t}} \tag{3.10}$$

where k_l is the thermal conductivity of the liquid, λ_l is the diffusivity. λ_l is defined as:

$$\lambda_l = \frac{k_l}{\rho_l c_{p,l}} \tag{3.11}$$

where ρ_l is the density of the liquid and $c_{p,l}$ is the specific heat of the liquid.

Computing the average of *eq.* (3.10) over the period of a single bubble (t_p) yields:

$$\dot{\bar{q}_q} = \frac{1}{t_p}\int_0^{t_p} \frac{k_l(T_w - T_l)}{\sqrt{\pi\lambda_l t}} dt = \frac{2k_l(T_w - T_l)}{\sqrt{\pi\lambda_l t_p}} \tag{3.12}$$

The assumption that has been made here is that the quenching occurs over the entire area of influence over the entire bubble period. This is somewhat inaccurate as the area beneath the bubble will grow over the bubble growth time, thus reducing the total quenching area of influence for the bubble. This results in an overall decrease in the area of influence which is significant if the difference between D_w and the diameter of influence (which is yet to be determined) is small and/or the bubble growth time is far larger than the bubble quenching time. Additionally, the enhanced quenching effect due to overlapping areas of influence, as was proposed by Del Valle and Kenning 1985 [35], has been omitted from this formulation.

Taking the area of influence into account and introducing a new parameter to account for the above mentioned shortfalls of the formulation, the final quenching heat flux can be written as:

$$\dot{q_Q} = C_{wt}\frac{2k_l}{\sqrt{\frac{\pi\lambda_l}{f}}}(T_w - T_l)A_b \tag{3.13}$$

where: C_{wt} is the bubble waiting time coefficient (a constant with a default value of 1 that is used to used to manually adjust the quenching heat flux independent of the evaporative or convective heat fluxes) and f is the frequency of bubble departure.

3.2.3 Evaporative Heat Flux

$\dot{q_E}$ is defined as:

$$\dot{q_E} = V_d N_w \rho_v h_{lv} f \tag{3.14}$$

where: V_d is the maximum volume of the bubble and $h_{lv} = h_v - h_l$ is the latent heat or heat of evaporation.

Assuming spherical bubbles, V_d is defined as [62]:

$$V_d = \frac{\pi D_w^3}{6} \tag{3.15}$$

3.3 RPI Closing Models

Four models are now required in order to provide a closed set of equations for the RPI wall boiling model. Those are the models for the maximum bubble departure diameter (D_w), the nucleation site density (N_w), the bubble departure frequency (f) and the area of influence constant (K). The heat transfer coefficient (h_c) is assumed to be computed in an analogous manner to that of single-phase simulation using the liquid properties. In addition, it should be noted that the bubble waiting time coefficient (C_{wt}) is a free parameter that may be explored.

3.3.1 Maximum Bubble Departure Diameter

The bubble departure diameter D_w is defined as the size of the bubble required to lift off from the surface and enter the bulk flow. It is an important variable when computing the evaporative and quenching heat fluxes. Some proposed correlations and methods of derivation are detailed below.

Fritz and Ende 1936 [51] (*eq.* (3.16) in *table 3.1*) utilised a dynamic force balance approach in order to derive an empirical solution for bubble departure diameter. The correlation was then calibrated by multiplying the solution by an experimentally determined constant of 0.0146. The experimental data considered hydrogen and water vapour bubbles in water [180]. The model is reported to pertain to a contact angle range of $59° \leq \theta \leq 125°$ according to [97].

Tolubinsky and Kostanchuk 1970 [178] considered the effect of pressure and subcooling on bubble departure diameter. They revealed that bubble diameter increases with reduced pressure and subcooling. The equation (*eq.* (3.17)) that has been attributed to them in literature [200] and implemented within *Ansys Fluent 2024* (shown in *table 3.1*) is, to the best of the author's knowledge, unrepresentative of the true correlation presented in their paper that was obtained by a dimensional analysis approach whereby coefficients were calibrated by many experiments utilising boiling water at various pressures and subcoolings. *Equation* (3.17) is believed to be simple exponential curve fit pertaining to a single one of their data sets. The addition of the limiting function is rather perplexing as subcoolings in excess of -38 K (i.e. the liquid would have to be superheated to 38 K above T_{sat}) would be necessary in order for its application to be relevant.

Kocamustafaogullari and Ishii 1983 [100] (*eq.* (3.18) in *table 3.1*) modified the Fritz and Ende 1936 [51] equation to account for the effect of pressure on bubble departure diameter.

Kirichenko et al. 1976 [98] (*eq.* (3.19) and *eq.* (3.20) in *table 3.1*) called into question the validity of the Fritz and Ende 1936 [51] correlation (*eq.* (3.16)) for low contact angle fluids. The argument was made that for low contact angle fluids ($\theta \approx 0$) it is reasonable to assume that bubble departure occurs at the microcavity edge as opposed to the flat surface of the wall (as was assumed by Fritz and Ende 1936 [51]). They proposed an empirical solution for low contact angle fluids as a function of cavity radius (for which an empirical solution was also proposed). The resulting correlation was then evaluated against experimental data utilising various cryogenic fluids including oxygen and nitrogen with good agreement [98], [96], [61].

A visual representation of the resulting bubble departure diameters using material properties of water (*table F.1*) and nitrogen (*table 4.1*) at $P_{sat=140\ \text{kPa}}$ is presented in *fig. 3.2*. As expected, the equation for *Tolubinsky* has an exponential trend that is identical for both fluids as it is simply a function of the subcooled temperature. The *Fritz* correlation predicts $D_w \approx 0.15$ mm at $\theta = 7°$. This coincides with *Kirichenko* at $\Delta T_w \approx 7$ K. The *Fritz* is linearly proportional to contact angle whilst the *Kirichenko* model is dependent on wall temperature and varies greatly at lower wall temperatures. What is of greater importance though, is that the *Kirichenko* model predicts reducing bubble sizes with increased wall temperatures (as one would expect due to the reduction in applicable nucleation cavity size with increased wall superheat). This reduction in size, whilst marginal past $\Delta T_w = 10$ K is crucial as it heavily influences the bubble departure frequency at this size range (to be discussed in *section 3.3.3*). The resulting plot for *Kocamustafaogullari* illustrates a slight modification of the *Fritz* correlation when considering water. However, when applying their same correction to the *Fritz* model to nitrogen the discrepancy is significant with the bubble departure diameter being severely underpredicted. Note that, $\theta \approx 40 - 70°$ for water on copper [117], thus bubbles of $D_w \geq 1$ mm are predicted by the $Fritz$ and $Kocamustafaogullari$ for water.

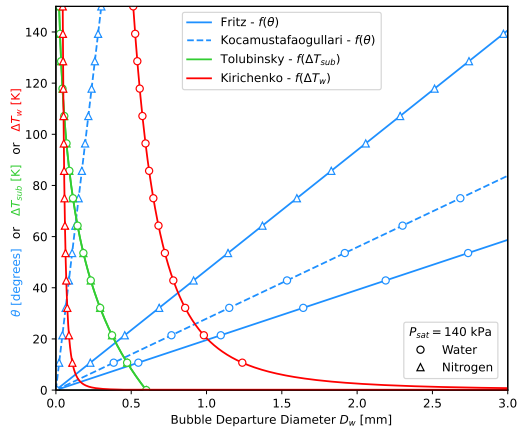

Figure 3.2: Correlations of bubble departure diameter as a function of (θ, ΔT_{sub}, ΔT_{sat}) for nitrogen and water ($P_{sat} = 140kPa$)

Table 3.1: Empirical and semi-empirical formulas for bubble departure diameter (D_w [m])

Reference	Correlation		Notes:
Fritz and Ende 1936 [51]	$D_w = 0.0146\theta\sqrt{\frac{2\sigma}{g(\rho_l - \rho_v)}}$	(3.16)	–
Tolubinsky and Kostanchuk 1970 [178]	$D_w = \min\left[0.0014, 0.0006e^{\frac{-\Delta T_{sub}}{45}}\right]$	(3.17)	–
Kocamustafaogullari and Ishii 1983 [100]	$D_w = 0.0012\left(\frac{\rho_l - \rho_v}{\rho_v}\right)^{0.9}\left[0.0146\theta\sqrt{\frac{2\sigma}{g(\rho_l - \rho_v)}}\right]$	(3.18)	–
Kirichenko et al. 1976 [98]	$D_w = 2\left[\frac{3}{4}\frac{\sigma}{g(\rho_l - \rho_v)}(2R_c)\right]^{1/3}$	(3.19)	R_c is the cavity radius. Used by: Li et al. 2009 [109]
	$R_c = \frac{2\sigma T_{sat}}{\rho_v h_{lv} \Delta T_w}$	(3.20)	

This is significantly larger than the 0.2mm predicted by *Kirichenko* for nitrogen. Therefore, in general, one expects the departure diameter of water bubbles to be greater than that of nitrogen.

3.3.2 Nucleation site density

Nucleation site density (N_w) is defined as the number of nucleation sites per square meter. Lemmert and Chawla 1977 [107] developed a correlation based on wall superheat for pool boiling of water (*eq.* (3.21) in *table 3.2*). Kocamustafaogullari and Ishii 1995 [101] developed a semi-empirical correlation for pool boiling taking into account the effect of wall superheat and surface tension (*eq.* (3.22) in *table 3.2*). Kirichenko et al. 1976 [96] developed a model for the boiling of cryogenic liquids also taking into account surface tension and wall temperature as well as proposing a dependence of the coefficients on different pressure ranges (*eq.* (3.23) in *table 3.2*).

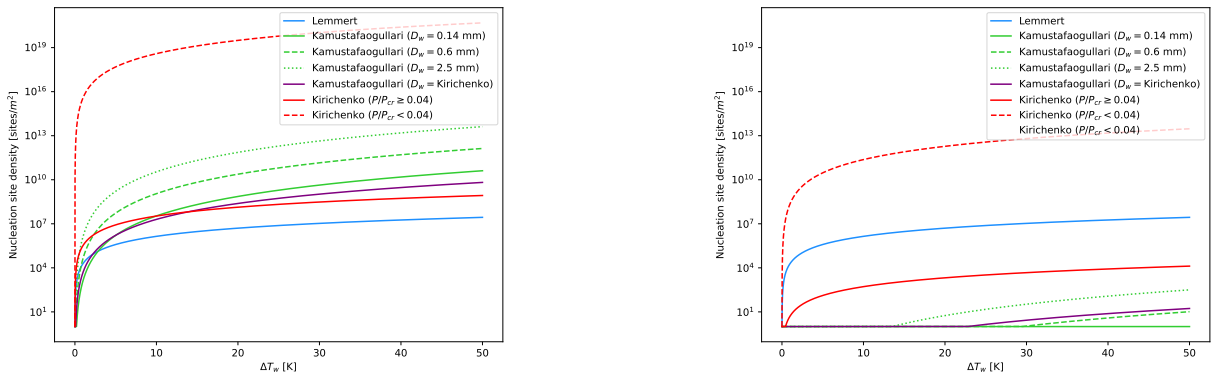

(a) Nitrogen ($P_{sat} = 140kPa$) *(b) Water ($P_{sat} = 140kPa$)*

Figure 3.3: Correlations of nucleation site density as a function of wall superheat

Figure 3.3 displays the plotted correlations presented in *table 3.2* utilising the properties of both water and nitrogen at $P_{sat} = 140$ kPa with the results being clipped to a minimum of 1 nucleation site per square meter. In general, the predicted nucleation site density for nitrogen is far greater than that of water. This is to be expected considering that the cavity size required for nitrogen is far smaller than water ($\frac{R_{c\ (water)}}{R_{c\ (nitrogen)}} \approx 250$ using *eq.* (3.20) with properties evaluated at $P_{sat} = 140$ kPa) implying an increased probability of suitable nucleation

Table 3.2: Empirical and semi-empirical formulas for nucleation site density (N_w [sites/m^2])

Reference	Correlation		Notes:
Lemmert and Chawla 1977 [107]	$N_w = (210\Delta T_w)^{1.805}$	(3.21)	–
Kocamustafaogullari and Ishii 1995 [101]	$N_w = \frac{f(\rho^*)R_c^{*-4.4}}{D_w^2}$ where: $\rho^* = \frac{\rho_l - \rho_v}{\rho_v}$	(3.22)	R_c is the cavity radius
	$f(\rho^*) = 2.157 \times 10^{-7}\rho^{*-3.2}(1 + 0.0049\rho^*)^{4.13}$		
	$R_c^* = \frac{2R_c}{D_w}$, $R_c = \frac{2\sigma T_{sat}}{\rho_v h_{lv}\Delta T_w}$		
Kirichenko et al. 1976 [96]	$N_w = C_n\left[\frac{h_{lv}\rho_v\Delta T_w}{\sigma T_{sat}}\right]^m$	(3.23)	Used by: Li et al. 2009 [109] to model flow boiling of liquid nitrogen
	$(P/P_{cr} \geq 0.04)\begin{cases} C_n = 1 \times 10^{-7} \\ m = 2 \end{cases}$		
	$(P/P_{cr} < 0.04)\begin{cases} C_n = 625 \times 10^{-6} \\ m = 3 \end{cases}$		

cavity sites for nitrogen on most surfaces.The *Lemmert* is the same regardless of material. In light of the other models, the *Lemmert* model grossly underpredicts the nucleation site density for nitrogen, whilst it is one of the higher predictions for water. The *Kamustafaogullari* model is rather sensitive to departure diameter with the nucleation site density increasing with decreased D_w.

Consider that the critical pressure (P_cr) for nitrogen is 3.3958 MPa. Therefore, assuming an operating pressure of 140kPa, $P/P_{cr} = 0.0412 \geq 0.04$, however if the operating pressure were to drop to 120kPa $P/P_{cr} = 0.035 < 0.04$. This is relevant as the operating pressure of the validation case that will be covered in *chapter 4* is within this range. Therefore both of the proposed *Kirichenko* correlation coefficients may need to be considered. However, if one computes the nucleation site density multiplied by the cavity area, one would expect the result to be bounded by 1:

$$\pi R_c^2 N_w \leq 1 \tag{3.24}$$

At the upper limit of $\pi R_c^2 N_w = 1$ this would imply that the entire area of the surface is occupied by active nucleation cavities. A value greater than 1 would imply that there is more cavity area than wall area on the same section of wall and thus a transition to film boiling as a result of coalescence is likely. Taking the cavity radius to be that defined by *eq.* (3.20) in *table 3.1*, $\pi R_c^2 N_w$ is then computed for all the correlations presented in *table 3.2* using nitrogen properties at $P_{sat} = 140$ kPa. Result are presented in *fig. 3.4*. All correlations except *Kirichenko* $P/P_{cr} < 0.04$ conform to the theoretical limit imposed by *eq.* (3.24). Whilst results slightly greater than 1 could conceivably be justified by considering the effect of extremely rough or porous walls it unlikely that areas in excess of 10 000m^2 per square meter of wall at wall superheats below 1K could be justified without immediate dryout/CHF occurring.

3.3.3 Frequency of Bubble Departure

The bubble departure frequency is defined as:

$$f = \frac{1}{t_p} = \frac{1}{t_g + t_w} \tag{3.25}$$

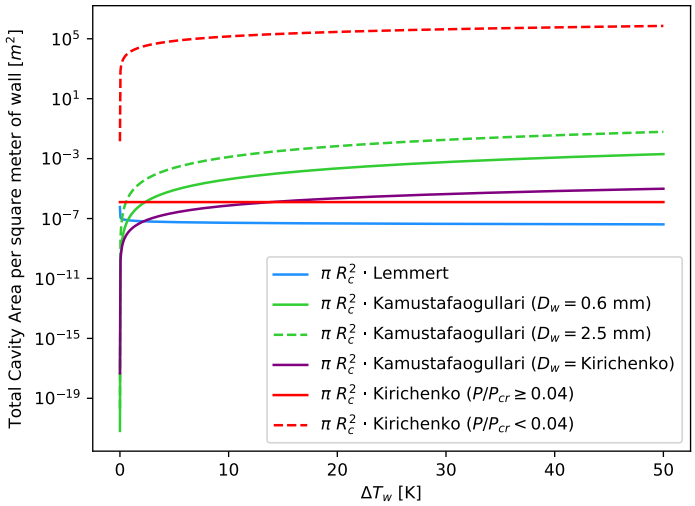

Figure 3.4: Total cavity area for nucleation site density correlations as a function of wall superheat [Nitrogen ($P_{sat} = 140kPa$)]

where: t_p is the total period between successive bubble departures, t_g is the bubble growth time and t_w is the waiting time between the departure of a bubble and the growth of a new bubble at the same nucleation site (due to the time required for bubble collapse following necking and the surface quenching that lowers the local fluid temperature thus requiring heating time before reaching thermal equilibrium and initiating regrowth [14]).

It is generally accepted in literature that departure frequency is related to departure diameter through an expression of the form: $fD_w^n = C$, where C is an experimentally determined constant or an empirically derived function of fluid properties and/or wall superheat and subcooling. n is a constant exponent. The computation of C and n have typically been divided into 3 approaches [78] [61], whereby different departure mechanisms are considered (see *table 3.3*).

1. **Hydrodynamic region:** In this region, bubble departure is directly related to the speed of bubble departure based on a force balance between the buoyancy and hydrodynamic drag (neglecting surface tension, inertia and viscous forces). This results in formulations with an exponent $n = 1/2$. Cole 1960 [31] coupled this approach with the assumption that dryout occurs when $fD_w = u_{bubble}$, to obtain his correlation (*eq.* (3.26) in *table 3.3*). This has been calibrated to match the departure frequency of water. It is the predominant relationship that has been utilised in the RPI boiling model to date.

2. **Transition region:** In this region frequency is reported to be related to the forces of surface tension, buoyancy and drag (of similar magnitude). Empirical solutions are reported to be extremely complex in nature and as a result correlations are typically obtained through non-dimensional analysis of experimental results [78]. The exponential range in this regime is typically $1/2 < n < 2$. A model of this form was proposed by Jakob and Fritz 1931 [79] (*eq.* (3.27) in *table 3.3*).

3. **Thermodynamic region:** In this region, the growth of a vapour bubble is determined only by the heat reserve of the superheated liquid layer. Frequency is the computed through the solution of the transient conduction problem at the surface (as was proposed by Ivey 1967 [78] and [126]). Nitrogen is reported to operate in this region [78]. The exponent is typically $n = 2$ for this region. Different correlations for departure frequency based on thermodynamic growth can be found in *table 3.3* (eq. (3.28), *eq.* (3.29), *eq.* (3.30) and *eq.* (3.31)).

The effects of the power (n) to which D_w is raised (and hence the different regions of bubble frequency departure) are clearly seen in the slope of the correlations in *fig. 3.5*. A consistent trend is that all models experience relatively large increases in frequency for $D_w < 0.1$, however thermodynamic region formulations are particularly sensitive. This will result in large discrepancies in total wall heat flux with small diameter changes (such as those found in the *Kirichenko* bubble departure diameter correlation *eq.* (3.19)) and will thus greatly influence wall temperature. As an additional note, the *Mickic* and *Hatton* correlations are highly sensitive to subcooling and wall superheat, respectively.

Table 3.3: Empirical and semi-empirical formulas for bubble departure frequency (f [Hz=1/s])

Reference	Correlation		Notes:
Cole 1960 [31]	$f = \left[\frac{4g(\rho_l - \rho_v)}{3C_D\rho_l D_w}\right]^{1/2}$	(3.26)	Evaluated for water. C_D is the drag coefficient and $C_D \approx 1$ for steam bubbles.
Jakob and Fritz 1931 [79]	$f = \frac{0.078}{D_w}$	(3.27)	Pool boiling
Ivey 1967 [78]	$f = \frac{23\pi\lambda_l}{D_w^2}$	(3.28)	Evaluated for pool boiling of Nitrogen
Mikic and Rohsenow 1969 [126]	$f = \left[\frac{0.83Ja(\pi\lambda_l)^{1/2}}{D_w}\right]^2$ $Ja = \frac{\rho_l c_{p,l}\Delta T_{sub}}{\rho_v h_{lv}}$	(3.29)	–
Tibiriçá and Ribatski 2014 [177]	$f = \left[\frac{0.003457}{D_w}\right]^2$	(3.30)	Evaluated for flow boiling of R134a and R245fa in small channels
Hatton and Hall 1966 [63]	$f = \frac{3}{\pi\lambda_l}\left[\frac{8k_l\sigma T_{sat}}{(h_{lv}\rho_v)^2 D_w R_c}\right]^2$	(3.31)	–

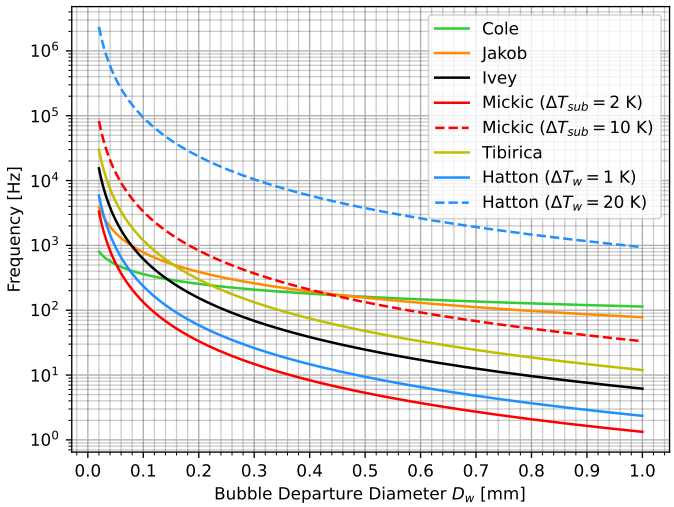

Figure 3.5: Correlations of bubble departure frequency as a function of bubble departure diameter [Nitrogen ($P_{sat} = 140kPa$)]

3.3.4 Area of Influence Constant

When a bubble departs it is thought to disturb/take with it an area of the superheated boundary layer that is directly proportional to its diameter (see *fig. 3.6*). The cumulative non-dimensional area of influence (β) can be expressed as:

$$\beta = \frac{N_w \pi D_i^2}{4} = K\frac{N_w \pi D_w^2}{4} \tag{3.32}$$

where (D_i) is the diameter of influence.

Relating this back to the actual total non-dimensional area of influence (A_b) expressed in *eq.* (3.3) (which is smaller due to neglect of overlapping areas):

$$A_b = \min(1, \beta) \tag{3.33}$$

The diameter of influence can be expressed as:

$$\therefore D_i = \sqrt{K} D_w \tag{3.34}$$

where K is the dimensionless area of influence constant mentioned in *section 3.2.1.* Thus K directly influences the size of the region on which quenching occurs following bubble departure. The exact value of K is somewhat ambiguous, with multiple constants and correlations being proposed in literature.

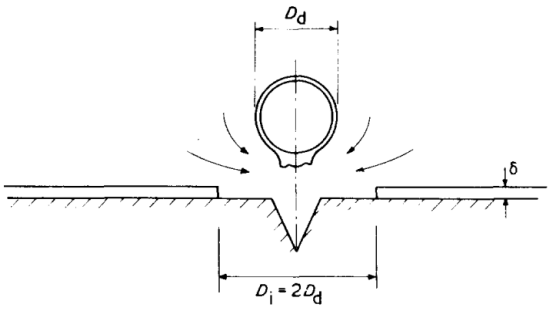

Figure 3.6: Departing bubble removing an area of superheated layer equivalent to twice its diameter, reproduced from [14]

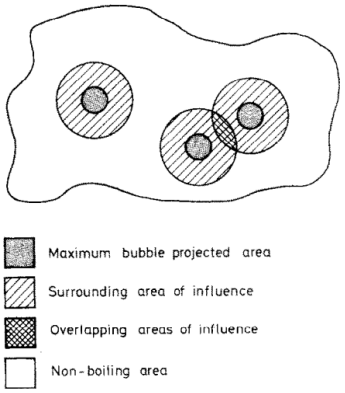

Figure 3.7: Partitioning of area, reproduced from [35]

Based on experimental observations, Chi-Yeh and Griffith 1965 [28] concluded that when a sphere departs from the bottom of a tank of water, it generates a flow toward the vortex ring forming in the sphere's wake, within a circle twice the diameter of the sphere. From this, they concluded that $K \approx 4$. This result has been utilised by a number of authors including [125] as an approximation within their proposed semi-empirical solutions.

Kenning and Del Valle M 1981 [89] first proposed the idea of accounting for reduction in the total area of influence as a result of the overlapping of adjacent area of influences (see *fig. 3.7*). This can be represented as:

$$A_b = \zeta\beta, \qquad \zeta \in (0, 1] \tag{3.35}$$

where ζ is some decaying function less than 1 that represents the ratio of actual to cumulative area of influence. This is a more general form of *eq.* (3.33) that can account for overlap of area of influence for $\beta < 1$. Assuming a random Poisson distribution of nucleation sites Kenning and Del Valle M 1981 [89] derived a theoretical function for ζ (eq. (3.36) in *table 3.4*).They also proposed the existence of a region surrounding the nucleation site in which other nucleation sites will be suppressed. This was supported by experimental data and the radius of this region was found to lie within the approximate range of $0.75D_i \leq R_{suppression} \leq D_i$ (when assuming $K = 4.8$ for flow boiling experimental data of water [186]). This is supported by observations of [42] for pool boiling of water. The result of this is that *eq.* (3.36) overestimates the amount of overlapped area ($\therefore$ underestimating A_b).

Del Valle and Kenning 1985 [35] examined the flow boiling of water at high heat fluxes (=70-95% CHF) and low subcoolings ($\Delta T_{sub} = 24 - 84$ K) within thin walled stainless steel tubes. They computed a reduction in K from 7.5 at $\dot{q} = 0.7$CHF to 5.8 at $\dot{q} = 0.95$CHF. This computation took into account the enhanced quenching of overlapped regions. They were somewhat sceptical of these large values and suggested non-uniform quenching (with the area closest to the bubble receiving enhanced quenching) as a possible amendment to the model. *Equation* (3.37) has been attributed to them in literature [195], although no mention of such a formula was made in [35]. They also noted a slight reduction in the suppression radius as the heat flux neared CHF, with the peak of the distribution tending towards $R_{suppression} = 0.5D_i$.

Judd and Hwang 1976 [84] (*eq.* (3.38) in *table 3.4*) conducted a pool boiling experiment utilising dichloromethane (methylene chloride) and determined that $K \approx 1.8$. Moghaddam and Kiger 2009 [129] (*eq.* (3.40) in *table 3.4*)

conducted pool boiling experiments using FC-72 and indicated that the area of influence is restricted to the bubble surface contact area, with a proposed value of $K \approx 0.25$. Kim 2009 [94] suggested that $K << 4$.

Yoo, Estrada-Perez, and Hassan 2018 [201] considered the area of influence based on the sliding distance (l_{slide}) of a single bubble. They defined $A_b = K l_{slide} \overline{D_{slide}}$ with $\overline{D_{slide}}$ representing the average sliding diameter over the entire sliding distance (*eq.* (3.39) in *table 3.4*).

Table 3.4: Empirical and semi-empirical formulas for area of influence constant (K) and the ratio of actual to cumulative area of influence (ζ)

Reference	Correlation		Notes:
Chi-Yeh and Griffith 1965 [28]	$K \approx 4$		–
Kenning and Del Valle M 1981 [89]	$\zeta = \frac{1 - e^{-\beta}}{\beta}$	(3.36)	Suppression of nucleation sites not considered in this formulation. It was suggested that $(2 \leq K \leq 5)$.
Del Valle and Kenning 1985 [35]	$7.5 \leq K \leq 5.8$ for: $0.7\text{CHF} \leq \dot{q} \leq 0.95\text{CHF}$		–
	$K = 4.8e^{-Ja/80}$	(3.37)	
Judd and Hwang 1976 [84]	$K \approx 1.8$	(3.38)	–
Yoo, Estrada-Perez, and Hassan 2018 [201]	$K = 3.7 + 10.4e^{-5.9Eo}$	(3.39)	For sliding of a single bubble
	$Eo = \frac{(\rho_l - \rho_v) g \overline{D_{slide}}^2}{\sigma}$		
Moghaddam and Kiger 2009 [129]	$K \approx 0.25$	(3.40)	–

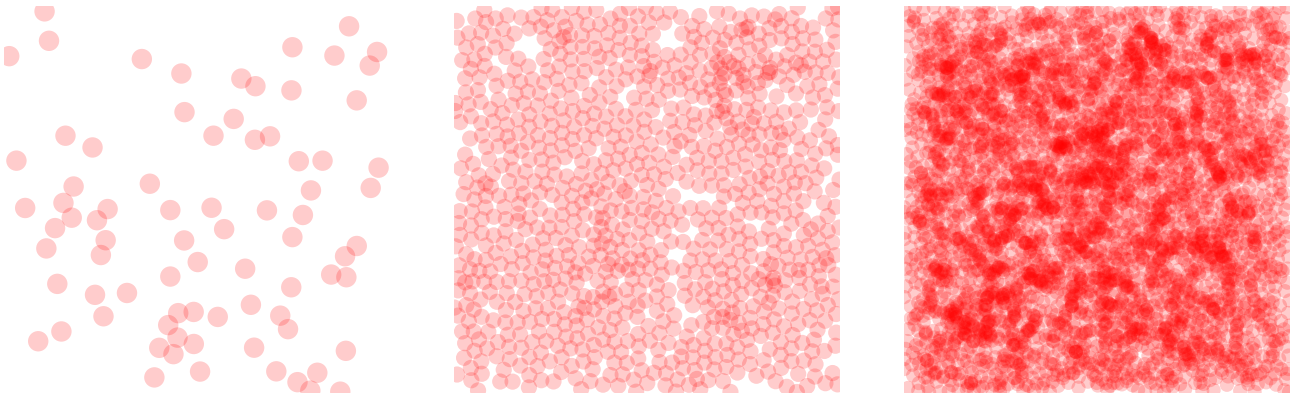

(a) $\Delta T_w = 6$ K *(b)* $\Delta T_w = 12$ K *(c)* $\Delta T_w = 18$ K

Figure 3.8: Monte Carlo simulation (reduced domain $L = 5$ mm, D_w =Kirichenko, N_w =Kocamustafaogullari, $K = 4$)

Monte Carlo Simulation

In order to assess the influence that K and ζ have on A_b, a Monte Carlo simulation (see *appendix C* for more detail) was conducted in which disks of diameter $D_i = \sqrt{K} D_w$ were randomly distributed within a square region (see *fig. 3.8*). Their positions were then iterative adjusted in order to weakly enforce the observation of [89]

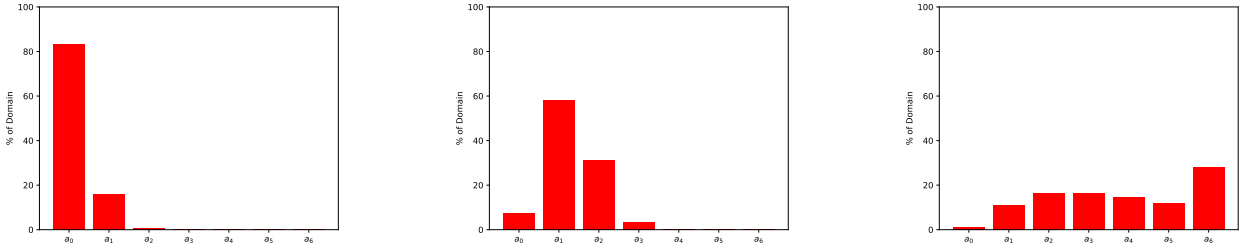

(a) $\Delta T_w = 6$ K *(b)* $\Delta T_w = 12$ K *(c)* $\Delta T_w = 18$ K

Figure 3.9: Average distribution of area within the domain (domain $L = 10$ mm, D_w =*Kirichenko,* N_w =*Kocamustafaogullari,* $K = 4$*)*

that nucleation sites suppress neighbouring nucleation sites within a distance of $R_{suppression} \approx 0.75 D_i$. The combination of $D_w = Kirichenko$ and $N_w = Kocamustafaogullari$, $Kirichenko$ together with $K = 2, 4$ was used to determine the number and size of the disks at a specific wall superheat.

The distribution of non-overlapped and overlapped areas were then calculated (see *fig. 3.9*) in order to obtain the percentage of the domain covered by each region: no area of influence (a_0), single area of influence (a_1), 2 overlapping areas of influence (a_2), 3 overlapping areas of influence (a_3), 4 overlapping areas of influence (a_4), 5 overlapping areas of influence (a_5) and 6 overlapping areas of influence (a_6). The distribution appears to follow a Poisson distribution as suggested by [89].

The following equation then holds true (where 7 and more overlapping areas of influence are binned into a_6):

$$\sum_{i=0}^{6} a_i = 1 \tag{3.41}$$

A_b can then be computed from:

$$A_b = \zeta\beta = 1 - a_0 \tag{3.42}$$

and β can be computed from (thus accounting for any loss in area at the border):

$$\beta = \sum_{i=1}^{n} (i \cdot a_i) \tag{3.43}$$

The resulting A_b vs β plot is shown for the two K values (*fig. 3.10*), alongside the predicted values utilising eq. (3.36) (statistical prediction of [89]) and *eq.* (3.3) (current implementation within Fluent 2024 R1). The choice of both nucleation site density (N_w) and area of influence constant (K) appears to have little impact on the relationship between β and A_b. Equation (3.36) appears to underpredict A_b as expected due to the neglected suppression radius in its formulation. *Equation* (3.3) appears to overpredict A_b. All simulations appear to follow a similar trend and a formula of the form:

$$A_b = 1 - e^{-1.5\beta^{1.2}} \tag{3.44}$$

has been proposed to better approximate the simulated results and provide a smooth curve fit. The non-differentiable nature of *eq.* (3.3) can result in sharp changes in the boiling heat transfer coefficient when solving the RPI wall boiling model both empirically or using CFD *fig. 4.55*, with the effect becoming more pronounced as the quenching heat flux is increased (through increases in C_{wt}, ΔT_{sub} or a combination of both).

3.3.5 Bubble Waiting Time Coefficient

The bubble waiting time coefficient (C_{wt}) appears in *eq.* (3.13) and is utilised in order to adjust the quenching heat flux independent of the evaporative and convective heat fluxes. There exist two mechanisms that influence this coefficient and drive its value in opposing directions (about the value of 1):

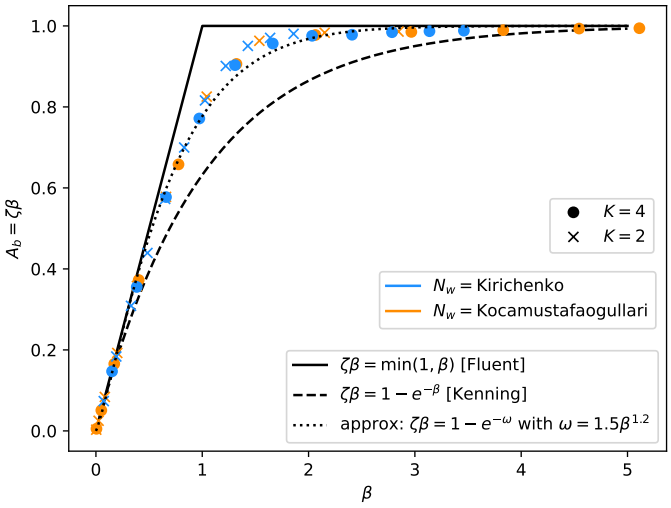

Figure 3.10: Impact of K and N_w on area of influence for a Monte Carlo simulation with eq. (3.3) *and* eq. (3.36) *shown for comparative purposes [nitrogen ($P_{sat} = 140$ kPa), $D_w = Kirichenko$, $\Delta T_{sub} = 2$ K]*

1. **CASE 1 - $C_{wt} < 1$:** For a single isolated nucleation site, the current quenching heat flux model (*eq.* (3.13)) with $C_{wt} = 1$ assumes that quenching happens over the entire area of influence for the entire bubble period. However, it is known from *section 3.3.3* that the total period of a bubble is the sum of its growth time and its waiting time. Therefore, it is safe to assume that quenching will happen over the entire area of influence for the waiting time, but there will be a gradual reduction in the area of influence during the growth time due to the increase in bubble diameter. Therefore smaller waiting times (in relation growth times and dependent on growth rate) would require decreasing values of C_{wt} in order to account for the reduction in area of influence over the bubble period.
2. **CASE 2 - $C_{wt} > 1$:** When considering multiple overlapping areas of influence (as found at higher heat fluxes), there will be enhanced quenching on the overlapping regions, necessitating an increase in quenching heat flux.

CASE 1 Computation

What follows is a computation of C_{wt} assuming the argument proposed in **CASE 1** for non-overlapping areas of influence. In order to compute the growth time let us assume the heat diffusion controlled growth equation proposed by Plesset and Zwick 1954 [146].

$$R(t) = R_0 + Ja\sqrt{\frac{12\lambda_l}{\pi}}\sqrt{t} \tag{3.45}$$

where R_0 is the initial bubble size at the start of the growth period which can be expressed by [14]:

$$R_0 = \frac{R_c \cos\Phi}{1 + \sin\Phi} \tag{3.46}$$

where Φ is the cavity half angle (*fig. 3.11*).

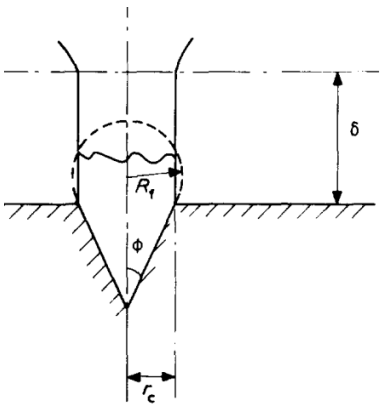

Figure 3.11: Cavity half angle, reproduced from [14]

Assuming a cavity angle of $\Phi \approx 15^\circ$ one obtains $R_0 \approx 0.8R_c$. R_c can then be solved with *eq.* (3.20) the result substituted into *eq.* (3.45) to obtain the radius of the bubble over time for a specified wall superheat. This computation can be taken a step further by imposing the constraint of departure when $R = D_w/2$. Thus the maximum growth time can be computed and the size of the bubble can be plotted over the entire bubble period (computed from the inverse of the bubble frequency). The results for such a plot utilising $D_w = Kirichenko$ and $f = Ivey$ are shown in *fig. 3.12* (although the process could be repeated for any combination of bubble departure diameter and

frequency correlations). *Figure 3.12* begins at $t = 0$ ms where the bubble radius is equivalent to R_0 (the value of which is several orders of magnitude less than the bubble departure radius and appears to be $R \approx 0$ μm). Thereafter, the bubble grows according to *eq.* (3.45) until $t = t_g$ and the departure diameter is reached at $R \approx 70$ μm. The bubble then departs and subcooled fluid floods the area beneath the bubble. This replaces the thermal boundary layer in an area of influence surrounding the bubble, as well as, locally lowers the wall temperature and potentially floods the nucleation site cavity. Thus, a short waiting time of $t = t_w$ is required to heat the surrounding fluid. Once the appropriate thermodynamic conditions are reached, bubble growth begins (at $t = t_p = 1/f$) and the cycle is seen to repeat (three bubble growth/departure events are shown in *fig. 3.12*).

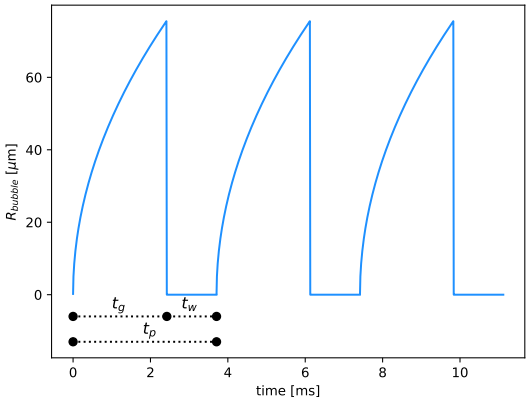

Figure 3.12: Bubble radius as a function of time [nitrogen (P_sat = 140 kPa), D_w =Kirichenko, f =Ivey, $\Delta T_w = 4$ K, $\Delta T_{sub} = 2$ K]

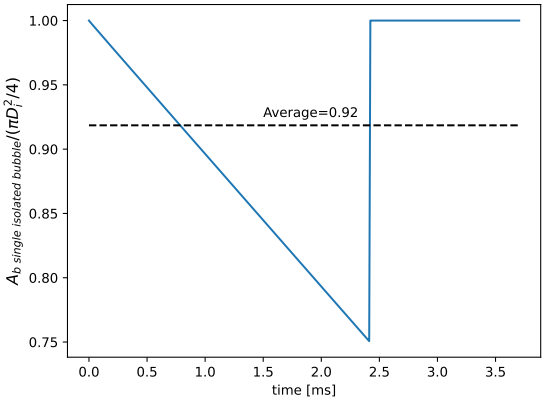

Figure 3.13: Reduction in the area of influence for a single nucleation site due to bubble growth [nitrogen (P_sat = 140 kPa), D_w =Kirichenko, f =Ivey, $\Delta T_w = 4$ K, $K = 4$, $\Delta T_{sub} = 2$ K]

The time dependent area of influence for a single isolated bubble ($A_{\text{b-single isolated bubble}}$) relative to an assumed constant area of influence ($\frac{\pi D_i^2}{4}$) is defined as:

$$A_{\text{b-single isolated bubble}} = \pi \left((D_i/2)^2 - R(t)^2 \right) \tag{3.47}$$

Equation (3.47) has been plotted for a single bubble period in *fig. 3.13*. The average area of influence can then be computed for a single bubble period at all wall superheats. This is equivalent to the integral of eq. (3.47) that has been shown in *eq.* (3.48):

$$\bar{A}_{\text{b-single isolated bubble}} = \frac{1}{t_p} \int_0^{t_p} \frac{1}{2} \int_0^{2\pi} \left((D_i/2)^2 - R(t)^2 \right) d\theta \, dt \tag{3.48}$$

The result normalised with respect to the constant maximum area of influence (for a single bubble) is shown in *fig. 3.14* for D_w =*Kirichenko* and a variety of frequency correlations as well as area of influence constants (K). Note that f=*Tibirica* and f =*Hatton* were omitted due to the predicted bubble periods being less than the minimum required growth time to achieve departure diameter. This hints at an incompatibility between these frequency correlations and the proposed bubble growth rate *eq.* (3.45). Perhaps a different correlation derived from neck controlled growth [14] having faster growth of the form $R(t) \approx R_0 + At^{1/3}$ (found in [20], [14]) may be more suitable. However, this is not explored here. On the whole, it appears that most correlation combinations remain relatively constant as wall superheat is increased with a large decay in value as K is decreased (due to a reduction in the non-affected area of influence outside of the bubble departure diameter).

In order to correct the quenching heat flux, C_{wt} can then be computed directly from:

$$C_{wt} = \bar{A}_{\text{b-single isolated bubble}} \cdot \frac{4}{\pi D_i^2} \tag{3.49}$$

Therefore *fig. 3.14* illustrates that $0.9 < C_{wt} < 1$ (for the selected correlations at $K = 4$ and assuming no overlap of areas of influence).

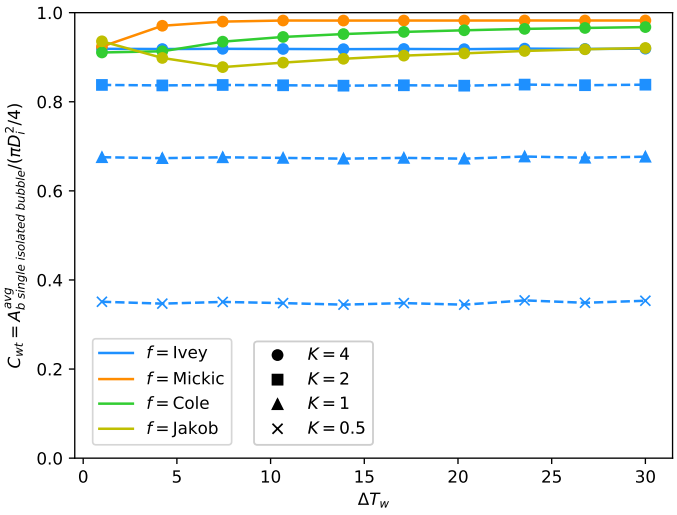

Figure 3.14: Predicted C_{wt} for non-overlapping conditions as a function of wall superheat [nitrogen ($P_sat = 140$ kPa), D_w =Kirichenko, $\Delta T_{sub} = 2$ K]

CASE 2 Computation

What follows is a detailed justification of the argument proposed in **CASE 2**, as well as a computation of C_{wt} utilising the Monte Carlo simulation proposed in *section 3.3.4*. This is compared to a theoretical correlation base on the work of Kenning and Del Valle M 1981 [89] who used a statistical argument that neglected the suppression radius about nucleation sites and is therefore expected to overpredict the degree of overlap and subsequently overpredict C_{wt}.

Let:

$$\dot{q_1} = \frac{2k_l}{\sqrt{\frac{\pi\lambda_l}{f}}}(T_w - T_l) \tag{3.50}$$

Therefore the quenching heat flux *eq.* (3.13) can be rewritten as:

$$\dot{q_Q} = C_{wt}\dot{q_1}A_b \tag{3.51}$$

But it is known from *section 3.3.4*, *eq.* (3.35) that $A_b = \zeta\beta$, therefore:

$$\dot{q_Q} = C_{wt}\dot{q_1}\zeta\beta \tag{3.52}$$

Kenning and Del Valle M 1981 [89] effectively proposed that:

$$\dot{q_Q} = \dot{q_1}\frac{(\pi\beta)^{1/2}}{2}\text{erf}(\beta^{1/2}) \tag{3.53}$$

Therefore, equating *eq.* (3.52) and *eq.* (3.53), rearranging and simplifying to solve for C_{wt} yields:

$$C_{wt} = \frac{(\pi\beta)^{1/2}\text{erf}(\beta^{1/2})}{2\zeta\beta} \tag{3.54}$$

Substituting *eq.* (3.36) for ζ results in the final theoretical correlation:

$$C_{wt} = \frac{(\pi\beta)^{1/2}\text{erf}(\beta^{1/2})}{2(1-e^{-\beta})} \tag{3.55}$$

When considering the Monte Carlo approach the same procedure is followed as in *section 3.3.4* in order to obtain the distribution of disks and the percentage area occupied by respective overlapping areas.

It is then assumed that:

$$\dot{q_Q} = C_{wt}\dot{q_1}(1 - a_0) = \sum_{i=1}^{6} \dot{q_1} A_i a_i \tag{3.56}$$

where $A_i \geq 1$ and represents the coefficient that accounts for enhanced quenching of overlapping regions.

Rearranging and simplifying *eq.* (3.56) to solve for C_{wt} yields:

$$C_{wt} = \frac{\sum_{i=1}^{6} A_i a_i}{1 - a_0} \tag{3.57}$$

This is relatively trivial to solve if the requisite coefficients are known. Kenning and Del Valle M 1981 [89] proposed a solution to this, but the formula presented in their paper was incomplete and its derivation not shown. As such the re-derived formula for these coefficients is shown *appendix B*. The net result is:

Table 3.5: Enhanced Quenching Coefficients

A_1	A_2	A_3	A_4	A_5	A_6
1	$\frac{4}{3}$	$\frac{14}{9}$	$\frac{46}{27}$	$\frac{146}{81}$	≈ 1.896

The theoretical [*eq.* (3.55)] and Monte Carlo, C_{wt} results are shown in *fig. 3.15*. Additionally, **CASE 1** and **CASE 2** were combined by first obtaining the area of influence (in the binned categories) outside the departure diameter $[a_0, a_{1o}, a_{2o}, a_{3o}, a_{4o}, a_{5o}, a_{6o}]$ and then computing:

$$C_{wt} = \frac{\sum_{i=1}^{6} A_i \left(0.68(a_i - a_{io}) + a_{io}\right)}{1 - a_0} \tag{3.58}$$

Where the value of 0.68 was obtained from *fig. 3.14* for $f = Ivey$ and $K = 1$.

Equation (3.58) accounts for both the effect of the reduction in area of influence due to bubble growth as well as enhanced quenching due to overlapping.

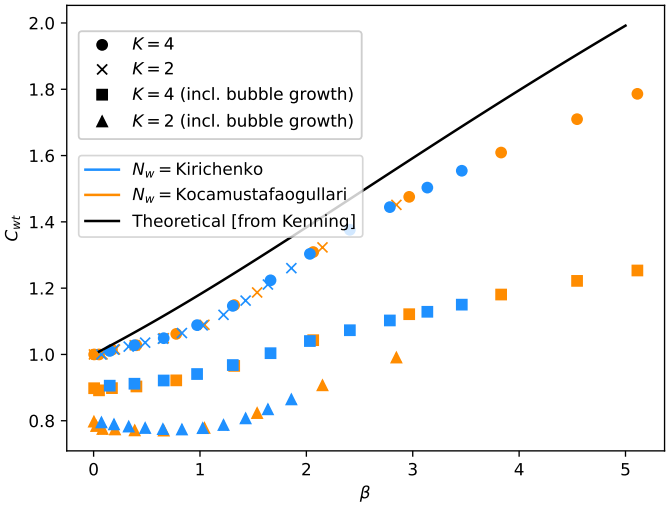

Figure 3.15: Monte Carlo Simulation of C_{wt} [nitrogen (P_{sat} = 140 kPa), D_w =Kirichenko, $f = Ivey$, ΔT_{sub} = 2 K]

The results of the Monte Carlo simulation using two nucleation site density correlations (N_w) and two area of influence constants (K) are shown in *fig. 3.15*. The theoretical formulation [*eq.* (3.55)] should be compared to the simulated results that take into account the suppression radius around the bubbles but do not account

for reduction in area of influence due to bubble growth (circle and x markers). As expected, the theoretical equation overpredicts C_{wt}. The difference in the path traveled for $K = 4$ and $K = 2$ when neglecting bubble growth [*eq.* (3.57)] is negligible, although β is seen to grow faster if K is increased (see *fig. 3.16* for evidence of this statement). When including bubble growth [*eq.* (3.58)] the bubble waiting time coefficient is seen to drop drastically (to between 0.9-1.2 for $K = 4$). This explains why the value of $C_{wt} \approx 1$ that has been used predominantly in literature to date yields fairly good correlation with experimental results as it represents (approximately) the average of C_{wt} when taking into account overlap and and reduction in area of influence due to bubble growth (assuming the impact of D_w is negligible). C_{wt} is seen to drop rapidly if K is lowered when including bubble growth. This correlates well with the observations of *fig. 3.14*. One would expect shorter growth times at equivalent bubble departure frequencies to shift the results including bubble growth (square and triangle markers) upwards towards the results excluding bubble growth (circle and x markers).

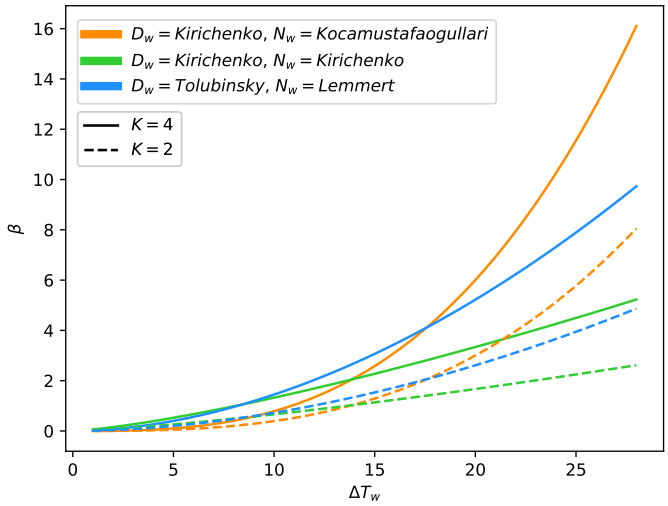

Figure 3.16: Cumulative non-dimensional area of influence as a function of wall superheat [nitrogen ($P_{sat} = 140$ kPa), $\Delta T_{sub} = 2$ K]

3.4 Simplified Empirical Model Solution Process

Assuming $\frac{\dot{q_C}}{\dot{q_W}} << 0.1$ in the fully nucleate boiling regime (as indicated by the results of [195] and [150]). Then one can approximate $\dot{q_W}$ as:

$$\dot{q_W} \approx \dot{q_E} + \dot{q_Q} \tag{3.59}$$

Assuming constant fluid properties (at P_{sat} or T_{sat}) and given the closing models presented in *section 3.3*, both $\dot{q_E}$ and $\dot{q_Q}$ reduce to functions of two variables: (ΔT_w, ΔT_{sub}). Thus a simple model can be constructed from any combination of closing correlations and used to evaluate the required heat flux to induce specified wall superheats at selected subcoolings (assumed to be constant) within the nucleate boiling regime. Such models are detailed in *appendix D* and have been implemented in *section 4.14*, *section 4.12* and *section 4.13* for comparative purposes to assist in the selection criterion for the appropriate boiling model pertaining to the validation case. However, it must be restated that such a simple approach neglects the convective heat transfer and does not account for: turbulent effects, velocity effects, vapour dispersion effects and variable liquid subcooling effects.

3.5 Summary

It was revealed in *section 3.3.1* that $D_w = Kirichenko$ (*eq.* (3.19)) was the most applicable equation for bubble departure diameter with respect to cryogenic fluids. The predicted departure diameter is approximately 0.2 mm with marginal reduction (< 0.1 mm) resulting from increases in wall superheat. This is approximately three times smaller than the value predicted using the *Tolubinsky* relation (*eq.* (3.17)) at low subcoolings. In general, nitrogen departure diameters are far smaller than those predicted for water under the same conditions.

As a result of the small departure diameters for nitrogen, the nucleation site densities increased for the correlations presented in *section 3.3.2* (in comparison to water). It was deemed that $N_w = Kirichenko\ P/P_{cr} < 0.04$ (*eq.* (3.23)) was implausible based on an argument relating to the total surface area occupied by the bubbles. The $N_w = Kirichenko\ P/P_{cr} \geq 0.04$ (derived for cryogenic fluids) and $N_w = Kamustafaogullari$ (derived for water but coupled with $D_w = Kirichenko$) predicted a similar range for nucleation site density, with $N_w = Kamustafaogullari$ predicting a more gradual rise in nucleation site density at low wall superheats but a higher nucleation site density at larger wall superheats (> 15 K). Thus there exists some debate as to the appropriate model to employ in the validation in *chapter 4*. The correlation for $N_w = Lemmert$ (derived for water) is a function of wall superheat only and predicted nucleation site densities two orders of magnitude lower than the aforementioned correlations for nitrogen.

Section 3.3.3 identified three distinct regions governing bubble departure frequency. Cryogenic fluids are reported to operate in the thermodynamic region where $f \propto 1/D_w^2$. $N_w = Ivey$ (eq. (3.28)) was seen as a plausible correlation for nitrogen.

The area of influence constant was thoroughly investigated with a Monte Carlo simulation being used to derive a new area of influence constant correlation of the form: $A_b = 1 - e^{-1.5\beta^{1.2}}$ (*eq.* (3.44)).

The bubble waiting time coefficient was likewise thoroughly investigated and the Monte Carlo was again used to determine the applicable range of this variable to lie between 0.9 and 1.2, for the tested cryogenic closing models, when accounting for the reduction in heat transfer area as a result of bubble growth.

Lastly a simplified empirical solution was proposed, neglecting convective heat transfer effects. This is to be used in the subsequent chapter to provide a comparative solution.

It is now pertinent to take the findings of *chapter 3* and apply them to the liquid nitrogen validation case presented in *chapter 4* using CFD. The validation case considers boiling on flat, singular needle and curved surfaces. The goal of the chapter is to establish numerical models capable of accurately simulating boiling on such surfaces (thus providing a framework for addressing the key objectives presented in *chapter 1* related to the effect of curvature, singular needle height and jet impingement height on the boiling curve and additional metrics). As shall be seen, *chapter 4* contains many sub-objectives, including:

- Taking a RPI boiling model developed for water and extending its application to the cryogenic case through the adjustment of BWTC.
- Determining the most appropriate nucleation site density correlation for the cryogenic model.
- Assessing the influence of the ill-defined experimental parameters of subcooling, velocity and pressure on the boiling curve results of the numerical models presented.
- Assessing the validity and effect of the newly proposed area of influence correlation

It is important to bear in mind that these sub-objectives within *chapter 4* are not only aimed at selecting numerical models that align with experimental data, but also lead to a deep understanding of these models. This will allow informed conclusions to be drawn in the parametric study (*chapter 5*).

Chapter 4

Validation

4.1 Introduction

The validation chapter begins with a detailed description of the experimental setup used by Zhang et al. 2011 [205]. Thereafter, two distinct numerical frameworks are introduced. The first numerical framework ($N1$) consists of commonly available RPI closing models developed for water. The second numerical framework ($N2$) considers the findings of *chapter 3* and consists of RPI closing models developed for cryogenic fluids and incorporates the newly proposed area of influence correlation. There exists some debate as to whether to close $N2$ with the nucleation site density of $N_w = Kirichenko$ or $N_w = Kocamustafaogullari$ and, as such, $N2$ was subdivided into two numerical models: $N2A$ (using $N_w = Kirichenko$) and $N2B$ (using $N_w = Kocamustafaogullari$). Thus three models $N1$, $N2A$ and $N2B$ are used throughout the validation chapter. Following the description of the numerical models, the material properties are discussed. This is succeeded by a description of the numerical domain, the implementation of the boundary conditions and the solution procedure. Thereafter, the influence of boundary location and input conditions are assessed in *section 4.7* and *section 4.8* respectively. The influence of the bubble waiting time coefficient on the boiling curve is then addressed in *section 4.10*. The steady-state assumption is then evaluated by comparing the results to a transient simulation. The effect of the bubble waiting time coefficient is then analysed in *section 4.10*. A mesh independence study is then conducted for the three numerical models. Having established confidence in the numerical accuracy of the models, $N1$ is analysed in detail. $N2A$ and $N2B$ are then compared and analysed, with an emphasis on understanding the influence of the different nucleation site density correlations. This is followed by an analysis of the the effect of the newly proposed non-dimensional area of influence correlation in *section 4.14*. A full comparison of the three models on every experimental boiling curve presented by Zhang et al. 2011 [205] is then shown (baring their experiment on a contaminated surface), with any deviations explained in light of findings from *section 4.8* or otherwise noted. Up until this point in the chapter, results have focused on the flat surface. A transition is then made in *section 4.16* whereby a full comparison of the numerical models against all experimental results for the hemispherical surface is provided. This is followed in *section 4.17* by a similar full comparison for the singular needle surface. Thereafter, a short discussion follows, whereby the performance of $N1$, $N2A$ and $N2B$ across all surfaces is evaluated. *Chapter 4* then concludes with a summary of recommendations on the numerical model and boundary conditions to be selected for use in the parametric study (*chapter 5*).

4.2 Experimental Setup

This validation case considers the experimental observations of Zhang et al. 2011 [205], aimed at investigating the influence of selected jet impingement parameters on the performance of medical cryoprobes. They noted the effect of increasing the heat flux on the wall super heat when making alterations to the inlet velocity, impingement height and impingement surface shape.

In the experiment, liquid nitrogen, held in a vacuum cryostat at an unspecified liquid temperature, was driven into the system inlet (shown in *fig. 4.1*) through the application of a constant elevated pressure nitrogen gas on the free-surface of the liquid. From there it was forced through a vertically aligned stainless steel inner tube of approximately 2.0 mm in diameter (assumed to be inner diameter measurement) before exiting the tube (a.k.a. jet) at a specified impingement height of 1.5 mm or 3.5 mm (depending on the experiment). The flow impinged on a heated copper surface of 5 mm in diameter. The velocity then underwent a direction change of π radians and was forced up through the annular space between the nested inner tube and the confining outer tube (radial

confinement) with ID=5 mm (as shown in the magnified view of *fig. 4.1*).

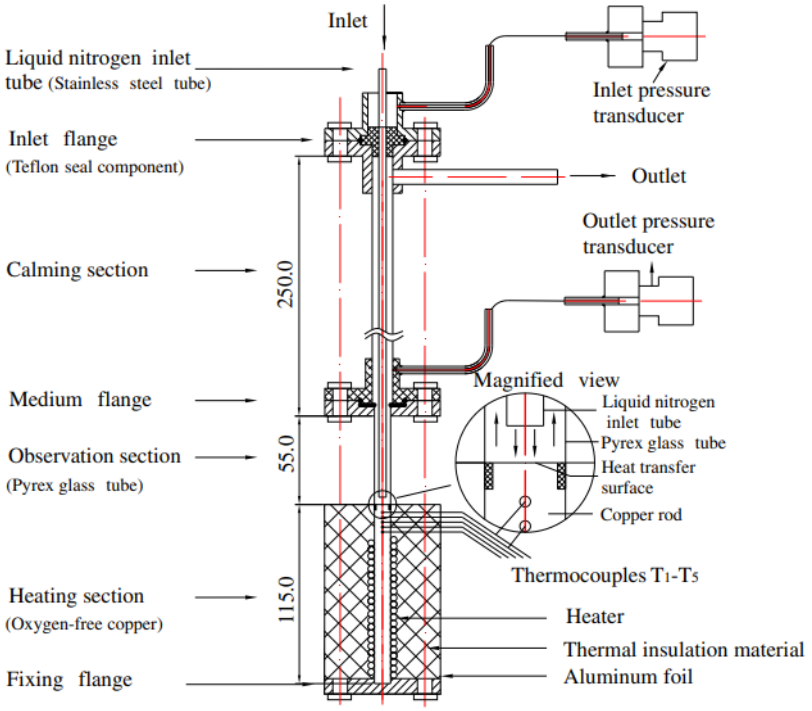

Figure 4.1: Experimental setup of Zhang et al. 2011, reproduced from [205]

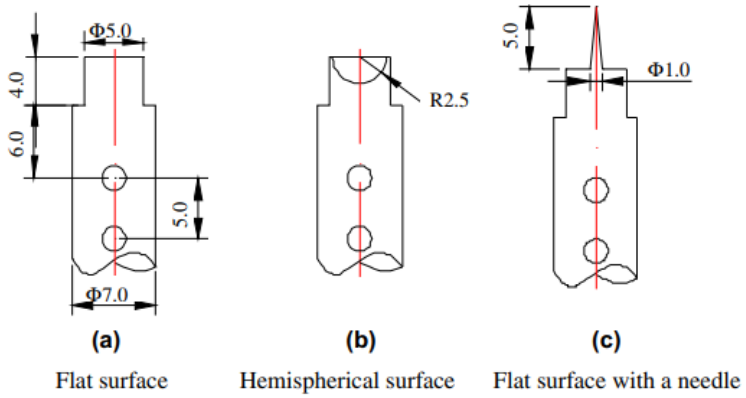

Figure 4.2: Impingement surfaces tested by Zhang et al. 2011, reproduced from [205]

The impingement surface is formed by the end of a copper rod of 115 mm in length. The performance of three separate surface geometries (shown in *fig. 4.2*) were tested under varying velocity and impingement height conditions by applying a specified heat flux to the copper rod and measuring the surface stagnation point wall temperature. The temperature itself was computed through the application of a 1D Fourier heat conduction equation, *eq.* (4.1), based on the recorded values of embedded thermocouples located beneath the surface, along the axis of the rod.

$$\dot{q} = k\frac{\Delta T}{\Delta x} \tag{4.1}$$

Due to the large thermal mass and high thermal conductivity of the rod, the surface stagnation point temperature was reported to be quazi-steady at a specified heat flux. It should, however, be noted that this observation could, in part, be attributed to extrapolated nature of the temperature readings.

Depending on the heated flux supplied to the surface, boiling may have occurred to differing extents, forming a liquid gas mixture that is conveyed through the annular space. Before exiting the system, the mixture flows through a vapourizer where it is heated until a vapour quality of 1 is achieved. A mass flow meter is then

used to measure the vapour mass flow rate (and relate that to the jet velocity in an unspecified manner) before exhausting to the atmosphere.

The apparatus surrounding the test section is held in an approximate vacuum (at a pressure of $\approx 2-5$ Pa) so as to reduce heat losses to the environment associated with natural convection.

The average jet velocity was varied in the range $v_j = 0.34$–1.11 m/s ($3\,700 \leq Re_j \leq 12\,200$) based on saturation properties of nitrogen at 140 kPa) by varying the constant free-surface pressure such that the resulting jet exit pressure was varied in the range $P_j = 101.3$–160.0 kPa. As the resulting Reynolds numbers are greater than 2 300, this indicates that the jet was operating in the turbulent regime upon exit.

The paper neglected to specify the inner tube wall thickness (t_{wall}), which was assumed to be $t_{wall} = 0.2$ mm.

Additionally, the jet subcooled temperature (ΔT_{sub}) was not specified. The issue of empirically computing the value is exacerbated by the lack of temperature readings within the cryostat and the unknown heat transfer that occurred (through the stainless steel inner tube) between the incoming jet and exiting fluid mixture. Thus, the influence of this parameter will be numerically investigated in *section 4.8*. Additionally as ranges were provided for the jet velocity and pressure measurements for each experiment, the influence of these parameters will also be investigated in *section 4.8*.

4.3 Numerical Framework

The multiphase Eulerian model coupled with the RPI wall boiling model is used within ANSYS Fluent 2024 R1 for all CFD simulations presented in this document. A summary of the Multiphase Eulerian framework is presented in *section 4.3.1*. Two separate RPI frameworks (designated $N1$ and $N2$) were utilised in conjunction with the presented Multiphase Eulerian framework. $N1$ attempts to extend the applicability of RPI closing models developed for either flow or pool boiling of water to the current cryogenic fluid application whilst $N2$ focuses on models developed specifically for cryogenic or low contact angle fluids. These RPI frameworks are detailed in *section 4.3.2* and *section 4.3.3* respectively, with $N2$ split into two models; $N2A$ ($N_w = Kirichenko$) and $N2B$ ($N_w = Kocamustafaogullari$); in order to assess the influence of nucleation site density. $N1$, $N2A$ ($N_w = Kirichenko$) and $N2B$ ($N_w = Kocamustafaogullari$) are used in the validation (*current: chapter 4*), whilst only $N2A$ ($N_w = Kirichenko$) is used in the subsequent parametric study (*chapter 5*).

4.3.1 Multiphase Eulerian framework

Presented below is a summary of the multiphase Eulerian sub-models used in this document (further detail can be found in *appendix A*):

- **Drag Coefficient** (C_{drag}): *Ishii, eq.* (A.27)
- **Lift Coefficient** (C_{lift}): *Tomiyama, eq.* (A.16)
- **Wall Lubrication Coefficient** (C_{wall}): *Antal et al., eq.* (A.23)
- **Turbulent Dispersion Force**: *Lopez de Bertodano, eq.* (A.25)
- **Turbulence interaction**: *Troshko Hassan*, [71]
- **Virtual Mass Coefficient (C_{vm}):** $C_{vm} = 0$
- **Heat Transfer Coefficient**: Two Resistance model with the liquid phase modeled using the *Ranz-Marshall* correlation and the vapour phase modeled using the *Tomiyama* correlation [71].
- **Interfacial Area Concentration**: *Ia-Particle, eq.* (A.6)
- **Turbulence Model**: *RNG* $k-\epsilon$ mixture turbulence model with scalable wall functions and both *Production Kato-Launder* and *Production Limiter* applied [71].
- **Turbulence Model Wall Function**: Non-equilibrium wall function (for $N1$) **OR** Scalable wall function (for $N2$) [71].

Note that a less mesh-dependent (see *section 4.11*) wall function has been selected for use with RPI framework $N1$.

The Non-local Boundary Field method (NLBF) in ANSYS Fluent R1-24 was used as a mesh independent method to determine the liquid temperature required to solve the quenching heat flux. This method projects a line of a specified length (0.4mm) perpendicular to the wall into the fluid domain and then uses a second order

averaging algorithm based on the temperature values of distributed points (4 in this case) along that line to extrapolate the temperature of the fluid to the wall [71].

4.3.2 RPI framework: N1

These closing models have been developed (in large part) for water, are readily available within ANSYS Fluent 2024 R1 and have been extensively used in literature for a variety of fluids. It is of interest to understand under what conditions such models can be extended to cryogenic applications.

Note: whilst the models have been developed for water, properties of liquid nitrogen are used where required in the correlations.

- **Departure Diameter** (D_w): $D_w = Tolubinsky$, *eq.* (3.17)
- **Nucleation Site Density** (N_w): $N_w = Lemmert$, *eq.* (3.21)
- **Departure Frequency** (f): $f = Cole$, *eq.* (3.26)
- **Area of influence** (A_b): $A_b = \min(1, \beta)$, *eq.* (3.3)
- **Area of influence Constant** (K): $K = Del\ Valle\ and\ Kenning$, *eq.* (3.37)
- **Bubble Waiting Time Coefficient** (C_{wt}): $C_{wt} = 3.142$ (refer to *section 4.10* for detail regarding selection of value)

4.3.3 RPI framework: $N2A$ and $N2B$

The models selected in these numerical frameworks have been chosen based on their applicability to cryogenic fluids. There existed some debate on whether to use $N_w = Kirichenko$ or $N_w = Kocamustafaogullari$ for the nucleation site density in this framework and thus both were explored in this chapter and have been denoted $N2A$ and $N2B$ respectively. However, $N_w = Kirichenko$ ($N2A$) was finally selected for use in the parametric study (*chapter 5*) for reasons stated in *section 4.13*.

These models are not readily available within ANSYS Fluent 2024 R1 and have been implemented using a custom user-defined function (UDF). The code for this UDF can be found in *appendix G*.

- **Departure Diameter** (D_w): $D_w = Kirichenko$, *eq.* (3.19) (selected for its applicability to cryogenic fluids. A limiter was applied (D_w =min(*eq.* (3.19),1e-3)) to avoid the prediction of an infinite bubble diameter at $\Delta T_w = 0$)
- **Nucleation Site Density** (N_w): $N_w = Kirichenko$, *eq.* (3.23) ($P/P_{cr} \geq 0.04$) for $N2A$ **OR** $N_w = Kocamustafaogullari$ *eq.* (3.22) for $N2B$ (see *section 4.13* for information regarding comparison)
- **Departure Frequency** (f): $f = Ivey$, *eq.* (3.28) (based on the expected thermodynamic bubble growth of nitrogen)
- **Area of influence** (A_b): $A_b = 1 - e^{-1.5\beta^{1.2}}$, *eq.* (3.44) (based on curve fit presented in *section 3.3.4*)
- **Area of influence Constant** (K): $K = 4$
- **Bubble Waiting Time Coefficient** (C_{wt}): $C_{wt} = 1.3$

4.4 Material Properties

4.4.1 Fluid Properties

N1: Constant material properties of liquid and vapour nitrogen at a specified saturation pressure is used. Saturation temperature is selected to be constant at the specified saturation pressure. The saturation pressure is selected based on the following criterion:

$$P_{sat} \begin{cases} 120 \text{ kPa} & \text{if } 0.34 \leq u_j \leq 0.44 \\ 140 \text{ kPa} & \text{if } 0.45 \leq u_j \leq 0.78 \\ 160 \text{ kPa} & \text{if } 0.93 \leq u_j \leq 1.11 \end{cases} \tag{4.2}$$

Refer to *Table 4.1* for fluid properties at these saturation pressures.

N2: Unless otherwise specified, variable liquid nitrogen properties as a function of absolute temperature (at $P_{sat} = 140$ kPa) is used (see *appendix F* for graphical representation of these property functions obtained from [172]). Vapour properties are treated as constant at saturation pressure ($P_{sat} = 140$ kPa). A saturation temperature at P_{sat} has been used. The contact angle for nitrogen on copper has been assumed to be $\theta \approx 7°$ [109] [21].

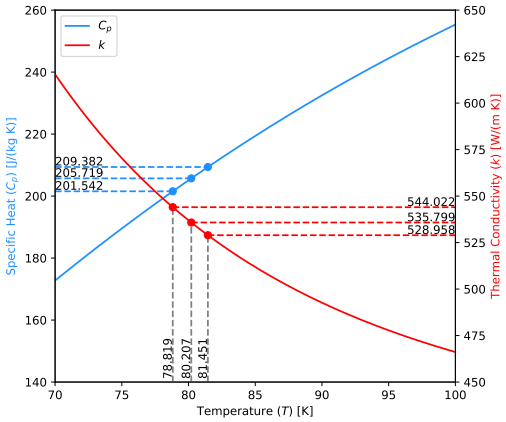

Figure 4.3: Specific heat and thermal conductivity of copper as a function of temperature, correlations obtained from [171]

4.4.2 Solid Properties

N1: The specific heat and thermal conductivity of copper was assumed to be constant at the specified saturation pressure.

N2: The specific heat and thermal conductivity of copper was assumed to be a function of temperature.

Values for specific heat and thermal conductivity were computed based on correlations from [171], represented graphically in *fig. 4.3* with the values at the specified saturation temperatures displayed in *table 4.1* highlighted. The density of copper was assumed to be constant at 8 978 kg/m^3 for both $N1$ and $N2$.

Table 4.1: Properties of nitrogen at specified saturation pressures, data obtained from [172]

P_{sat} [Pa]	T_{sat} [K]	Phase	ρ [kg/m^3]	Enthalpy h [J/kg]	Entropy s [J/(kg · K)]	C_p [J/(kg · K)]	μ [Pa · s]	k [W/(m · K)]	σ [N/m]
120e3	78.819	liquid	799.39	3007.6	38.219	2048.9	1.518e-4	0.14193	8.549e-3
		vapour	5.3917	2.0027e5	2540.9	1135.1	5.559e-6	7.3621e-3	
140e3	80.207	liquid	792.98	5868.9	73.889	2056.7	1.440e-4	0.13918	8.238e-3
		vapour	6.2182	2.0126e5	2510.0	1146.7	5.668e-6	7.5311e-3	
160e3	81.451	liquid	787.15	8446.7	105.47	2064.5	13.75e-4	0.13671	7.961e-3
		vapour	7.0377	2.0212e5	2483.3	1158.1	5.767e-6	7.686e-3	

4.5 Numerical Domain and Boundary Conditions

4.5.1 Numerical Domain

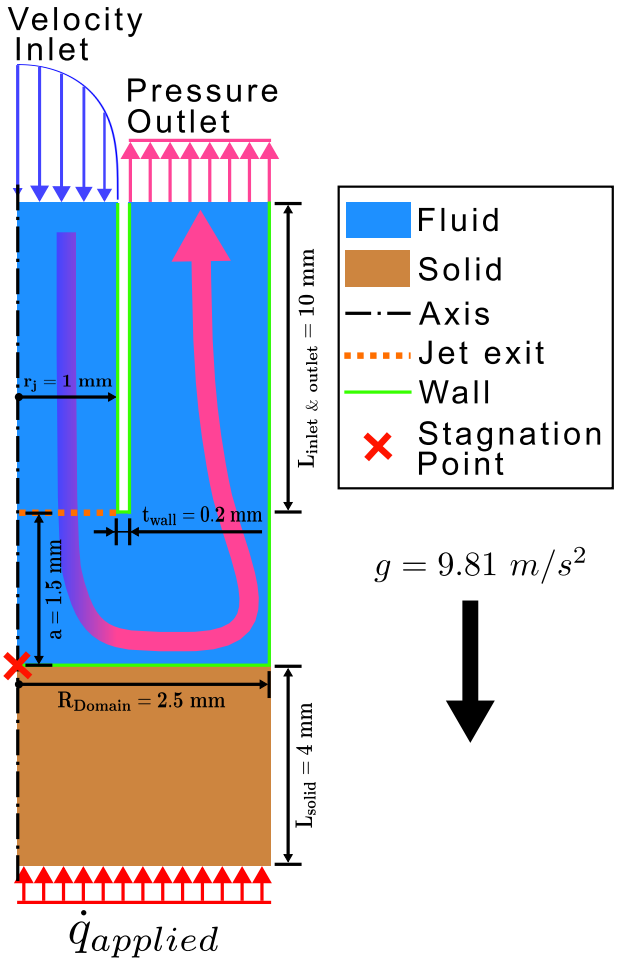

Figure 4.4: Flat plate numerical domain [Diagram not drawn to scale]

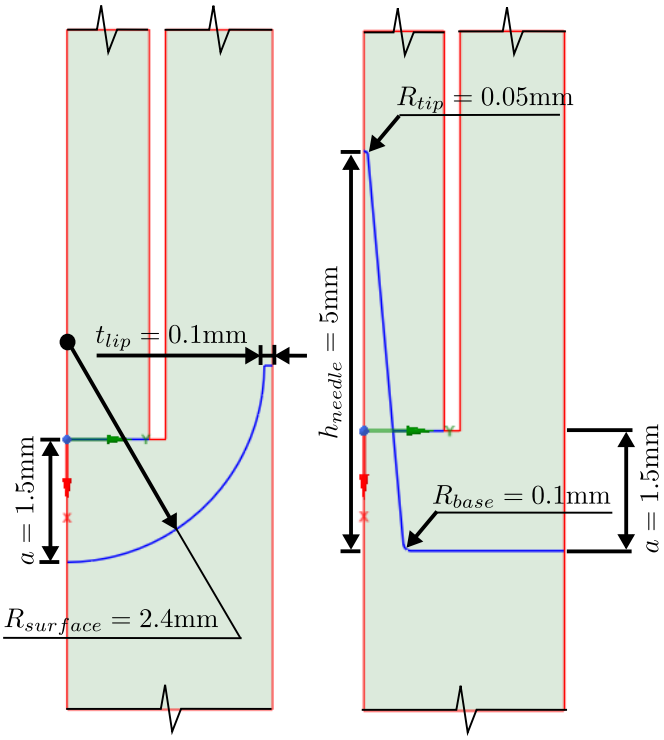

Figure 4.5: Truncated domain of hemispherical and singular needle surfaces [Drawn to scale]

A 2D and axisymmetric domain is used for all simulations in this dissertation. A diagram of the numerical domain is shown in *fig. 4.4* for the flat surface. The axis is along the left hand edge. The generalised path of the fluid is represented by the blue/pink arrow. Fluid enters the domain at the inlet, undergoes a 90° turn as it impinges onto the wall of the solid surface (where boiling occurs), travels along the solid wall before encountering the wall of the outer radially confining tube, where it is forced to undergo another 90° rotation prior to flowing up and out through the outlet. The solid has been modelled with a length of 4 mm. The inlet and outlet are specified at the same hydrostatic height so that the pressure drop across the system can be easily monitored.

The hemispherical and singular needle surfaces are shown in *fig. 4.5*. A small lip ($t_{lip} = 0.1$ mm) was added to the outer edge of the hemisphere in order to replicate the non-negligible lip thickness expected in the experimental setup. Additionally, the needle has received a rounding at the tip ($R_{tip} = 0.05$ mm) and a fillet at the base ($R_{base} = 0.1$ mm) in order to assist with meshing in that region.

The stagnation point has been defined as the location along the axis with a distance of a (impingement height) from the jet exit. This is shown in *fig. 4.4* for the flat surface. Note, this definition implies that the stagnation point is located within the centre of the needle at the base of the needle for the singular needle surface.

Dimensions shown in *fig. 4.4* and *fig. 4.5* are utilised in all simulations unless otherwise stated.

4.5.2 Boundary Conditions

Numerical Domain and BC summary:

- 2D Axisymmetric
- Gravitational force of $g = 9.81$ m/s^2 applied vertically downwards as shown in *fig. 4.4*.
- Constant pressure outlet
- Adiabatic walls, except for solid-fluid interface where a coupled boundary condition allow conjugate heat transfer between the solid and the fluid.
- No-slip velocity boundary condition on all walls
- Constant specified heat flux ($\dot{q}_{applied}$) applied to the base of the solid
- Constant pressure outlet at a specified value of $P_j = 120, 140$ or 160 kPa (absolute)

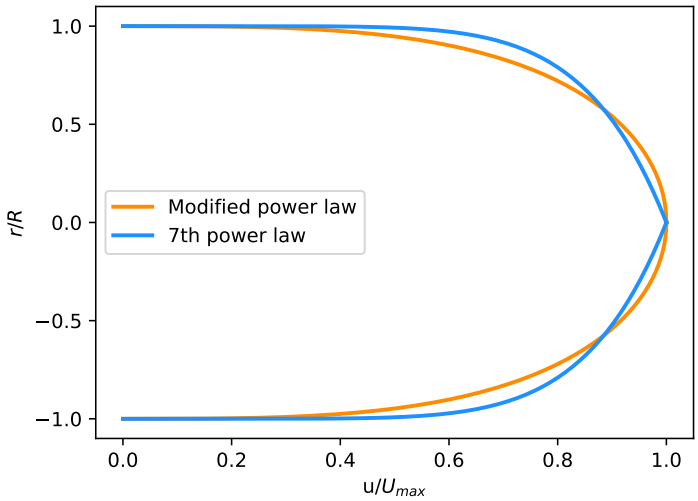

Figure 4.6: Non-dimensional inlet velocity profile using eq. (4.3) *and* eq. (4.5)

A modified version of the seventh power law velocity profile is specified at the inlet [160] :

$$\frac{u_j}{U_{max}} = \left[1 - \left(\frac{r}{R}\right)^2\right]^{1/n} \tag{4.3}$$

with n:

$$n = 0.77 \ln Re_j - 3.47 \tag{4.4}$$

The seventh power law equation is [160]:

$$\frac{u_j}{U_{max}} = \left[1 - \left(\frac{r}{R}\right)\right]^{1/7} \tag{4.5}$$

U_{max} is the maximum velocity at the centreline of a pipe and can be computed from the average velocity (U_{avg}) using [160]:

$$U_{avg} = \left[\frac{2B(2/m, (n+1)/n)}{m}\right] U_{max} \tag{4.6}$$

where B is the beta function (Euler integral of the first kind) [160]. (m=2 and n=*eq.* (4.4)) for *eq.* (4.3) and (m=1 and n=7) for *eq.* (4.5). The average velocity computed as the mean of the experimental range is used to compute the modified velocity profile (*eq.* (4.3)) for all simulations.

The modified version (*eq.* (4.3)) is compared against the seventh power law velocity profile (*eq.* (4.5)) in *fig. 4.6*. With the advantage of the modified version being that it is differentiable at the centre.

The turbulence intensity of fully developed flow in a smooth pipe can be computed as [71]:

$$I = 0.16Re^{-1/8} \tag{4.7}$$

For the Reynolds number range of $Re = 3\ 700 - 12\ 200$, the corresponding turbulence intensity range is $I = 5 - 6\%$. An inlet turbulence intensity of $I = 5\%$ was therefore selected as a constant for all simulations.

4.6 Solver, Solution Process and Temperature Definition

4.6.1 Solver

A steady-state, pressure-velocity coupled solver was used in Ansys Fluent 2024 R1 for all simulations (unless otherwise specified). The pressure was computed using a "PRESTO!" scheme, whilst the momentum, volume fraction, turbulent kinetic energy, turbulent dissipation rate and energy were computed using a first-order upwind scheme (as utilised by [114] and [195] in order to improve numerical convergence).

4.6.2 Solution Process

In order to establish the velocity profile in the domain, the input heat flux is initially set to zero. A hybrid initialization is then used and the simulation is run until all residuals converge to below 1e-3. The results are then saved and the heat flux is increased to 5 W/cm^2. The simulation is then run until the deviation in average wall temperature, measured on the surface on which the heat flux is applied, is below 1e-4. The under-relaxation factors are then sequentially lowered until all residuals are below 1e-4 and the deviation in average wall temperature (again, measured on the surface on which the heat flux is applied) is below 1e-8. This resulted in a maximum ratio of power imbalance to input power $\left(\frac{\dot{Q}_{total}}{\dot{Q}_{applied}}\right)$ of approximately 3.3% (for the simulation shown in *fig. 4.7*). The results are then saved and the heat flux is increased by 5 W/cm^2 in order to mimic the effect of traversing up the boiling curve. The stagnation point superheat as a function of iterations is plotted in *fig. 4.7*. The same figure also shows the heat flux applied to the base of the solid ($\dot{q}_{applied}$) and the heat flux through the wall-fluid interface both as a function of iterations.

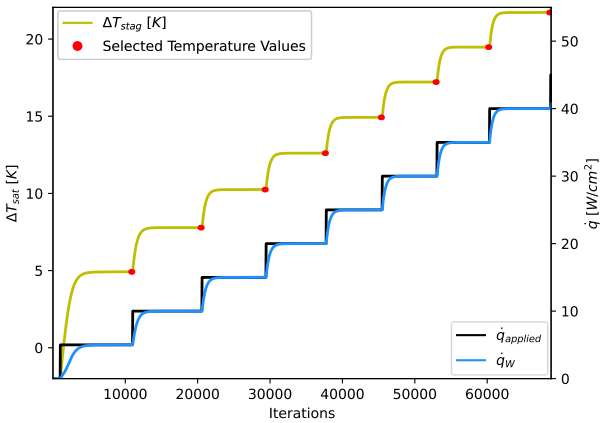

Figure 4.7: Stagnation point wall superheat, applied heat flux and heat flux through the wall into the fluid as a function of iterations [nitrogen ($P_{sat} = 140$ kPa), Numerical Framework=N2A, case="Flat Surface", $a = 1.5$ mm, $v_j = 0.615$ m/s, $\Delta T_{sub} = 2$ K, mesh=M2, steady-state solver]

4.6.3 Temperature Definition

Three methods of measuring the wall temperature are compared in *fig. 4.8*. These methods are investigated to be able to compare the three types of surfaces with each other. The first is a point-like measurement of the temperature at the stagnation point (T_{stag}) and is used to compute the stagnation point wall superheat (ΔT_{stag}):

$$\Delta T_{stag} = T_{stag} - T_{sat} \tag{4.8}$$

where T_{sat} is computed based on the inlet pressure of the jet.

The second is the extrapolated average wall temperature $T_{ex,avg}$. This is computed using a 1D conduction equation:

$$\dot{q}_{applied} = \frac{k_{copper}(T_{bot,avg} - T_{ex,avg})}{L_{solid}} \tag{4.9}$$

where $T_{bot,avg}$ is the average temperature on the lower surface of the solid to which the heat flux is applied and L_{solid} is the vertical distance from the bottom surface to the stagnation point. k_{copper} is the thermal conductivity of the solid (based on *fig. 4.3* at the fluid's saturation temperature). The extrapolated average wall superheat is then computed using:

$$\Delta T_{ex,avg} = T_{ex,avg} - T_{sat} \tag{4.10}$$

The third method of obtaining the wall superheat is using the average wall temperature on the upper surface ($T_{w,avg}$):

$$\Delta T_{w,avg} = T_{w,avg} - T_{sat} \tag{4.11}$$

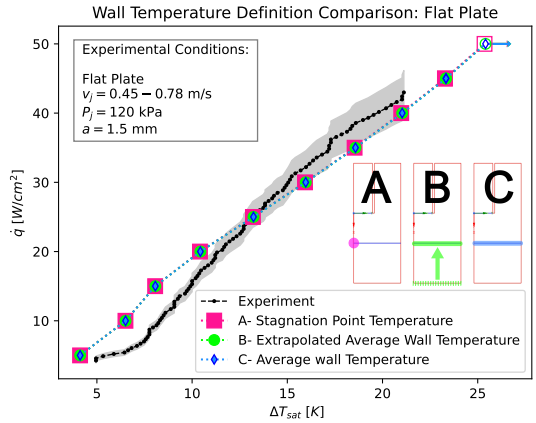

(a) Flat surface [$v_j = 0.615$ m/s]

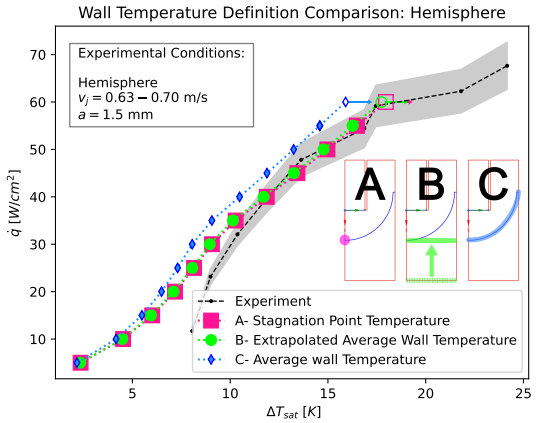

(b) Hemispherical surface [$v_j = 0.665$ m/s]

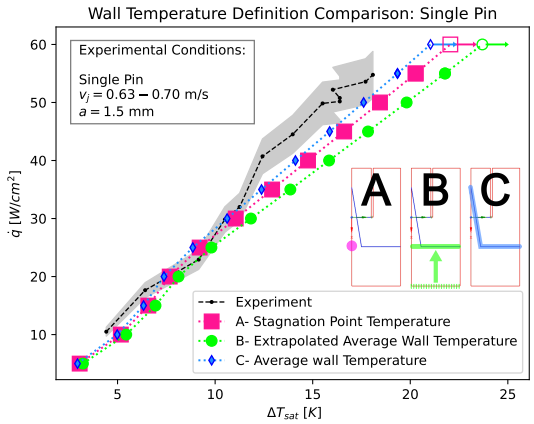

(c) Singular needle surface [$v_j = 0.665$ m/s]

*Figure 4.8: Different methods of defining wall temperature and the impact on wall super heat temperature for the: **a**-flat surface, **b**-hemispherical and **c**-singular needle validation cases [Numerical Framework=N1, $\Delta T_{sub} = 2$ K, mesh=M2, $L_{solid} = 4$ mm, $L_{inlet\ \&\ outlet} = 10$ mm]*

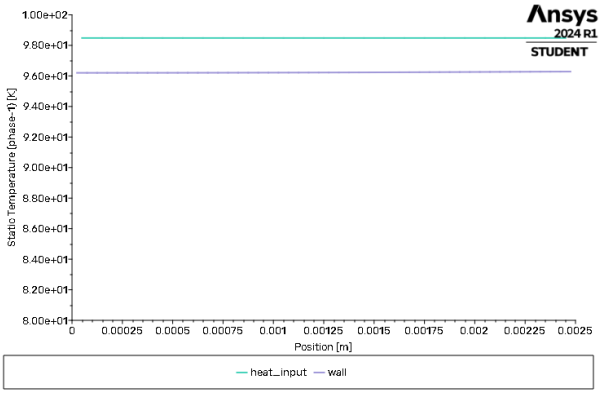

(a) Flat surface [$v_j = 0.615$ m/s]

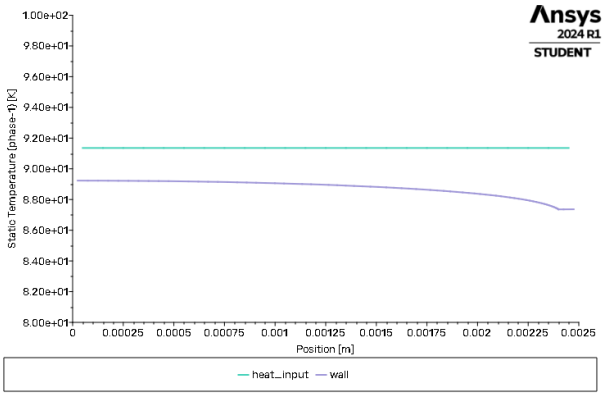

(b) Hemispherical surface [$v_j = 0.665$ m/s]

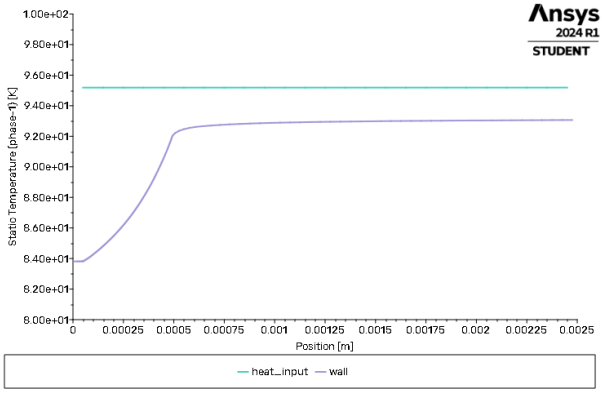

(c) Singular needle surface [$v_j = 0.665$ m/s]

Figure 4.9: Static wall temperature as a function of radial distance along the upper surface (wall) and lower surface (heat$_i$nput) for the ***a****-flat surface,* ***b****-hemispherical and* ***c****-singular needle validation cases presented in* fig. 4.8 *at* $\dot{q}_{applied} = 30$ W/cm^2

As can be seen from *fig. 4.8a* the three definitions of wall superheat provide similar results for the flat surface. This is supported by observations of *fig. 4.9a* where the upper and lower wall temperatures (for a representative $\dot{q}_{applied} = 30$ W/cm^2 case) are approximately constant and are offset by a temperature that corresponds to the temperature difference computed from the 1D conduction equation (*eq.* (4.9)).

Figure 4.8b shows that the average upper wall temperature predicts superheat that is the lowest. As seen in *fig. 4.9b*, the upper wall temperature appears to decay with distance from the stagnation point, resulting in a lower average wall temperature. The temperature along the lower wall appears to be more uniform in nature (see *fig. 4.9b*) and when averaged and extrapolated, results in a value that is marginally lower (by ≈ 0.1 K) than the stagnation point superheat.

Like the hemispherical surface, the singular needle surface has a average wall superheat that is lower than the other methods of measuring wall superheat (see *fig. 4.8c*). This results from the large low surface temperatures seen on the needle surface (refer to *fig. 4.9c* upper wall temperature for 0-0.5 mm). However, unlike the hemispherical case, the wall superheat at the stagnation point of the needle is lower than the extrapolated average wall superheat which can likely be attributed to the large temperature gradients at the stagnation point (see *fig. 4.10c*) as a result of the improved heat transfer from the needle located directly above the stagnation point. This results in a large roll-off in temperature along the solid axis just below the stagnation point (see *fig. 4.10d*) that serves to lower the stagnation point superheat.

Based on the above comparison, wall temperature is obtained using the extrapolated average wall temperature for all simulations shown in this dissertation. This is assumed to be valid for the validation cases presented in *chapter 4* as Zhang et al. 2011 [205] used a 1D conduction equation to extrapolate the temperature from thermocouples located 10 mm below the stagnation point. As seen in *fig. 4.9* the average wall temperature on the lower surface is approximately constant at a depth of 4 mm below the stagnation point. Therefore it is expected that this will remain the case at 10 mm below the stagnation point and thus averaging and extrapolating the lower wall temperature should yield near identical results to the method used by Zhang et al. 2011 [205]. Furthermore, using the average extrapolated wall temperature is viewed as a more representative measure of the performance of the surface were an object (that requires cooling) to be placed at the minimum depth beneath the surface.

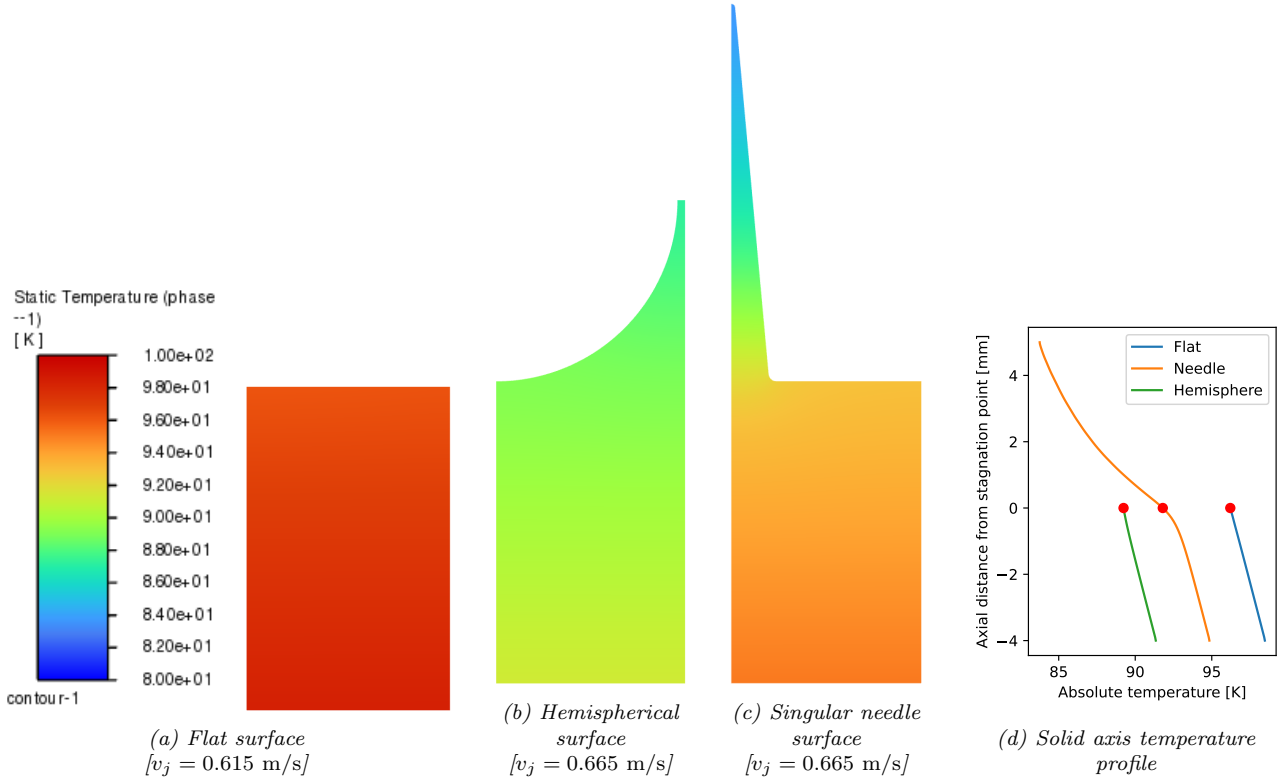

(a) Flat surface $[v_j = 0.615$ m/s$]$

(b) Hemispherical surface $[v_j = 0.665$ m/s$]$

(c) Singular needle surface $[v_j = 0.665$ m/s$]$

(d) Solid axis temperature profile

*Figure 4.10: Contour of absolute temperature within the solid for the flat surface (*a*), hemispherical (*b*) and singular needle (*c*) validation cases presented in* fig. 4.8 *at* $\dot{q}_{applied} = 30$ W/cm^2*. The temperature profile along the solid axis for the three cases is shown in (*d*) (with the stagnation "point" represented by a red dot).*

4.7 Effect of Boundary Location

4.7.1 Inlet and Outlet Length

Initial comparison of steady-state simulations using *N2B* revealed that there was an influence of inlet and outlet length on the wall superheat with longer inlet and outlet lengths resulting in lower boiling heat transfer coefficients (reduced gradient), that caused progressive divergence (shift of the wall superheat values to the right) as the simulation progressed up the boiling curve, as shown in *fig. 4.11a*.

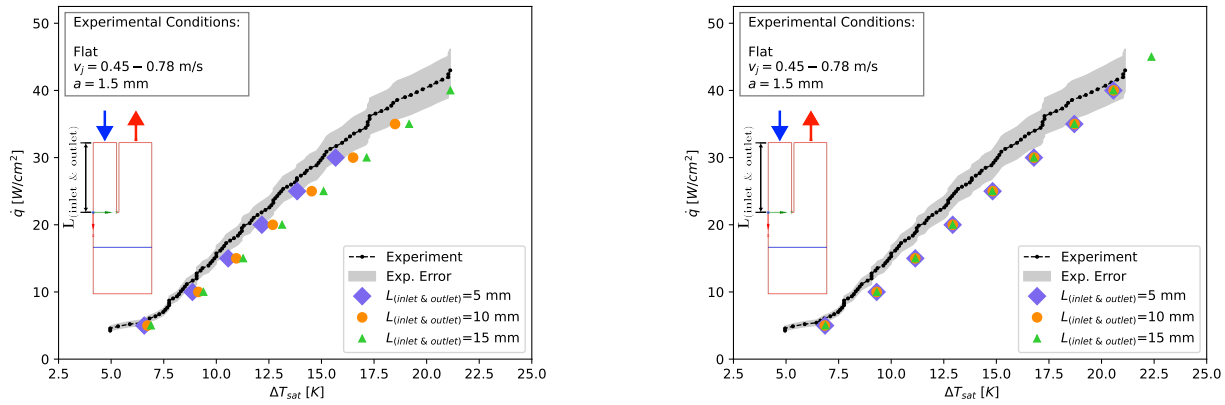

(a) No inlet refinement *(b) 2 mm inlet refinement*

Figure 4.11: Influence of inlet and outlet boundary location on computational results using numerical framework N2B [nitrogen ($P_{sat} = 140$ kPa), case="Flat Surface", $a = 1.5$ mm, $v_j = 0.615$ m/s, $\Delta T_{sub} = 2$ K, mesh=M2, $L_{solid} = 4$ mm] (Diagrams shown: $a = 1.5$ mm with $L_{inlet\ \&\ outlet}$ and L_{solid} truncated to 3 mm and 2 mm respectively for display purposes)

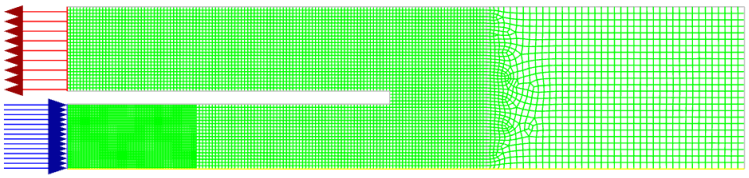

Figure 4.12: 2 mm refined inlet shown for $L_{inlet\ \ outlet} = 5$ mm [mesh=M2, $a = 1.5$ mm, $L_{solid} = 4$ mm, case=Flat Surface]

However, it was found that after refining a 2 mm section at the inlet (see *fig. 4.12*), the wall temperature phenomenon disappeared (see *fig. 4.11b*). As can be seen from *fig. 4.13b*, prior to refinement, there existed multiple jump discontinuities in the Non-local boundary field (NLBF) temperature. The NLBF temperature is used as the liquid temperature value for the convective (*eq.* (3.2)) and quenching (*eq.* (3.13)) heat transfer components of the RPI wall boiling model. Following refinement, the NLBF temperature yielded a smooth profile along the wall, with relatively little deviation occurring as the inlet length was increased (compare $L_{inlet\ \&\ outlet} = 5$ mm (refined) and $L_{inlet\ \&\ outlet} = 10$ mm (refined)). As a result of the NLBF temperature being being greater for the refined case than the non-refined case, there is a reduction in convective heat flux (see *fig. 4.13f*) as the temperature difference between the wall and the "fluid" (NLBF temperature) is reduced. A higher NLBF temperature also results in a reduction in quenching heat flux, again due to a lower temperature differential between the wall and "fluid" (see *fig. 4.13h*). This necessitates an increase in the evaporative heat flux (see *fig. 4.13g*) in order to ensure that $q_{applied} = \dot{q_C} + \dot{q_E} + \dot{q_Q}$. The only mechanism through which this can occur is though an increase in the wall temperature, which results in an increased nucleation site density and departure frequency, thereby increasing the evaporative heat flux, mass transfer at the wall (see *fig. 4.13e*) and vapour fraction along the wall (see *fig. 4.13d*). This explains why refining the $L_{inlet\ \&\ outlet} = 5$ mm yields a large increase in surface temperature when the refined inlet is used. A similar argument can be made for the $L_{inlet\ \&\ outlet} = 10$ mm and $L_{inlet\ \&\ outlet} = 15$ mm cases pre and post inlet refinement. The exact reason for the origination of the jump discontinuity in the NLBF temperature is somewhat mysterious. As can be seen in *fig. 4.13a* and *fig. 4.13c* there are slight deviations in flow variables along the wall, such as the wall y^+ and turbulent kinetic energy along the wall pre and post-refinement. However, it cannot be ascertained whether such deviations are a direct result of the inlet boundary condition or merely a byproduct of the increased vapour

in the domain. Furthermore, how minor changes in flow variables (include temperature in this argument) would yield nonlinear interpolations in the NLBF temperature that results in jump discontinuities is unknown. The only definitive conclusion that can be drawn from these results is that discontinuities in the NLBF temperature may have a large influence on the boiling curve and refining the inlet appears to prevent such discontinuities (at least for the flat surface case).

$L_{inlet\ \&\ outlet} = 10$ mm was selected with the 2 mm inlet refinement strategy for all subsequent simulations.

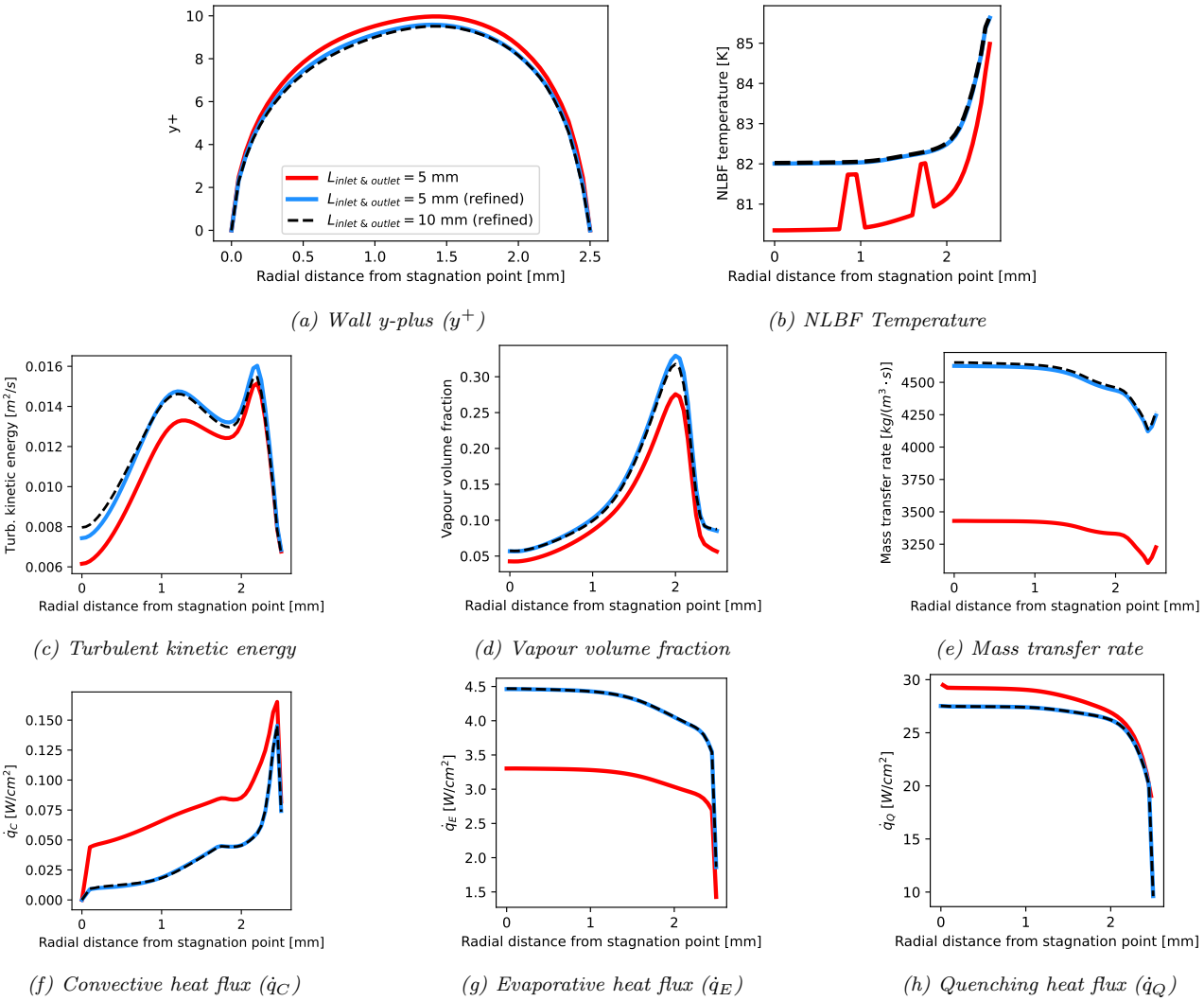

(a) Wall y-plus (y^+) *(b) NLBF Temperature*

(c) Turbulent kinetic energy *(d) Vapour volume fraction* *(e) Mass transfer rate*

(f) Convective heat flux ($\dot{q}_C$) *(g) Evaporative heat flux ($\dot{q}_E$)* *(h) Quenching heat flux ($\dot{q}_Q$)*

*Figure 4.13: Impingement wall quantities (**a**-Wall y-plus, **b**-NLBF Temperature, **c**-Turbulent kinetic energy, **d**-Vapour volume fraction, **e**-Mass transfer rate, **f-h**-convective, evaporative and quenching heat fluxes) for the unrefined inlet at $L_{inlet\ \ outlet} = 5$ mm (fig. 4.11a) and the refined inlets of $L_{inlet\ \ outlet} = 5, 10$ mm (fig. 4.11b) at $\dot{q}_{applied} = 30$ W/cm^2*

4.7.2 Solid Length

As shown in *fig. 4.14*, the thickness of the solid had no visible effect on the wall temperature for the tested range. $L_{solid} = 4$ mm was selected for all subsequent simulations.

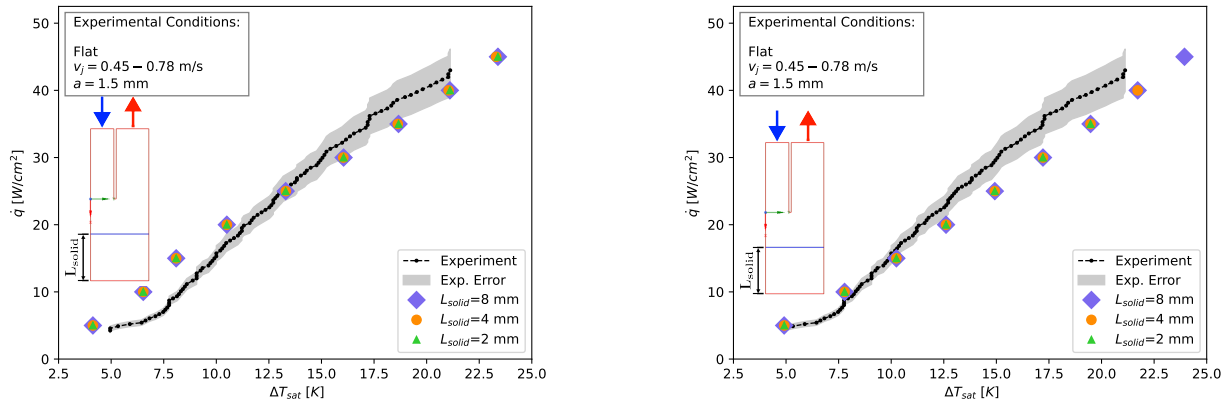

(a) Numerical Framework=N1 *(b) Numerical Framework=N2A*

Figure 4.14: Influence of solid boundary location on computational results [nitrogen ($P_{sat} = 140$ kPa), case="Flat Surface", $a = 1.5$ mm, $v_j = 0.615$ m/s, $\Delta T_{sub} = 2$ K, mesh=M2, $L_{inlet\ \&\ outlet} = 10$ mm] (Diagrams shown: $a = 1.5$ mm with $L_{inlet\ \&\ outlet}$ and L_{solid} truncated on inserted icon to 3 mm and 2 mm respectively for display purposes)

4.8 Influence of Ill-defined Parameters

The parameters of jet subcooling were not explicitly mentioned in the paper by Zhang et al. 2011 [205]. Furthermore, the average jet velocity magnitude was supplied within a given range for each experimental case and the pressure range over the entire experiment was stipulated (as opposed to stipulated ranges for each experimental case). Deviations in these variables may or may not have marked influence on the boiling curves and, as such, sensitivity analyses are presented below in order to assess the impact of these variables.

4.8.1 Sub-cooling

As shown in *fig. 4.16* increasing the subcooling at the inlet results in a horizontal shift of the boiling curve to the left. This is in agreement with observations of [17] and [115] stated in *section 2.4.3*. Using $\dot{q}_{applied} = 30$ W/cm^2 as a representative sample point, this can be attributed to a reduction in the liquid temperature near the wall (refer to *fig. 4.17*) and hence a reduction in the NLBF temperature with increased subcooling (*fig. 4.15a*) which results in an increase in the convective and quenching (see *fig. 4.15b*) heat fluxes, thereby reducing the wall temperature. As expected, this leads to a lower evaporative heat flux (*fig. 4.15c*). This corresponds with a reduction in vapour fraction within the domain (see *fig. 4.18*).

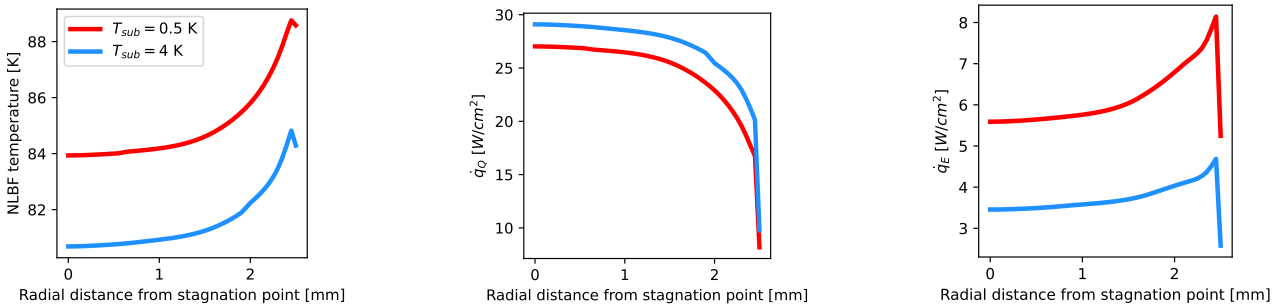

(a) NLBF Temperature *(b) Quenching heat flux ($\dot{q}_Q$)* *(c) Evaporative heat flux ($\dot{q}_E$)*

*Figure 4.15: Impingement wall quantities (**a**-NLBF Temperature, **b-c**-quenching and evaporative heat fluxes) for different subcoolings using N1 at $\dot{q}_{applied} = 30$ W/cm^2*

Note that liquid temperatures in excess of the saturation temperature ($T_{sat} = 80.207$ K for the current simulations) are predicted in *fig. 4.17*. This can likely be attributed to the non-instantaneous mass transfer that

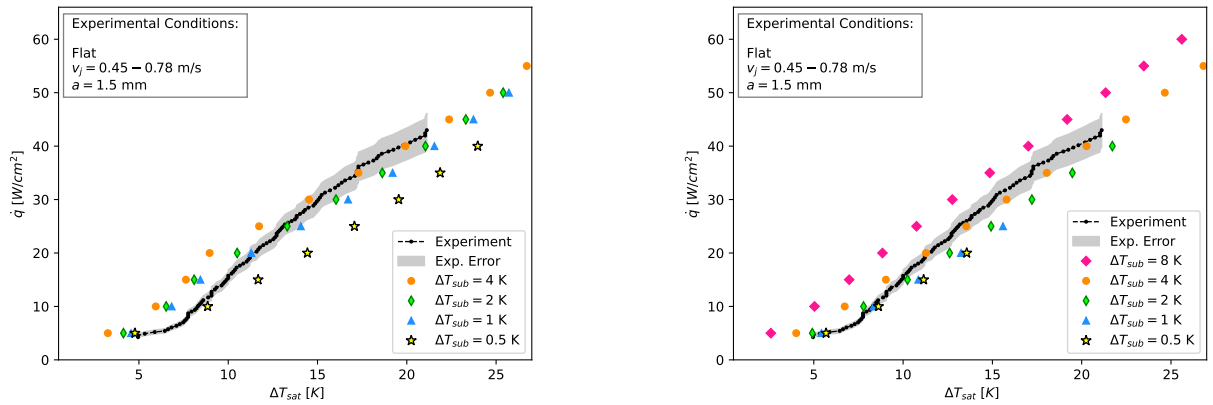

(a) Numerical Framework=N1 *(b) Numerical Framework=N2A*

Figure 4.16: Effect of jet subcooled temperature on boiling curve [nitrogen ($P_{sat} = 140$ kPa), case="Flat Surface", $a = 1.5$ mm, $v_j = 0.615$ m/s, mesh=M2]

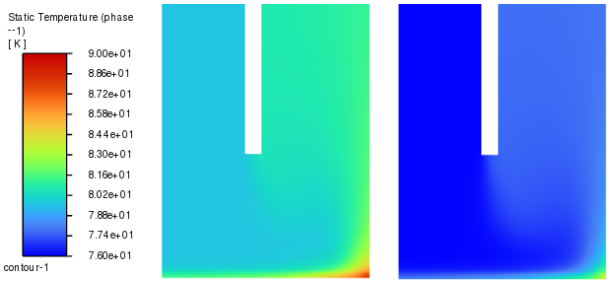

a) $\Delta T_{sub} = 0.5$ K b) $\Delta T_{sub} = 4$ K

Figure 4.17: Contour plot of liquid temperature for different subcoolings using N1 at $\dot{q}_{applied} = 30$ W/cm^2 (truncated domain)

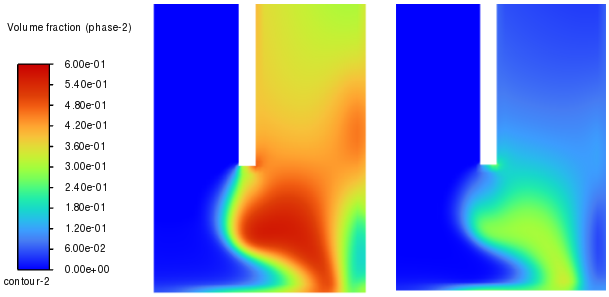

a) $\Delta T_{sub} = 0.5$ K b) $\Delta T_{sub} = 4$ K

Figure 4.18: Contour plot of vapour fraction for different subcoolings using N1 at $\dot{q}_{applied} = 30$ W/cm^2 (truncated domain)

occurs between the fluid and vapour as a result of the two resistance model used to compute the heat transfer between the phases (see *section 4.3.1*).

4.8.2 Velocity

As shown in *fig. 4.19*, there exists a minor dependence of wall superheat on average jet inlet velocity (v_j). The general trend for both $N1$ and $N2A$ is that increased velocities result in increased BHTCs that shifts the boiling curve to the left. This aligns with the observations of [185], [205] and [8] stated in *section 2.4.2*.

As shown in *fig. 4.22*, increased velocities result in lower vapour fractions within the domain. Of particular interest is the reduction in vapour fraction near the heated surface. Several mechanisms may be responsible for this, each contributing to a varying degree. The first is due to the increased momentum of the fluid that is better at sweeping vapour away from the surface, thus leading to lower vapour residence time. The second is that there is more intense mixing (due to the higher velocity) with a larger quantity of cold fluid which results in higher rates of vapour condensation. The third explanation is that the larger volumetric flow rate of fluid more efficiently pierces the vapour near the wall, resulting in a reduction in the liquid temperature near the wall (as evidenced by *fig. 4.20a*). This in turn results in increased convective (*fig. 4.20d*) and quenching heat transfer (*fig. 4.20c*). This leads to a lower evaporative heat flux (*fig. 4.20b*) and hence less vapour is produced thereby resulting in lower quantities of vapour in the domain. Increased vapour quantity also results in a distortion of the velocity profile, increasing the volume of fluid that escapes out the side of the jet (see *fig. 4.21*).

The reduction in NLBF temperature with increased velocity (*fig. 4.20a*) and its impact on the heat flux partitioning (*fig. 4.20 b,c,d*) is thought to be the primary cause for increasing the BHTC and shifting the boiling curve to the left. However, it is also expected that the reduction in vapour fraction near the wall and hence the increase in wall-liquid contact area contributes to the reduction in wall temperature (due to the fact that the RPI wall boiling model only considers heat transfer to the liquid).

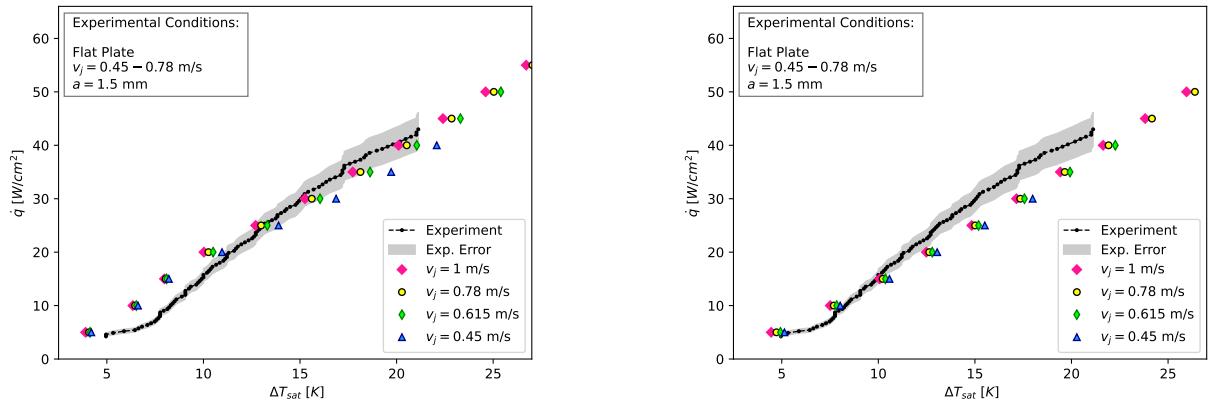

(a) Numerical Framework=N1

(b) Numerical Framework=N2A

Figure 4.19: Effect of average jet inlet velocity on wall superheat when using **a**-$N1$ *and* **b**-$N2A$ *[nitrogen ($P_{sat} = 140$ kPa), case="Flat Surface", $a = 1.5$ mm, $\Delta T_{sub} = 2$ K, mesh=M2]*

In the case of numerical framework $N1$, there is a pronounced shift in the boiling curve to the right as the velocity is reduced from $v_j = 0.615$ m/s to $v_j = 0.45$ m/s with applied heat fluxes above 20 W/cm^2 (see fig. 4.19a). This phenomenon does not appear to manifest itself when using $N2A$ (fig. 4.19b). In order to better understand this, the average bubble departure diameter $[D_w]$(*fig. 4.25a*), average bubble departure frequency $[f]$(*fig. 4.25b*), average nucleation site density $[N_w]$(*fig. 4.25c*) and average vapour generation rate $[\frac{D_w^3}{6} N_w f]$ (*fig. 4.25d*) were plotted for $N1$ and $N2A$ at $v_j = 0.45$ m/s and $v_j = 0.615$ m/s. As can be seen from *fig. 4.25d*, when the applied heat flux surpasses 20 W/cm^2 there is an almost exponential increase in vapour generation rate for $N1$, whilst the vapour generation rate of $N2A$ appears to continue growing linearly. This exponential increase in vapour generation rate is primarily a result of the increasing bubble departure diameter that has a large influence on the volume of vapour being produced (due to it being cubed when computing the evaporative heat flux eq. (3.14)). Bearing this in mind, when comparing *fig. 4.22* with *fig. 4.24* one can observe that the increase in vapour quantity as the velocity is reduced from $v_j = 1$ m/s to $v_j = 0.45$ m/s is far greater for $N1$ than $N2A$, as expected. It is therefore theorised that for $N1$, slight increases in wall temperature (due to a reduction in velocity in this case) can result in minor increases in bubble departure diameter that result in exponential increases in vapour generation rate, causing higher quantities of vapour to be present near the wall. This reduces the liquid-wall contact area and as the RPI wall boiling model only considers heat transfer to the liquid, this effectively reduces the area over which heat transfer can occur, increasing the "effective heat flux" which necessitates larger wall temperatures to achieve adequate heat transfer rates for energy balance equilibrium. The larger wall temperatures also result in larger bubble departure diameters causing a feedback

loop that manifests itself in the large increases in wall superheat seen in *fig. 4.19a*.

It should be additionally noted that both $N1$ and $N2A$ produce a stagnation point in the outermost corner of the domain as the flow is forced to turn 90° due to the radially confining wall (as shown in both *fig. 4.21* and *fig. 4.23*).

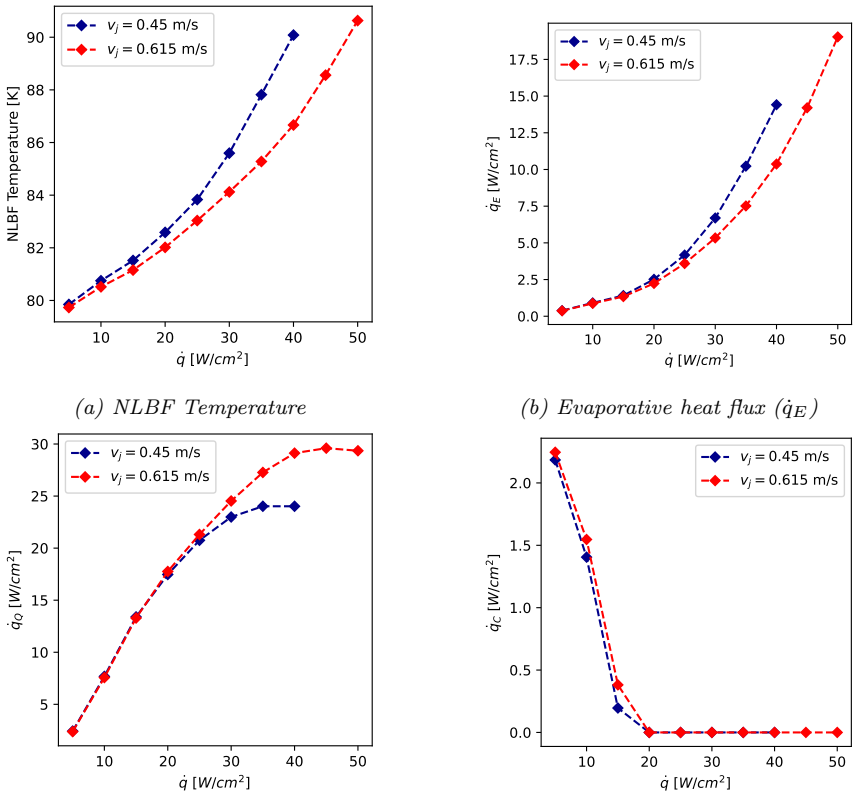

(a) NLBF Temperature

(b) Evaporative heat flux ($\dot{q}_E$)

(c) Quenching heat flux ($\dot{q}_Q$)

(d) Convective heat flux ($\dot{q}_C$)

*Figure 4.20: Average impingement wall quantities (**a**-NLBF Temperature, **b-d**-evaporative, quenching and convective heat fluxes) using N1 over the applied heat flux range presented in* fig. 4.19a *for $v_j = 0.45$ m/s and $v_j = 0.615$ m/s*

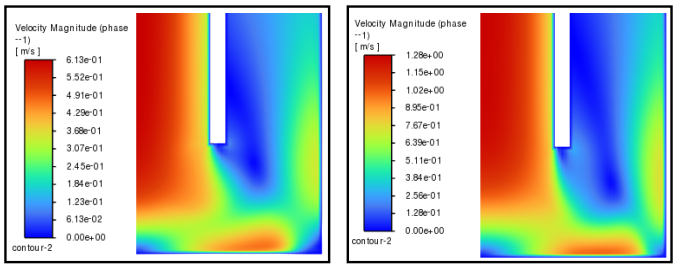

a) $v_j = 0.45$ m/s b) $v_j = 1$ m/s

Figure 4.21: Contour plot of velocity magnitude for different average jet inlet velocities using $N1$ at $\dot{q}_{applied} = 30$ W/cm^2 (truncated domain)

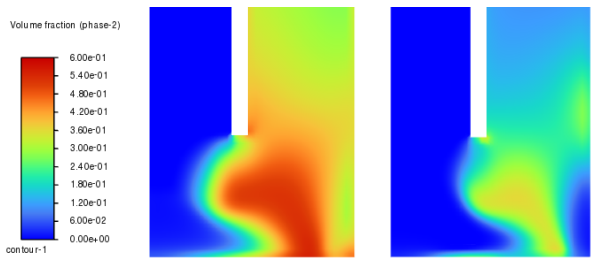

a) $v_j = 0.45$ m/s b) $v_j = 1$ m/s

Figure 4.22: Contour plot of vapour fraction for different average jet inlet velocities using $N1$ at $\dot{q}_{applied} = 30$ W/cm^2 (truncated domain)

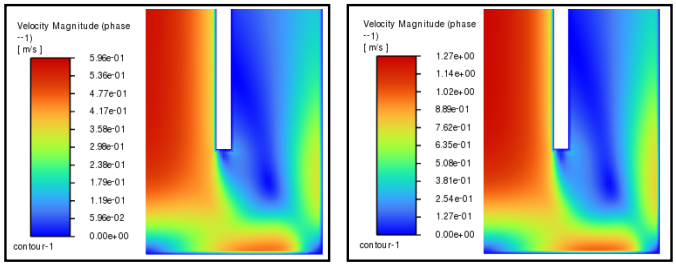

a) $v_j = 0.45$ m/s b) $v_j = 1$ m/s

Figure 4.23: Contour plot of velocity magnitude for different average jet inlet velocities using N2A at $\dot{q}_{applied} = 30$ W/cm^2 (truncated domain)

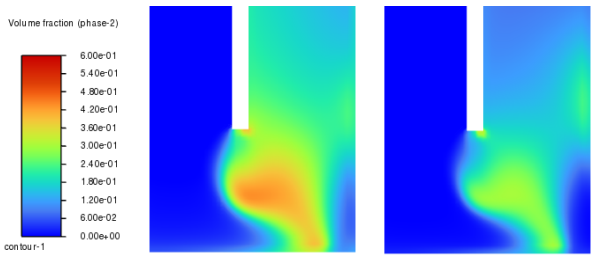

a) $v_j = 0.45$ m/s b) $v_j = 1$ m/s

Figure 4.24: Contour plot of vapour fraction for different average jet inlet velocities using N2A at $\dot{q}_{applied} = 30$ W/cm^2 (truncated domain)

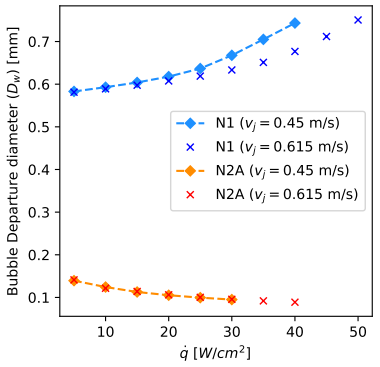

(a) Bubble departure diameter (D_w)

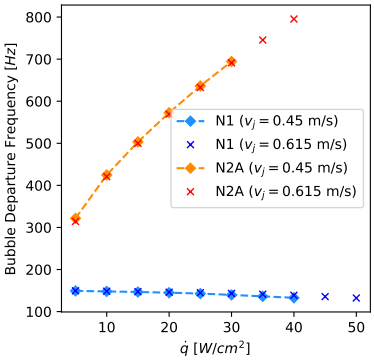

(b) Bubble departure frequency (f)

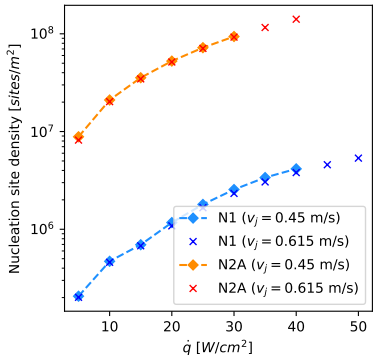

(c) Nucleation site density (N_w)

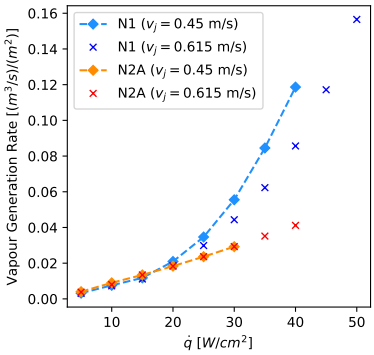

(d) Vapour generation rate

*Figure 4.25: Average impingement wall quantities (**a**-Bubble departure diameter, **b**-Bubble departure frequency, **c**-Nucleation site density, **d**-Vapour generation rate) over the applied heat flux range presented in* fig. 4.19 *for both N1 and N2A*

4.8.3 Pressure

Figure 4.26 shows that all numerical frameworks exhibit a shift of the boiling curve to the right with decreasing pressure. This is in agreement with the observations presented in literature (refer to *section 2.3.1*). It is evident that $N2A$ and $N2B$ are more significantly affected by the change in pressure. It was initially thought that this could attributed to the variable liquid (see *fig. 4.27*, *fig. 4.28* and *fig. 4.29*) and solid properties (see *fig. 4.30*) used in $N2A$ and $N2B$ (compared to the fixed properties used in $N1$). However, there is little evidence for this as the properties of the fluid at the wall are the same for $N1$ (specified at the saturation pressure) and $N2A$ (see *fig. 4.31*).

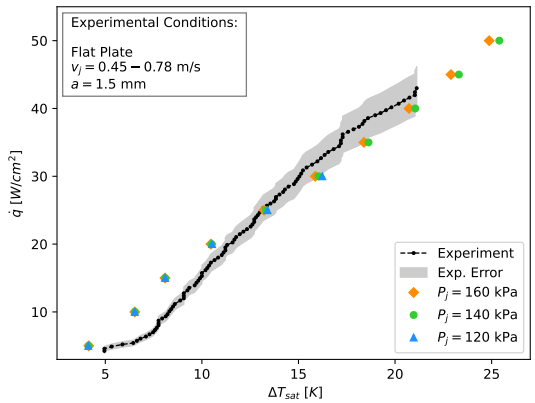

(a) Numerical Framework=N1

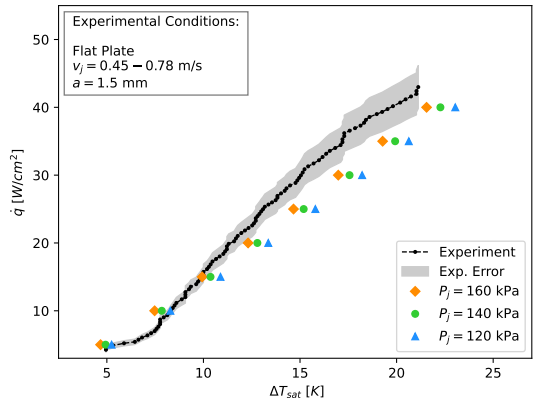

(b) Numerical Framework=N2A

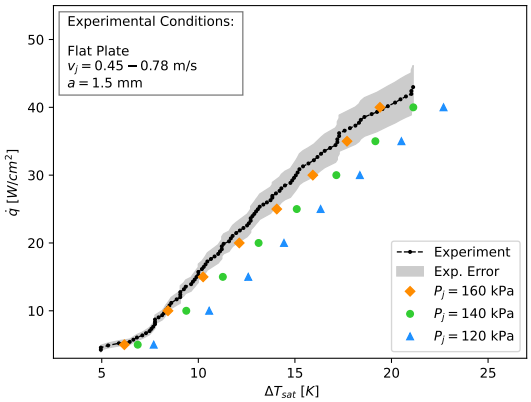

(c) Numerical Framework=N2B

Figure 4.26: Effect of inlet pressure [nitrogen, case="Flat Surface", $a = 1.5$ mm, $v_j = 0.615$ m/s, $\Delta T_{sub} = 2$ K, mesh=M2]

When observing *fig. 4.32* one can see that the vapour fraction in the domain is almost identical when using $N1$ and comparing $P_j = 120$ kPa and $P_j = 160$ kPa at $\dot{q}_{applied} = 30$ W/cm^2. However, there is a notable increase in vapour fraction for $P_j = 160$ kPa when using $N2A$ (see *fig. 4.33*). This is confirmed by *fig. 4.34b* that compares the vapour fraction along the wall of $P_j = 120$ kPa and $P_j = 160$ kPa at $\dot{q}_{applied} = 30$ W/cm^2 (when using $N2A$). *Figure 4.34a* shows that $P_j = 120$ kPa has a reduced subcooling temperature compared to $P_j = 160$ kPa. This is most likely attributed to the higher thermal conductivity of the fluid (see *fig. 4.29*) that allows heat to propagate through the fluid faster and thus results in an increase of fluid temperature near the wall. One would expect that, with a reduced subcooling, $P_j = 120$ kPa would have reduced quenching and convective heat flux components. However, counter intuitively, the opposite is observed in *fig. 4.34c* and *fig. 4.34e*. Furthermore, the evaporative heat flux is significantly higher for $P_j = 160$ kPa (*fig. 4.34d*). The conclusion that can be drawn from this is that the RPI closing models (bubble departure diameter, nucleation site density and departure frequency) that govern the evaporative heat transfer are significantly affected by the change in pressure when using $N2A$ and $N2B$ and less so when using $N1$. This is confirmed when comparing the average bubble departure diameter, nucleation site density and departure frequency in *fig. 4.35*.

Consider the evaporative heat transfer equation for $N2A$ as the pressure is increased from $P_j = 160$ kPa. The fluctuation of the individual components in *eq.* (3.14) are represented graphically below:

$$\dot{q}_E = \frac{\pi D_w^3}{6} N_w \rho_v h_{lv} f$$

As expected from literature, the nucleation site density increases with increasing pressure and it is believed that this increase plays the most significant role in the increase in the evaporative heat transfer. The reason for this is that enthalpy and density changes appear ho have little effect when using $N1$ and thus one would not expect a large impact when using $N2A$. The frequency is a slightly more nuanced variable, but has very little deviation for $N2A$ (see *fig. 4.35c* at higher heat fluxes). Thus that leaves the increase in nucleation site density as the only plausible explanation for driving the increase in evaporative heat transfer.

Thus nucleation site density correlations that are dependent on fluid properties (such as $N_w = Kirichenko$, *eq.* (3.23) ($P/P_{cr} \geq 0.04$) and $N_w = Kocamustafaogullari$ *eq.* (3.22)) can result in large sensitivity of the evaporative heat flux to pressure variations. The increase of latent heat transfer with increasing pressure (via the increase of the evaporative heat flux) then results in a decrease in the wall temperature seen in *fig. 4.26*.

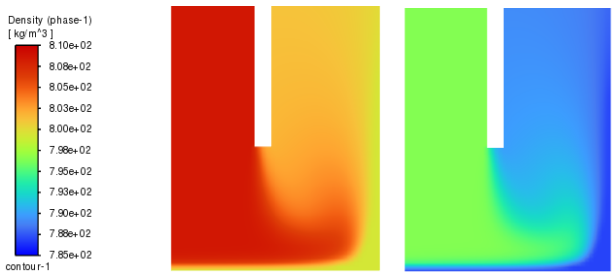

a) $P_j = 120$ kPa b) $P_j = 160$ kPa

Figure 4.27: Contour plot of liquid density (ρ_l) for different operating pressures using $N2A$ at $\dot{q}_{applied} = 30$ W/cm^2 (truncated domain)

a) $P_j = 120$ kPa b) $P_j = 160$ kPa

Figure 4.28: Contour plot of liquid specific heat ($c_{p,l}$) for different operating pressures using $N2A$ at $\dot{q}_{applied} = 30$ W/cm^2 (truncated domain)

a) $P_j = 120$ kPa b) $P_j = 160$ kPa

Figure 4.29: Contour plot of liquid thermal conductivity for different operating pressures using $N2A$ at $\dot{q}_{applied} = 30$ W/cm^2 (truncated domain)

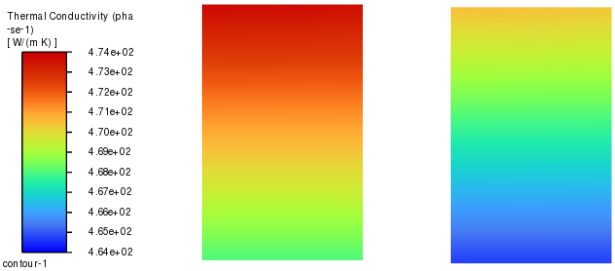

a) $P_j = 120$ kPa b) $P_j = 160$ kPa

Figure 4.30: Contour plot of solid thermal conductivity for different operating pressures using $N2A$ at $\dot{q}_{applied} = 30$ W/cm^2

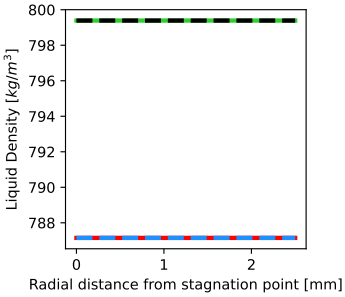

(a) Liquid Density (ρ_l)

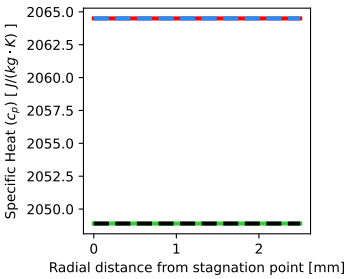

(b) Specific Heat ($C_{p,l}$)

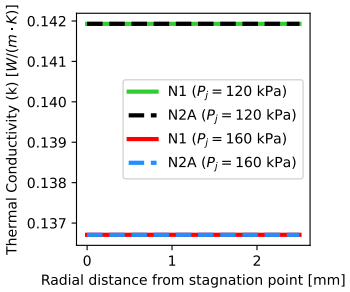

(c) Thermal Conductivity (k_l)

*Figure 4.31: Impingement wall quantities (**a**-Liquid Density, **b**-Specific Heat and **c**-Thermal Conductivity) for different operating pressures using both $N1$ and $N2A$ at $\dot{q}_{applied} = 30$ W/cm^2*

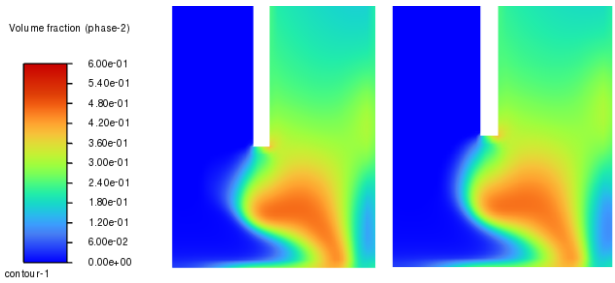

a) $P_j = 120$ kPa b) $P_j = 160$ kPa

Figure 4.32: Contour plot of vapour volume fraction for different operating pressures using $N1$ at $\dot{q}_{applied} = 30$ W/cm^2 (truncated domain)

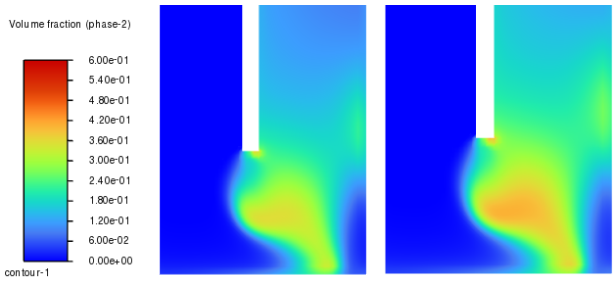

a) $P_j = 120$ kPa b) $P_j = 160$ kPa

Figure 4.33: Contour plot of vapour volume fraction for different operating pressures using $N2A$ at $\dot{q}_{applied} = 30$ W/cm^2

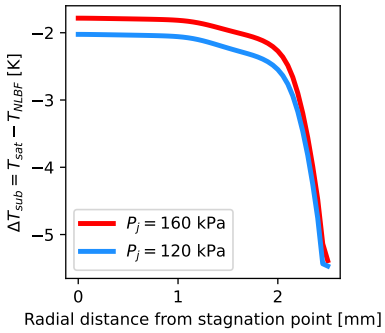

(a) Local liquid subcooling

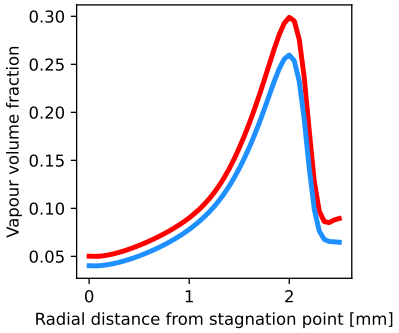

(b) Vapour volume fraction

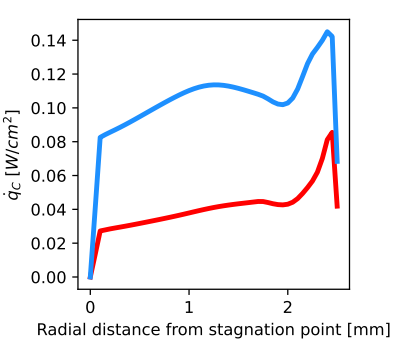

(c) Convective heat flux ($\dot{q}_C$)

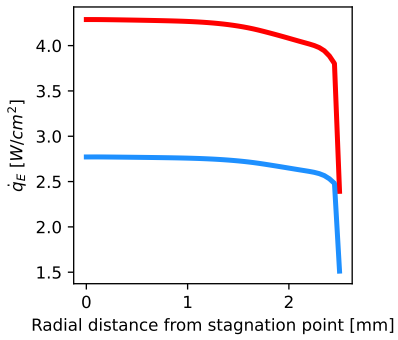

(d) Evaporative heat flux ($\dot{q}_E$)

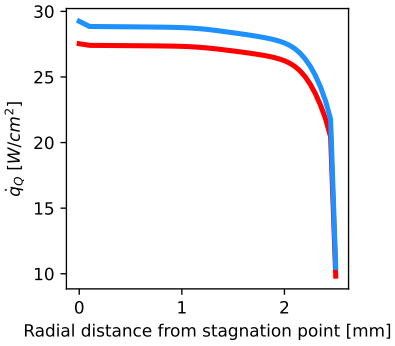

(e) Quenching heat flux ($\dot{q}_Q$)

*Figure 4.34: Impingement wall quantities (**a**-Local liquid subcooling, **b**-Vapour volume fraction, **c-e**-convective, evaporative and quenching heat fluxes) for different operating pressures using $N2A$ at $\dot{q}_{applied} = 30$ W/cm^2*

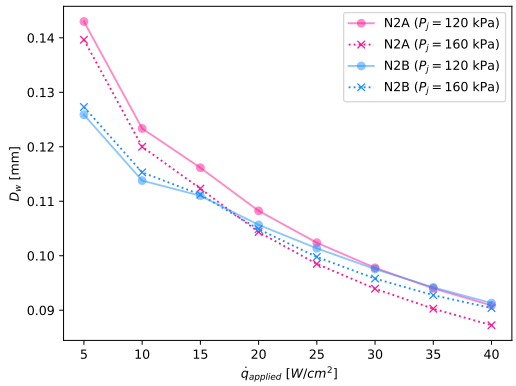

(a) Average bubble departure diameter (N2A and N2B)

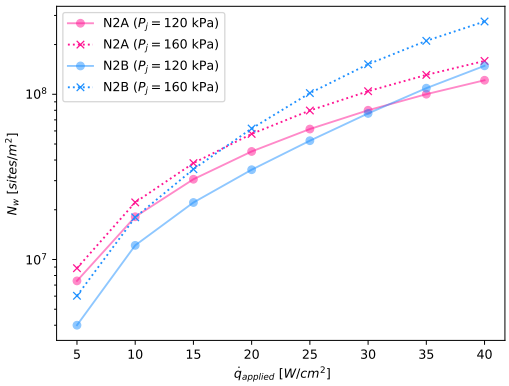

(b) Average nucleation site density (N2A and N2B)

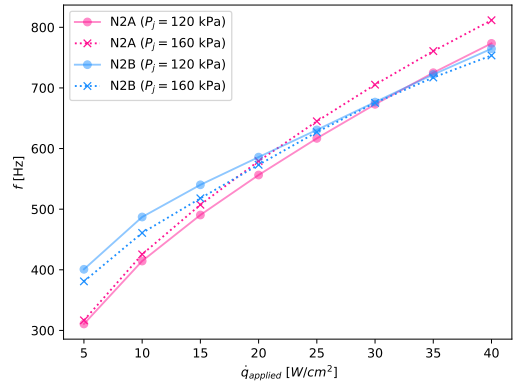

(c) Average bubble departure frequency (N2A and N2B)

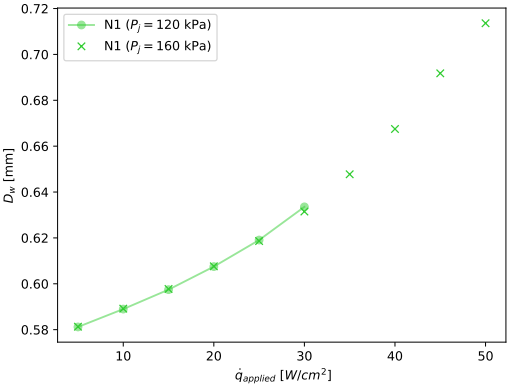

(d) Average bubble departure diameter (N1)

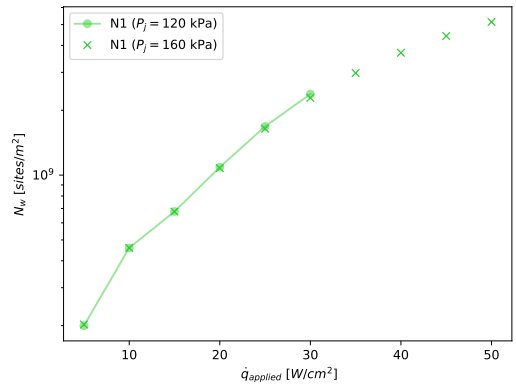

(e) Average nucleation site density (N1)

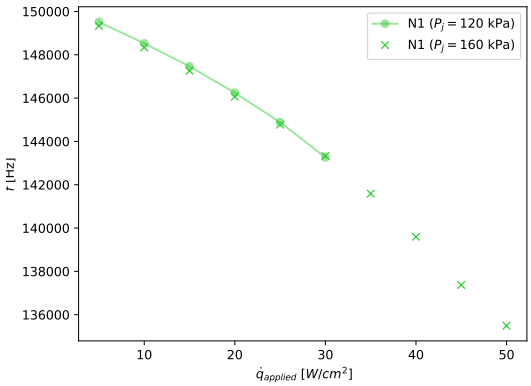

(f) Average bubble departure frequency (N1)

*Figure 4.35: Average impingement wall quantities (**a**-Bubble departure diameter (N2A and N2B), **b**-Nucleation site density (N2A and N2B), **c**-Bubble departure frequency (N2A and N2B), **d**-Bubble departure diameter (N1), **e**-Nucleation site density (N1) and **f**-Bubble departure frequency (N1)) for different operating pressures using N1, N2A and N2B*

4.9 Evaluation of steady-state Assumption

All results presented up until this point have made use of a steady-state solver. This section explores the validity of this assumption in relation to the current boiling application. To do so, the steady-state solutions obtained using using numerical framework $N1$ at $\dot{q}_{applied} = 5, 20$ and 40 W/cm^2 were run using a transient solver for 5 seconds. Two separate timesteps ($\Delta t = 0.001$ and 0.0001 s) were used to assess the time step dependence of the simulation.

An important metric when when selecting a transient timestep is the Courant number (CFL), defined as:

$$CFL = \frac{\Delta t V_{max}}{h} \tag{4.12}$$

where Δt is the time step, V_{max} is the maximum velocity in the domain (for simplicity, this was computed from the maximum inlet velocity) and h is the minimum cell size in the fluid domain.

It is preferable that the $CFL \leq 1$ (indicating that a fluid particle traverses a distance less than or equal to a single cell width within a singular timestep), however, CFL values as high as 5 were used by Ludick et al. 2023 [114]. The timesteps of $\Delta t = 0.001$ and 0.0001 s equate to a CFL of 16.16 and 1.62 respectively for the simulation presented in *fig. 4.36*. It is evident from the figure that the effect of timestep on wall superheat is negligible at lower heat fluxes (with both transient simulations producing near identical results at $\dot{q}_{applied} = 5$ and 20 W/cm^2). However, there does appear to be a minor influence of timestep at high heat fluxes, with the smallest timestep having slightly higher (≈ 0.5 K) superheats at $\dot{q}_{applied} = 40$ W/cm^2.

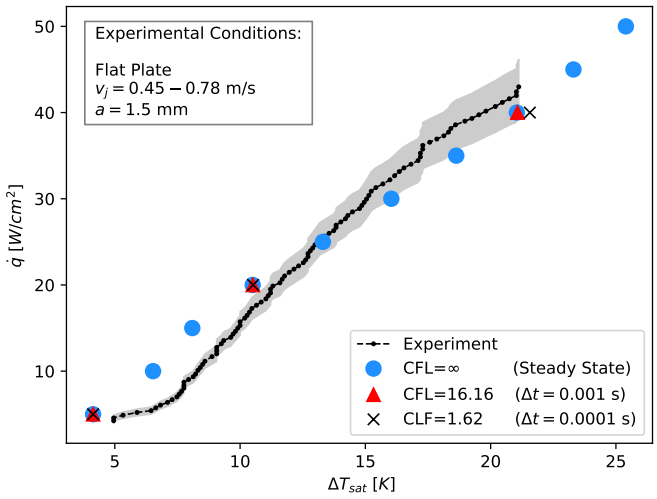

Figure 4.36: Transient boiling curve results (reported superheats averaged between 2-4 s) [nitrogen ($P_{sat} = 140$ kPa), case="Flat Surface", $a = 1.5$ mm, $v_j = 0.615$ m/s, $\Delta T_{sub} = 2$ K, mesh=M2, numerical framework=N1]

When comparing the average inlet pressure in *fig. 4.38a*, one observes that there is minimal difference between the steady-state solver and both transient simulations at $\dot{q}_{applied} = 5$ W/cm^2. Furthermore, there don't appear to be any significant fluctuations for the transient simulation. This is likely due to the low vapour fraction within the domain at this heat flux (see *fig. 4.39a*) and hence the close approximation of the steady-state and transient solutions. However, at higher heat fluxes we see that the steady-state solver consistently overpredicts the average inlet pressure required to drive flow through the domain, with large deviations ($\approx$ 30Pa) noted in *fig. 4.38c*. For this reason, it is recommended that the inaccuracy of pressure drop prediction obtained using the steady-state solver should be stated whenever analysing such data, particularly at high heat fluxes. Both transient simulations exhibit minor fluctuations at $\dot{q}_{applied} = 20$ W/cm^2 (*fig. 4.38b*). The fluctuations for $\Delta t = 0.001$ s are large (amplitude$\approx$ 5 Pa) at $\dot{q}_{applied} = 40$ W/cm^2 (*fig. 4.38c*). The fluctuations for $\Delta t = 0.0001$ s are significantly reduced at the same heat flux. Perhaps the rise and fall of the average inlet pressure (in the case of the transient simulations) as the applied heat flux is increased can be attributed to the vapour initially breaking up and disrupting the flow, but at a certain point (≥ 20 W/cm^2 in this case) there is enough vapour generated such that the buoyancy forces of the vapour assist in dragging the liquid towards the outlet, thus reducing the inlet pressure required to drive the flow through the system. This hypothesis is left for exploration in future work.

Figure 4.39 displays the maximum vapour volume fraction along the wall for the transient and steady-state simulations at the three specified heat fluxes. At 5 W/cm^2 there is a minimal difference between the transient solutions. The difference grows with increasing heat flux, with the larger timestep having a maximum vapour fraction along the wall of 0.135 less than the smaller timestep simulation at 40 W/cm^2. This is weakly supported by comparing *fig. 4.41b* and *fig. 4.41c* whereby the smallest timestep appears to have significantly more vapour in the domain. The term 'weakly supported' has been used in this context as *fig. 4.41b* and *fig. 4.41c* represent instantaneous values computed at $t = 5$ s and may be subject to transient variations in volume fraction distribution. The steady-state solution has a maximum deviation of ≈ 0.03 from the smallest timestep simulation, initially over predicting the maximum volume fraction (at 5 W/cm^2 and 20 W/cm^2) and then under predicting the the maximum volume fraction at 40 W/cm^2. *Figure 4.41* reveals that the vapour fraction magnitude and distribution are similar between the steady-state and $\Delta t = 0.0001$ s solutions.

Figure 4.40 reveals that the general velocity magnitude and profile are similar for all three simulations. The only notable deviation is at the outer edge of the jet, post exit, whereby there appears to be a local increase in velocity. This increase corresponds with an increase in vapour fraction (*fig. 4.41*) and thus it is assumed that the increased vapour plays a minor role in distorting the liquid velocity profile in this region.

Figure 4.42 reveals that the NLBF temperature (*Figure 4.42a*) when using the smallest timestep is higher than the steady-state solution, resulting in reduced quenching (*Figure 4.42f*) near the outer edge of the domain and increased evaporative heat transfer (*Figure 4.42e*). This results in the increased vapour fraction seen in *fig. 4.41*. The convective heat transfer (*Figure 4.42d*) is zero due to the non-dimensional area of influence having reached a value of 1 at this heat flux, thus negating the convective heat transfer as explained in *section 3.2.1*.

The final takeaway from this section is that the steady-state solution is reasonably accurate at low heat fluxes when compared to the $\Delta t = 0.0001$ s solution across a range of variables including: extrapolated wall superheat, inlet pressure, and vapour fraction. However, the results tend to deviate as the heat flux is increased. Near the end of the experimental boiling curve (at 40 W/cm^2) the steady-state solution underpredicts the wall superheat by approximately 0.5 K (or 2.4%). This results in a slight underprediction of the vapour fraction which has a minor (almost negligible) impact on the velocity profile. Based on the fact that there is a low deviation in the wall superheat (unarguably the most important variable of interest) and there is a significant reduction in computational time when using the steady-state simulation it has been decided that steady-state simulation will be used throughout the remainder of this dissertation.

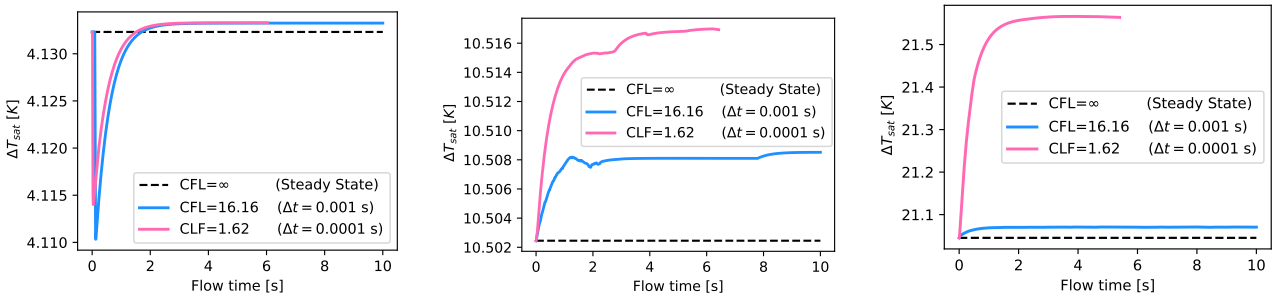

(a) $\dot{q}_{applied} = 5$ W/cm^2 *(b)* $\dot{q}_{applied} = 20$ W/cm^2 *(c)* $\dot{q}_{applied} = 40$ W/cm^2

Figure 4.37: Average extrapolated wall superheat as a function of flow time at **a**-$\dot{q}_{applied} = 5$ W/cm^2, **b**-$\dot{q}_{applied} = 20$ W/cm^2 *and* **c**-$\dot{q}_{applied} = 40$ W/cm^2 *[nitrogen, case="Flat Surface", $a = 1.5$ mm, $v_j = 0.615$ m/s, $\Delta T_{sub} = 2$ K, mesh=M2, numerical Framework=N1]*

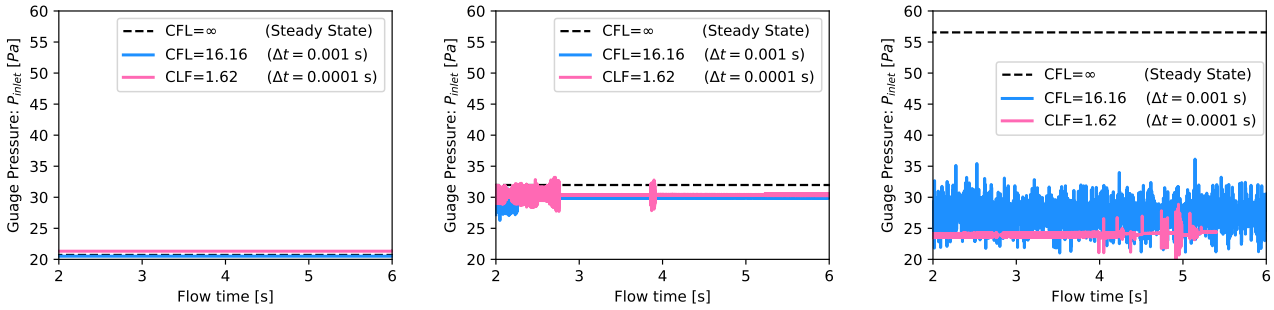

(a) $\dot{q}_{applied} = 5$ W/cm^2 (b) $\dot{q}_{applied} = 20$ W/cm^2 (c) $\dot{q}_{applied} = 40$ W/cm^2

Figure 4.38: Average inlet pressure (gauge pressure) as a function of flow time at **a**-$\dot{q}_{applied} = 5$ W/cm^2, **b**-$\dot{q}_{applied} = 20$ W/cm^2 *and* **c**-$\dot{q}_{applied} = 40$ W/cm^2 *[nitrogen, case="Flat Surface", $a = 1.5$ mm, $v_j = 0.615$ m/s, $\Delta T_{sub} = 2$ K, mesh=M2, numerical Framework=N1]*

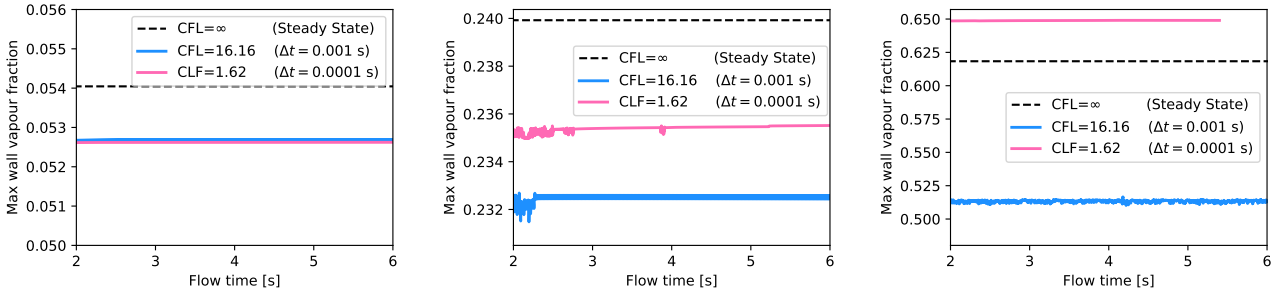

(a) $\dot{q}_{applied} = 5$ W/cm^2 (b) $\dot{q}_{applied} = 20$ W/cm^2 (c) $\dot{q}_{applied} = 40$ W/cm^2

Figure 4.39: Maximum vapour volume fraction along the impingement wall as a function of flow time at **a**-$\dot{q}_{applied} = 5$ W/cm^2, **b**-$\dot{q}_{applied} = 20$ W/cm^2 *and* **c**-$\dot{q}_{applied} = 40$ W/cm^2 *[nitrogen, case="Flat Surface", $a = 1.5$ mm, $v_j = 0.615$ m/s, $\Delta T_{sub} = 2$ K, mesh=M2, numerical Framework=N1]*

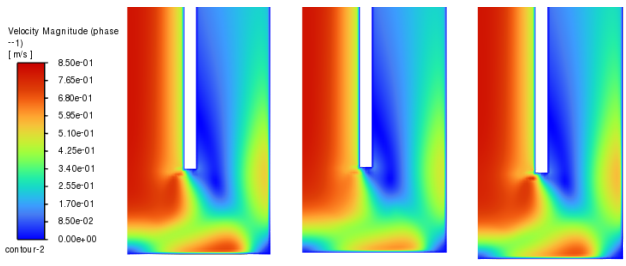

a) Steady State b) $\Delta t = 0.001$ s c) $\Delta t = 0.0001$ s

Figure 4.40: Contour plot of velocity magnitude at $\dot{q}_{applied} = 40$ W/cm^2 for the simulations presented in fig. 4.36 *(transient data plotted at $t = 5$ s)*

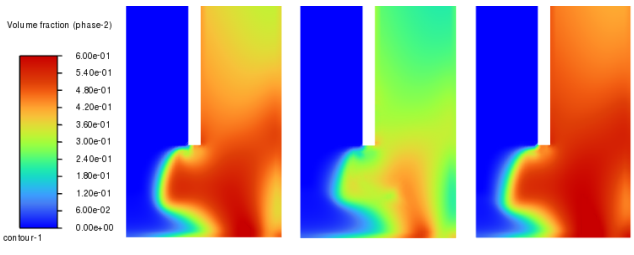

a) Steady State b) $\Delta t = 0.001$ s c) $\Delta t = 0.0001$ s

Figure 4.41: Contour plot of vapour fraction at $\dot{q}_{applied} = 40$ W/cm^2 for the simulations presented in fig. 4.36 *(transient data plotted at $t = 5$ s)*

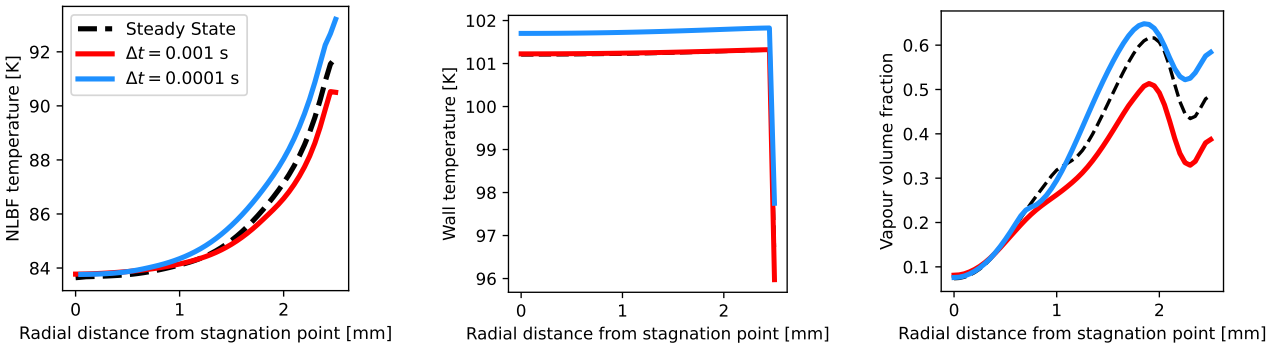

(a) NLBF Temperature *(b) Wall temperature* *(c) Vapour volume fraction*

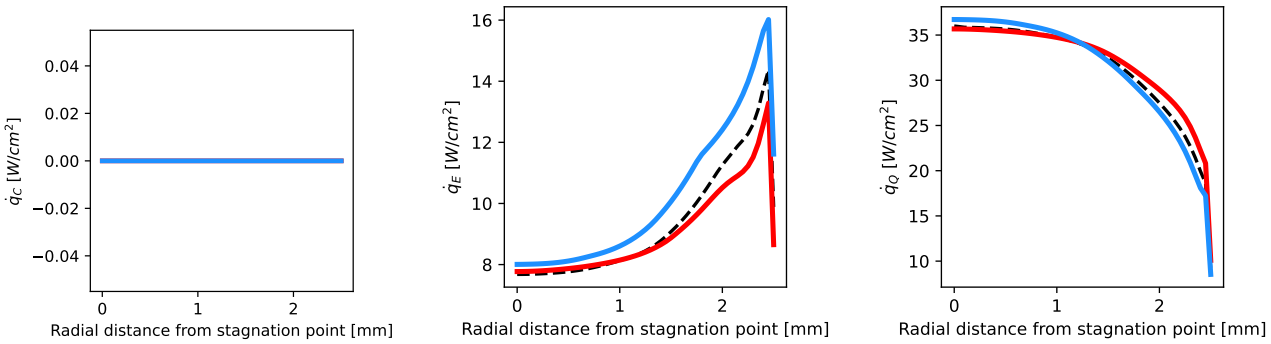

(d) Convective heat flux ($\dot{q}_C$) *(e) Evaporative heat flux ($\dot{q}_E$)* *(f) Quenching heat flux ($\dot{q}_Q$)*

*Figure 4.42: Impingement wall quantities (**a**-NLBF Temperature, **b**-Wall temperature, **c**-Vapour volume fraction, **d-f**-convective, evaporative and quenching heat fluxes) at $\dot{q}_{applied} = 40$ W/cm^2 for the simulations presented in* fig. 4.36 *(transient data plotted at $t = 5$ s)*

4.10 Bubble Waiting Time Coefficient

The bubble waiting time coefficient (C_{wt}) is thoroughly discussed in *section 3.3.5*. It is an independent modeling constant that appears as a multiplier in the quenching heat flux correlation. It is used in order to independently alter the quenching heat flux contribution to the overall heat flux in the RPI wall boiling model equation (*eq.* (3.1)). Ideally, a curve fit should have been obtained from *fig. 3.15* in order to model C_{wt} as a function of cumulative non-dimensional area of influence (β). However, the version of ANSYS Fluent used in this dissertation (2024 R1) only permitted a constant value to be selected and as such implementation of a variable bubble waiting time coefficient is left for future work.

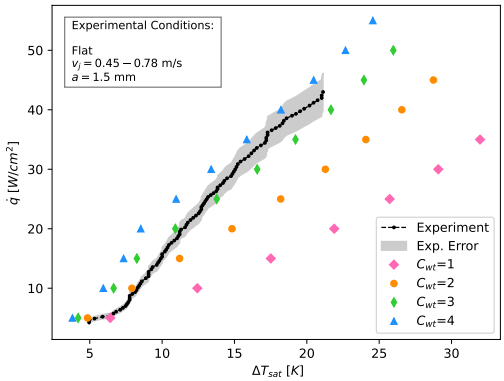

(a) N1

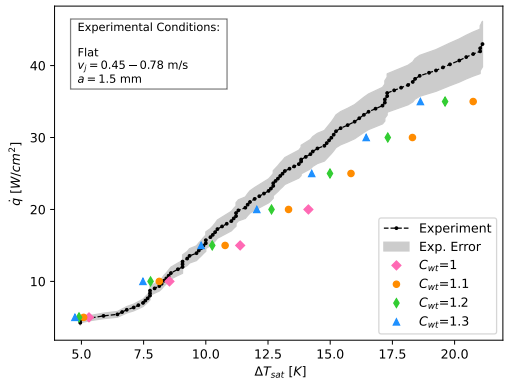

(b) N2A

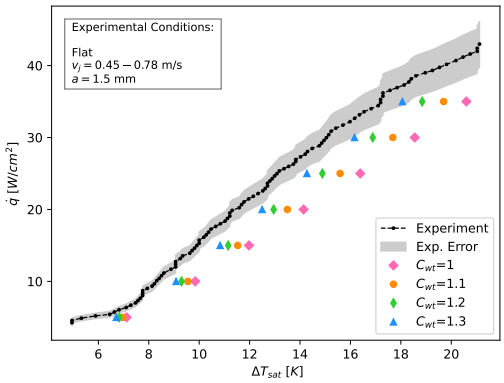

(c) N2B

Figure 4.43: Effect of bubble waiting time coefficient [nitrogen ($P_{sat} = 140$ kPa), case="Flat Surface", $a = 1.5$ mm, $v_j = 0.615$ m/s, $\Delta T_{sub} = 2$ K, mesh=M2]

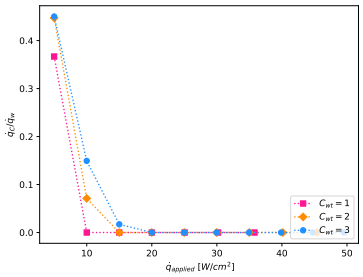

(a) $\bar{q}_C/\bar{q}_W$

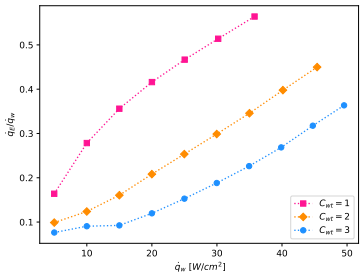

(b) $\bar{q}_E/\bar{q}_W$

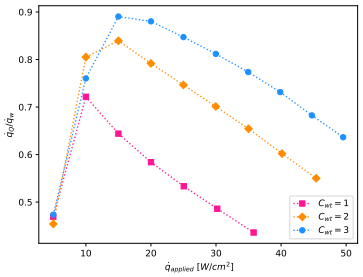

(c) $\bar{q}_Q/\bar{q}_W$

Figure 4.44: Effect of bubble waiting time coefficients on heat flux partitioning [nitrogen, case="Flat Surface", $a = 1.5$ mm, $v_j = 0.615$ m/s, $\Delta T_{sub} = 2$ K, mesh=M2, numerical Framework=N1]

Figure 4.43 illustrates that increasing the bubble waiting time coefficient results in an increase in the boiling heat transfer coefficient. A value of $C_{wt} = 3.142$ was selected as the default value for numerical framework $N1$ as this coincides closely with the experimental boiling curve. However, it is difficult for one to theoretically

justify such large C_{wt} values. If one utilises the theoretical correlation from [89] (*eq.* (3.55)), which overpredicts the true value of C_{wt} (for reasons stated in *section 3.3.5*), a value of $C_{wt} = 3.142$ would imply an average cumulative non-dimensional area of influence in excess of 12 (refer to *fig. 3.15*). This indicates that the average surface area occupied by the bubbles is more than 12 times larger than the wall area. Values as high as this would imply full blanketing of the domain, thus making it unlikely that the fluid could reach the surface to quench the overlapping areas.

On the other hand, a value of $C_{wt} = 1.3$ was selected as the default value for numerical framework $N2A$ and $N2B$. This is slightly higher than the applicable range of $C_{wt} = 1 - 1.2$ computed in *section 3.3.5* when accounting for the reduction in quenching area due to bubble growth. However the value is not unjustifiably high and could be explained by a slightly higher area of influence factor (K) or slightly slower bubble growth rate.

Figure 4.44 illustrates that the quenching heat flux is increased as C_{wt} is increased. This implies that a lower evaporative heat flux is required to satisfy energy balance at the wall. As the evaporative heat flux is largely dependent on the RPI closing models (D_w, N_w and f) which are in turn dependent on the wall temperature, a reduction in evaporative heat flux necessitates a reduction in wall temperature as seen in *fig. 4.43*.

4.11 Mesh Independence Study

An orthogonal structured mesh of uniform size is utilized in the fluid domain (for the flat surface, a paved mesh is used for all curved and singular needle surfaces). The 2mm section of mesh at the inlet is refined by doubling the cell count in that region. There is a gradual increase in cell size as one progresses from the solid-fluid interface into the main body of the solid. The bulk of the solid cells are twice as large as the fluid cells so as to reduce computational cost in the static solid region where a single energy equation is being solved. Four meshes are used in the mesh independence study. These are shown in *fig. 4.45* along with the number of cells in the fluid domain and the average cell size (in meters) in each of the solid and fluid domains.

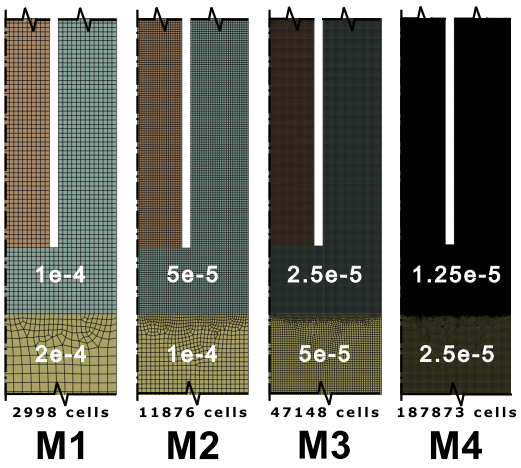

Figure 4.45: Truncated view of meshes used in mesh independence study with cell size in meters indicated in the fluid and solid domains respectively

The resulting boiling curves are shown in *fig. 4.46*. When using numerical framework $N1$ (*fig. 4.46b*) one observes that higher mesh densities appear to have lower wall temperatures near the onset of nucleate boiling with the discrepancy between the mesh densities appearing to diminish as one proceeds further up the boiling curve (excluding M1). This reduction in wall temperature at the lower portion of the boiling curve is due to grid generated turbulence (see *fig. 4.47*) that results from the non-equilibrium turbulence wall function being ill-suited to model turbulence generation with y^+ values below 30 [71]. *Figure 4.47a* shows that the y^+ value along the wall is below 30 and decreases with increasing mesh refinement. This results in greater turbulence generation within the domain. This enhances the convective heat flux (see *fig. 4.47a*) and results in a reduction in wall temperature with increased refinement. However, as the convective heat flux decays (due to an increase in wall temperature that results in an increase in the non-dimensional area of influence) the dependence on the mesh refinement diminishes.

Figure 4.46b and *fig. 4.46c* show that refining the mesh gradually shifts the boiling curve slightly to the right for both $N2A$ and $N2B$. The exception is at the lowest heat flux where the finest mesh shows a large shift to the left. As this region is predominantly governed by convection and does not form the primary focus of this dissertation, the reason for this was not explored. When comparing M2 with M4 it was found that there is a deviation of 1.59% for $N1$ (excluding values below (15 W/cm^2), a deviation of 0.48% for $N2A$ (excluding values below (10 W/cm^2) and a deviation of 0.84% for $N2B$ (excluding values below (10 W/cm^2). Thus mesh $M2$ was deemed to be sufficiently accurate and was selected for use throughout the remainder of the dissertation.

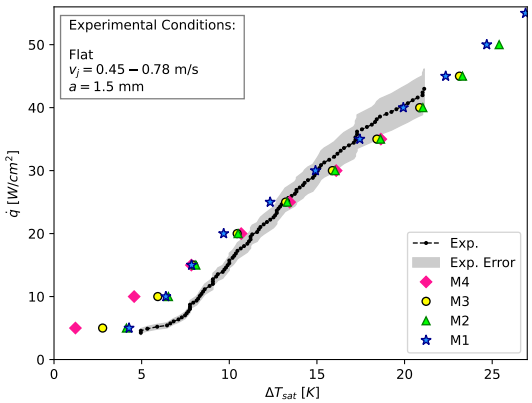

(a) Numerical Framework=N1

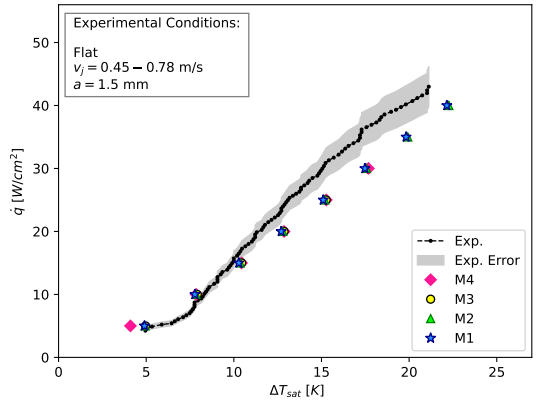

(b) Numerical Framework=N2A

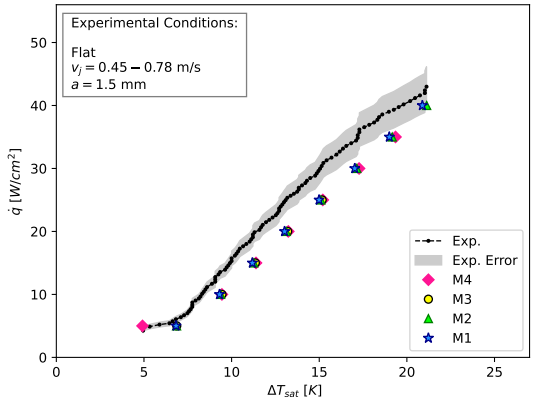

(c) Numerical Framework=N2B

Figure 4.46: Mesh Independence Study [nitrogen ($P_{sat} = 140$ kPa), case="Flat Surface", $a = 1.5$ mm, $v_j = 0.615$ m/s, $\Delta T_{sub} = 2$ K]

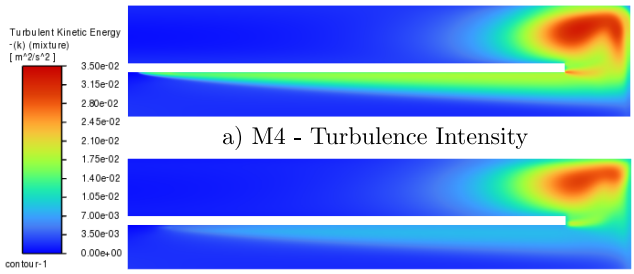

a) M4 - Turbulence Intensity

b) M2 - Turbulence Intensity

Figure 4.47: Turbulence intensity of mesh M4 and M2 at $\dot{q}_{applied} = 10$ W/cm^2 obtained from the simulations presented in fig. 4.46a

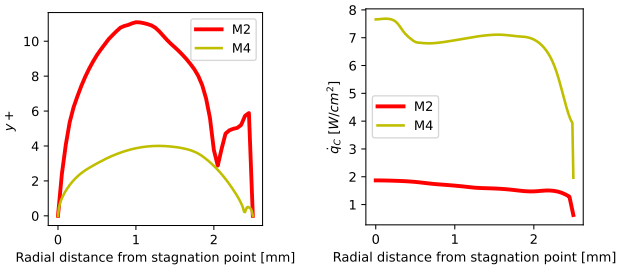

(a) y^+ *(b) $\dot{q}_C$*

*Figure 4.48: Impingement wall quantities (**a**-Wall y-plus, **b**-Quenching heat flux) at $\dot{q}_{applied} = 10$ W/cm^2 for the simulations presented in* fig. 4.46a

4.12 Simplified empirical model vs CFD using model $N1$

The CFD results of $N1$ are compared to the simplified empirical model results (*appendix D.1*, *appendix E*) (that exclude convective heat transfer) in *fig. 4.50*. The CFD wall superheat is slightly lower than the empirical solution ($C_{wt} = 3.142$) at 5 W/cm^2. This is attributed to the fact that the convective heat transfer is accounted for in the CFD simulation which lowers the wall temperature. From 10 W/cm^2 onwards, however, the CFD wall superheats are in excess of the predicted empirical results. In this region the convective heat transfer plays a diminishing role as the non-dimensional area of influence rises to a value of 1 (thus reducing the convective heat flux contribution according to *eq.* (3.2)). Note the slight discrepancy between the empirical and CFD non-dimensional area of influence as a result of the Jakob number used within *eq.* (3.37) being dependent on local liquid subcooling.

The reason for the increased wall superheat between the CFD and empirical solution is primarily due to the fact that the RPI wall boiling model neglects heat transfer to the vapour at the wall. Thus, as soon as there is an appreciable vapour fraction in the cell closest to the wall, there is less fluid to transfer heat to and thus a higher temperature difference is needed in order to maintain the specified wall heat flux. Perhaps this can be improved in the future by incorporating a function into the simplified empirical model that accounts for the reduction in liquid-wall contact area due to vapour production such that the results better align with the CFD results. The model could then be further extended to account for heat transfer to the newly designated vapour.

The NLBF temperature increase is another possible reason for the wall superheat increase. This diminishes the quenching heat transfer which implies that a larger evaporative heat transfer is required to maintain energy balance at the wall. This is facilitated through a rise in wall temperature (which serves to further diminish the quenching heat transfer). The empirical solution assumes quenching at the inlet subcooled temperature (assumed to be constant) and thus does not account for the increase in liquid temperature with increased applied heat flux. The increase in NLBF liquid temperature also increases the bubble departure diameter (*eq.* (3.17)) which serves to further elevate the evaporative heat flux. Furthermore, the increase in NLBF liquid temperature results in a reduction in departure frequency (*eq.* (3.26)) which serves to further diminish the quenching heat flux (*eq.* (3.13)). The explanation would not be complete without acknowledging that the reduction in departure frequency and nucleation site density (*eq.* (3.21)) also result in a decrease in the evaporative heat flux. However, this is offset by the increase in bubble departure diameter which has a larger impact due to the fact that it is cubed when computing the evaporative heat flux (*eq.* (3.14)).

The simplified empirical model combines numerous empirical models into a single solution and can be cheaply solved (in a single iteration if an array is used as the input parameter) whilst the CFD model is far more computationally expensive. However, the CFD model accounts for many more variables both near and far from the wall that influence the solution. These include: velocity effects, volume fraction distribution, forces acting on the vapour, changes in local liquid subcooling etc...

When using a bubble waiting time coefficient of 2 in the simplified empirical model the results align far better with the CFD and experimental results thus indicating that more reasonable values of C_{wt} can be used in the simplified empirical model.

The large increase in the evaporative heat flux results in a large vapour volume fraction within the domain at higher heat fluxes (compared to $N2A$ and $N2B$), as is shown in *fig. 4.49*.

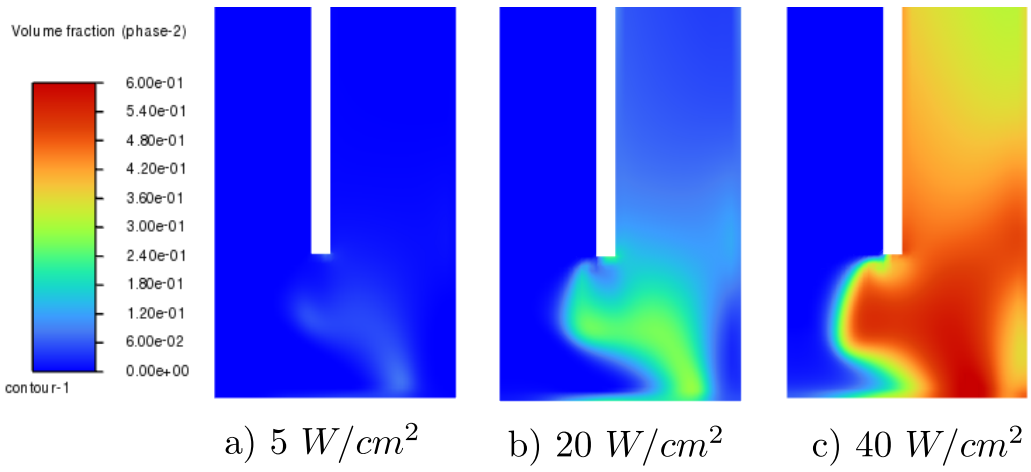

Figure 4.49: Truncated domain showing vapour fraction for $N1$ at various heat fluxes [nitrogen ($P_{sat} = 140$ kPa), mesh=M2, case="Flat Surface", $a = 1.5$ mm, $v_j = 0.78$ m/s, $\Delta T_{sub} = 2$ K]

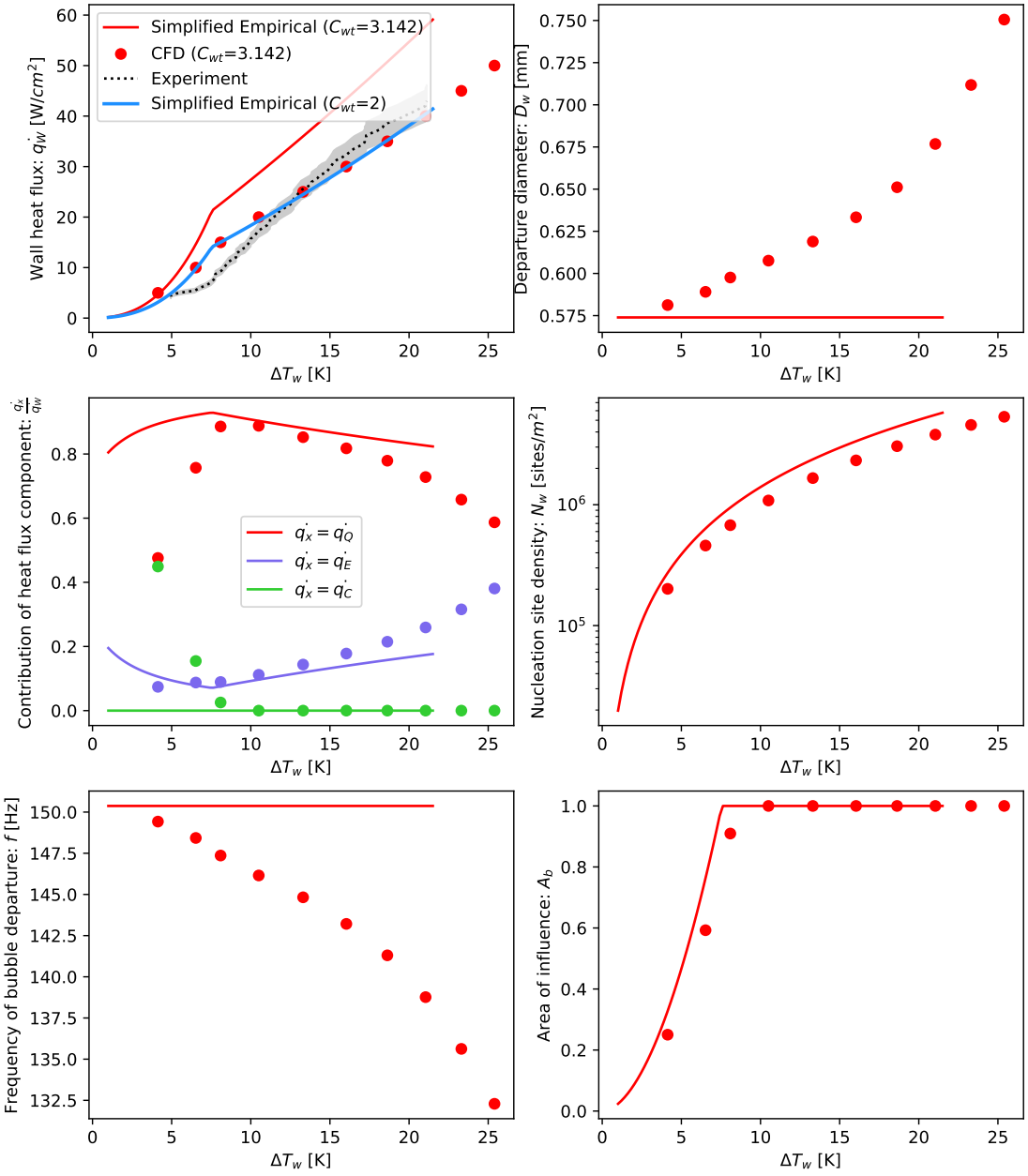

*Figure 4.50: Simplified empirical (*appendix D.1, appendix E*) and CFD results obtained using* $N1$ *[nitrogen (*$P_{sat} = 140$ kPa*), mesh=M2, case="Flat Surface",* $a = 1.5$ mm, $v_j = 0.615$ m/s, $\Delta T_{sub} = 2$ K*]. The simplified empirical model for* $C_{wt} = 2$ *has only been shown in the wall superheat graph (top left figure), whilst quantities for* $C_{wt} = 3$ *have been shown in all graphs*

4.13 Comparison of $N2A$ and $N2B$

Comparing the wall superheat of $N_w = Kirichenko$ ($N2A$) and $N_w = Kocamustafaogullari$ ($N2B$) in *fig. 4.53*, one notes that $N_w = Kocamustafaogullari$ experiences slightly delayed incipience but has a slightly higher BHTC (steeper slope) than $N_w = Kirichenko$. The frequency and departure diameter remain fairly consistent with empirical values across both models. As expected from *section 3.3.2*, the $N_w = Kocamustafaogullari$ initially predicts fewer nucleation sites than that of $N_w = Kirichenko$ but at $\Delta T_w \approx 15$ K surpasses $N_w = Kirichenko$. This is reflected in the heat flux contributions whereby $N_w = Kirichenko$ initially starts off with a higher evaporative component but is soon overtaken by $N_w = Kocamustafaogullari$ which is seen to increase drastically towards the top of the experimental boiling curve. Again this is further supported by *fig. 4.51* and *fig. 4.52* that shows that the vapour fraction is initially higher for $N_w = Kirichenko$ (at 5W/cm^2) but at the higher heat flux (at 40W/cm^2) the $N_w = Kocamustafaogullari$ model predicts larger quantities of vapour. It should be noted that one would perhaps expect larger vapour fractions at 40W/cm^2 for both models and this may potentially be a shortfall of the model. Additionally there appears to be a lack of vapour in the outer corner of the domain where the flow turns. This is somewhat intriguing as it is a stagnation point and should thus have very slow flow with the maximum developed thermal boundary layer thickness. One would therefore expect large vapour production in this region. However, due to the uneven heat flow within the solid as a result of the insulating effect of the vapour near the outer edge, both the evaporative and quenching heat fluxes taper off sharply in the outer corner as shown in *fig. 4.34e* and *fig. 4.34d*.

The CFD wall superheat of $N_w = Kocamustafaogullari$ is below that predicted by the empirical solution at the lower portion of the boiling curve ($\dot{q_W} \leq 10$ W/cm^2). This arises from the fact that the convective heat transfer is neglected in the empirical solution and is clearly shown to have a relatively large impact at the lower portion of the boiling curve. The convective heat transfer accounts for over 60% of the total heat flux contribution at $\dot{q_W} = 5$ W/cm^2 for the $N_w = Kocamustafaogullari$ simulation. It is expected that a similar trend would be noted for the $N_w = Kirichenko$ simulation if lower heat fluxes were used.

However, past a certain point, the wall superheat is greater than expected for both models. The reason for this is less obvious than for $N1$ in *section 4.12* as there is only a minor reduction in quenching heat flux (due to increased NLBF liquid temperature). As the RPI wall closing models (D_w, N_w and f) are not dependent on the local liquid temperature for both $N2A$ and $N2B$ there is no significant influence on the heat flux partitioning. Therefore the only other reason for the increase in wall superheat is due to the fact that the RPI wall boiling model neglects heat transfer to the vapour at the wall (as mentioned at the end of *section 4.12*).This would maintain the same heat flux partitioning but necessitate an increase in wall temperature in order to account for the reduction in liquid-wall contact area.

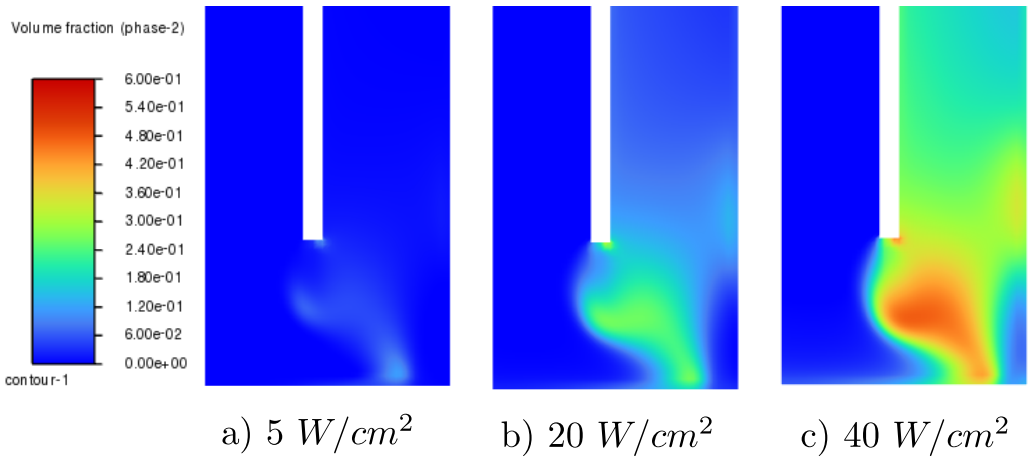

Figure 4.51: Truncated domain showing vapour fraction for N2A at various heat fluxes [nitrogen ($P_{sat} = 140$ kPa), mesh=M2, case="Flat Surface", $a = 1.5$ mm, $v_j = 0.78$ m/s, $\Delta T_{sub} = 2$ K]

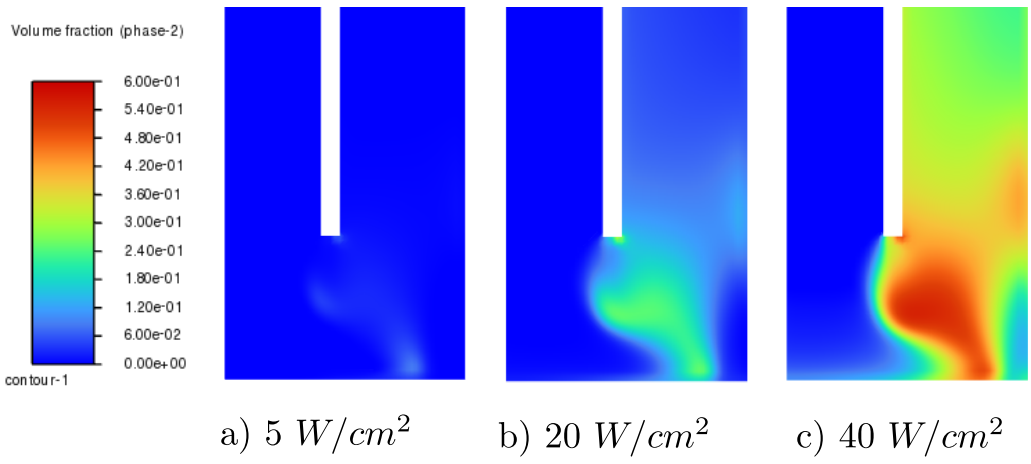

Figure 4.52: Truncated domain showing vapour fraction for N2B at various heat fluxes [nitrogen (P_{sat} = 140 kPa), mesh=M2, case="Flat Surface", a = 1.5 mm, v_j = 0.78 m/s, ΔT_{sub} = 2 K]

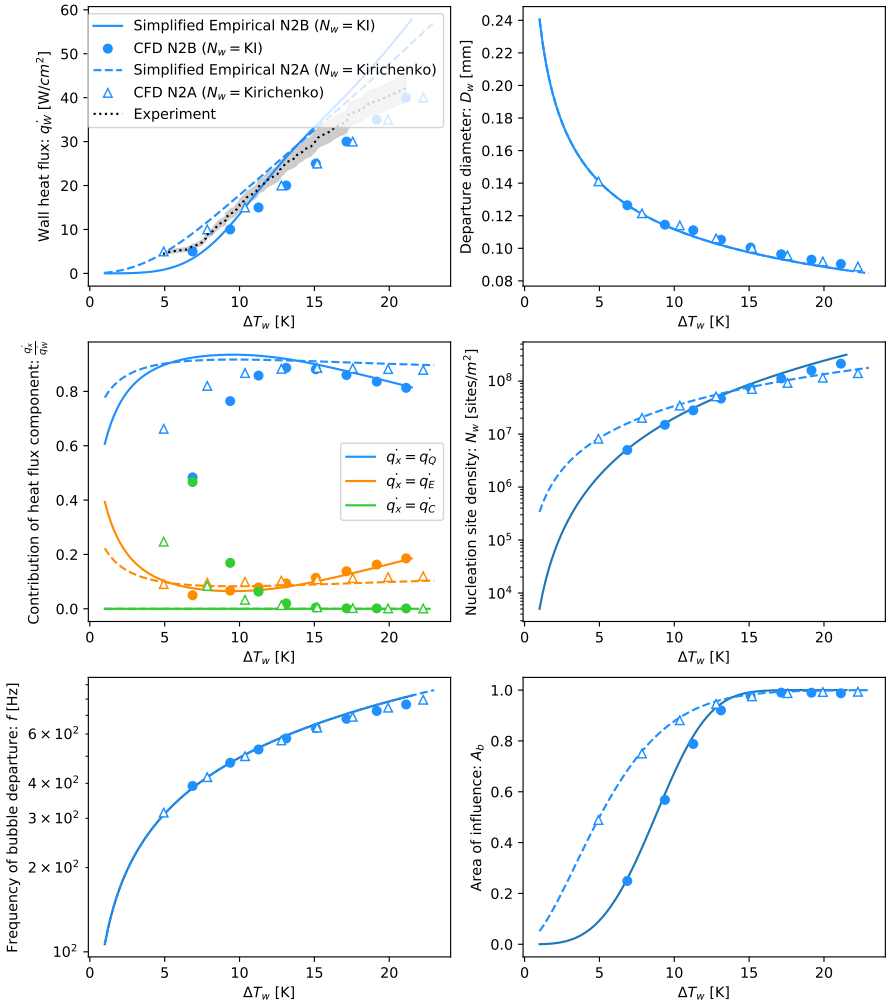

*Figure 4.53: Simplified empirical (*appendix D.2, appendix E*) and CFD comparison of the effect of the different nucleation site density correlations used in N2A and N2B [nitrogen (P_{sat} = 140 kPa), mesh=M2, case="Flat Surface", a = 1.5 mm, v_j = 0.615 m/s, ΔT_{sub} = 2 K]*

4.14 Effect of Non-dimensional Area of Influence Correlation

Figure 4.54a shows the results of a simulation run using different correlations for the non-dimensional area of influence and the expected empirical solution based on *section 3.4*, *appendix D.2* and *appendix E*. The sharp cutoff in the area of influence imposed by the formula $A_b = \min(1, \beta)$ (see *fig. 4.54b*) results in a characteristic cusp in the boiling curve (see *fig. 4.54a*) as the boiling heat transfer coefficient (representing the slope of the boiling curve) suddenly transitions from from an increasing value to a lesser constant value. This is more pronounced for numerical framework $N1$ with large quenching heat fluxes that may be caused by large bubble waiting time coefficients (*fig. 4.55a*) or large subcoolings (*fig. 4.55b*). Both the theoretical formula of Kenning and Del Valle M 1981 [89] ($A_b = 1 - e^{-\beta}$) and the empirically proposed formula of *section 3.3.4* ($A_b = 1 - e^{-1.5\beta^{1.2}}$) have smooth transitions between the onset of nucleate boiling and the fully developed nucleate boiling regime (based on the empirical solutions presented in *fig. 4.54a* and *fig. 4.55c*). This is more inline with what one would expect in a real experiment, baring hysteresis effects. The deviation is predominantly at the lower half of the boiling curve (in *fig. 4.54a*) as the non-dimensional area of influences converge to the maximum value of 1 above $\Delta T_w \approx 20$ K, resulting in a convergence of the wall superheat. Additionally the deviation between ($A_b = \min(1, \beta)$) and ($A_b = 1 - e^{-1.5\beta^{1.2}}$) is a maximum of ≈ 1 K, with a similar maximum deviation between ($A_b = 1 - e^{-\beta}$) and ($A_b = 1 - e^{-1.5\beta^{1.2}}$).

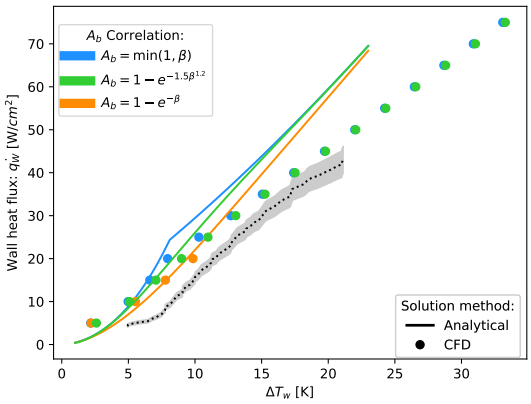

*(a) Empirical (*appendix D.2, appendix E*) and CFD (N2A) results comparing wall superheat for different of area of influence correlations*

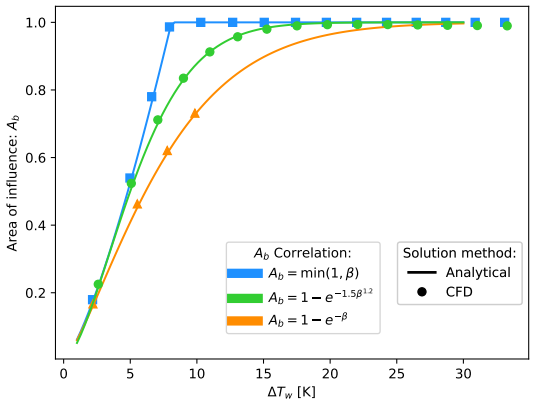

*(b) Empirical (*appendix D.2, appendix E*) and CFD (N2A) results comparing area of influence for different of area of influence correlations*

Figure 4.54: Non- dimensional area of influence and its effect on the boiling curve [nitrogen ($P_{sat} = 140$ kPa), Numerical Framework=N2A, case="Flat Surface", $a = 1.5$ mm, $v_j = 0.615$ m/s, $\Delta T_{sub} = 8$ K, mesh=M2, $K = 4$]

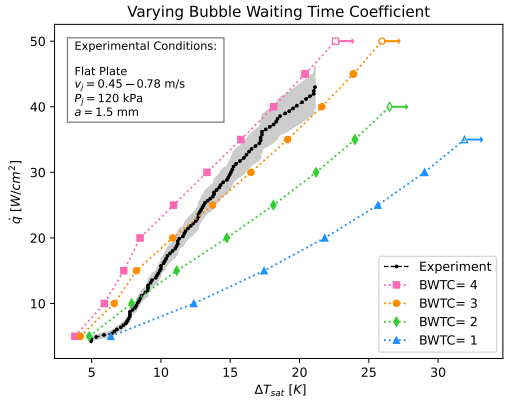

(a) The effect of bubble waiting time coefficient on wall superheat (CFD N1) [$A_b = min(1, \beta)$, $\Delta T_{sub} = 2$ K]

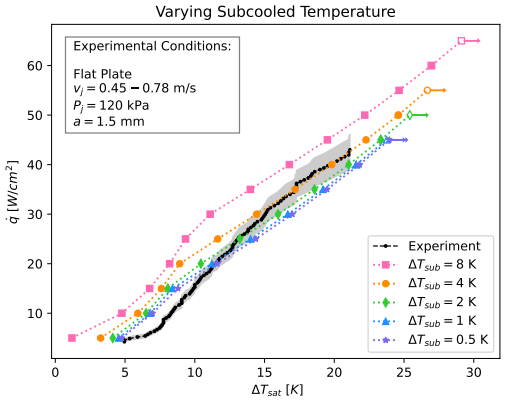

(b) The effect of subcooling temperature on wall superheat (CFD N1) [$A_b = min(1, \beta)$, $C_{wt} = 3.142$]

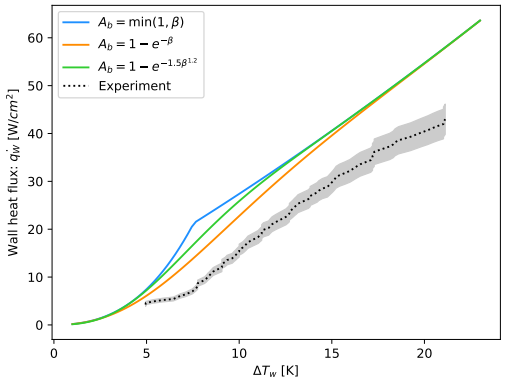

*(c) Simplified empirical solution (*appendix D.1, appendix E*) for N1 [$\Delta T_{sub} = 2$ K, $C_{wt} = 3.142$]*

Figure 4.55: Cusp in boiling curve due to eq. (3.3) *[nitrogen ($P_{sat} = 140$ kPa), Numerical Framework=N1, mesh=M2, case="Flat Surface", $a = 1.5$ mm, $v_j = 0.78$ m/s]*

4.15 Comparison of Numerical Frameworks for all Flat Surface Experimental Cases

Figure 4.56 displays the performance of $N1$, $N2A$ and $N2B$ across the results of all the experiments conducted by Zhang et al. 2011 [205] for the flat surface. Note that two different subcoolings are used as the value of the subcooling is not clearly defined in the experimental paper. Additionally, the velocity and impingement height varies between *4.56 a-d*. All models are well within the 30% range of the experimental results that is commonly reported as acceptable in literature. Some models have converged at values well in excess of the experimental critical heat flux. This indicates that the current models are not suitable for prediction of this variable. The boiling heat transfer coefficients of $N1$ and $N2A$ are similar with $N2B$ having a slightly higher BHTC.

Increasing the subcooling results in a shift of the boiling curve to the left, a result that is consistent with the findings of *section 4.8.1*. More favourable results were obtained with $\Delta T_{sub} = 4$ K for both $N2A$ and $N2B$. However, $N1$ exhibited satisfactory results with $T_{sub} = 2$ K.

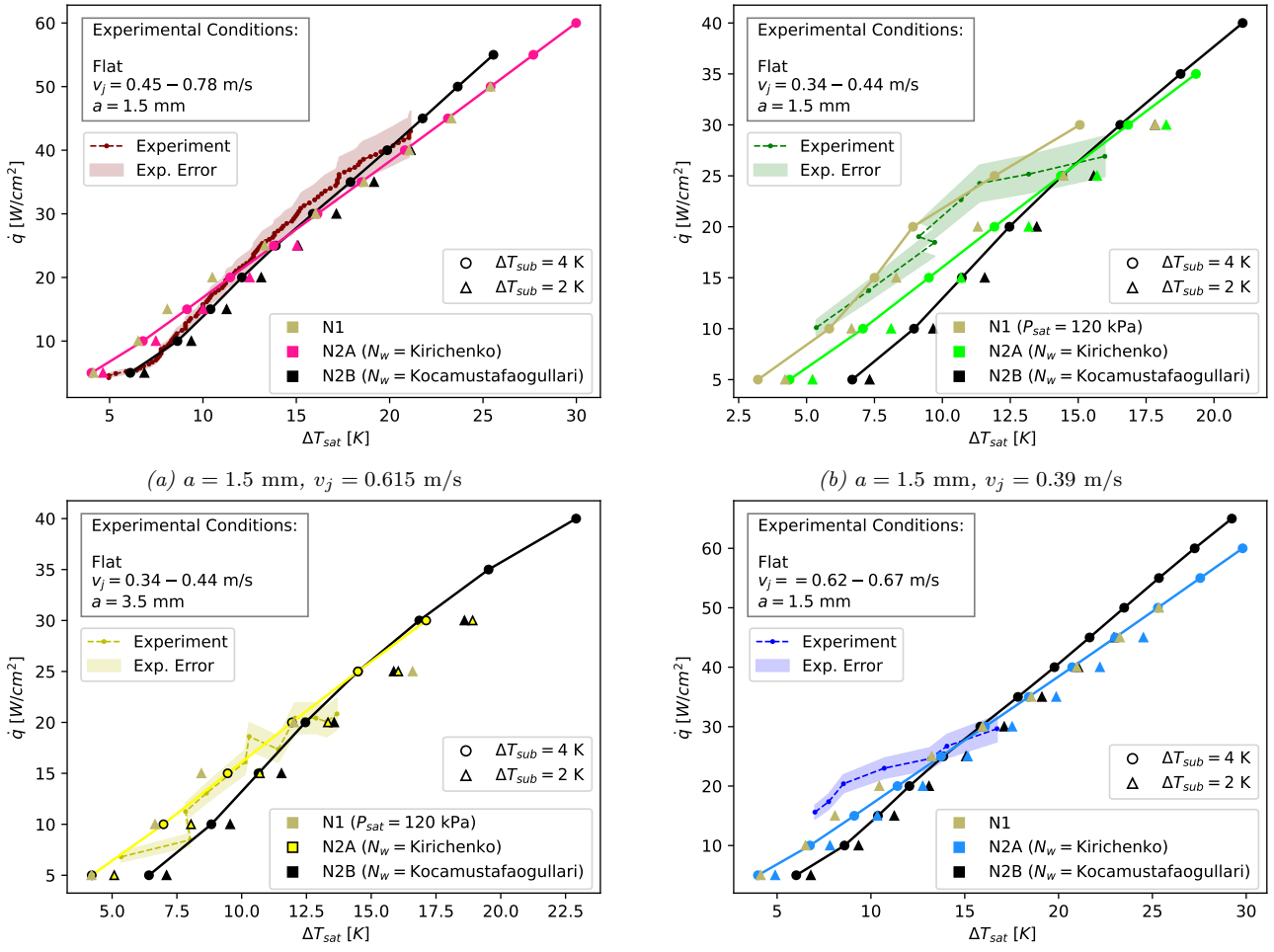

(a) $a = 1.5$ mm, $v_j = 0.615$ m/s

(b) $a = 1.5$ mm, $v_j = 0.39$ m/s

(c) $a = 3.5$ mm, $v_j = 0.39$ m/s

(d) $a = 1.5$ mm, $v_j = 0.645$ m/s

Figure 4.56: Flat surface validation under various experimental conditions [nitrogen ($P_{sat} = 140$ kPa), mesh=M2, case="Flat Surface"]

4.16 Comparison of Numerical Frameworks for all Hemispherical Surface Experimental Cases

Figure 4.57 displays the the performance of $N1$, $N2A$ and $N2B$ across the results of all the experiments conducted by Zhang et al. 2011 [205] for the hemispherical surface at $a = 1.5$ mm. Likewise, *Figure 4.60* displays the performance of $N1$, $N2A$ and $N2B$ across the results of all the experiments conducted by Zhang et al. 2011 [205] for the hemispherical surface at $a = 3.5$ mm.

$N1$ ($\Delta T_{sub} = 2$ K) underpredicts the wall superheat at low velocities ($v_j = 0.39$ m/s), particularly at lower heat fluxes ($\dot{q}_{applied} \leq 30$ W/cm^2) for both impingement heights. However, there is a notable improvement

in the comparison between the experimental results and CFD results of $N1$ at the higher jet velocities. $N2A$ ($\Delta T_{sub} = 4$ K) is similar in performance to $N1$ ($\Delta T_{sub} = 2$ K) with a slight increase in wall superheat past $\dot{q}_{applied} \leq 20$ W/cm^2. All models are well within the 30% range of the experimental results that is commonly reported as acceptable in literature.

The velocity profiles at $a = 1.5$ mm and $a = 3.5$ mm are shown in *fig. 4.59* and *fig. 4.62*. There appears to be a slightly higher velocity along the surface for the lower impingement height.

The vapour fraction contours at $a = 1.5$ mm and $a = 3.5$ mm are shown in *fig. 4.58* and *fig. 4.61* respectively. Both contour plots show that the vapour tends to accumulate in the low velocity re-circulation zone in the centre of the domain. At the highest heat flux displayed ($\dot{q}_{applied} \geq 50$ W/cm^2) , it can be seen that the vapour is more dispersed at $a = 3.5$ mm. Whilst the $a = 1.5$ mm appears to have a large amount of vapour emanating from the outer lip and a concentration of vapour trapped at the lip near the jet exit.

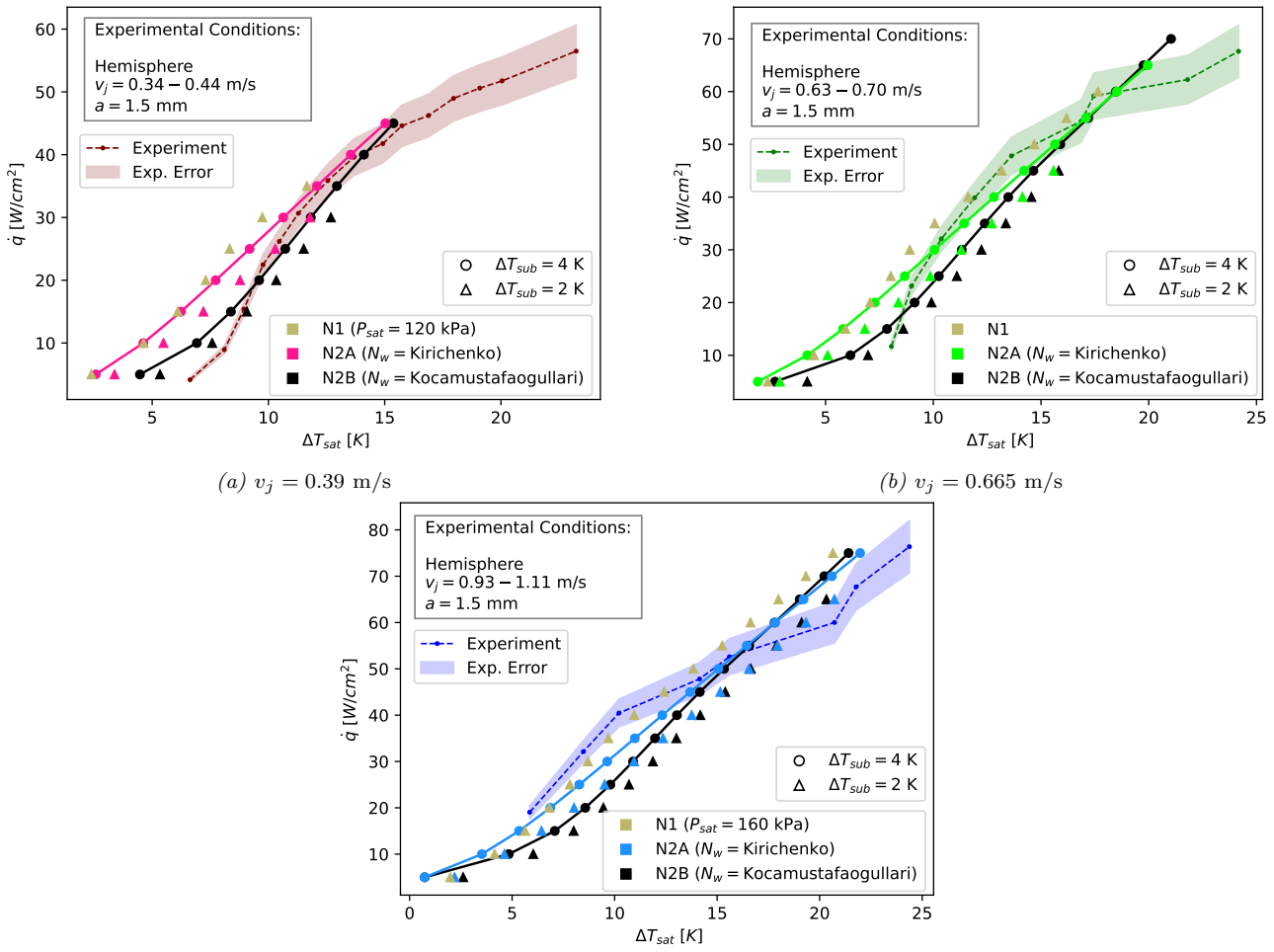

(a) $v_j = 0.39$ m/s

(b) $v_j = 0.665$ m/s

(c) $v_j = 1.02$ m/s

Figure 4.57: $a = 1.5$ mm Hemispherical surface validation at various inlet velocities [nitrogen ($P_{sat} = 140$ kPa), mesh=M2, case="Hemispherical Surface"]

4.17 Comparison of Numerical Frameworks for all Single Pin Surface Experimental Cases

Figure 4.65 displays the performance of $N1$, $N2A$ and $N2B$ across the results of all the experiments conducted by Zhang et al. 2011 [205] for the single needle surface at $a = 1.5$ mm. Likewise, *Figure 4.68* displays the performance of $N1$, $N2A$ and $N2B$ across the results of all the experiments conducted by Zhang et al. 2011 [205] for the single needle surface at $a = 3.5$ mm.

All models overpredict the wall temperature (even at $\Delta T_{sub} = 4$ K). Possible explanations include: the model is not suitable for such surfaces, the extrapolated wall temperature introduces a source of error (as shown in *section 4.6.3*, using the stagnation point temperature would shift the graph to the left by approximately 0.5 K at the lower heat fluxes and up to 2.5 K at the higher heat fluxes which would significantly improve the CFD

a) 10 W/cm^2 b) 30 W/cm^2 c) 60 W/cm^2

Figure 4.58: Truncated domain showing vapour fraction at various heat fluxes for the hemispherical surface [nitrogen (P_{sat} = 140 kPa), Numerical Framework=N2A, mesh=M2, case="Hemispherical Surface", a = 1.5 mm, v_j = 0.665 m/s, ΔT_{sub} = 4 K]

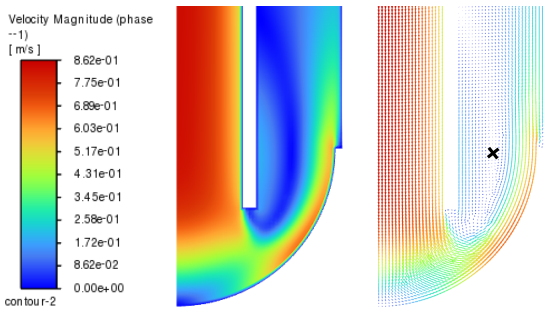

Figure 4.59: Truncated domain showing velocity magnitude contour plot (left) and vector plot (right) at $\dot{q}_{applied}$ = 10 W/cm^2 for the hemispherical surface (centre of re-circulation zone marked with an 'x') [nitrogen (P_{sat} = 140 kPa), Numerical Framework=N2A, mesh=M2, case="Hemispherical Surface", a = 1.5 mm, v_j = 0.665 m/s, ΔT_{sub} = 4 K]

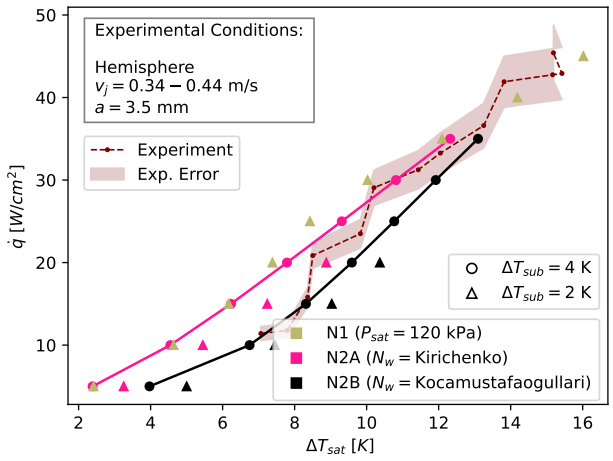

(a) v_j = 0.39 m/s

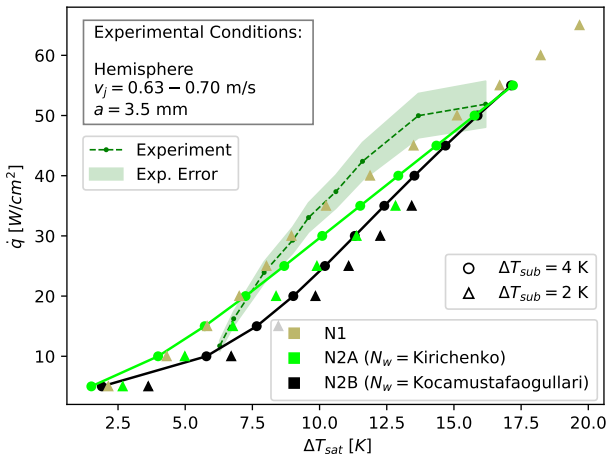

(b) v_j = 0.665 m/s

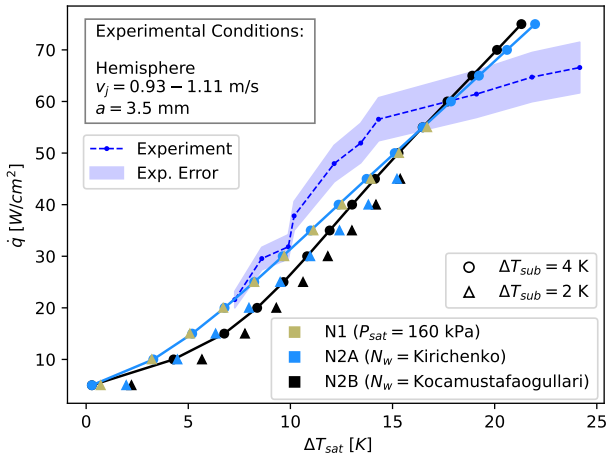

(c) v_j = 1.02 m/s

Figure 4.60: a = 3.5 mm Hemispherical surface validation at various inlet velocities [nitrogen (P_{sat} = 140 kPa), mesh=M2, case="Hemispherical Surface"]

results) or experiments using this surface were conducted at a higher pressure or lower subcooling. Regardless of this, the boiling heat transfer coefficient (slope of the boiling curve) is reasonably accurate for all models tested.

a) 10 W/cm^2 b) 30 W/cm^2 c) 50 W/cm^2

Figure 4.61: Truncated domain showing vapour fraction at various heat fluxes for the hemispherical surface [nitrogen (P_{sat} = 140 kPa), Numerical Framework=N2A, mesh=M2, case="Hemispherical Surface", a = 3.5 mm, v_j = 0.665 m/s, ΔT_{sub} = 4 K]

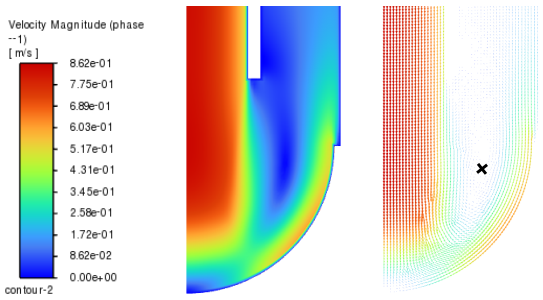

Figure 4.62: Truncated domain showing velocity magnitude contour plot (left) and vector plot (right) at $\dot{q}_{applied}$ = 10 W/cm^2 for the hemispherical surface (centre of re-circulation zone marked with an 'x') [nitrogen (P_{sat} = 140 kPa), Numerical Framework=N2A, mesh=M2, case="Hemispherical Surface", a = 3.5 mm, v_j = 0.665 m/s, ΔT_{sub} = 4 K]

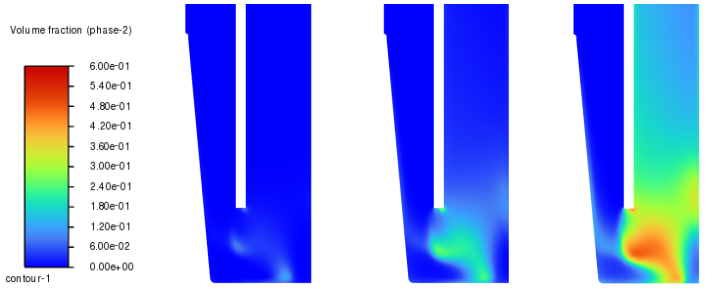

a) 10 W/cm^2 b) 30 W/cm^2 c) 60 W/cm^2

Figure 4.63: Truncated domain showing vapour fraction at various heat fluxes for the singular needle surface [nitrogen (P_{sat} = 140 kPa), Numerical Framework=N2A, mesh=M2, case="Singular Needle", a = 1.5 mm, v_j = 0.665 m/s, ΔT_{sub} = 4 K]

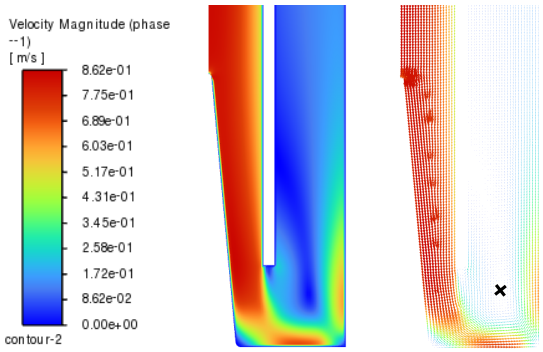

Figure 4.64: Truncated domain showing velocity magnitude contour plot (left) and vector plot (right) at $\dot{q}_{applied}$ = 10 W/cm^2 for the singular needle surface (centre of re-circulation zone marked with an 'x') [nitrogen (P_{sat} = 140 kPa), Numerical Framework=N2A, mesh=M2, case="Singular Needle", a = 1.5 mm, v_j = 0.665 m/s, ΔT_{sub} = 4 K]

4.18 Discussion

It has been shown in *section 4.15*, *section 4.16* and *section 4.17* that $N1$ can be used to predict the wall superheat with reasonable accuracy. Furthermore, $N1$ produces more vapour towards the top of the experimental boiling curve compared to $N2A$ and $N2B$. This is what one expects as the experimental CHF is approached and dryout is reached. However, it was decided that the model be neglected from consideration for implementation in the parametric study based on the implausibly high bubble waiting time coefficient (see section 4.10) that was used to force the results to be within an acceptable range. Additionally the prediction of such large bubble departure diameters ($>$ 0.7 mm) in the confined domain is far larger than one would expect for cryogenic fluids. Thus any analysis of heat flux partitioning and vapour in the domain should be called into question as the model is being forced to operate beyond its intended application. A key takeaway from the exploration of this model is then that it can be used for cryogenic applications if one is willing to overlook the theoretical implications of modifying the BWTC.

That leaves $N2A$ and $N2B$ left for consideration for implementation in the parametric study. To summarise the performance of these numerical frameworks, an integrated error measure was formulated based on the boiling curve data. The root mean squared deviation (RMSD) of the wall superheat determined at the experimentally measured data points and the corresponding CFD value (computed from a linear interpolation between the CFD points and evaluated at the experimental heat flux) is shown in *table 4.2* and *table 4.3* for $N2A$ and $N2B$ respectively (at ΔT_{sub} = 4 K as that was the best subcooling for both models). If the experimental heat flux was out of range of the interpolated CFD value, that experimental value was discarded in the RMSD calculation for that specific CFD simulation. The average RMSE across all simulations for [Numerical framework=$N2A$,

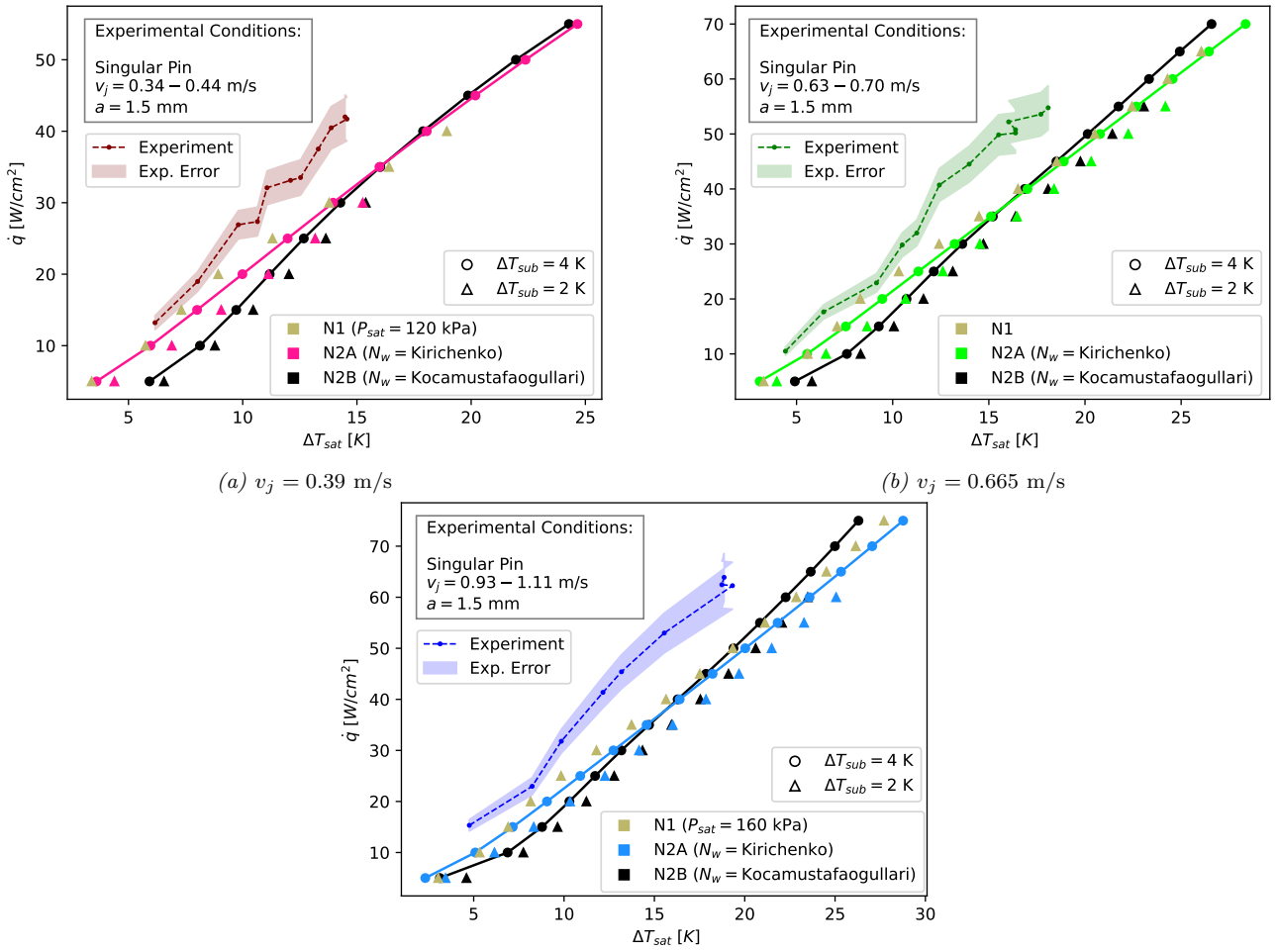

(a) $v_j = 0.39$ m/s

(b) $v_j = 0.665$ m/s

(c) $v_j = 1.02$ m/s

Figure 4.65: $a = 1.5$ mm Singular needle surface validation at various inlet velocities [nitrogen ($P_{sat} = 140$ kPa), mesh=M2, case="Singular Needle Surface"]

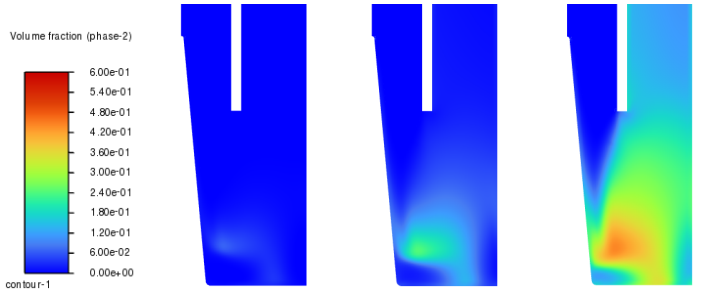

a) 10 W/cm^2 b) 30 W/cm^2 c) 60 W/cm^2

Figure 4.66: Truncated domain showing vapour fraction at various heat fluxes for the singular needle surface [nitrogen ($P_{sat} = 140$ kPa), Numerical Framework=N2A, mesh=M2, case="Singular Needle", $a = 3.5$ mm, $v_j = 0.665$ m/s, $\Delta T_{sub} = 4$ K]

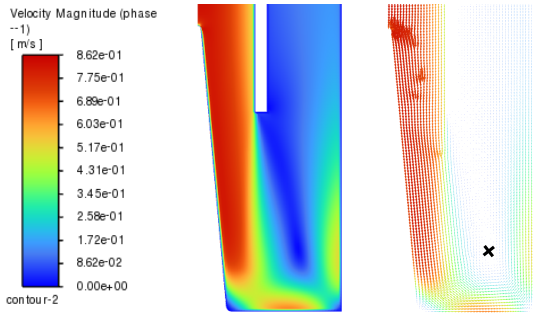

Figure 4.67: Truncated domain showing velocity magnitude contour plot (left) and vector plot (right) at $\dot{q}_{applied} = 10$ W/cm^2 for the singular needle surface (centre of re-circulation zone marked with an 'x') [nitrogen ($P_{sat} = 140$ kPa), Numerical Framework=N2A, mesh=M2, case="Singular Needle", $a = 3.5$ mm, $v_j = 0.665$ m/s, $\Delta T_{sub} = 4$ K]

$N_w = Kirichenko$, $\Delta T_{sub} = 4$ K] is 2.468 (*table 4.2*). The average RMSD across all simulations for [Numerical framework=$N2B$, $N_w = Kocamustafaogullari$, $\Delta T_{sub} = 4$ K] is 2.545 (*table 4.3*). Considering that $N2A$ uses $N_w = Kirichenko$ model which has been developed for cryogenic fluids and has a lower deviation than $N2B$, it has been decided that this model will be utilised for all CFD simulations presented in the parametric study (*chapter 5*). Furthermore, as $N2A$ was the most accurate across all the surfaces in the $v_j = 0.45 - 0.78$ m/s velocity range, a jet inlet velocity of $v_j = 0.78$ m/s was chosen for use in the parametric study.

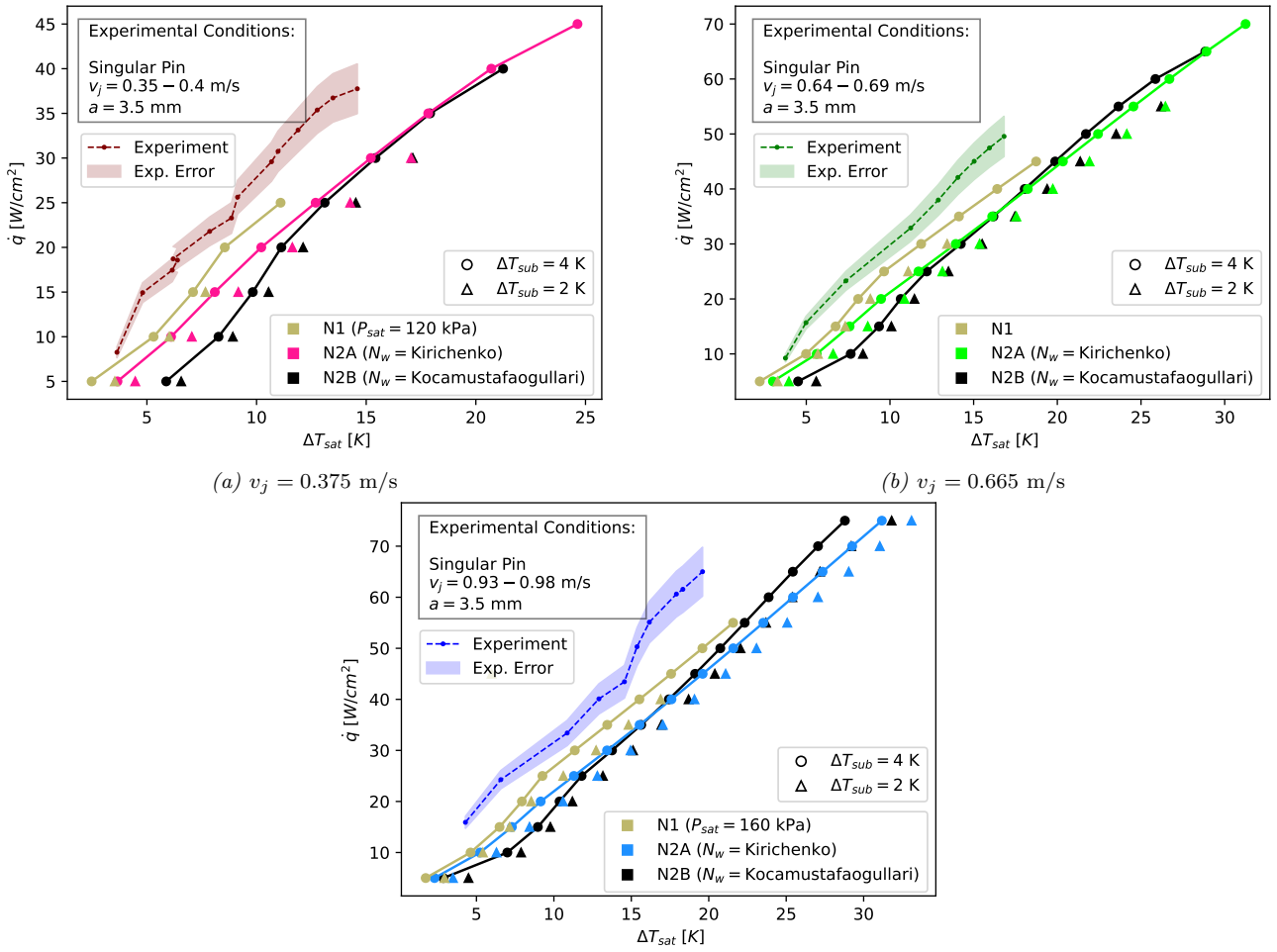

(a) $v_j = 0.375$ m/s

(b) $v_j = 0.665$ m/s

(c) $v_j = 0.955$ m/s

Figure 4.68: $a = 3.5$ mm Singular needle surface validation at various inlet velocities [nitrogen ($P_{sat} = 140$ kPa), mesh=M2, case="Singular Needle Surface"]

Figure 4.69 displays the comparison of various properties along the impingement wall for the three surfaces at $\dot{q}_{applied} = 30$ W/cm^2 for $N2A$. The results indicate that there is increased convective heat transfer (*fig. 4.69d*) at the needle tip with reduced quenching (*fig. 4.69f*)) and evaporation (*fig. 4.69e*) at the needle tip. The curved surface has the lowest temperature, with the majority of the vapour being generated at the outer lip. A concerning observation is that the NLBF temperature has discontinuities for the single needle and hemispherical surfaces (*fig. 4.69a*). As was shown in *section 4.7* this can have direct impact on the quenching heat flux and convective heat flux (note the discontinuous nature of the solution in *fig. 4.69d* and *fig. 4.69f*) and result in a boundary length and mesh dependence influence (not shown). It is suspected that interpolation errors in the calculation are responsible for this effect, however as the source code is unavailable it is left for future work to explore the reason for this non-linearity and its impact on the wall superheat.

Table 4.2: Root mean square deviation from reported experimental values [Numerical framework=$N2A$, $N_w = Kirichenko$, $\Delta T_{sub} = 4$ K]

	$v_j = 0.34 - 0.44$ m/s	$v_j = 0.45 - 0.78$ m/s	$v_j = 0.93 - 1.11$ m/s	Average
Flat Surface	1.357	1.24	–	1.299
Hemispherical Surface	1.823	1.243	1.606	1.557
Singular Needle Surface	3.489	3.961	5.029	4.16
Average	2.223	2.148	3.318	2.468

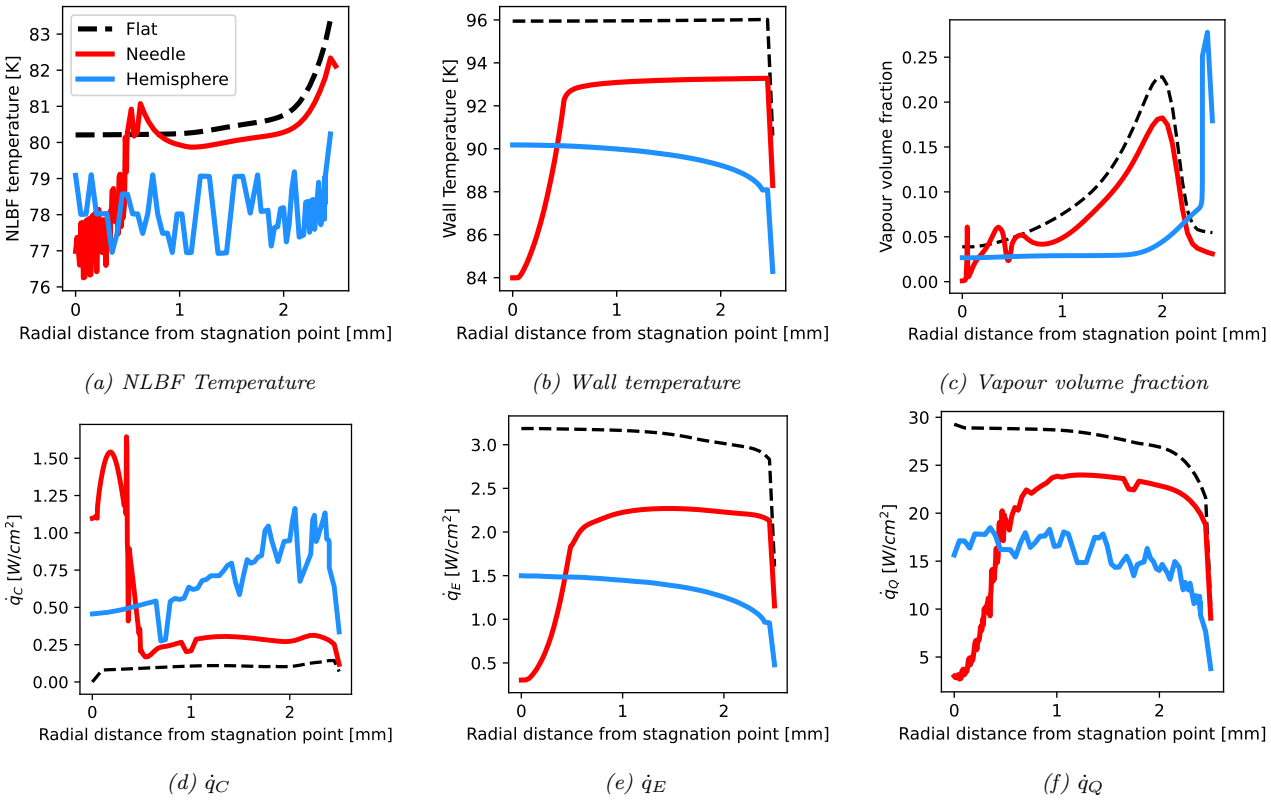

(a) NLBF Temperature *(b) Wall temperature* *(c) Vapour volume fraction*

(d) $\dot{q}_C$ *(e) $\dot{q}_E$* *(f) $\dot{q}_Q$*

*Figure 4.69: Impingement wall quantities (**a**-NLBF Temperature, **b**-Wall temperature, **c**-Vapour volume fraction, **d-f**-convective, evaporative and quenching heat fluxes) for the flat, singular needle and hemispherical surfaces at $\dot{q}_{applied} = 30$ W/cm^2 [nitrogen ($P_{sat} = 140$ kPa), Numerical Framework=N2A, mesh=M2, $a = 1.5$ mm, $v_j = 0.645 - 0.665$ m/s, $\Delta T_{sub} = 4$ K]*

Table 4.3: Root mean square deviation from reported experimental values [Numerical framework=N2B, $N_w = Kocamustafaogullari$, $\Delta T_{sub} = 4$ K]

	$v_j = 0.34 - 0.44$ m/s	$v_j = 0.45 - 0.78$ m/s	$v_j = 0.93 - 1.11$ m/s	Average
Flat Surface	1.362	1.667	–	1.515
Hemispherical Surface	0.654	1.632	2.212	1.499
Singular Needle Surface	4.047	4.101	4.688	4.279
Average	2.021	3.184	3.45	2.545

4.19 Summary

The validation introduced the experimental setup, numerical frameworks ($N1$, $N2A$ and $N2B$), material properties, boundary conditions and solution process. It was reasoned in *section 4.6.3* that an appropriate measure of the wall superheat can be obtained through use of the average extrapolated wall temperature. The boundary location effects were mitigated through use of a 2mm mesh refinement at the inlet. A sensitivity analysis revealed that all the CFD models are sensitive to subcooling with a 2 K increase in subcooling resulting in an approximately 2.5 K shift of the boiling curve to the left. Velocity showed less sensitivity with increased velocities increasing the boiling heat transfer coefficient thus decreasing the wall superheat towards the top of the experimental boiling curve. $N1$ proved to have a low sensitivity to pressure change whilst the boiling curve of $N2A$ and $N2B$ where significantly shifted to the left with increased pressure. This was attributed largely to the dependency of the nucleation site density correlations (of $N_w = Kirichenko$ and $N_w = Kocamustafaogullari$) on the fluid properties at the wall. Transient simulations were conducted and compared with the steady-state results. It was revealed that the steady wall superheat was within 2.4% of the finest timestep solution, with minor deviations in velocity and volume fraction. *Section 4.10* revealed that increasing the bubble waiting time coefficient increased the quenching heat flux and the boiling heat transfer coefficient. The cusp in the boiling curve generated by the sharp cutoff in non-dimensional area of influence correlation ($A_b = \min(1, \beta)$) was demonstrated. It was shown that the newly proposed non-dimensional area of influence model ($A_b = 1 - e^{-1.5\beta^{1.2}}$) produced a smooth transition in the boiling curve (from the lower to upper portion of the boiling curve) with minor deviation from the sharp cutoff correlation ($A_b = \min(1, \beta)$) in the lower to middle portion of the boiling

curve. A mesh independence study was conducted in which model $N1$ displayed deviation in the lower portion of the boiling curve due to grid generated turbulence. Mesh M2 (fluid cell size of 5e-5 m) was within 0.84% of the finest mesh used for $N2A$ and $N2B$. It was concluded that mesh M2 was sufficient for use. The $N1$ numerical framework was analysed, revealing that the liquid temperature and vapour fraction at the wall both contribute to an increase in wall temperature compared to the empirical solution of *section 3.4*. $N2A$ and $N2B$ were compared to assess the effect of the nucleation site density correlation on the boiling curve. It was revealed that both models are quenching dominated. $N_w = Kirichenko$ ($N2A$) resulted in a lower boiling heat transfer coefficient and a reduction in vapour near the experimental CHF compared to $N_w = Kocamustafaogullari$ ($N2B$). All of the experimental boiling curves for the flat surface, hemispherical surface and singular needle surface (at different impingement height and velocities) were shown compared to the CFD results of the three numerical frameworks at two subcooling ($\Delta T_{sub} = 2$ K $\Delta T_{sub} = 4$ K). All numerical frameworks were able to satisfactorily predict the experimental wall superheat, however, it was concluded that $N2A$ at $\Delta T_{sub} = 4$ K and $v_j = 0.78$ m/s is the most appropriate model for use in the parametric study.

Having proven mesh independence, the validity of the steady-state assumption and determined the most appropriate numerical model, a parametric study can now be undertaken to fully explore the effect of curvature, needle height and impingement height on the boiling curve.

Chapter 5

Parametric Study

5.1 Introduction

This chapter addresses the impact of surface curvature ($k = 0 - 0.42$), needle height ($h_{needle} = 0 - 5$ mm) and jet impingement height ($a = 0.5 - 5.5$ mm) on the nucleate boiling curve. Where applicable, contour plots of velocity, vapour volume fraction and solid temperature are provided alongside plots of wall heat flux partitioning, bubble departure diameter, nucleation site density and departure frequency in order to explain and changes observed in the boiling curves. The chapter begins with single parameter variations and ends with a full search of the 3D parameter space (k, h_{needle}, a). Emphasis is placed on identifying the geometric configuration that results in the highest boiling heat transfer coefficient (steepest slope of the boiling curve).

All simulations are run using numerical framework $N2A$, with $\Delta T_{sub} = 4$ K, $v_j = 0.78$ m/s, mesh=M2 and utilising nitrogen with variable liquid properties at $P_{sat} = 140$ kPa.

5.2 Surface Curvature

Recall from *section 2.2.3* that surface curvature (k) can be defined according to *eq.* (2.6) (repeated below for convenience).

$$k = \frac{d_j}{D_{surface}} = \frac{r_j}{R_{surface}}$$

The domains of the different surface curvatures tested in this section are shown in *fig. 5.1*. As can be seen, the choice to alter $R_{surface}$ has been made in order to vary the surface curvature. This has been done such that a curvature value of 0 corresponds to the flat plate case and the curvature value of 0.42 corresponds to the hemispherical case. Alternatively one could have elected to alter the jet radius (r_j), however, this directly alters the area of the outflow and will have a large impact on the system pressure that may not be adequately captured by the current model as the fluid properties are a function of temperature only. *Figure 5.2a* displays the boiling curve as a function of the applied heat flux. From it, one can observe a clear trend of increased boiling heat transfer coefficient (increased gradient) and decreased wall superheat (shift to the left) with increased surface curvature. *Figure 5.3* displays the quadratic growth of surface area with increasing curvature. Taking this into account, it is desirable to re-plot the results of *fig. 5.2a* such that the influence of surface area is removed. In order to do so, the average wall heat flux and surface augmentation factor are introduced.

The average heat flux through the wall ($\bar{\dot{q}}_w$) can be defined as:

$$\bar{\dot{q}}_w = \frac{\dot{q}_{applied}}{S_{aug}} = \bar{\dot{q}}_C + \bar{\dot{q}}_E + \bar{\dot{q}}_Q \tag{5.1}$$

where S_{aug} is the surface augmentation factor (S_{aug}) and is defined as the ratio of wall surface area (A_{surf}) to projected area normal to the jet axis (A_{proj}) (see *fig. 5.4* for a visual representation of this area for an arbitrary impingement wall shape):

$$S_{aug} = \frac{A_{surf}}{A_{proj}} \tag{5.2}$$

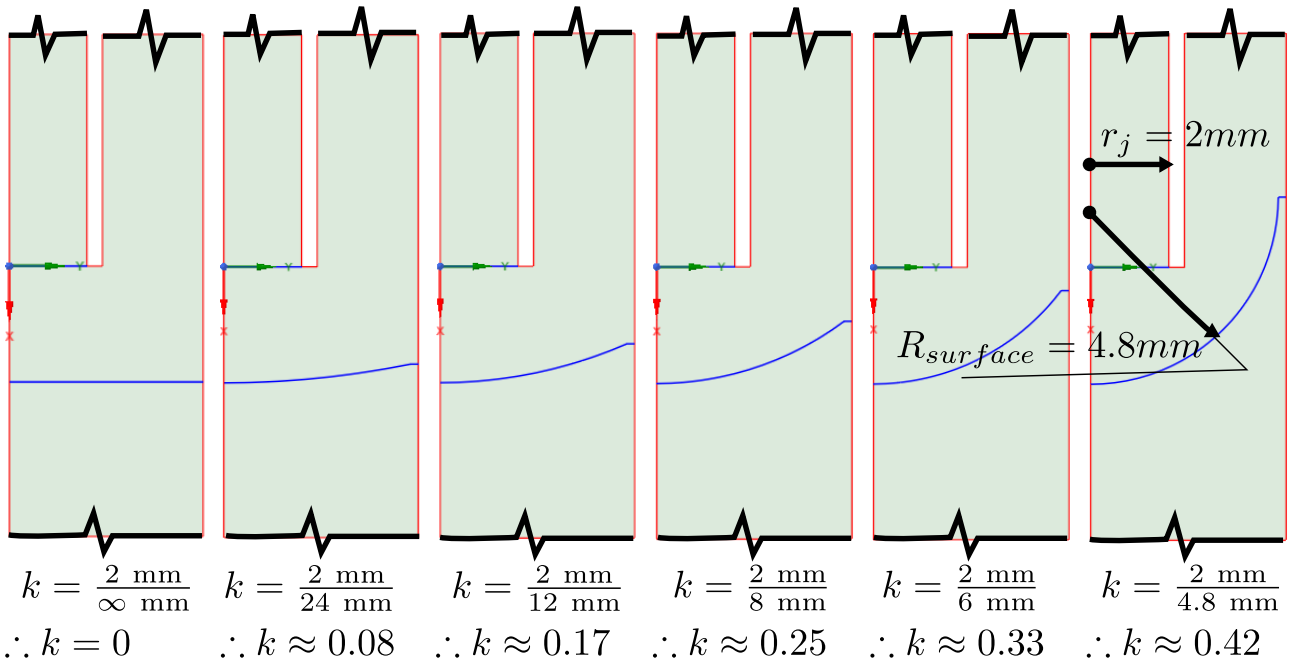

Figure 5.1: Surface curvature domains [$a = 1.5$ mm]

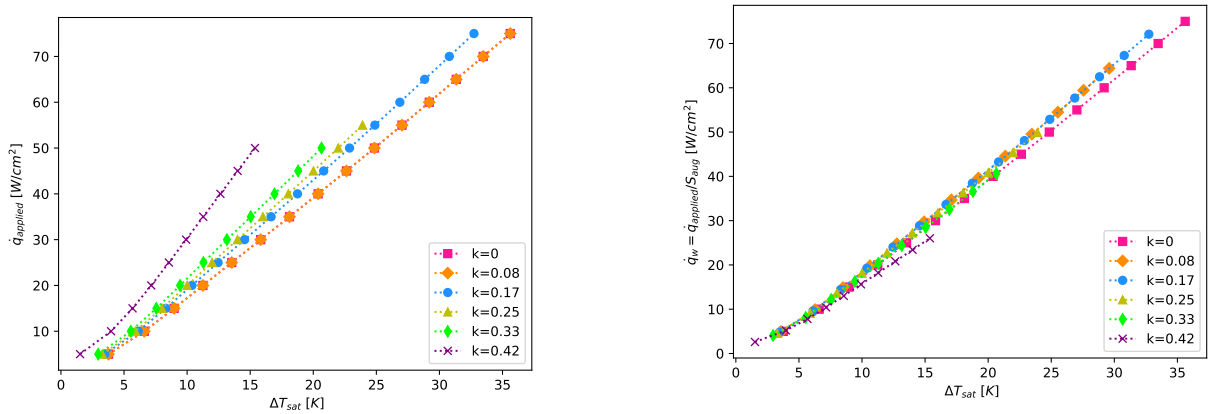

(a) $\dot{q}_{applied}$ *(b)* $\bar{\dot{q}}_w = \frac{\dot{q}_{applied}}{S_{aug}}$

Figure 5.2: Boiling curve based on $\dot{q}_{applied}$ and $\dot{q}_w$ for different surface curvatures [nitrogen ($P_{sat} = 140$ kPa), $a = 1.5$ mm, $v_j = 0.78$ m/s, $\Delta T_{sub} = 4$ K, mesh=M2, numerical framework=N2A]

The nucleate boiling curve based on the average wall heat flux is plotted in *fig. 5.2b*. This reveals that the nucleate boiling curves nearly collapse onto one another when accounting for the increase in surface area due to curvature. Thus the conclusion that can be drawn is that increased surface area plays a predominant role in improving the boiling heat transfer coefficient (when using $\dot{q}_{applied}$ to plot the boiling curve). This is in agreement with statements made by Inoue et al. 1995 [74], Aihara et al. 1993 [8] and Zhang et al. 2011 [205] in *section 2.4.6* who hypothesised that increased surface area is one of the major contributing factors for the enhancement in nucleate boiling seen with increased surface curvature.

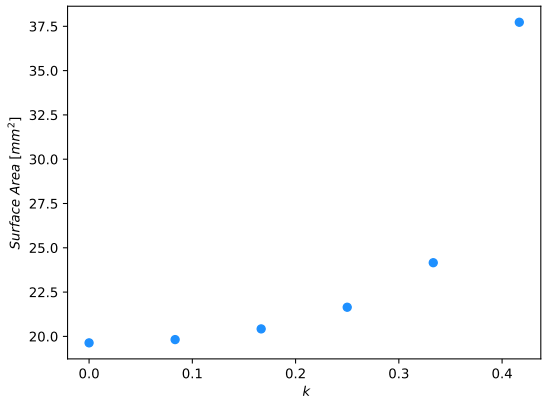

Figure 5.3: Impingement wall surface area as a function of curvature

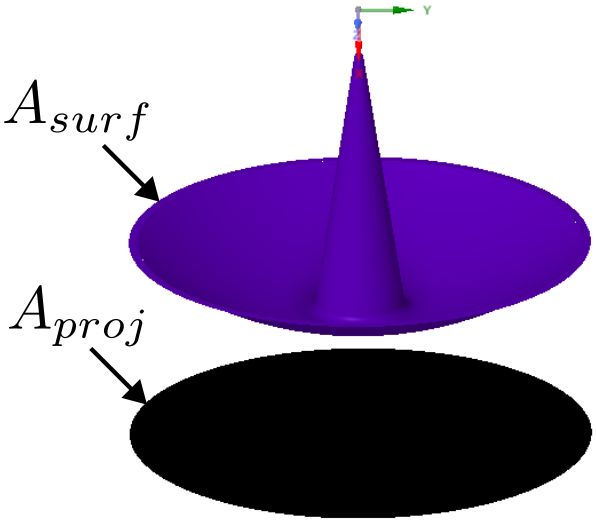

Figure 5.4: Areas used to calculate surface augmentation factor (S_{aug})

Figure 5.5 displays a selection of average impingement wall quantities as a function of applied heat flux ($\dot{q}_{applied}$) for differing surface curvatures. *Figure 5.5a* reveals that the convective heat flux component forms a larger portion of the total heat flux through the wall for larger surface curvatures. This observation can largely be explained by the fact that the surfaces with larger surface area have lower average wall heat fluxes and therefore progress up the boiling curve (plotted using $\bar{\dot{q}}_W$) at a slower rate. As the boiling curve is dominated by convective heat flux in the beginning, it stands to reason that a slower progression up the boiling curve (plotted using $\bar{\dot{q}}_W$) will result in delayed decay of the convective heat flux (when plotting $\bar{\dot{q}}_C/\bar{\dot{q}}_W$ vs $\dot{q}_{applied}$). This is confirmed by plotting $\bar{\dot{q}}_C/\bar{\dot{q}}_W$ vs $\bar{\dot{q}}_W$ in *fig. 5.6a* and noting that the curves nearly collapse onto one another when normalising by surface area. A similar argument based on the impact of the slower progression rate up the boiling curve as a result of increased surface curvature (and hence increased area) can be used to explain the majority of the trends found in the evaporative heat flux (*fig. 5.5b*) and quenching heat flux (*fig. 5.5c*) components. The obvious exception, however, is the flat surface ($k = 0$) which fails to neatly collapse onto the other curves for the evaporative heat flux component when normalising by surface area (*fig. 5.6b*). The reason for this can be found in *fig. 5.6h* which reveals that the NLBF temperature (used as the liquid temperature in the quenching equation [*eq.* (3.13)]) is significantly higher for the flat surface after normalising by surface area. This in turn results in a slightly lower quenching heat flux and thus higher evaporative heat flux. It is suspected that the reason for the increased NLBF temperature can be traced to the fact that the NLBF temperature has a smooth solution for the flat surface whilst there are discontinuities as soon as any features (such as curvature) are added to the surface. The exact nature of these discontinuities are unknown as mentioned in *section 4.18*. The increase in surface area with surface curvature is also responsible for a reduction in wall temperature that results in the collapse of the curves for bubble departure diameter (*fig. 5.5d*), nucleation site density (*fig. 5.5e*), bubble departure frequency (*fig. 5.5f*), and area of influence (*fig. 5.5g*) plotted using $\dot{q}_{applied}$ nearly onto one another when plotted using $\bar{\dot{q}}_W$ (see *fig. 5.6d*, *fig. 5.6e*, *fig. 5.6f* and *fig. 5.6g*).

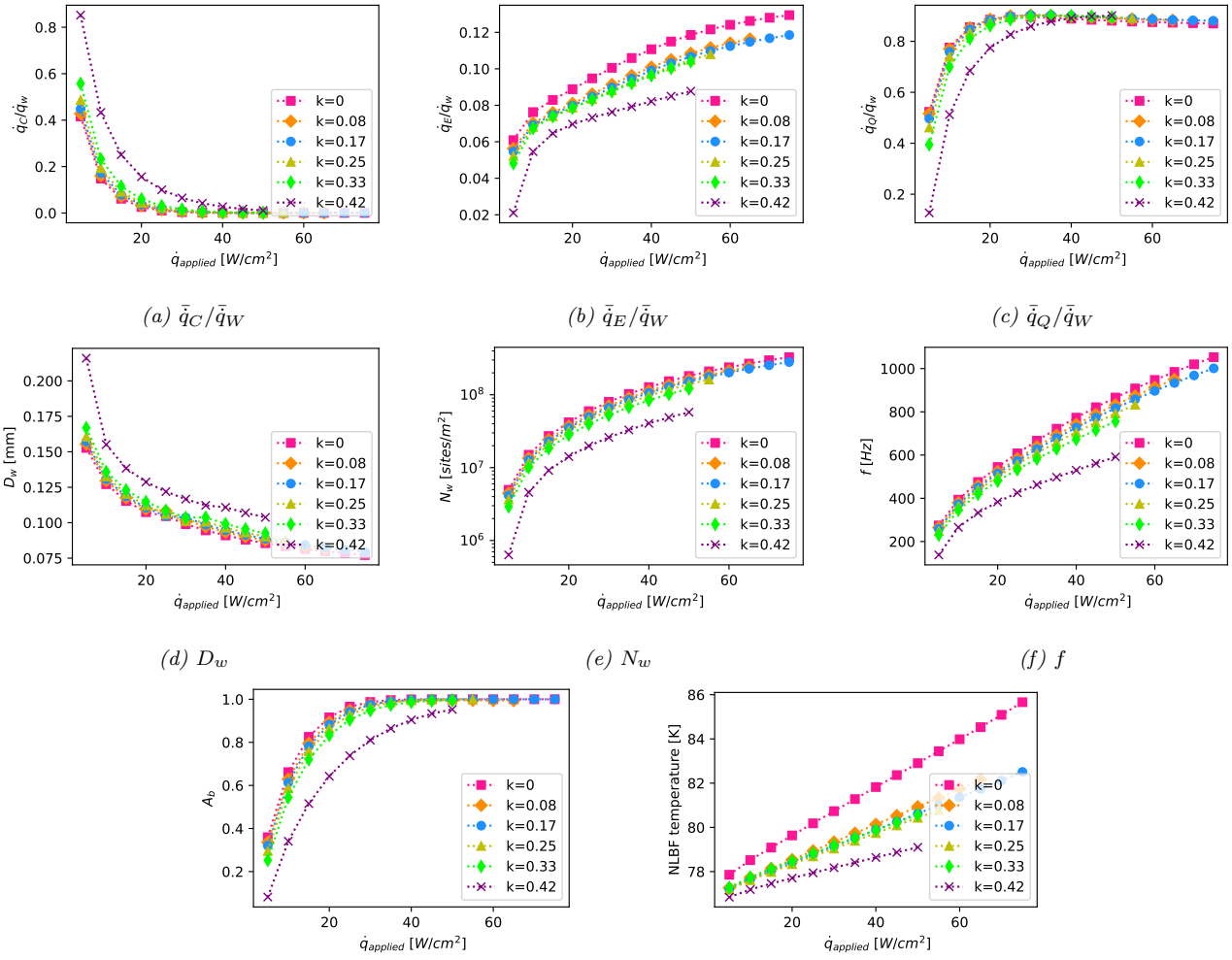

(a) $\bar{\dot{q}}_C/\bar{\dot{q}}_W$ *(b)* $\bar{\dot{q}}_E/\bar{\dot{q}}_W$ *(c)* $\bar{\dot{q}}_Q/\bar{\dot{q}}_W$

(d) D_w *(e)* N_w *(f)* f

(g) A_b *(h) NLBF temperature*

*Figure 5.5: Average wall quantities (**a-c**-convective, evaporative and quenching heat flux components, **d**-Bubble departure diameter, **e**-Nucleation site density, **f**-Bubble departure frequency, **g**-Non-dimensional area of influence, **h**-NLBF Temperature) as a function of applied heat flux for differing surface curvatures [nitrogen ($P_{sat} = 140$ kPa), $a = 1.5$ mm, $v_j = 0.78$ m/s, $\Delta T_{sub} = 4$ K, mesh=M2, numerical framework=N2A]*

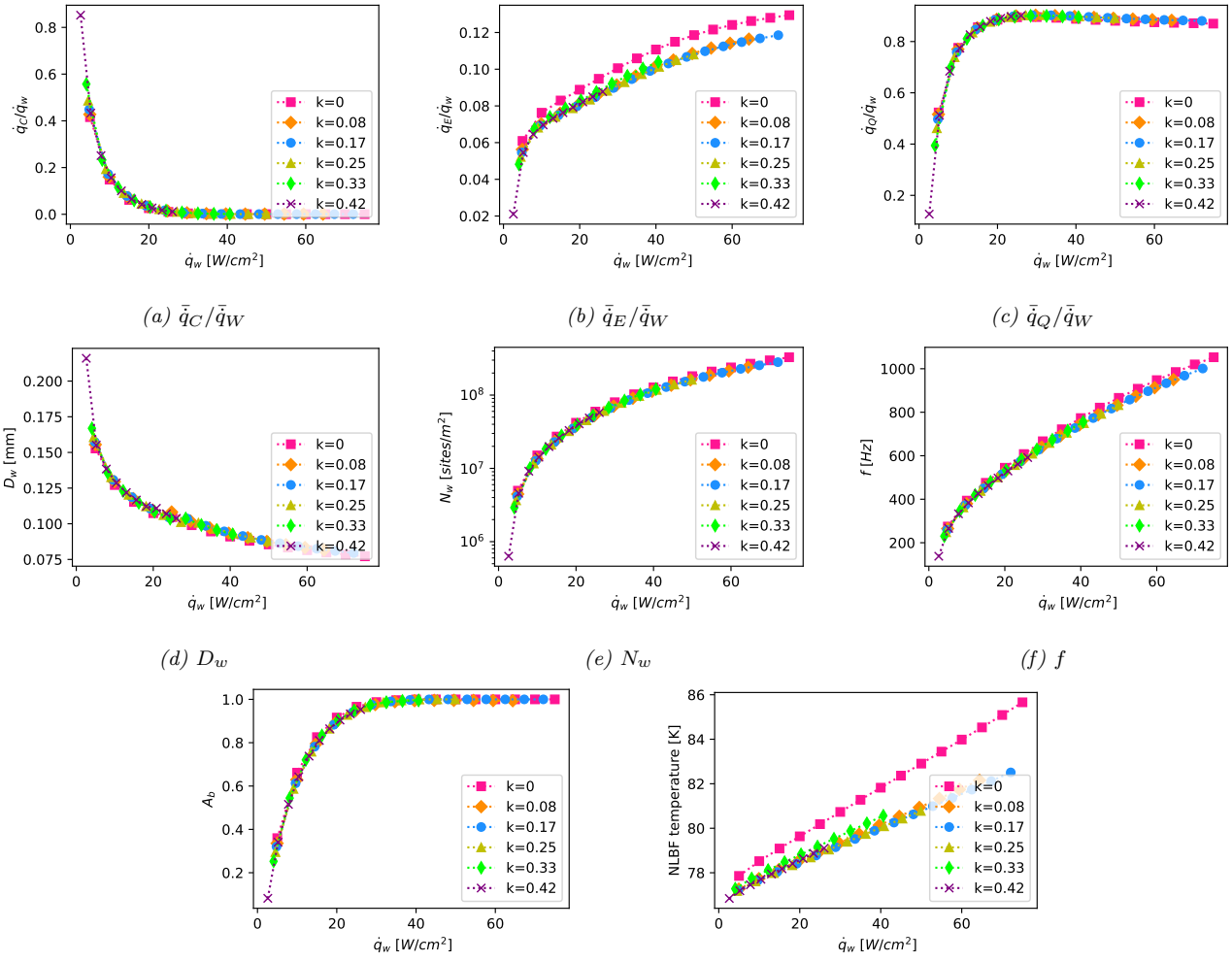

(a) $\bar{\dot{q}}_C/\bar{\dot{q}}_W$ *(b)* $\bar{\dot{q}}_E/\bar{\dot{q}}_W$ *(c)* $\bar{\dot{q}}_Q/\bar{\dot{q}}_W$

(d) D_w *(e)* N_w *(f)* f

(g) A_b *(h) NLBF temperature*

*Figure 5.6: Average wall quantities (**a-c**-convective, evaporative and quenching heat flux components, **d**-Bubble departure diameter, **e**-Nucleation site density, **f**-Bubble departure frequency, **g**-Non-dimensional area of influence, **h**-NLBF Temperature) as a function of average wall heat flux for differing surface curvatures [nitrogen ($P_{sat} = 140$ kPa), $a = 1.5$ mm, $v_j = 0.78$ m/s, $\Delta T_{sub} = 4$ K, mesh=M2, numerical framework=N2A]*

The contour plot of vapour volume fraction is shown for three curvatures at $\dot{q}_{applied} = 40$ W/cm^2 in *fig. 5.7*. The plot reveals an overall reduction in cumulative vapour fraction with increased surface curvature (due to the lower average wall heat flux). For all curvatures, there appears to be a tendency for vapour to be trapped at the outer edge of the jet exit tip. *Figure 5.8* displays the velocity magnitude contour with velocity vectors overlaid at $\dot{q}_{applied} = 40$ W/cm^2. It reveals that there is a small separation zone in this region with low velocity flow that is responsible for entrapment of vapour at the nozzle tip.

Figure 5.7 additionally reveals that the location of maximum vapour production transitions from near the outer edge of the domain (but not in the corner) (in *fig. 5.7a*) to boiling on the lip at the highest curvature (*fig. 5.7c*). This is reinforced by *fig. 5.11c* that displays a gradual shift of the vapour volume fraction peak to the right as the surface curvature is increased.

Figure 5.7 shows that the bulk portion of the the vapour produced accumulates in the large re-circulation zone produced by the turning flow. The centre of this re-circulation zone is marked in *fig. 5.8* with an 'x' and is seen to increase in height (relative to the stagnation point) as the surface curvature is increased.

There is a more gentle transition of the velocity from the impingement wall to the outer radially confining wall with increased curvature (*fig. 5.8*).

Figure 5.9 displays the liquid temperature contours. It is difficult to make direct comparison between the figures due to the difference in wall superheat between the surfaces at the displayed $\dot{q}_{applied} = 40$ W/cm^2. However, one can note that the stagnation point in the outer corner (or at the lip) has the largest fluid temperature due in part to the slow moving fluid in these regions and the fact that the thermal boundary layer has reached its maximum development as a result of fluid flow over the heated wall. *fig. 5.11a* confirms this observation of increased liquid temperature at the outer edge of the wall which results in reduced quenching in this region *fig. 5.11f*.

Figure 5.10 displays the solid temperature. Again, comparisons are made difficult by the difference in average wall superheat between the surfaces at the displayed $\dot{q}_{applied} = 40$ W/cm^2. However, one can conclusively state the temperature along the upper surface of the flat wall ($k = 0$) is approximately constant and as the curvature increases there is a larger disparity between the stagnation point temperature and the temperature at the outer edge of the domain. This is presumably a result of a combination of the thermal resistance of the solid and the outer edge of the domain having a larger surface area for heat to be transferred thorough and hence having a larger convective heat transfer (as seen in *fig. 5.11d*). This requires a lower wall superheat and therefore lower quenching (*fig. 5.11f*) and evaporative (*fig. 5.11e*) heat flux (and hence lower wall temperature) to maintain energy balance at the outer portion of the wall.

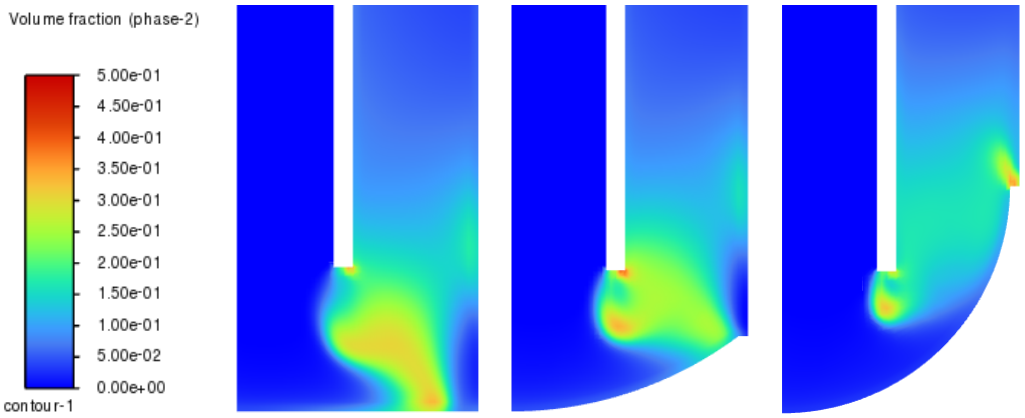

Figure 5.7: Truncated domain showing vapour fraction for different surface curvatures at $\dot{q}_{applied} = 40$ W/cm^2 [nitrogen ($P_{sat} = 140$ kPa), Numerical Framework=N2A, mesh=M2, $a = 1.5$ mm, $v_j = 0.78$ m/s, $\Delta T_{sub} = 4$ K]

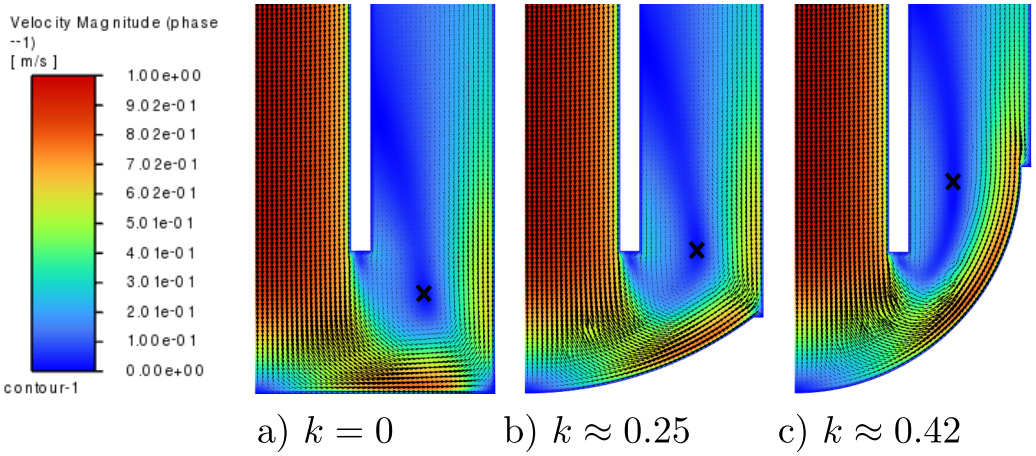

Figure 5.8: Truncated domain showing liquid velocity for different surface curvatures at $\dot{q}_{applied} = 40$ W/cm^2 (center of re-circulation zone marked with an 'x') [nitrogen ($P_{sat} = 140$ kPa), Numerical Framework=N2A, mesh=M2, $a = 1.5$ mm, $v_j = 0.78$ m/s, $\Delta T_{sub} = 4$ K]

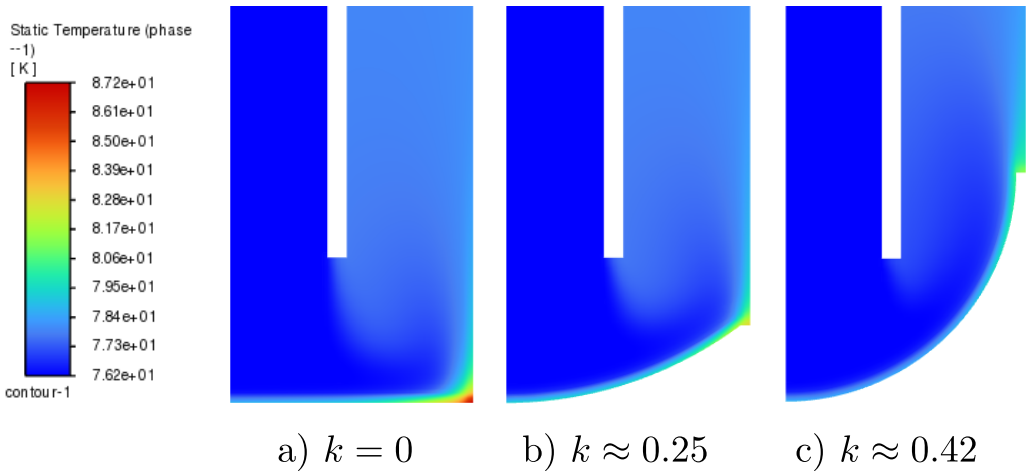

Figure 5.9: Truncated domain showing liquid temperature for different surface curvatures at $\dot{q}_{applied} = 40$ W/cm^2 [nitrogen ($P_{sat} = 140$ kPa), Numerical Framework=N2A, mesh=M2, $a = 1.5$ mm, $v_j = 0.78$ m/s, $\Delta T_{sub} = 4$ K]

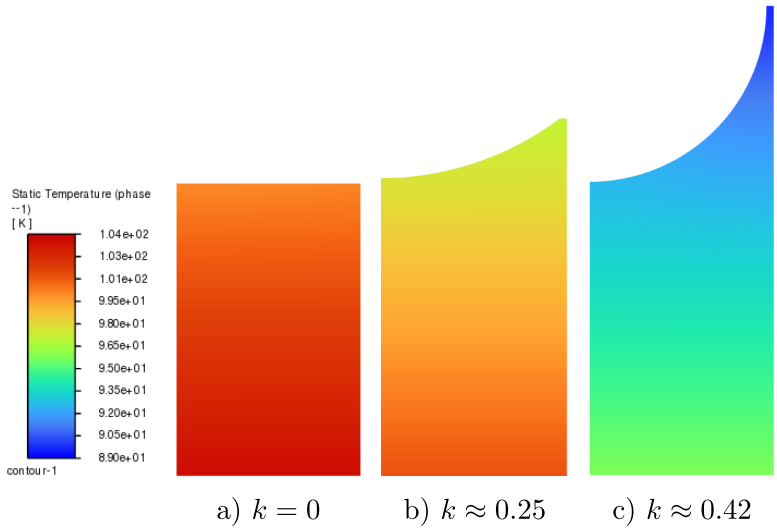

Figure 5.10: Truncated domain showing solid temperature for different surface curvatures at $\dot{q}_{applied} = 40$ W/cm^2 [nitrogen ($P_{sat} = 140$ kPa), Numerical Framework=N2A, mesh=M2, $a = 1.5$ mm, $v_j = 0.78$ m/s, $\Delta T_{sub} = 4$ K]

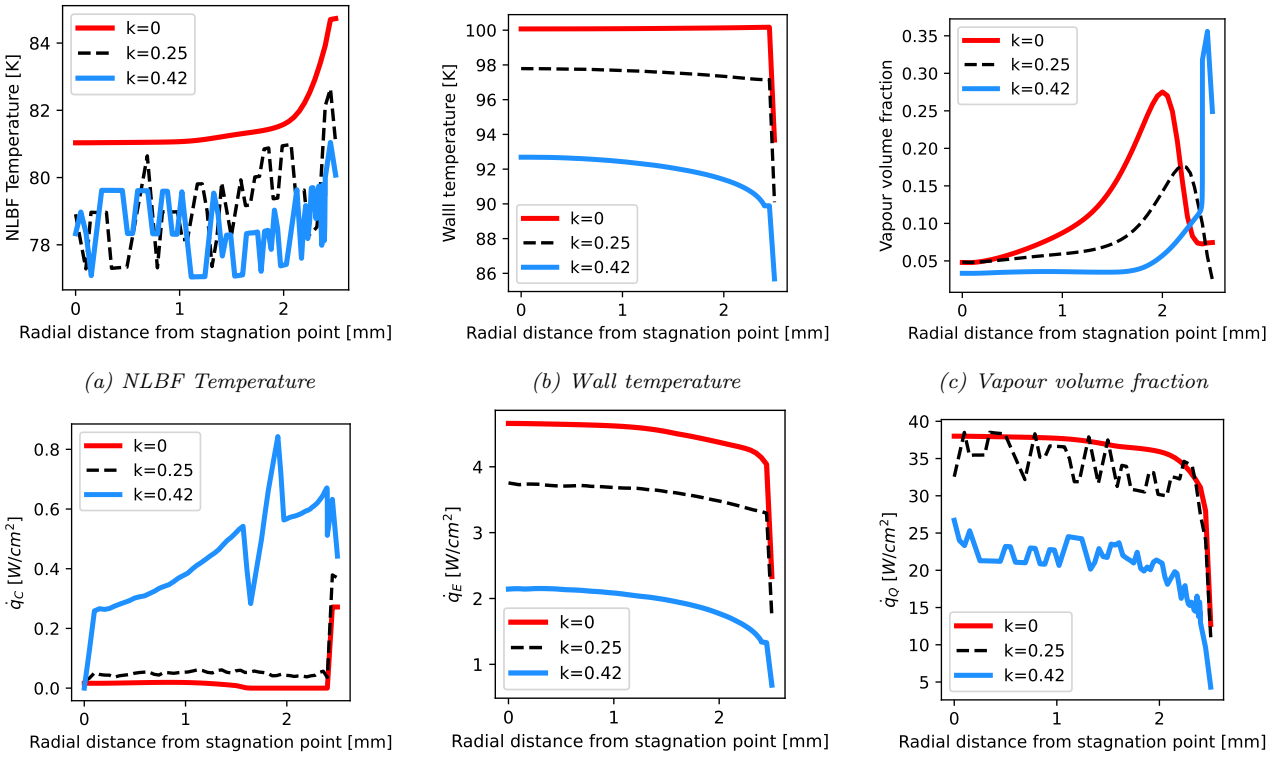

(a) NLBF Temperature *(b) Wall temperature* *(c) Vapour volume fraction*

(d) Convective heat flux ($\dot{q}_C$) *(e) Evaporative heat flux ($\dot{q}_E$)* *(f) Quenching heat flux ($\dot{q}_Q$)*

*Figure 5.11: Impingement wall quantities (**a**-NLBF Temperature, **b**-Wall temperature, **c**-Vapour volume fraction, **d-f**-convective, evaporative and quenching heat fluxes) for different curvatures at $\dot{q}_{applied} = 40$ W/cm^2 [nitrogen ($P_{sat} = 140$ kPa), Numerical Framework=N2A, mesh=M2, $a = 1.5$ mm, $v_j = 78$ m/s, $\Delta T_{sub} = 4$ K]*

Now that the effect of increased surface area as a result of increased surface curvature has been addressed, it is time to evaluate whether the increase in curvature had any other contributing effects. Care has been taken to state that the curves 'nearly' collapsed onto one another when accounting for surface area. There are indeed some minor variations in average wall quantities that will now be explored. *Figure 5.12* displays the impingement wall superheat as a function of curvature at $\bar{q}_W = 20$ W/cm^2 (obtained through linear interpolation of the CFD results presented in *fig. 5.2b*). There appears to be a local minimum at $k \approx 0.1$. However, one should be skeptical of including the value obtained at $k = 0$ in the analysis of the results as this is likely attributed to the smooth solution of the NLBF temperature (as previously stated). Nevertheless, there appears to be a clear trend of increasing wall superheat resulting from increasing curvature for $k > 0.1$. This would suggest that increasing curvature actually serves to degrade the heat transfer performance of the surface if the effect of increased surface area is negated. However, it should be noted that *fig. 5.12* has been plotted based on the extrapolated wall superheat and whilst this may be a fair measure when comparing the performance of the different curved and needled surfaces (based on the practical mounting application when attaching such surfaces to the top of heated flat surfaces such as microelectronic chip dies), it does obscure the actual wall properties that govern the heat flux distribution. The average wall surface heat flux has therefore been plotted in *fig. 5.13*. This reveals that the average wall superheat (based on the average wall surface temperature) experiences a marked reduction for the curved surfaces. Furthermore, it is not apparently obvious that increased surface curvature degrades the heat transfer characteristics of the surface in *fig. 5.13*.

Turning one's attention to *fig. 5.14*, plotted at $\bar{q}_W = 20$ W/cm^2 for a variety of average impingement wall quantities[1], one notes a clear peak in convective heat flux contribution at $k = 0.25$ (*fig. 5.14a*). This can be attributed to the fact that the non-dimensional area of influence is the lowest at $k = 0.25$ (*fig. 5.14g*) and therefore the convective component will be degraded the least by the $(1 - A_b)$ factor found in convective heat flux equation ($\dot{q_C} = h_C(T_w - T_l)(1 - A_b)$ *eq.* (3.2)). Another contributing factor is that the temperature difference between the wall and fluid $(T_w - T_l)$ has a local maximum near $k = 0.25$ (*fig. 5.14i*) thus further enhancing the convective component at this curvature value. One may note that $k = 0.42$ also has a low average non-dimensional area of influence (*fig. 5.14g* and a high wall-liquid temperature difference (*fig. 5.14i*) and yet has a notably reduced convective heat flux component compared to $k = 0.25$ (*fig. 5.14a*). This stems from the reduction in average bubble departure frequency (*fig. 5.14f*) with increased curvature that results in a larger quenching heat flux component at $k = 0.42$ (*fig. 5.14c*) thereby reducing the evaporative (*fig. 5.14b*) and convective components (*fig. 5.14a*). Whilst this discussion is intriguing, it is worth bearing in mind that the convective heat flux forms a small component of the total heat flux at $\bar{q}_W = 20$ W/cm^2 ($\bar{q}_C/\bar{q}_W \leq 0.035$)

The evaporative heat flux component is largest for $k = 0$ (*fig. 5.14b*) due to its elevated average nucleation site density (*fig. 5.14e*) and frequency (*fig. 5.14f*) as a result of the increased wall temperature (*fig. 5.13*). There is a spike in the evaporative heat flux component at $k = 0.33$ for similar reasons.

The quenching heat flux component (*fig. 5.14b*) appears to have a peak near $k = 0.08$ and a trough near $k = 0.33$. Ignoring the flat surface one can see that the quenching heat flux contribution appears to decrease with increasing curvature until there is a sharp spike at $k = 0.42$. This is possibly due to the reduction in bubble departure frequency (*fig. 5.14f*) and increased wall-liquid temperature difference (*fig. 5.14i*) and its impact on the quenching heat flux equation (*eq.* (3.13)) as mentioned previously.

From a general overview of *fig. 5.14* one can observe that the evaporative heat flux component, nucleation site density, bubble departure frequency, non-dimensional area of influence and NLBF temperature all appear to follow a similar trend to the average surface wall superheat. It should be stated that the accuracy of these results are thrown into question based on the discontinuous NLBF temperature found on curved surfaces. A shortfall of the current model is that the saturation temperature has been selected as a constant at the specified saturation pressure. Therefore one of the mechanisms hypothesised by Inoue et al. 1995 [74] to improve boiling on curved surfaces (due to increases in local subcooling as a result of increased pressure along the wall with increased curvature *section 2.4.6*) has been negated. It is left for future work to determine the influence of variable saturation temperature (as a function of local pressure) for jet impingement onto different curvatures when using the RPI wall boiling model.

[1]Note that the reported values of N_w, D_w, f and A_b in *fig. 5.14* have been obtained from the CFD simulations. They are individually computed within each wall fluid cell based on the local fluid properties and wall temperature before averaging along the wall and plotting in *fig. 5.14*.

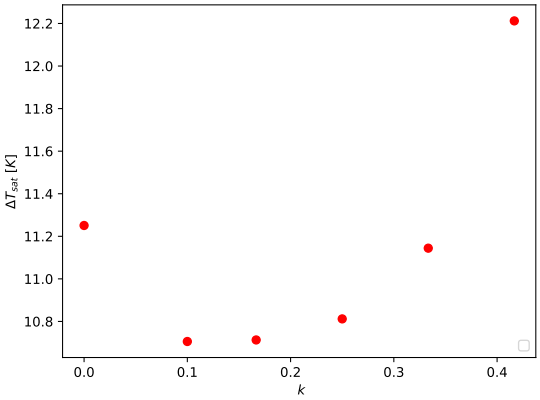

Figure 5.12: Impingement wall superheat as a function of curvature at $\bar{q}_W = 20$ W/cm^2 (based on the average extrapolated wall temperature)

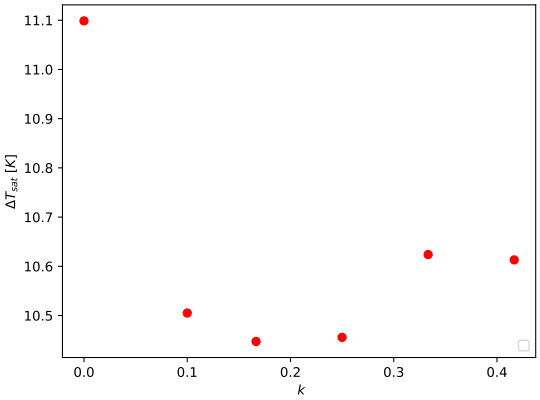

Figure 5.13: Impingement wall superheat as a function of curvature at $\bar{q}_W = 20$ W/cm^2 (based on the average wall surface temperature)

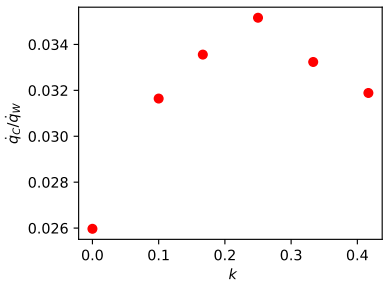

(a) $\bar{q}_C/\bar{q}_W$

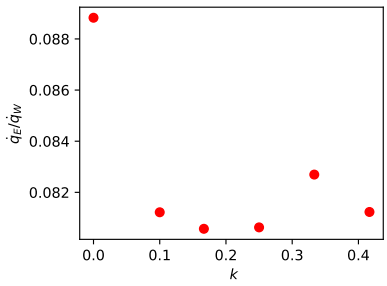

(b) $\bar{q}_E/\bar{q}_W$

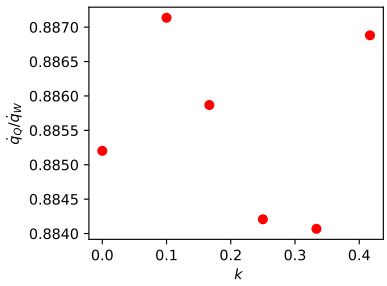

(c) $\bar{q}_Q/\bar{q}_W$

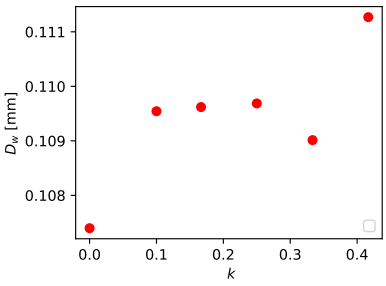

(d) D_w

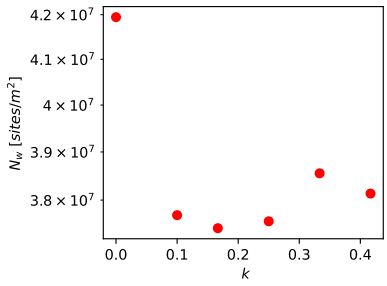

(e) N_w

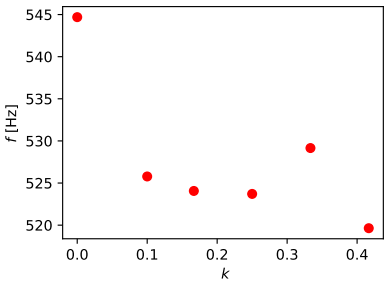

(f) f

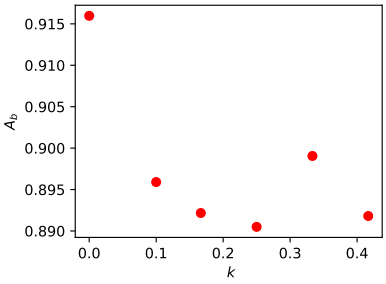

(g) A_b

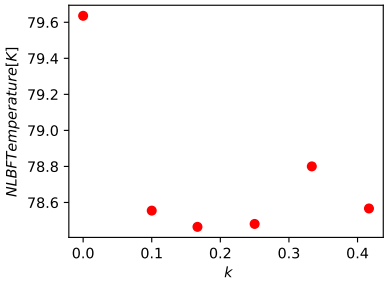

(h) NLBF temperature

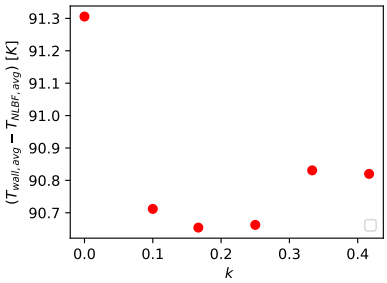

(i) Wall-liquid temperature difference ($T_w - T_l$)

*Figure 5.14: Average impingement wall quantities (**a-c**-convective, evaporative and quenching heat fluxes components, **d**-Bubble departure diameter, **e**-Nucleation site density, **f**-Bubble departure frequency, **g**-Non-dimensional area of influence, **h**-NLBF Temperature, **i**-Wall-liquid temperature difference) as a function of curvature at $\bar{q}_W = 20$ W/cm^2 [nitrogen ($P_{sat} = 140$ kPa), $a = 1.5$ mm, $v_j = 0.78$ m/s, $\Delta T_{sub} = 4$ K, mesh=M2, numerical framework=N2A]*

5.3 Needle Height

This section aims to explore the effects of needle height (varied between $h_{needle} = 0 - 5$ mm) on the boiling curve. The domains used are shown in *fig. 5.15*. Like *section 5.2* the introduction of the needle creates additional surface area (*fig. 5.16*) that results in a reduction of the average surface heat flux. Thus two wall superheat plots are shown in *fig. 5.17*, one that uses the applied heat flux *fig. 5.17a* and one that uses average wall heat flux *fig. 5.17b* (computed using the surface augmentation factor in order to normalise the results with respect to surface area). *Figure 5.17a* illustrates a clear trend of increased boiling heat transfer coefficient (increased gradient) as well as reduced wall superheat (shift to the left) with increased needle height. However, this is largely due to increased surface area as the results are reversed in *fig. 5.17b* when accounting for the increased surface area.

A selection of average wall quantities are plotted using $\dot{q}_{applied}$ in figure *fig. 5.18*. Similar to *section 5.2* the surface with the largest surface area (and therefore largest needle height) proceeds up the boiling curve at a slower rate due to the reduction in average wall heat flux with increased area. Therefore the largest needle has higher convective (*fig. 5.18a*) and reduced evaporative (*fig. 5.18b*) and quenching (*fig. 5.18c*) heat flux components as is typical in the lower portion of the boiling curve. Additionally, the reduced average wall superheat for the larger needle (*fig. 5.17a*) results in larger bubble departure diameters (*fig. 5.18d*), and reduced nucleation site density (*fig. 5.18e*), frequency (*fig. 5.18f*) and non-dimensional area of influence (*fig. 5.18g*). The heat flux partitioning appears to be quenching dominated (similar to the results presented in *section 5.2*). It can be noted that the average outlet liquid temperature (*fig. 5.18i*) is identical for all surfaces as the same quantity of heat ($\dot{q}_{applied}$) is being input into the base of all of the solids. The average outlet volume fraction (*fig. 5.18i*) reduces slightly as the needle height is increased due to the reduction in the evaporative heat flux (*fig. 5.18b*).

When plotting the average wall quantities using $\bar{\dot{q}}_W$ one obtains the results shown in *fig. 5.19*. The average outlet liquid temperature and outlet volume fraction are seen to reduce as the needle height is increased in *fig. 5.19h* and *fig. 5.19i* respectively. This is a result of the applied heat flux being reduced with increased surface area when plotting using the average wall heat flux. The discrepancy between the other variables in *fig. 5.19* is minor and can possibly be attributed to the fact that the extrapolated wall superheat has been used in place of the average wall superheat.

The wall temperature appears to drop off markedly towards the tip of the needle as shown in *fig. 5.23*. This is a result of the diminishing overall heat flux (*fig. 5.24 d-f*) as one approaches the tip. This may result in large thermal stresses that may induce crack growth under repeated operation cycles.

The reduced wall temperature (*fig. 5.23*), increased surface area (*fig. 5.16*) and decreased liquid temperature on the needle (*fig. 5.22* and *fig. 5.24a*) with increased needle height results in increased convective heat flux (*fig. 5.24d*) and diminished evaporative (*fig. 5.24e*) and quenching (*fig. 5.24f*) heat fluxes along the needle.

Unlike *section 5.2*, the discontinuities in the NLBF Temperature (*fig. 5.24a*) have less of an impact on the results as the discontinuities are restricted to the needle surface which forms a small portion of the total heat transfer from the wall due to the diminishing total heat flux near the tip.

The peak in vapour volume fraction appears to remain in the same location near the outer corner of the wall regardless of needle height (*fig. 5.20* and *fig. 5.24c*).

The introduction of the needle removes the stagnation point along the jet axis and introduces a new stagnation point at the base of the needle (*fig. 5.21*). This new stagnation point appears to behave in a similar manner to the stagnation point at the outer edge of the domain, with a local liquid hotspot created in both corners (seen in *fig. 5.22* and the peak in NLBF temperature in *fig. 5.24a* at ≈ 0.6 mm from the stagnation point).

When analysing the vapour volume fraction contour plot (*fig. 5.20*) at $\dot{q}_{applied} = 40$ W/cm^2, one can observe that the quantity of vapour within the domain reduces slightly as the needle height increases. This is a direct result of the reduction in evaporative heat flux with increasing needle height (*fig. 5.18b* and *fig. 5.24e*). An additional observation is that small quantities of vapour are produced along the length of the needle that then depart from the surface before the stagnation point at the base of the needle and join the bulk of the vapour in the re-circulation zone. The location of the re-circulation zone appears to remain largely unaffected by the introduction of the needle (*fig. 5.21*).

The impingement wall superheat as a function of needle height is plotted in *fig. 5.25* in order to isolate any additional effects of needle height independent of surface area effects. The plot indicated that increased needle height serves to degrade the heat transfer performance and increase the wall superheat when normalising by surface area. However, like in *section 5.2*, such a statement whilst not incorrect, is somewhat misleading due to the fact that the extrapolated wall temperature is being used to compute the superheat in *fig. 5.25*. If one were to use the average impingement wall temperature, one obtains the plot shown in *fig. 5.26*. This indicates

that large needle height may actually result in improvements in the local wall heat transfer. The conclusion is slightly clouded by the low wall superheat at $h_{needle} = 2$ mm shown in *fig. 5.26*. This low wall superheat is a direct result of the increased average quenching heat flux contribution at $h_{needle} = 2$ mm (*fig. 5.27c*) The cause of this is thought to be attributed to a slightly lower NLBF temperature, however, the evidence supporting this is weak.

It is worth bearing in mind that the method of computing the wall superheat can have a large influence on the interpretation of the results.

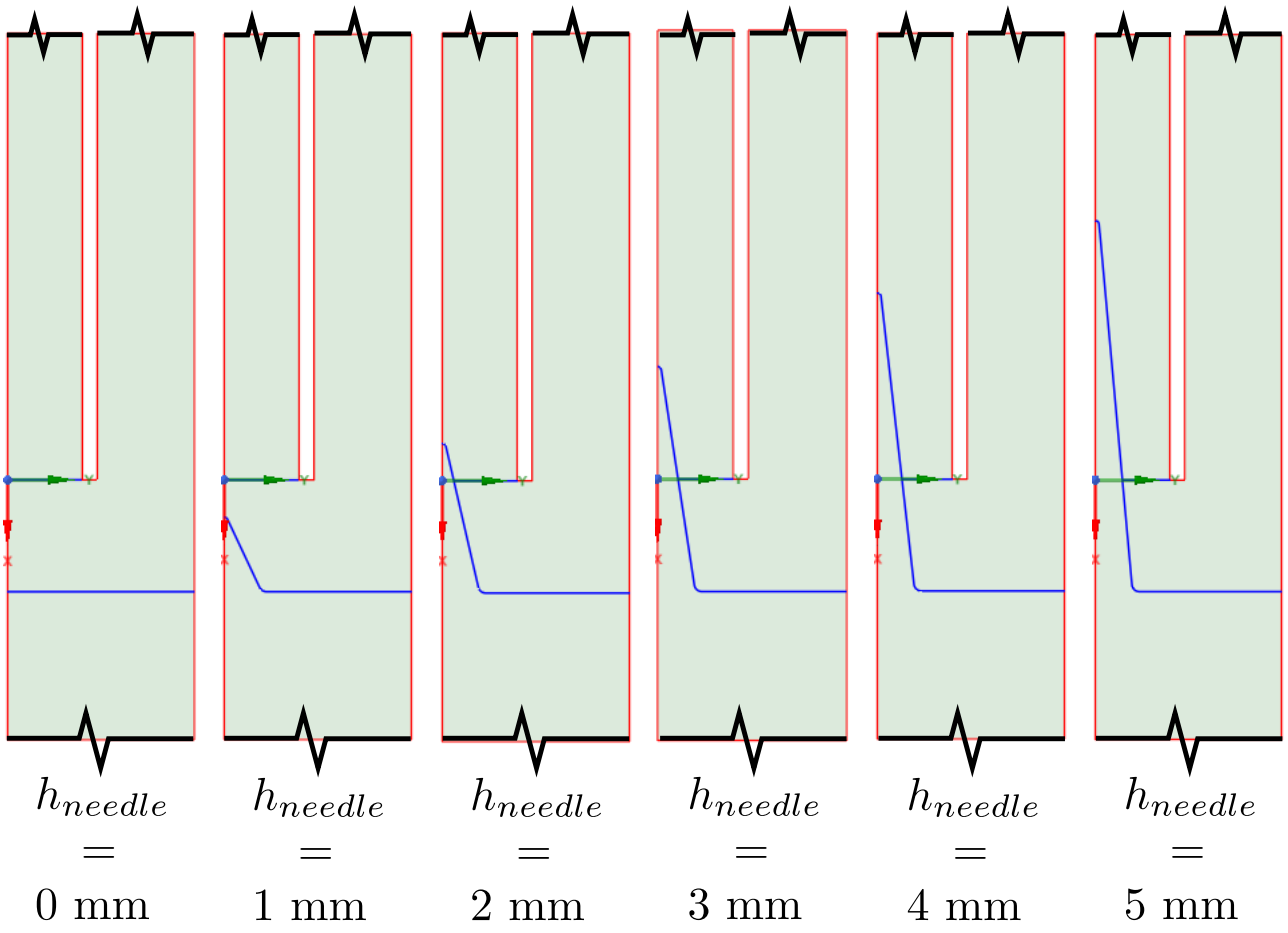

Figure 5.15: Singular needle domains with varying needle height [$a = 1.5$ mm]

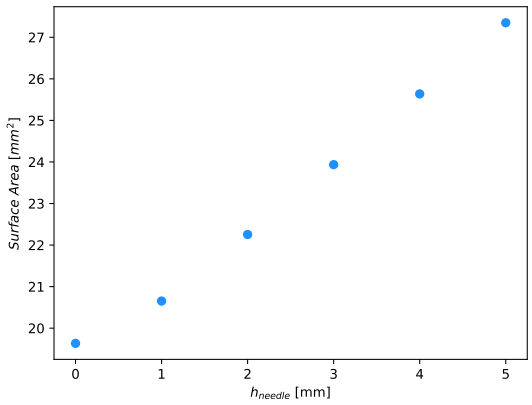

Figure 5.16: Impingement wall surface area as a function of needle height

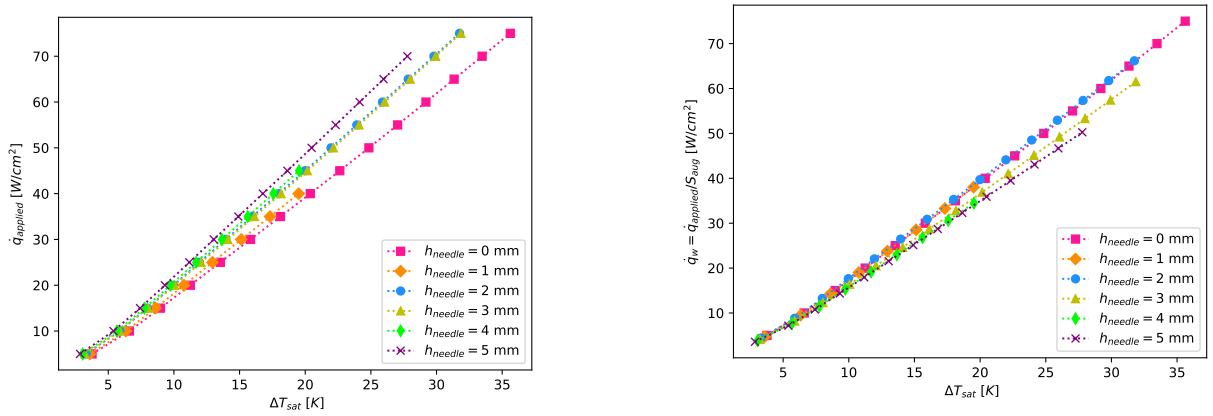

(a) $\dot{q}_{applied}$ *(b)* $\bar{\dot{q}}_w = \frac{\dot{q}_{applied}}{S_{aug}}$

Figure 5.17: Boiling curve based on $\dot{q}_{applied}$ *and* $\dot{q}_w$ *for different needle heights [nitrogen (*$P_{sat} = 140$ kPa*),* $a = 1.5$ *mm,* $v_j = 0.78$ m/s, $\Delta T_{sub} = 4$ K, *mesh=M2, numerical framework=N2A]*

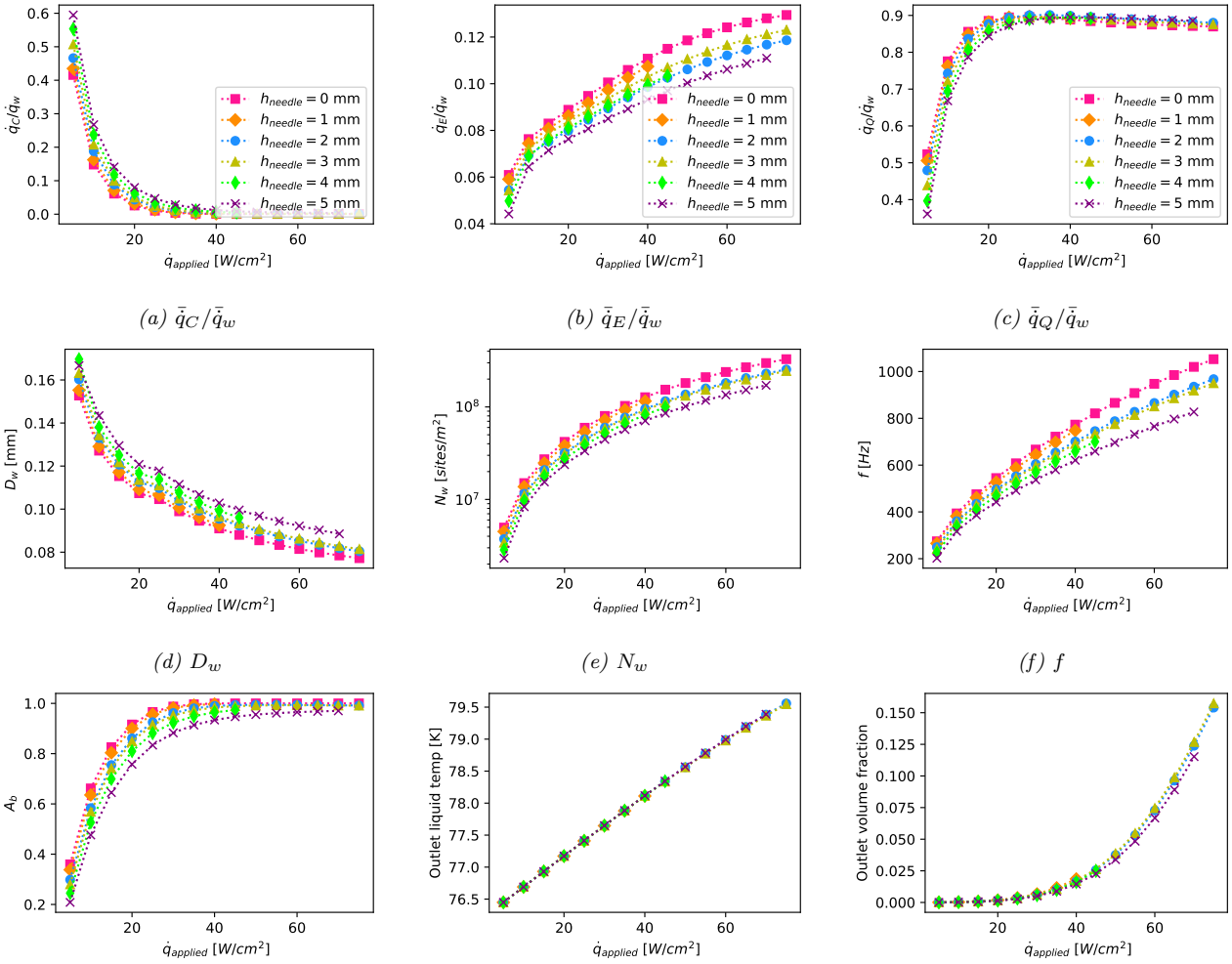

(a) $\bar{\dot{q}}_C/\bar{\dot{q}}_w$ *(b)* $\bar{\dot{q}}_E/\bar{\dot{q}}_w$ *(c)* $\bar{\dot{q}}_Q/\bar{\dot{q}}_w$

(d) D_w *(e)* N_w *(f)* f

(g) A_b *(h) Outlet liquid temperature (i) Outlet vapour volume fraction*

*Figure 5.18: Average wall quantities (**a-c**-convective, evaporative and quenching heat flux components, **d**-Bubble departure diameter, **e**-Nucleation site density, **f**-Bubble departure frequency, **g**-Non-dimensional area of influence, **h**-NLBF Temperature) as a function of applied heat flux for differing needle heights [nitrogen (*$P_{sat} = 140$ kPa*),* $a = 1.5$ *mm,* $v_j = 0.78$ m/s, $\Delta T_{sub} = 4$ K, *mesh=M2, numerical framework=N2A]*

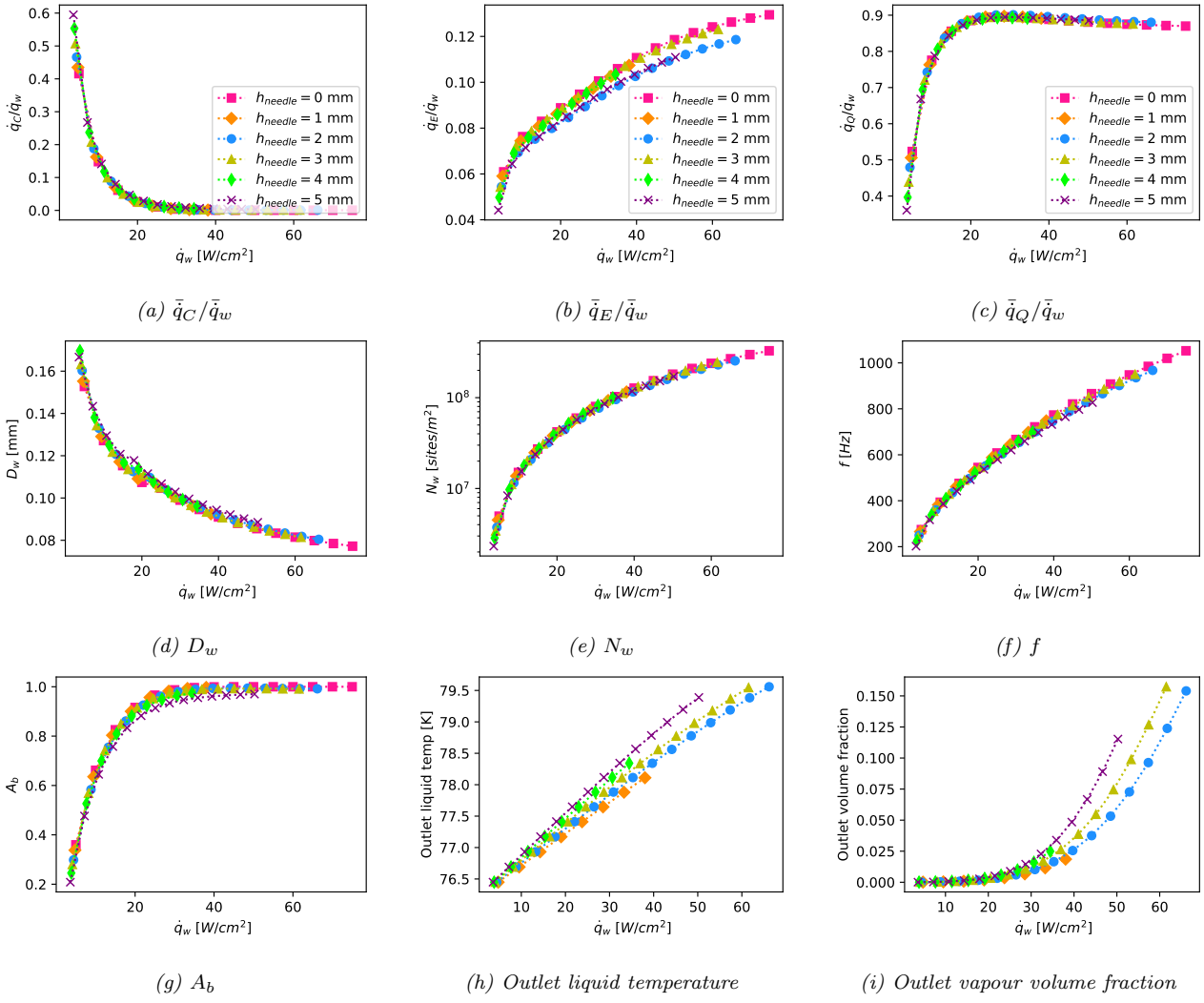

(a) $\bar{q}_C/\bar{q}_w$ *(b)* $\bar{q}_E/\bar{q}_w$ *(c)* $\bar{q}_Q/\bar{q}_w$

(d) D_w *(e)* N_w *(f)* f

(g) A_b *(h) Outlet liquid temperature* *(i) Outlet vapour volume fraction*

*Figure 5.19: Average wall quantities (**a-c**-convective, evaporative and quenching heat flux components, **d**-Bubble departure diameter, **e**-Nucleation site density, **f**-Bubble departure frequency, **g**-Non-dimensional area of influence, **h**-NLBF Temperature) as a function of average wall heat flux for differing needle heights [nitrogen (P_{sat} = 140 kPa), a = 1.5 mm, v_j = 0.78 m/s, ΔT_{sub} = 4 K, mesh=M2, numerical framework=N2A]*

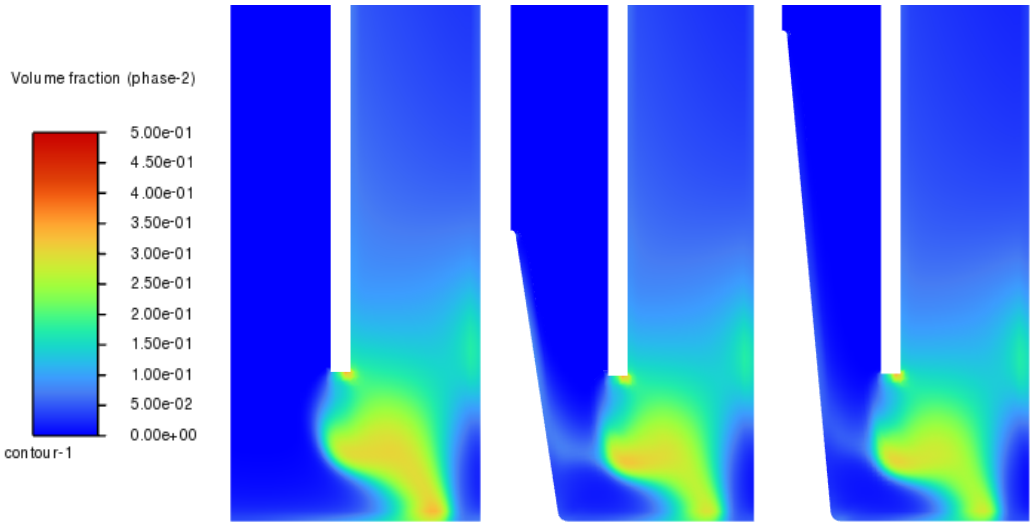

a) h_{needle} = 0 mm b) h_{needle} = 3 mm c) h_{needle} = 5 mm

Figure 5.20: Truncated domain showing vapour fraction for different needle heights at $\dot{q}_{applied}$ = 40 W/cm^2 [nitrogen (P_{sat} = 140 kPa), Numerical Framework=N2A, mesh=M2, a = 1.5 mm, v_j = 0.78 m/s, ΔT_{sub} = 4 K]

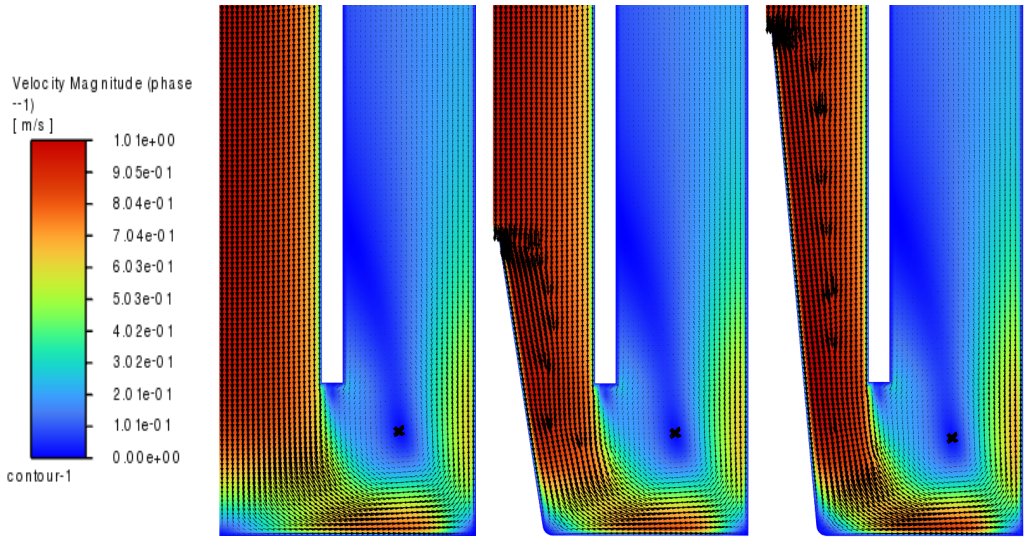

a) $h_{needle} = 0$ mm b) $h_{needle} = 3$ mm c) $h_{needle} = 5$ mm

Figure 5.21: Truncated domain showing liquid velocity for different needle heights at $\dot{q}_{applied} = 40$ W/cm^2 (center of re-circulation zone marked with an 'x') [nitrogen ($P_{sat} = 140$ kPa), Numerical Framework=N2A, mesh=M2, $a = 1.5$ mm, $v_j = 0.78$ m/s, $\Delta T_{sub} = 4$ K]

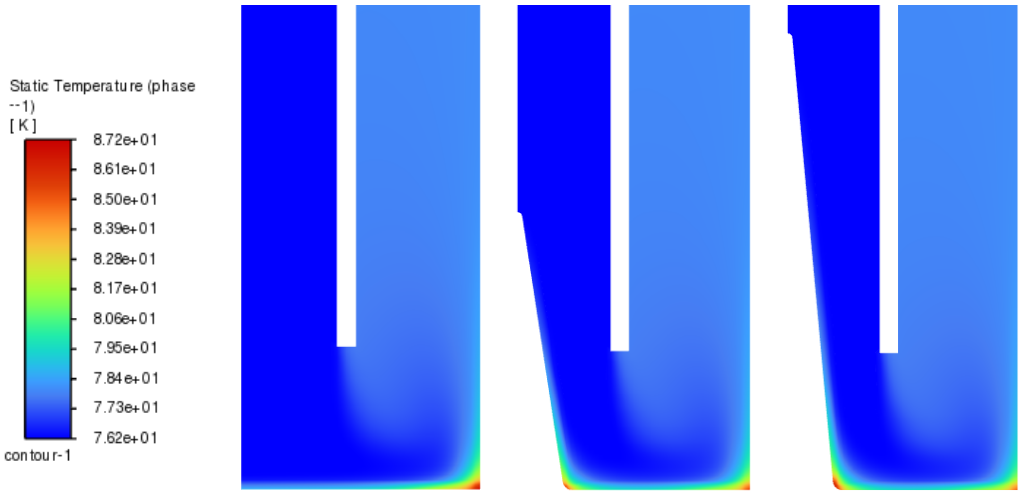

a) $h_{needle} = 0$ mm b) $h_{needle} = 3$ mm c) $h_{needle} = 5$ mm

Figure 5.22: Truncated domain showing liquid temperature for different needle heights at $\dot{q}_{applied} = 40$ W/cm^2 [nitrogen ($P_{sat} = 140$ kPa), Numerical Framework=N2A, mesh=M2, $a = 1.5$ mm, $v_j = 0.78$ m/s, $\Delta T_{sub} = 4$ K]

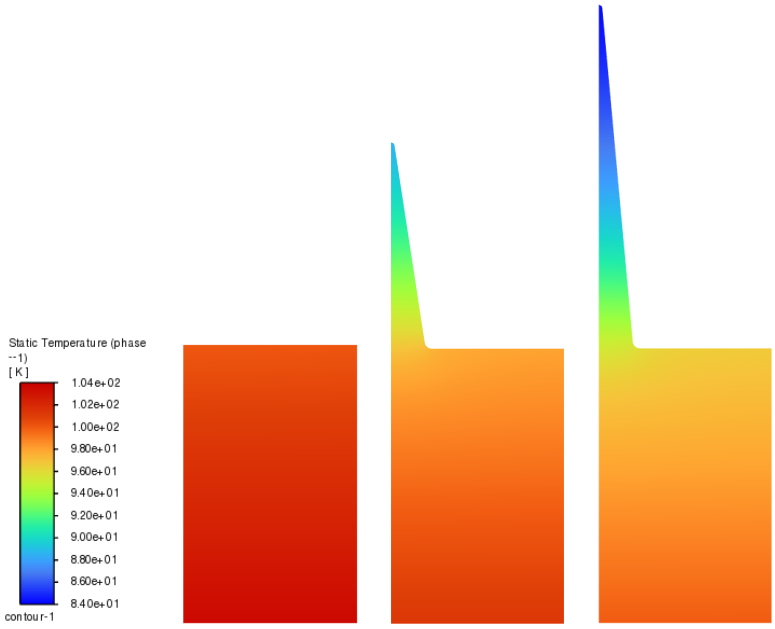

a) $h_{needle} = 0$ mm b) $h_{needle} = 3$ mm c) $h_{needle} = 5$ mm

Figure 5.23: Truncated domain showing solid temperature for different needle heights at $\dot{q}_{applied} = 40$ W/cm^2 [nitrogen ($P_{sat} = 140$ kPa), Numerical Framework=N2A, mesh=M2, $a = 1.5$ mm, $v_j = 0.78$ m/s, $\Delta T_{sub} = 4$ K]

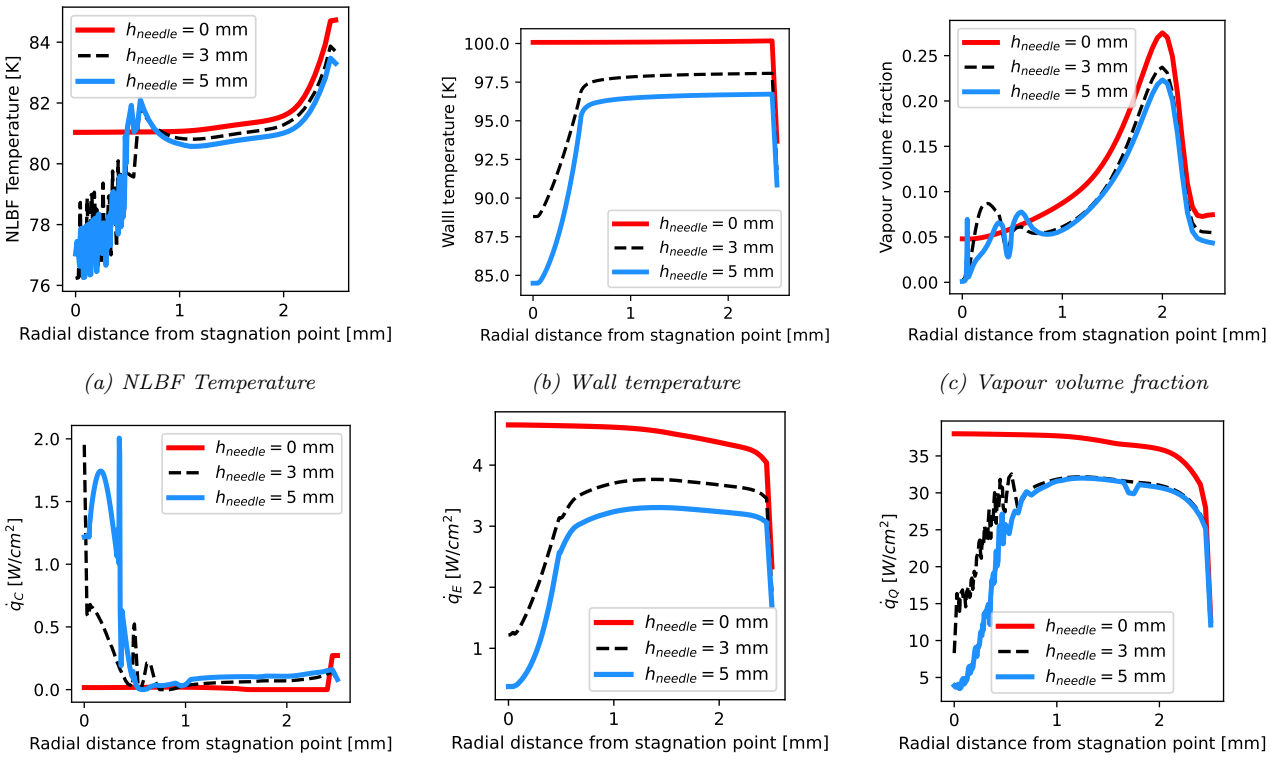

(a) NLBF Temperature *(b) Wall temperature* *(c) Vapour volume fraction*

(d) Convective heat flux ($\dot{q}_C$) *(e) Evaporative heat flux ($\dot{q}_E$)* *(f) Quenching heat flux ($\dot{q}_Q$)*

*Figure 5.24: Impingement wall quantities (**a**-NLBF Temperature, **b**-Wall temperature, **c**-Vapour volume fraction, **d-f**-convective, evaporative and quenching heat fluxes) for different needle heights at $\dot{q}_{applied} = 40$ W/cm^2 [nitrogen ($P_{sat} = 140$ kPa), Numerical Framework=N2A, mesh=M2, $a = 1.5$ mm, $v_j = 78$ m/s, $\Delta T_{sub} = 4$ K]*

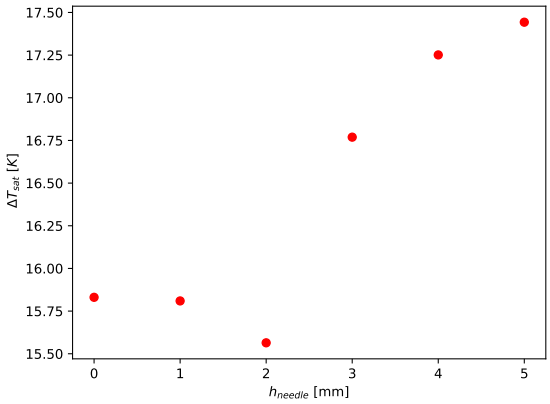

Figure 5.25: Impingement wall superheat as a function of needle height at $\bar{q}_W = 30$ W/cm^2 (based on the average extrapolated wall temperature)

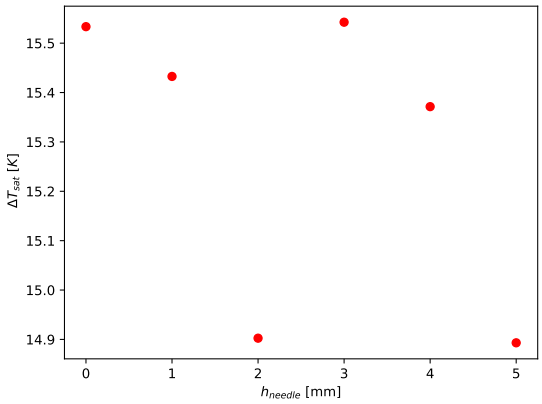

Figure 5.26: Impingement wall superheat as a function of needle height at $\bar{q}_W = 30$ W/cm^2 (based on the average wall surface temperature)

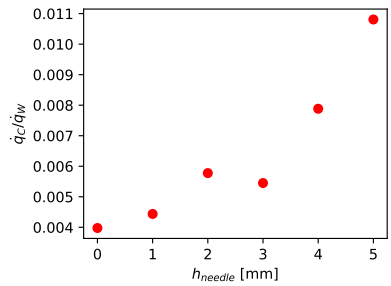

(a) $\bar{q}_C/\bar{q}_w$

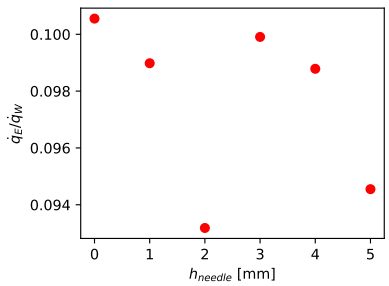

(b) $\bar{q}_E/\bar{q}_w$

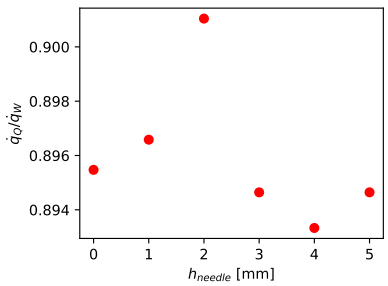

(c) $\bar{q}_Q/\bar{q}_w$

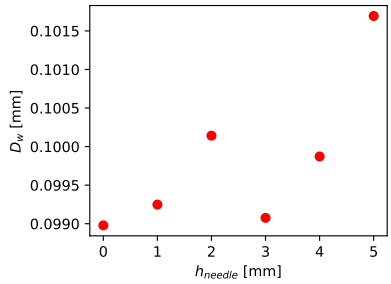

(d) D_w

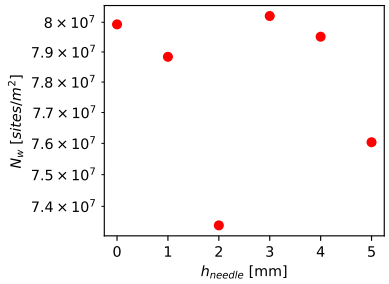

(e) N_w

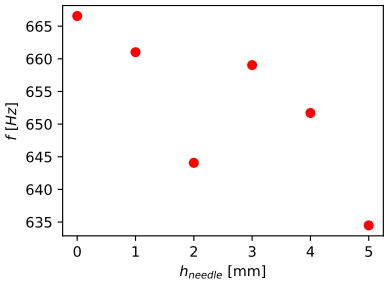

(f) f

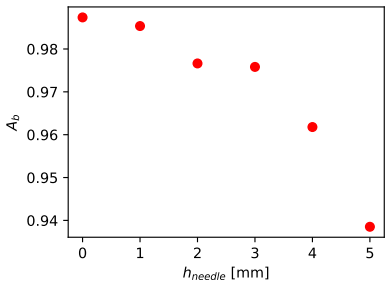

(g) A_b

*Figure 5.27: Average impingement wall quantities (**a-c**-convective, evaporative and quenching heat fluxes components, **d**-Bubble departure diameter, **e**-Nucleation site density, **f**-Bubble departure frequency, **g**-Non-dimensional area of influence, **h**-NLBF Temperature) as a function of needle height at $\bar{q}_W = 20$ W/cm^2 [nitrogen ($P_{sat} = 140$ kPa), $a = 1.5$ mm, $v_j = 0.78$ m/s, $\Delta T_{sub} = 4$ K, mesh=M2, numerical framework=N2A]*

5.4 Jet Impingement Height

The jet impingement height is varied between $a = 0.5$ mm and $a = 5.5$ mm as shown in *fig. 5.28*. The boiling curve based on $\dot{q}_{applied}$ (which is equivalent to $\bar{\dot{q}}_W$ for these flat impingement surfaces) is shown in *fig. 5.29*. The boiling curve reveals that there is a gradual increase in boiling heat transfer coefficient with decreased impingement height between $a = 5.5 - 1.5$ mm. However, there appears to be a large increase in BHTC at $a = 0.5$ mm. This is likely due to the increased velocity magnitude parallel to the impingement surface (as shown in *fig. 5.31*) that results from the confining effects of the jet nozzle. This results in increased convective heat transfer along the wall (see *fig. 5.34d*). Furthermore, the increased velocity results in a reduction in the NLBF temperature (*fig. 5.34a*) and therefore increased quenching (particularly near the outer corner as shown in *fig. 5.34f*) and lower wall superheat. This combination of increased convective and quenching heat flux components results in a lower evaporative heat flux component (*fig. 5.34e*). However, it is interesting to note that the peak in the volume fraction along the wall (see *fig. 5.34c*) increases and shifts to the right with decreasing impingement height.

Another notable observation from *fig. 5.29* is that whilst the boiling heat transfer coefficient (slope) appears to continually increase as the jet impingement height is lowered, there is also a notable shift of the boiling curve to the left with increased impingement height (except at $a = 0.5$mm where there is a large shift to the left due to the low NLBF temperature and therefore large convective and quenching heat fluxes). This shift of the boiling curve to the left with increased impingement height is possibly attributed to the increase in fluid-wall contact area as the vapour concentration at the wall diminishes (see *fig. 5.30* and *fig. 5.34c*). In general, vapour is more dispersed throughout the domain as the impingement height is increased as a result of increased mixing with the fluid jet.

The centre of the re-circulation zone is slightly lower for $a = 0.5$ mm (see *fig. 5.31*). There is minimal variation in the position of the centre of the re-circulation zone as the impingement height in increased from $a = 3.5$ mm to $a = 5.5$ mm.

The temperature profile is nearly constant at the impingement wall regardless of the impingement height (see *fig. 5.34b*) with the temperature varying linearly as towards the lower surface of the solid (see *fig. 5.33*).The liquid temperature is seen to increase with increasing impingement height (*fig. 5.32*).

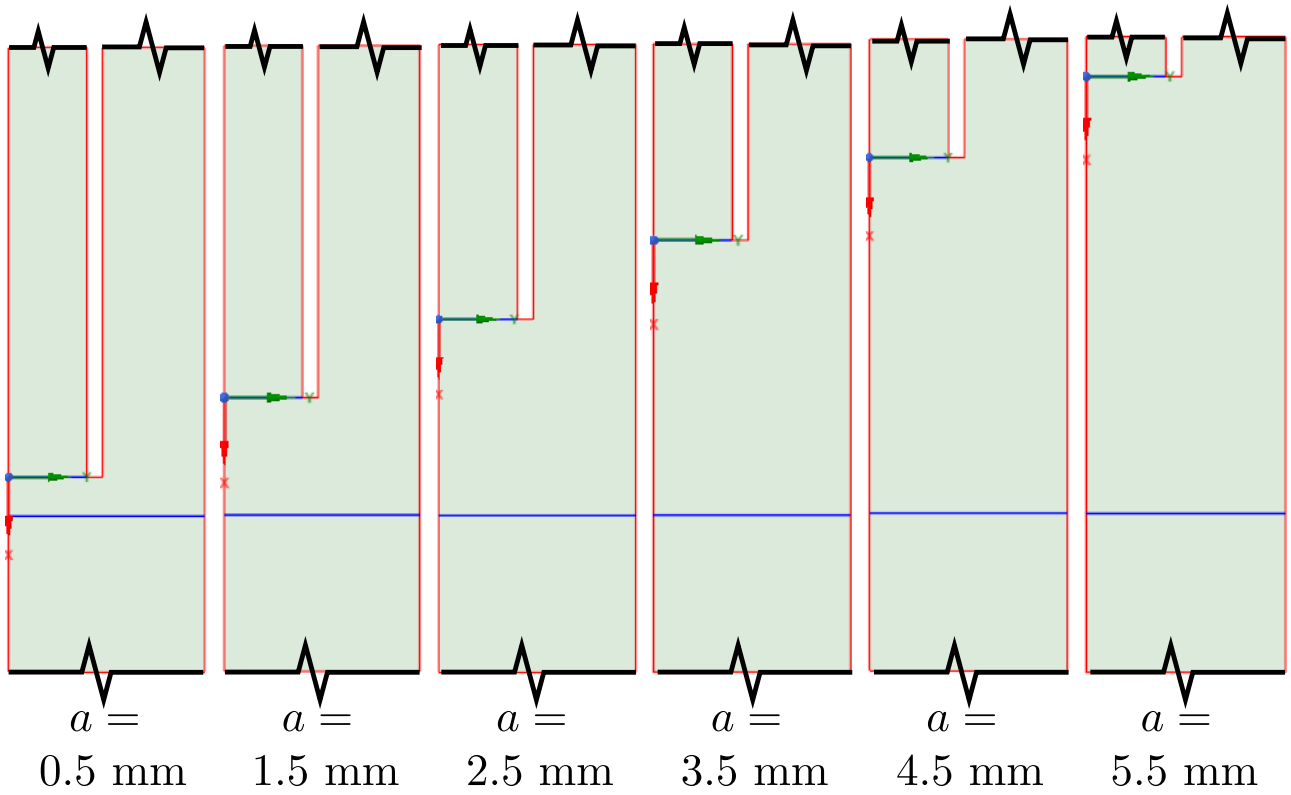

Figure 5.28: Domains displaying varying impingement height on a flat surface [$k = 0$, $h_{needle=0\ \text{mm}}$]

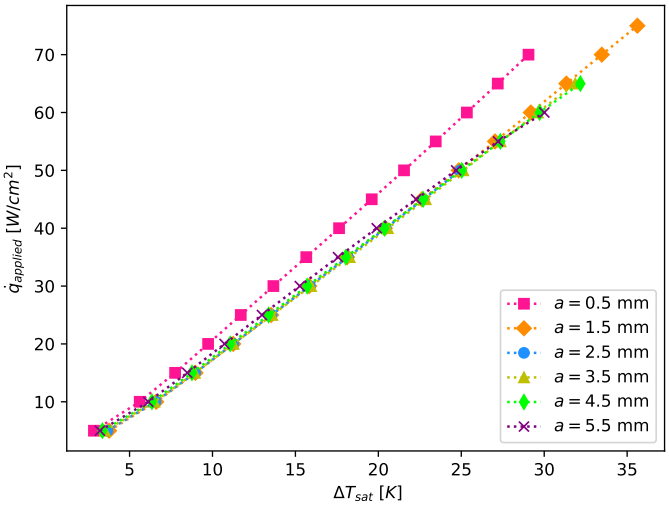

Figure 5.29: Boiling curve based on $\dot{q}_{applied}$ for different impingement heights [nitrogen ($P_{sat} = 140$ kPa), $k = 0$, $h_{needle} = 0$ mm, $v_j = 0.78$ m/s, $\Delta T_{sub} = 4$ K, mesh=M2, numerical framework=N2A]

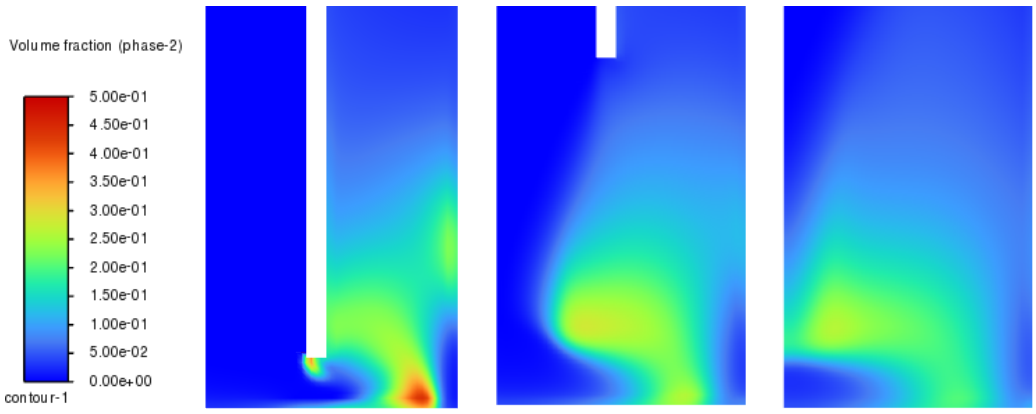

Figure 5.30: Truncated domain showing vapour fraction for different impingement heights $\dot{q}_{applied} = 40$ W/cm^2 [nitrogen ($P_{sat} = 140$ kPa), Numerical Framework=N2A, mesh=M2, $k = 0$, $h_{needle} = 0$ mm, $v_j = 0.78$ m/s, $\Delta T_{sub} = 4$ K]

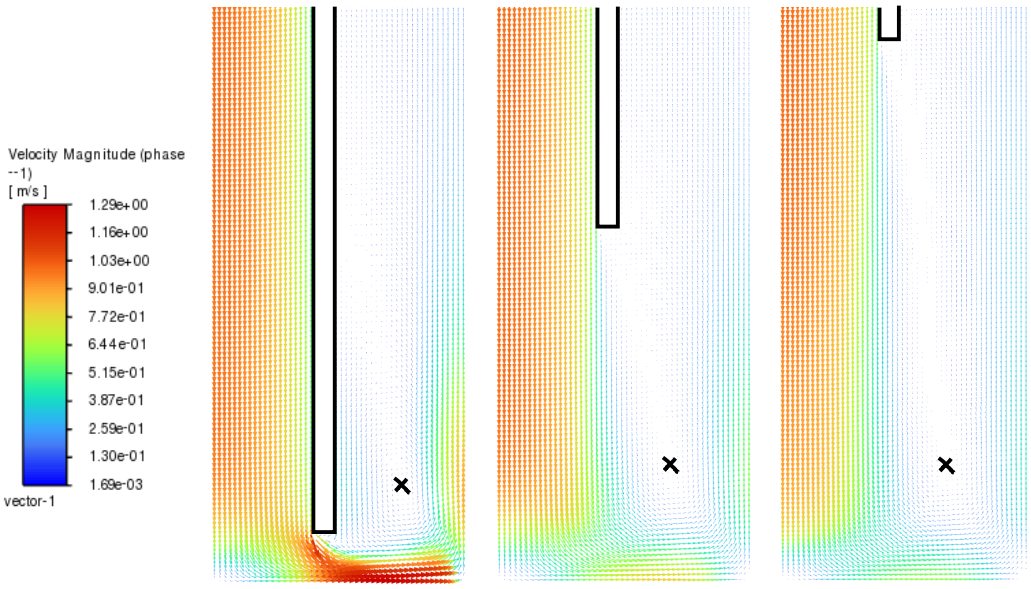

Figure 5.31: Truncated domain showing liquid velocity vector plot for different impingement heights at $\dot{q}_{applied} = 40$ W/cm^2 (centre of re-circulation zone marked with an 'x') [nitrogen ($P_{sat} = 140$ kPa), Numerical Framework=N2A, mesh=M2, $k = 0$, $h_{needle} = 0$ mm, $v_j = 0.78$ m/s, $\Delta T_{sub} = 4$ K]

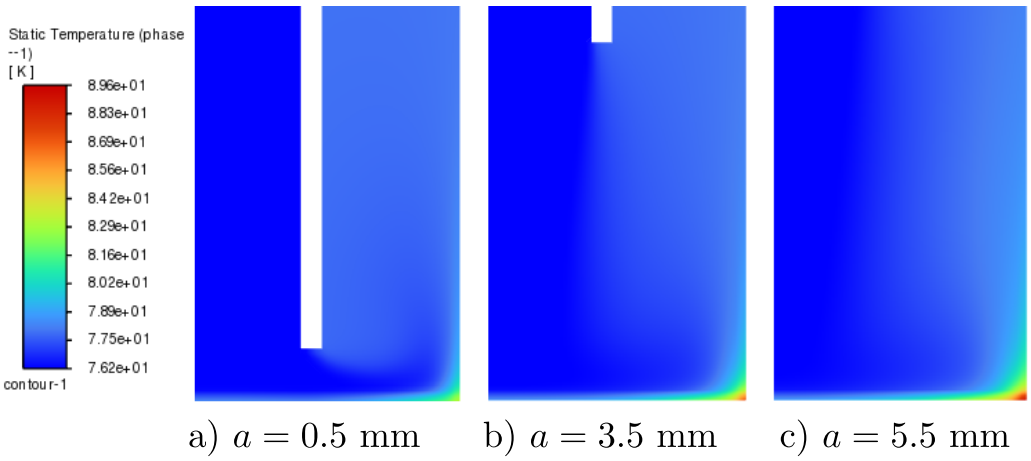

Figure 5.32: Truncated domain showing liquid temperature for different impingement heights at $\dot{q}_{applied} = 40$ W/cm^2 [nitrogen ($P_{sat} = 140$ kPa), Numerical Framework=N2A, mesh=M2, $k = 0$, $h_{needle} = 0$ mm, $v_j = 0.78$ m/s, $\Delta T_{sub} = 4$ K]

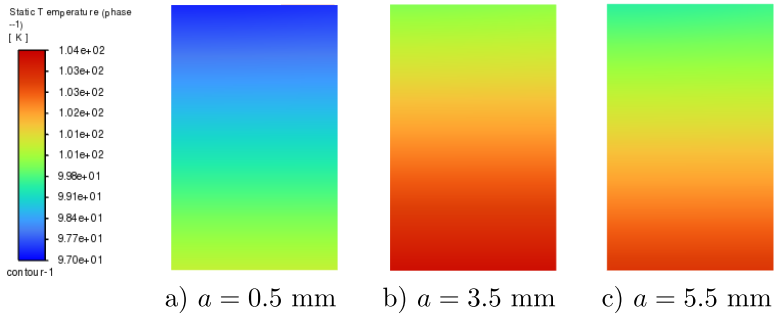

Figure 5.33: Truncated domain showing solid temperature for different impingement heights at $\dot{q}_{applied} = 40$ W/cm^2 [nitrogen ($P_{sat} = 140$ kPa), Numerical Framework=N2A, mesh=M2, $k = 0$, $h_{needle} = 0$ mm, $v_j = 0.78$ m/s, $\Delta T_{sub} = 4$ K]

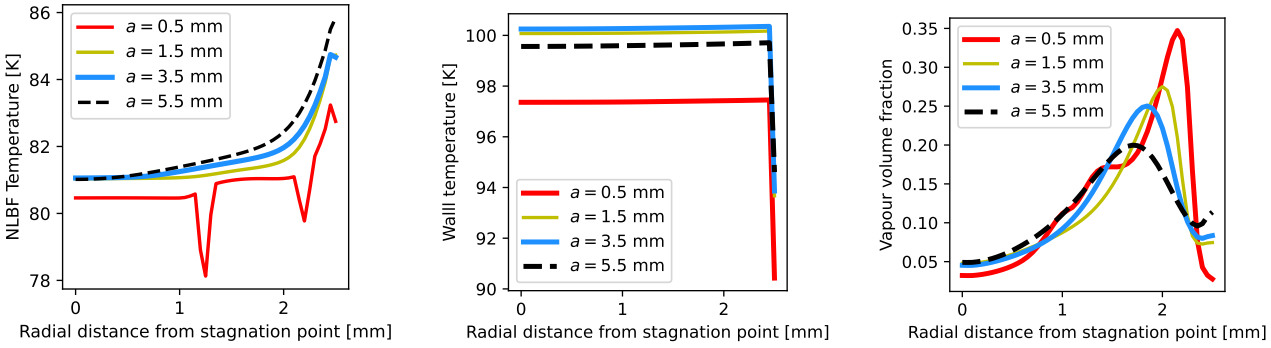

(a) NLBF Temperature *(b) Wall temperature* *(c) Vapour volume fraction*

(d) Convective heat flux ($\dot{q}_C$) *(e) Evaporative heat flux ($\dot{q}_E$)* *(f) Quenching heat flux ($\dot{q}_Q$)*

*Figure 5.34: Impingement wall quantities (**a**-NLBF Temperature, **b**-Wall temperature, **c**-Vapour volume fraction, **d-f**-convective, evaporative and quenching heat fluxes) for different impingement heights at $\dot{q}_{applied} = 40$ W/cm^2 [nitrogen ($P_{sat} = 140$ kPa), Numerical Framework=N2A, mesh=M2, $k = 0$, $h_{needle} = 0$ mm, $v_j = 78$ m/s, $\Delta T_{sub} = 4$ K]*

5.5 Joint Variation of Surface Curvature, Needle Height and Jet Impingement Height

The parameter space being considered is composed of three independent variables within the folowing limits:

1. $k = 0 - 0.42$
2. $h_{needle} = 0 - 5$ mm
3. $a = 0.5 - 5.5$ mm

The parameter space was evenly divided into 216 ($6 \times 6 \times 6$) individual sample points. However, due errors in the code used to generate the geometries, infeasible geometric configurations (nozzle end lies within the solid), poor convergence (due to large velocity gradients) and server errors, some of the sample points were neglected. The number of sample points used thus totaled to 184 points. This was deemed sufficient to grasp the underlying trends in the sample space. Three geometries for a random selection of parameter combinations have been shown in *fig. 5.35*.

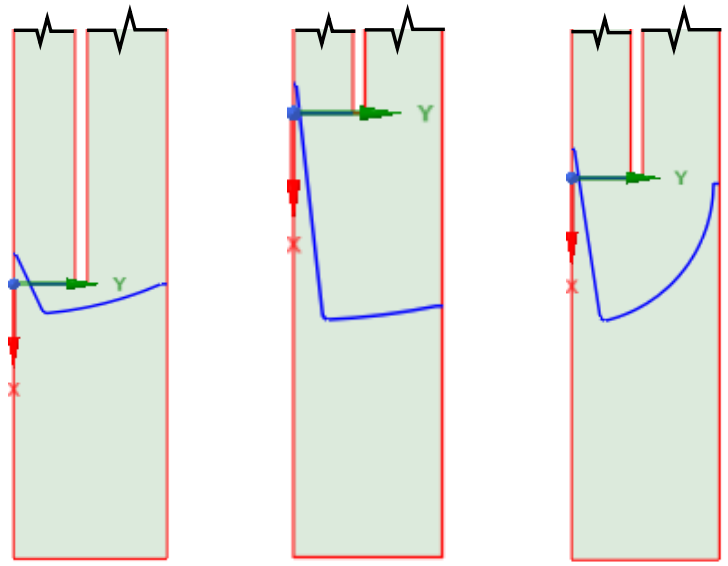

a)	b)	c)
$k = 0.17$	$k = 0.08$	$k = 0.42$
$h_{needle} = 1$ mm	$h_{needle} = 4$ mm	$h_{needle} = 3$ mm
$a = 0.5$ mm	$a = 3.5$ mm	$a = 2.5$ mm

Figure 5.35: Random selection of sample domains

The boiling heat transfer coefficient [BHTC] (slope of the boiling curve computed from gradient obtained by a linear approximation of the each boiling curve) is shown for all the tested sample points as a function of jet impingement height in *fig. 5.36*. The data reveal that for low surface curvatures ($k \leq 0.08$ with no needle) the boiling heat transfer coefficient increases with decreased impingement height (see *fig. 5.39a*). However, as soon as the surface curvature is greater than $k = 0.08$ there is a peak in the boiling heat transfer coefficient such that the BHTC initially increases with decrease in jet impingement height (from $a = 5.5$ mm) until it reaches a maximum and then decreases with further reduction in impingement height. The location of the peak shifts rightward with increased curvature, from $a = 1.5$ mm at $k = 0.17$ to $a = 2.5$ mm at $k = 0.42$ (for a surface without a needle). The introduction of a needle on a flat surface has a similar effect of introducing a local maximum in the BHTC at $a \approx 1.5$ mm (see *fig. 5.39b*). On average, increased curvature and increased needle height both serve to independently increase the BHTC (see *fig. 5.39c*). The optimum parameter combination was found to be [$a = 1.5$ mm, $k = 0.42$ and $h_{needle} = 4$ mm] with a BHTC of 3.66 W/(cm^2·K).

Figure 5.37 displays the boiling heat transfer coefficient as a function of curvature for all tested sample points. The results on surfaces with and without needles (of all needle heights) indicate that increased surface curvature results in a quadratic increase in BHTC as a result of the increased surface area being the dominant driving mechanism.

Figure 5.38 displays that increased needle height results in an approximately linear increase of the BHTC. Again, this is attributed to the growth of the surface area with increasing needle height.

The linear approximation for determining BHTC is a potential source of error as the nonlinear portion at the bottom of the boiling curve can result in lowering of the approximated boiling heat transfer coefficient. This is most notable at high surface curvatures [*fig. 5.2a*] and large needle heights [*fig. 5.17a*] as a result of the increased surface area causing lower average wall heat fluxes and therefor slower progression up the boiling curve, with more points residing in the transition to nucleate boiling regime.

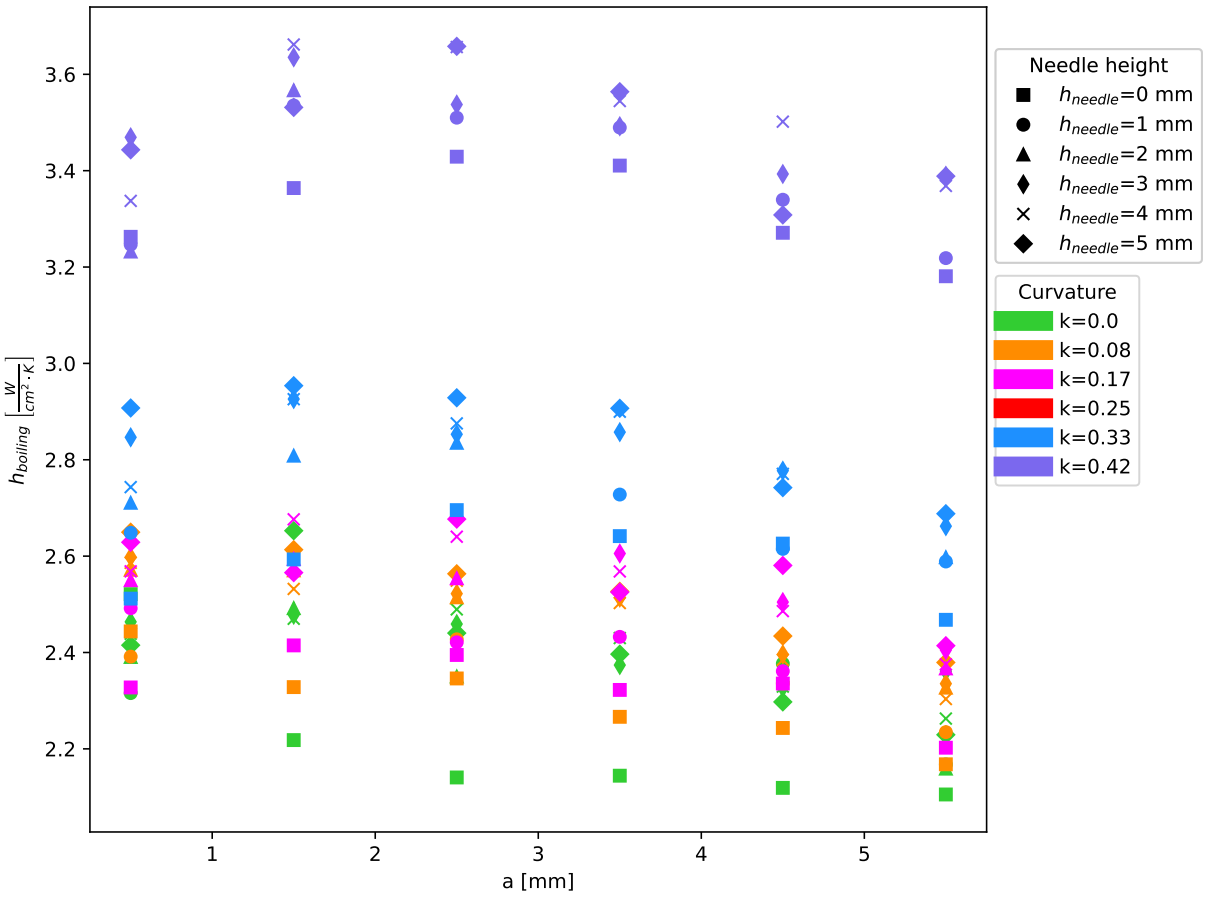

Figure 5.36: Boiling heat transfer coefficient ($h_{boiling}$-based on a linear fit applied to the boiling curve obtained using $\dot{q}_{applied}$ and the extrapolated wall temperature) as a function of impingement height (a), for different curvatures and needle heights [nitrogen (P_{sat} = 140 kPa), Numerical Framework=N2A, mesh=M2, $k = 0$, $h_{needle} = 0$ mm, v_j = 78 m/s, ΔT_{sub} = 4 K]

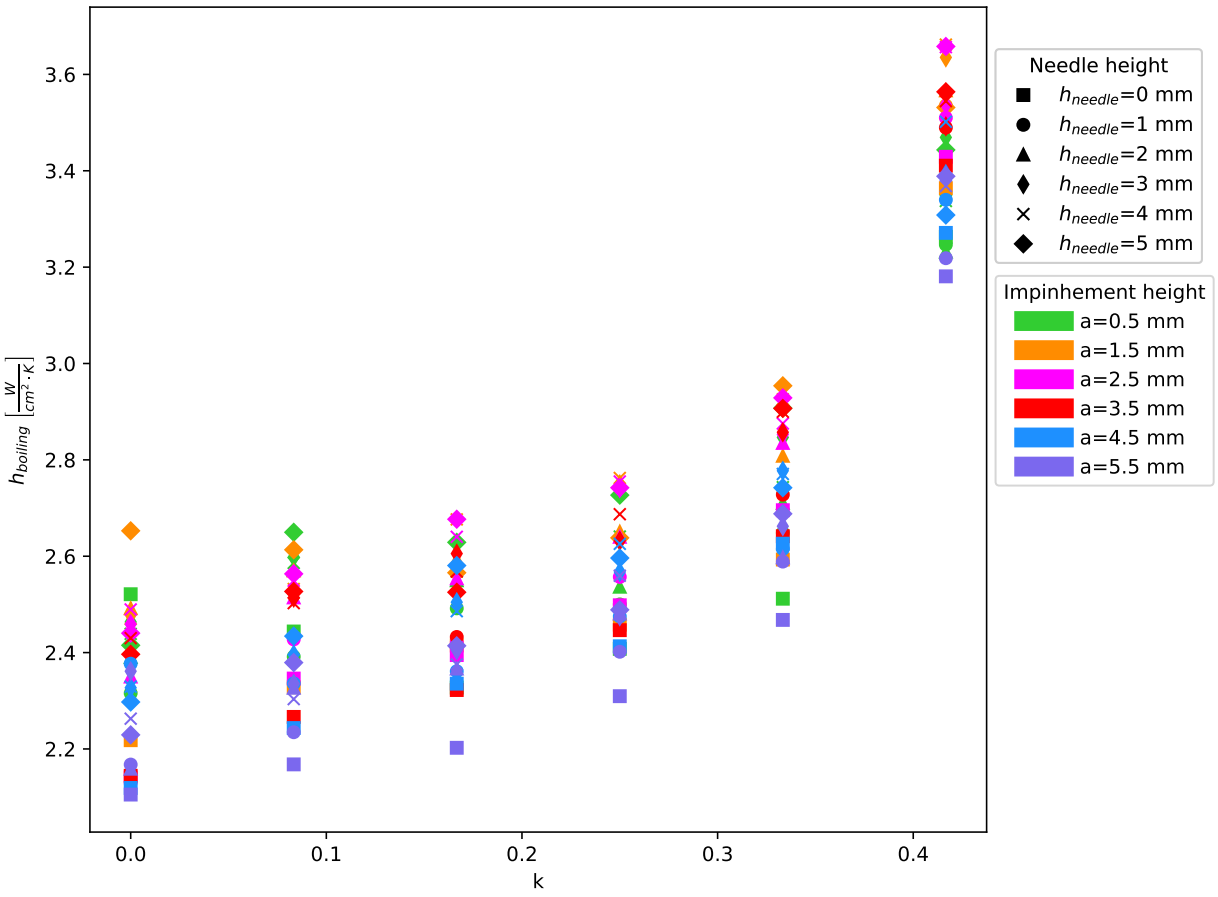

Figure 5.37: Boiling heat transfer coefficient ($h_{boiling}$-based on a linear fit applied to the boiling curve obtained using $\dot{q}_{applied}$ and the extrapolated wall temperature) as a function of surface curvature (k), for different impingement heights and needle heights [nitrogen ($P_{sat} = 140$ kPa), Numerical Framework=N2A, mesh=M2, $k = 0$, $h_{needle} = 0$ mm, $v_j = 78$ m/s, $\Delta T_{sub} = 4$ K]

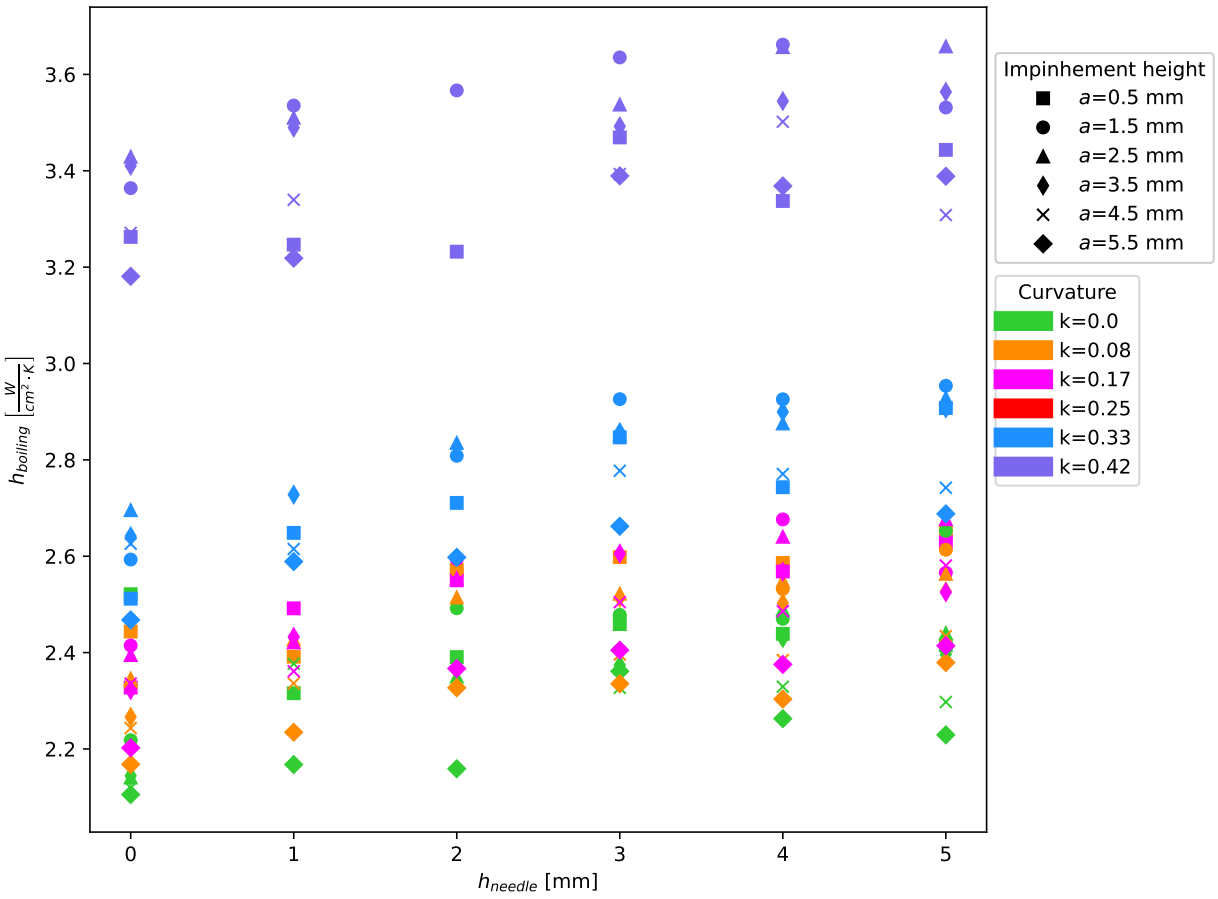

Figure 5.38: Boiling heat transfer coefficient ($h_{boiling}$-based on a linear fit applied to the boiling curve obtained using $\dot{q}_{applied}$ and the extrapolated wall temperature) as a function of needle height (a), for different curvatures and impingement heights [nitrogen ($P_{sat} = 140$ kPa), Numerical Framework=N2A, mesh=M2, $k = 0$, $h_{needle} = 0$ mm, $v_j = 78$ m/s, $\Delta T_{sub} = 4$ K]

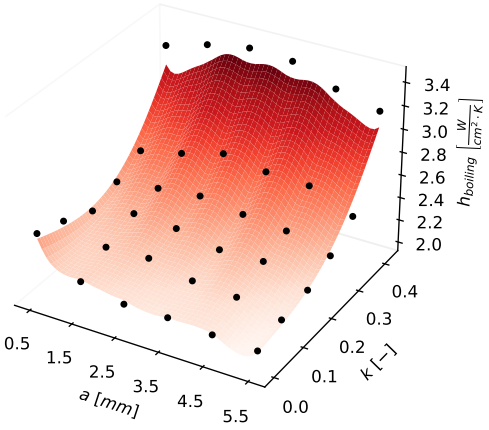

(a) Impingement height and surface curvature (Fixed variable: $h_{needle} = 0$ mm)

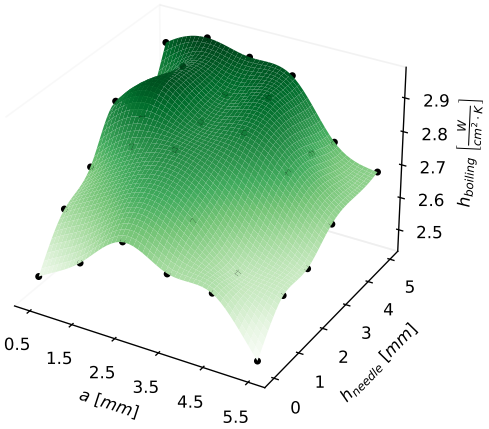

(b) Impingement height and needle height (Fixed variable: $k = 0.33$)

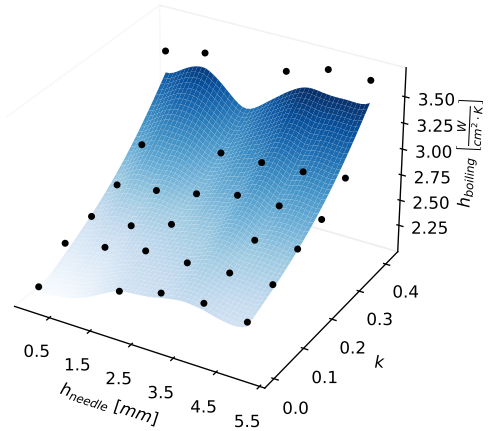

(c) Needle height and surface curvature (Fixed variable: $a = 2.5$ mm)

Figure 5.39: 3-D contour plots of boiling heat transfer coefficient as a function of **a**-$[a, k]$, **b**-$[a, h_{needle}]$, **c**-$[h_{needle}, k]$ *with the third parameter specified as a constant in each of the plots*

5.6 Summary

This chapter explored the impact of surface curvature ($k = 0 - 0.42$), needle height ($h_{needle} = 0 - 5$ mm) and jet impingement height ($a = 0.5 - 5.5$ mm) on the nucleate boiling curve. It was found that increased surface curvature resulted in quadratic increases in the boiling heat transfer coefficient (increased slope of the boiling curve) and a shift of the boiling curve to the left. This was found to be a direct result of the increased surface area on higher curvature surfaces. Increased needle height on flat surfaces was found to cause approximately linear increases in the boiling heat transfer coefficient with the improvements again largely associated with increases in the surface area. Decreased jet impingement height was shown to improve the boiling heat coefficient as a result of improved convective and quenching heat transfer. A large parametric study was then conducted on a variety of surfaces with different combinations of surface curvature, needle height and jet impingement height. It was revealed that increased surface curvature and needle height consistently resulted in improvements in the boiling heat transfer coefficient. However, decreased impingement height had mixed effects, improving the boiling heat transfer coefficient as it was decreased from its maximum value $a = 5.5$ mm until it reached a peak (with the location dependent on the curvature and needle height combination) and then reducing the boiling heat transfer coefficient with subsequent reduction in the impingement height. The optimum parameter combination was found to be [$a = 1.5$ mm, $k = 0.42$ and $h_{needle} = 4$ mm] with a boiling heat transfer coefficient of 3.66 W/(cm^2·K). This brings a conclusion to the key objectives presented in *chapter 1*. A summary of the findings and key insights obtained in this dissertation are presented in *chapter 6*.

Chapter 6

Conclusion and Future Work

6.1 Conclusion

Chapter 2 conducted a literature review of single phase jets, boiling and multiphase jets. Key findings from this chapter pertaining to multiphase jets include:

1. Hysteresis and temperature excursion effects exist in experimental boiling curves.
2. Increased jet velocity resulted in marginal improvement of the boiling heat transfer coefficient (BHTC) for liquid nitrogen jets and notably increased the critical heat flux (CHF).
3. Reduced impingement height increased the BHTC.
4. Cryogenic fluids, such as liquid nitrogen, with low surface tension and high wettability resulted in small bubble departure diameters.
5. Increased surface curvature enhanced the BHTC and CHF, with increased surface area, increased normal pressure gradients and pressure along the wall cited as possible reasons.
6. A singular pin addition decreased wall superheat and shifted the boiling curve left, with mixed effects on BHTC.
7. The multiphase Eulerian model coupled with the RPI wall boiling model is an effective method of modeling jet impingement boiling.
8. The RPI wall boiling model requires special attention for cryogenic fluids with high wettability, necessitating different RPI closing models.

Chapter 3 critically assessed the applicability of various RPI closing models for use in cryogenic applications. Key findings from this chapter include:

1. $D_w = Kirichenko$ (*eq.* (3.19)) is the most appropriate bubble departure diameter correlation for cryogenic fluids, predicting departure diameters approximate five times smaller than $D_w = Tolubinsky$ (*eq.* (3.17)) when considering liquid nitrogen at low subcoolings.
2. As a result of the small departure diameters for nitrogen, the nucleation site densities increased for the correlations presented in *section 3.3.2* (in comparison to water).
3. It was deemed that $N_w = Kirichenko\ P/P_{cr} < 0.04$ (*eq.* (3.23)) was implausible based on an argument relating to the total surface area occupied by the bubbles.
4. $N_w = Kirichenko\ P/P_{cr} \geq 0.04$ (derived for cryogenic fluids) and $N_w = Kamustafaogullari$ (derived for water but coupled with $D_w = Kirichenko$) predicted a similar range for nucleation site density, with $N_w = Kamustafaogullari$ predicting a more gradual rise in nucleation site density at low wall superheats but a higher nucleation site density at larger wall superheats (> 15 K).
5. The correlation for $N_w = Lemmert$ (derived for water) is a function of wall superheat only and predicted nucleation site densities two orders of magnitude lower than $N_w = Kamustafaogullari$ and $N_w = Kirichenko\ P/P_{cr} \geq 0.04$ when considering liquid nitrogen.
6. A new area of influence correlation was proposed ($A_b = 1 - e^{-1.5\beta^{1.2}}$ *eq.* (3.44)) based on the results of a Monte Carlo simulation considering the overlapping area of a distribution of circular disks.

7. The bubble waiting time coefficient was found to vary in a range of $C_{wt} = 1 - 1.2$ when considering an area of influence factor of $K = 4$ and taking into account the reduction in quenching area due to bubble growth.
8. A simplified empirical solution was proposed, neglecting convective heat transfer effects.

Chapter 4 validated three separate CFD models against the experimental results of Zhang et al. 2011 [205] on flat, hemispherical and singular needle surfaces under a variety of jet impingement velocities and impingement heights. Key findings from this chapter include:

1. Refining a 2mm section of mesh at the inlet resulted in a smooth solution of the non-local boundary field (NLBF) temperature (used for the liquid temperature in the quenching (*eq.* (3.13)) and evaporative (*eq.* (3.14)) heat flux equations). This mitigated the effect of the boundary location distance on the wall superheat.
2. A sensitivity analysis revealed that all the CFD models are sensitive to subcooling with a 2 K increase in subcooling resulting in an approximately 2.5 K shift of the boiling curve to the left. This was attributed to an increase in convective and quenching heat fluxes.
3. Jet velocity showed less sensitivity than subcooling with increased velocities resulting in increased the boiling heat transfer coefficient and thus decreased the wall superheat towards the top of the experimental boiling curve.
4. The CFD model developed for water (denoted $N1$) proved to have a low sensitivity to pressure change whilst the boiling curve of the cryogenic CFD models (denoted $N2A$ and $N2B$) where significantly shifted to the left with increased pressure. This was largely attributed to the dependency of the nucleation site density correlations (of $N_w = Kirichenko$ used in $N2A$ and $N_w = Kocamustafaogullari$ used in $N2B$) on the fluid properties at the wall and their resulting increase with a reduction in pressure.
5. The steady-state boiling curve displayed good correlation with transient results (using $\Delta t = 0.1$ ms) at lower heat fluxes with a deviation of 2.4% at the highest heat flux tested ($\dot{q}_{applied} = 40$ W/cm^2) and minor deviations in velocity, volume fraction and heat flux partitioning.
6. Increasing the bubble waiting time coefficient resulted in an increase in the quenching heat flux and hence the boiling heat transfer coefficient.
7. The cusp in the boiling curve generated by the sharp cutoff in non-dimensional area of influence correlation ($A_b = \min(1, \beta)$) was demonstrated. It was shown that the newly proposed non-dimensional area of influence model ($A_b = 1 - e^{-1.5\beta^{1.2}}$) produced a smooth transition in the boiling curve (from the lower to upper portion of the boiling curve) with minor deviation from the sharp cutoff correlation ($A_b = \min(1, \beta)$) in the lower to middle ($10 - 30$ W/cm^2) portion of the boiling curve.
8. Mesh M2 (fluid cell size of 5e-5m) was within 0.84% of the finest mesh used for the cryogenic CFD models ($N2A$ and $N2B$) and was selected for use in the parametric study.
9. The water-based CFD model was analysed, revealing that the liquid temperature and vapour fraction at the wall both contribute to an increase in wall temperature compared to the empirical solution of presented in *chapter 3*.
10. $N_w = Kirichenko$ (used in $N2A$) resulted in a lower boiling heat transfer coefficient and a reduction in vapour near the experimental CHF compared to $N_w = Kocamustafaogullari$ (used in $N2B$).
11. The cryogenic model ($N2A$) had an average root mean squared deviation of 1.299 K when compared to the combined flat surface experimental boiling curve results (considering different velocities and impingement heights). The average root mean squared deviation across all hemispherical surface experiments was 1.557 K and across the singular needle surfaces was 4.16 K (predominantly over-predicting wall superheat). The lowest combined deviation across all the surfaces occurred in a velocity range of $v_j = 0.45 - 0.78$ m/s and at a subcooling $\Delta T_{sub} = 4$ K.

Chapter 5 explored the impact of surface curvature ($k = 0 - 0.42$), needle height ($h_{needle} = 0 - 5$ mm) and jet impingement height ($a = 0.5 - 5.5$ mm) on the nucleate boiling curve. Key findings from this chapter include:

1. Increased surface curvature resulted in quadratic increases in the boiling heat transfer coefficient (increased slope of the boiling curve) and a shift of the boiling curve to the left, primarily as a result of the increased surface area.
2. Increased needle height was found to cause approximately linear increases in the boiling heat transfer coefficient, primarily as a result of the increased surface area.

3. Decreased impingement height was found to have mixed effects, improving the boiling heat transfer coefficient as it was decreased from its maximum value $a = 5.5$ mm until it reached a peak (with the location dependent on the curvature and needle height combination) and then reducing the boiling heat transfer coefficient with subsequent reduction in the impingement height.
4. The optimum parameter combination was found to be [$a = 1.5$ mm, $k = 0.42$ and $h_{needle} = 4$ mm] with a boiling heat transfer coefficient of 3.66 W/(cm^2·K).

6.2 Future Work

Whilst the CFD models presented in this paper proved successful in predicting cryogenic jet impingement boiling heat transfer on a variety of surfaces, various possible improvements and unexplained areas of interest were noted throughout the dissertation. These include:

- Extend the arguments presented in *section 3.3.4* and *section 3.3.5* and explore the impact of departure diameter (D_w) on both the area of influence (A_b) and bubble waiting time coefficient C_{wt}.
- Obtain a correlation for bubble waiting time coefficient C_{wt} based on the results presented in *fig. 3.15* and explore its impact on the boiling curve when implementing it in a CFD code or the simplified empirical model.
- Independently explore the effect of the bubble departure diameter, bubble departure frequency and nucleation site density correlations presented in chapter 3 when implemented into a CFD code.
- Fully explore the mechanism behind the non-monotonic rise and fall of inlet pressure with increased heat flux noted in *section 4.9* when using a transient solver.
- Incorporating a function into the simplified empirical model that accounts for the reduction in liquid-wall contact area due to vapour production and introduce a heat transfer term to account for heat transfer to the newly designated vapour region.
- Explore the reason for the discontinuities noted in the NLBF temperature and its overall impact on CFD results (*section 4.18*).
- Determine the influence of variable saturation temperature (as a function of local pressure) for jet impingement onto different curvatures when using the RPI wall boiling model.

Bibliography

[1] URL: https://en.wikipedia.org/wiki/G%C3%B6rtler_vortices.

[2] S. Abishek, R. Narayanaswamy, and V. Narayanan. "Effect of heater size and Reynolds number on the partitioning of surface heat flux in subcooled jet impingement boiling". In: *International Journal of Heat and Mass Transfer* 59 (2013), pp. 247–261. ISSN: 0017-9310. DOI: https://doi.org/10.1016/j.ijheatmasstransfer.2012.12.021. URL: https://www.sciencedirect.com/science/article/pii/S0017931012009763.

[3] Arthur W Adamson. "An adsorption model for contact angle and spreading". In: *Journal of Colloid and Interface Science* 27.2 (1968), pp. 180–187. ISSN: 0021-9797. DOI: https://doi.org/10.1016/0021-9797(68)90025-8. URL: https://www.sciencedirect.com/science/article/pii/0021979768900258.

[4] Arthur W Adamson. "Potential distortion model for contact angle and spreading. II. Temperature dependent effects". In: *Journal of Colloid and Interface Science* 44.2 (1973), pp. 273–281. ISSN: 0021-9797. DOI: https://doi.org/10.1016/0021-9797(73)90219-1. URL: https://www.sciencedirect.com/science/article/pii/0021979773902191.

[5] Shakeel Ahmad et al. "Lattice Boltzmann study of bubble dynamics and heat transfer on a hybrid rough surface with a cavity-pillar structure". In: *International Communications in Heat and Mass Transfer* 119 (2020). Cited by: 19. DOI: 10.1016/j.icheatmasstransfer.2020.104896. URL: https://www.scopus.com/inward/record.uri?eid=2-s2.0-85096172399&doi=10.1016%2fj.icheatmasstransfer.2020.104896&partnerID=40&md5=c01c544083f186bc68de745bf8c78122.

[6] Zahir U. Ahmed, Yasir M. Al-Abdeli, and Ferdinando G. Guzzomi. "Impingement pressure characteristics of swirling and non-swirling turbulent jets". In: *Experimental Thermal and Fluid Science* 68 (2015), pp. 722–732. ISSN: 0894-1777. DOI: https://doi.org/10.1016/j.expthermflusci.2015.07.017. URL: https://www.sciencedirect.com/science/article/pii/S0894177715001946.

[7] Ho Seon Ahn et al. "The effect of capillary wicking action of micro/nano structures on pool boiling critical heat flux". In: *International Journal of Heat and Mass Transfer* 55.1-3 (2012), pp. 89–92.

[8] Toshio Aihara et al. "Boiling heat transfer of a micro-impinging jet of liquid nitrogen in a very slender cryoprobe". In: *International Journal of Heat and Mass Transfer* 36 (1993), pp. 169–175. URL: https://api.semanticscholar.org/CorpusID:120264373.

[9] Yazan Alatrash et al. "Experimental and numerical investigation of local bubble parameters for subcooled flow boiling in a pressurized annulus". In: *International Journal of Heat and Mass Transfer* 194 (2022), p. 123040. ISSN: 0017-9310. DOI: https://doi.org/10.1016/j.ijheatmasstransfer.2022.123040. URL: https://www.sciencedirect.com/science/article/pii/S0017931022005130.

[10] Luz Amaya-Bower and Taehun Lee. "Single bubble rising dynamics for moderate Reynolds number using Lattice Boltzmann Method". In: *Computers and Fluids* 39.7 (2010). Cited by: 162, pp. 1191–1207. DOI: 10.1016/j.compfluid.2010.03.003. URL: https://www.scopus.com/inward/record.uri?eid=2-s2.0-77952585076&doi=10.1016%2fj.compfluid.2010.03.003&partnerID=40&md5=cd9460636ce71b6891bf2e88e24d18b3.

[11] SP Antal, RT Lahey Jr, and JE Flaherty. "Analysis of phase distribution in fully developed laminar bubbly two-phase flow". In: *International journal of multiphase flow* 17.5 (1991), pp. 635–652.

[12] Dion S. Antao, Yangying Zhu, and Evelyn N. Wang. "Boiling on Enhanced Surfaces". In: *Handbook of Thermal Science and Engineering*. Cham: Springer International Publishing, 2018, pp. 1747–1793. ISBN: 978-3-319-26695-4. DOI: 10.1007/978-3-319-26695-4_43. URL: https://doi.org/10.1007/978-3-319-26695-4_43.

[13] K. H. Ardron and G. Giustini. "On the wetting behavior of surfaces in boiling". In: *Physics of Fluids* 33.11 (Nov. 2021), p. 111302. ISSN: 1070-6631. DOI: 10.1063/5.0069686. eprint: https://pubs.aip.org/aip/pof/article-pdf/doi/10.1063/5.0069686/18627531/111302_1_5.0069686.pdf. URL: https://doi.org/10.1063/5.0069686.

[14] W.B. Bald. "Cryogenic heat transfer research at Oxford: Part 1 — nucleate pool boiling". In: *Cryogenics* 13.8 (1973), pp. 457–469. ISSN: 0011-2275. DOI: https://doi.org/10.1016/0011-2275(73)90002-7. URL: https://www.sciencedirect.com/science/article/pii/0011227573900027.

[15] SG Bankoff. "Ebullition from solid surfaces in the absence of a pre-existing gaseous phase". In: *Transactions of the American Society of Mechanical Engineers* 79.4 (1957), pp. 735–740.

[16] AVRAM BAR-COHEN and T. W. SIMON. "wall Superheat Excursions in the Boiling incipience of Dielectric Fluids". In: *Heat Transfer Engineering* 9.3 (1988), pp. 19–31. DOI: 10.1080/01457638808939668. eprint: https://doi.org/10.1080/01457638808939668. URL: https://doi.org/10.1080/01457638808939668.

[17] E. Bergles and C. -F. Ma. "Boiling jet impingement cooling of simulated microelectronic chips". In: *Heat Transfer in Electronic Equipment - 1983*. Jan. 1983, pp. 5–12.

[18] D.C. Besnard and F.H. Harlow. "Turbulence in multiphase flow". In: *International Journal of Multiphase Flow* 14.6 (1988), pp. 679–699. ISSN: 0301-9322. DOI: https://doi.org/10.1016/0301-9322(88)90068-7. URL: https://www.sciencedirect.com/science/article/pii/0301932288900687.

[19] Amy Rachel Betz, James Jenkins, Daniel Attinger, et al. "Boiling heat transfer on superhydrophilic, superhydrophobic, and superbiphilic surfaces". In: *International Journal of Heat and Mass Transfer* 57.2 (2013), pp. 733–741.

[20] M. E. Bland. "Bubble nucleation in cryogenic fluids". PhD thesis. University of Oxford, 1970.

[21] PJ Brennan and EA Skrabek. "Design and development of a prototype static cryogenic heat transfer system". In: *NASA CR-121939* (1971).

[22] Eric A Browne, Michael K Jensen, and Yoav Peles. "Microjet array flow boiling with R134a and the effect of dissolved nitrogen". In: *International journal of heat and mass transfer* 55.4 (2012), pp. 825–833.

[23] Eric A Browne et al. "Microjet array single-phase and flow boiling heat transfer with R134a". In: *International Journal of Heat and Mass Transfer* 53.23-24 (2010), pp. 5027–5034.

[24] Walter Herbert Bruckner. "Hardenability of carburizing steels". In: *University of Illinois. Engineering Experiment Station. Bulletin; no. 320* (1939).

[25] Alan Burns et al. "The Favre Averaged Drag Model for Turbulent Dispersion in Eulerian Multi-Phase Flows". In: vol. 392. Jan. 2004.

[26] Ruander Cardenas and Vinod Narayanan. "Heat transfer characteristics of submerged jet impingement boiling of saturated FC-72". In: *International Journal of Heat and Mass Transfer* 55.15 (2012), pp. 4217–4231. ISSN: 0017-9310. DOI: https://doi.org/10.1016/j.ijheatmasstransfer.2012.03.063. URL: https://www.sciencedirect.com/science/article/pii/S0017931012002128.

[27] Han Chi-Yeh and Peter Griffith. "The mechanism of heat transfer in nucleate pool boiling—Part I: Bubble initiaton, growth and departure". In: *International Journal of Heat and Mass Transfer* 8.6 (1965), pp. 887–904. ISSN: 0017-9310. DOI: https://doi.org/10.1016/0017-9310(65)90073-6. URL: https://www.sciencedirect.com/science/article/pii/0017931065900736.

[28] Han Chi-Yeh and Peter Griffith. "The mechanism of heat transfer in nucleate pool boiling—Part II: The heat flux-temperature difference relation". In: *International Journal of Heat and Mass Transfer* 8.6 (1965), pp. 905–914. ISSN: 0017-9310. DOI: https://doi.org/10.1016/0017-9310(65)90074-8. URL: https://www.sciencedirect.com/science/article/pii/0017931065900748.

[29] H.H. Cho, K.M. Kim, and Jiwoon Song. "Applications of impingement jet cooling systems". In: *Cooling Systems: Energy, Engineering and Applications* (Mar. 2011), pp. 37–67.

[30] R.C. Chu et al. "Thermal management roadmap: Cooling electronic products from hand-held dvices to supercomputers". In: (May 2003).

[31] R. Cole. "A Photographic Study of Pool Boiling in the Region of the Critical Heat Flux". In: *Annual Meeting - American Institute of Chemical Engineers* 6 (Dec. 1960). ISSN: 0196-7282. DOI: 10.1002/aic.690060405. URL: https://www.osti.gov/biblio/4085668.

[32] R. J. Copeland. "Boiling heat transfer to a water jet impinging on a flat surface". PhD thesis. Southern Methodist University, Dallas, TX., 1970.

[33] Cristina Cornaro et al. "Jet impingement cooling of a convex semi-cylindrical surface". In: *International Journal of Thermal Sciences* 40.10 (2001), pp. 890–898. ISSN: 1290-0729. DOI: https://doi.org/10.1016/S1290-0729(01)01275-3. URL: https://www.sciencedirect.com/science/article/pii/S1290072901012753.

[34] Smreeti Dahariya and Amy R. Betz. "High pressure pool boiling: Mechanisms for heat transfer enhancement and comparison to existing models". In: *International Journal of Heat and Mass Transfer* 141 (2019), pp. 696–706. ISSN: 0017-9310. DOI: https://doi.org/10.1016/j.ijheatmasstransfer.2019.07.016. URL: https://www.sciencedirect.com/science/article/pii/S0017931019301243.

[35] Victor H. Del Valle and D.B.R. Kenning. "Subcooled flow boiling at high heat flux". In: *International Journal of Heat and Mass Transfer* 28.10 (1985), pp. 1907–1920. ISSN: 0017-9310. DOI: https://doi.org/10.1016/0017-9310(85)90213-3. URL: https://www.sciencedirect.com/science/article/pii/0017931085902133.

[36] Fatih Demiray and Jungho Kim. "Microscale heat transfer measurements during pool boiling of FC-72: effect of subcooling". In: *International Journal of Heat and Mass Transfer* 47.14 (2004), pp. 3257–3268. ISSN: 0017-9310. DOI: https://doi.org/10.1016/j.ijheatmasstransfer.2004.02.008. URL: https://www.sciencedirect.com/science/article/pii/S0017931004000493.

[37] V.S. Devahdhanush and Issam Mudawar. "Review of Critical Heat Flux (CHF) in Jet Impingement Boiling". In: *International Journal of Heat and Mass Transfer* 169 (2021), p. 120893. ISSN: 0017-9310. DOI: https://doi.org/10.1016/j.ijheatmasstransfer.2020.120893. URL: https://www.sciencedirect.com/science/article/pii/S0017931020338254.

[38] VS Devahdhanush and Issam Mudawar. "Critical heat flux of confined round single jet and jet array impingement boiling". In: *International Journal of Heat and Mass Transfer* 169 (2021), p. 120857.

[39] Xiaomeng Dong and Zhijian Zhang. "Mechanism study of bubble maximum diameter in the subcooled boiling flow for low-pressure condition". In: *International Journal of Heat and Mass Transfer* 164 (2021), p. 120585. ISSN: 0017-9310. DOI: https://doi.org/10.1016/j.ijheatmasstransfer.2020.120585. URL: https://www.sciencedirect.com/science/article/pii/S0017931020335213.

[40] D.A. Drew and S.L. Passman. "Theory of Multicomponent Fluids". In: *Applied Mathematical Sciences* 135 (1998), pp. 65–213.

[41] DA Drew and RT Lahey. *In particulate Two-phase Flow. 709 Butterworth*. 1993.

[42] R. I. Eddington and D. B. R. Kenning. "The prediction of flow boiling bubble populations from gas bubble nucleation experiments". In: *Proc. 6th Int. Heat Transfer Co (Toronto),i, 275280*. 1978.

[43] Srinath Ekkad and David Kontrovitz. "Jet impingement heat transfer on dimpled target surfaces". In: *International Journal of Heat and Fluid Flow* 23 (Feb. 2002), pp. 22–28. DOI: 10.1016/S0142-727X(01)00139-4.

[44] Srinath V. Ekkad and Prashant Singh. "A Modern Review on Jet Impingement Heat Transfer Methods". In: *Journal of Heat Transfer* 143.6 (Apr. 2021), p. 064001. ISSN: 0022-1481. DOI: 10.1115/1.4049496. eprint: https://asmedigitalcollection.asme.org/heattransfer/article-pdf/143/6/064001/6688652/ht_143_06_064001.pdf. URL: https://doi.org/10.1115/1.4049496.

[45] Engineers$_{E}$*dge*. *Water Boiling Graph Curve at 1 Atmosphere*. URL: https://www.engineersedge.com/heat_transfer/water_boiling_graph_curve_13825.htm.

[46] Derwalt Erasmus, Matti Lubkoll, and Theodor von Backström. "Jet impingement heat transfer within a hemisphere". In: *Heat and Mass Transfer* (June 2021). DOI: 10.1007/s00231-020-02977-9.

[47] Kazem Esmailpour, Arad Azizi, and Seyed Mostafa Hosseinalipour. "Numerical study of Jet Impingement Subcooled Boiling on the Superheated Surfaces". In: *Scientia Iranica* 26.4 (2019), pp. 2369–2381.

[48] Pablo Fariñas Alvariño et al. "Experimental investigation of the CHF of HFE-7100 under pool boiling conditions on differently roughened surfaces". In: *International Journal of Heat and Mass Transfer* 139 (2019), pp. 269–279. ISSN: 0017-9310. DOI: https://doi.org/10.1016/j.ijheatmasstransfer.2019.04.142. URL: https://www.sciencedirect.com/science/article/pii/S0017931018346714.

[49] H. Mojiri Forooshani, M. Aliofkhazraei, and H. Bagheri. "Fabrication of hierarchical dual structured (HDS) nickel surfaces and their corrosion behavior". In: *Journal of Alloys and Compounds* 784 (2019), pp. 556–573. ISSN: 0925-8388. DOI: https://doi.org/10.1016/j.jallcom.2019.01.079. URL: https://www.sciencedirect.com/science/article/pii/S0925838819300878.

[50] Thomas Frank, Junmei Shi, and Alan D Burns. "Validation of Eulerian multiphase flow models for nuclear safety application". In: *proceeding of the third international symposium on two-phase modelling and experimentation, Pisa, Italy*. Citeseer. 2004, pp. 22–25.

[51] W Fritz and W Ende. *Maximum Volume of Vapor Bubbles, Phys*. 1936.

[52] Marcin Froissart et al. "Heat exchange enhancement of jet impingement cooling with the novel humped-cone heat sink". In: *Case Studies in Thermal Engineering* 28 (2021), p. 101445. ISSN: 2214-157X. DOI: https://doi.org/10.1016/j.csite.2021.101445. URL: https://www.sciencedirect.com/science/article/pii/S2214157X21006080.

[53] Masahiro Furuya, Akira Inoue, and Ryuji Tanno. "Critical heat flux and convective heat transfer with a two-dimensional liquid jet impinging on flat and concave surfaces". In: *Nippon Kikai Gakkai Ronbunshu. B Hen (Transactions of the Japan Society of Mechanical Engineers. Part B)* 61 (1995).

[54] Ming Gao et al. "An investigation of microlayer beneath nucleation bubble by laser interferometric method". In: *International Journal of Heat and Mass Transfer* 57.1 (2013), pp. 183–189. ISSN: 0017-9310. DOI: https://doi.org/10.1016/j.ijheatmasstransfer.2012.10.017. URL: https://www.sciencedirect.com/science/article/pii/S0017931012007831.

[55] Robert Gardon and J.Cahit Akfirat. "The role of turbulence in determining the heat-transfer characteristics of impinging jets". In: *International Journal of Heat and Mass Transfer* 8.10 (1965), pp. 1261–1272. ISSN: 0017-9310. DOI: https://doi.org/10.1016/0017-9310(65)90054-2. URL: https://www.sciencedirect.com/science/article/pii/0017931065900542.

[56] C Gau and CM Chung. "Surface curvature effect on slot-air-jet impingement cooling flow and heat transfer process". In: (1991).

[57] S.M. Ghiaasiaan. *Two-Phase Flow, Boiling, and Condensation: In Conventional and Miniature Systems*. Cambridge University Press, 2007. ISBN: 9781139468909. URL: https://books.google.co.za/books?id=PeyaebUxEsgC.

[58] Shuai Gong and Ping Cheng. "Lattice Boltzmann simulations for surface wettability effects in saturated pool boiling heat transfer". In: *International Journal of Heat and Mass Transfer* 85 (2015), pp. 635–646. ISSN: 0017-9310. DOI: https://doi.org/10.1016/j.ijheatmasstransfer.2015.02.008. URL: https://www.sciencedirect.com/science/article/pii/S0017931015001714.

[59] Shuai Gong, Ping Cheng, and Xiaojun Quan. "Two-dimensional mesoscale simulations of saturated pool boiling from rough surfaces. Part I: Bubble nucleation in a single cavity at low superheats". In: *International Journal of Heat and Mass Transfer* 100 (2016). Cited by: 46, pp. 927–937. DOI: 10.1016/j.ijheatmasstransfer.2016.04.085. URL: https://www.scopus.com/inward/record.uri?eid=2-s2.0-84966550912&doi=10.1016%2fj.ijheatmasstransfer.2016.04.085&partnerID=40&md5=14ab2a36c345d10ededaab85447f2dfe.

[60] Peter Griffith and John D. Wallis. "THE ROLE OF SURFACE CONDITIONS IN NUCLEATE BOILING. Technical Report No. 14". In: 1958. URL: https://api.semanticscholar.org/CorpusID:136972010.

[61] V . A. GRIGORIEV, Y. M. PAVLOV, and E. V. AMETHISTOV. *BOILING CRYOGENIC LIQUIDS*. MOSCOW "ENERGY", 1977. URL: http://nt-mpei.ru/lib/Grigoriev_Kipenie-kriogennyh-gidkostey.pdf.

[62] Junping Gu et al. "Modeling of subcooled boiling by extending the RPI wall boiling model to ultra-high pressure conditions". In: *Applied Thermal Engineering* 124 (2017), pp. 571–584. ISSN: 1359-4311. DOI: https://doi.org/10.1016/j.applthermaleng.2017.06.017. URL: https://www.sciencedirect.com/science/article/pii/S1359431117318859.

[63] A. P. Hatton and I. S. Hall. "PHOTOGRAPHIC STUDY OF BOILING ON PREPARED SURFACES". In: *Proceeding of International Heat Transfer Conference 3* (1966). URL: https://api.semanticscholar.org/CorpusID:146203065.

[64] Nhan Hien Hoang et al. "A mechanistic model for predicting the maximum diameter of vapor bubbles in a subcooled boiling flow". In: *International Journal of Heat and Mass Transfer* 94 (2016), pp. 174–179. ISSN: 0017-9310. DOI: https://doi.org/10.1016/j.ijheatmasstransfer.2015.11.051. URL: https://www.sciencedirect.com/science/article/pii/S0017931015306396.

[65] B. Hoeneisen and C.A. Mead. "Fundamental limitations in microelectronics—I. MOS technology". In: *Solid-State Electronics* 15.7 (1972), pp. 819–829. ISSN: 0038-1101. DOI: https://doi.org/10.1016/0038-1101(72)90103-7. URL: https://www.sciencedirect.com/science/article/pii/0038110172901037.

[66] FJ Hong et al. "Confined jet array impingement boiling of subcooled aqueous ethylene glycol solution". In: *International Communications in Heat and Mass Transfer* 56 (2014), pp. 165–173.

[67] C.J. Hoogendoorn. "The effect of turbulence on heat transfer at a stagnation point". In: *International Journal of Heat and Mass Transfer* 20.12 (1977), pp. 1333–1338. ISSN: 0017-9310. DOI: https://doi.org/10.1016/0017-9310(77)90029-1. URL: https://www.sciencedirect.com/science/article/pii/0017931077900291.

[68] Peter Hrycak. "Heat transfer and flow characteristics of jets impinging on a concave hemispherical plate". In: *International Heat Transfer Conference Digital Library*. Begel House Inc. 1982.

[69] Y. Y. Hsu. "On the Size Range of Active Nucleation Cavities on a Heating Surface". In: *Journal of Heat Transfer* 84.3 (Aug. 1962), pp. 207–213. ISSN: 0022-1481. DOI: 10.1115/1.3684339. eprint: https://asmedigitalcollection.asme.org/heattransfer/article-pdf/84/3/207/5559712/207_1.pdf. URL: https://doi.org/10.1115/1.3684339.

[70] Yanxin Hu et al. "Marangoni effect on pool boiling heat transfer enhancement of self-rewetting fluid". In: *International Journal of Heat and Mass Transfer* 127 (2018), pp. 1263–1270. ISSN: 0017-9310. DOI: https://doi.org/10.1016/j.ijheatmasstransfer.2018.08.003. URL: https://www.sciencedirect.com/science/article/pii/S0017931018328151.

[71] ANSYS Inc. *ANSYS Fluent Theory Guide*. Release 24.1. 2024.

[72] A Inoue et al. "Studies on a cooling of high heat flux surface in fusion reactor by impinging planar jet flow". In: *Fusion Engineering and Design* 51-52 (2000), pp. 781–787. ISSN: 0920-3796. DOI: https://doi.org/10.1016/S0920-3796(00)00178-2. URL: https://www.sciencedirect.com/science/article/pii/S0920379600001782.

[73] A Inoue et al. "Studies on cooling by two-dimensional confined jet flow of high heat heat flux surface in fusion reactor". In: *Nuclear Engineering and Design* 200.1 (2000), pp. 317–329. ISSN: 0029-5493. DOI: https://doi.org/10.1016/S0029-5493(99)00329-5. URL: https://www.sciencedirect.com/science/article/pii/S0029549399003295.

[74] A Inoue et al. "Two-dimensional impinging jet cooling of high heat flux surfaces in magnetic confinement fusion reactors". In: *Fusion Engineering and Design* 28 (1995). Proceedings of the Third International Symposium on Fusion Nuclear Technology, pp. 81–89. ISSN: 0920-3796. DOI: https://doi.org/10.

1016/0920-3796(95)90024-1. URL: https://www.sciencedirect.com/science/article/pii/0920379695900241.

[75] Seikan Ishigai, Shigeyasu Nakanishi, and Toshiaki Ochi. "Boiling heat transfer for a plane water jet impinging on a hot surface". In: *International Heat Transfer Conference Digital Library*. Begel House Inc. 1978.

[76] Mamoru Ishii. "Two-fluid model for two-phase flow". In: *Multiphase science and technology* 5.1-4 (1990).

[77] Mamoru Ishii and Novak Zuber. "Drag coefficient and relative velocity in bubbly, droplet or particulate flows". In: *AIChE Journal* 25.5 (1979). Cited by: 1238, pp. 843–855. DOI: 10.1002/aic.690250513. URL: https://www.scopus.com/inward/record.uri?eid=2-s2.0-0018515453&doi=10.1002%2faic.690250513&partnerID=40&md5=859872a7e88a950b74a8137cf3bca99a.

[78] H.J. Ivey. "Relationships between bubble frequency, departure diameter and rise velocity in nucleate boiling". In: *International Journal of Heat and Mass Transfer* 10.8 (1967), pp. 1023–1040. ISSN: 0017-9310. DOI: https://doi.org/10.1016/0017-9310(67)90118-4. URL: https://www.sciencedirect.com/science/article/pii/0017931067901184.

[79] Max Jakob and W Fritz. "Versuche über den Verdampfungsvorgang". In: *Forschung auf dem Gebiet des Ingenieurwesens A* 2.12 (1931), pp. 435–447.

[80] K. Jambunathan et al. "A review of heat transfer data for single circular jet impingement". In: *International Journal of Heat and Fluid Flow* 13.2 (1992), pp. 106–115. ISSN: 0142-727X. DOI: https://doi.org/10.1016/0142-727X(92)90017-4. URL: https://www.sciencedirect.com/science/article/pii/0142727X92900174.

[81] Ooi Jen Wai, Prem Gunnasegaran, and Hasril Hasini. "Effect of hybrid nanofluids concentration and swirling flow on jet impingement cooling". In: *Nanomaterials* 12.19 (2022), p. 3258.

[82] Benjamin Jones, John McHale, and Suresh Garimella. "The Influence of Surface Roughness on Nucleate Pool Boiling Heat Transfer". In: *Birck and NCN Publications* 131 (Dec. 2009). DOI: 10.1115/1.3220144.

[83] S.F. Jones, G.M. Evans, and K.P. Galvin. "Bubble nucleation from gas cavities — a review". In: *Advances in Colloid and Interface Science* 80.1 (1999), pp. 27–50. ISSN: 0001-8686. DOI: https://doi.org/10.1016/S0001-8686(98)00074-8. URL: https://www.sciencedirect.com/science/article/pii/S0001868698000748.

[84] R. L. Judd and K. S. Hwang. "A Comprehensive Model for Nucleate Pool Boiling Heat Transfer Including Microlayer Evaporation". In: *Journal of Heat Transfer* 98.4 (Nov. 1976), pp. 623–629. ISSN: 0022-1481. DOI: 10.1115/1.3450610. eprint: https://asmedigitalcollection.asme.org/heattransfer/article-pdf/98/4/623/5753684/623_1.pdf. URL: https://doi.org/10.1115/1.3450610.

[85] Sang-Joon Lee Jungho Lee. "STAGNATION REGION HEAT TRANSFER OF A TURBULENT AXISYMMETRIC JET IMPINGEMENT". In: *Experimental Heat Transfer* 12.2 (1999), pp. 137–156. DOI: 10.1080/089161599269753. eprint: https://doi.org/10.1080/089161599269753. URL: https://doi.org/10.1080/089161599269753.

[86] T Kamata, S Kumagai, and T Takeyama. "Boiling heat transfer to an impinging jet spurted into a narrow space (part II, space with a limited end)". In: *Heat transfer. Japanese research* 17.4 (1988), pp. 1–11.

[87] T Kamata, S Kumagai, and T Takeyama. "Boiling heat transfer to an impinging jet spurted into a narrow space. I: Space with an open end". In: *Heat transfer. Japanese research* 17.5 (1988), pp. 71–80.

[88] Yoshiro Katto and M. Kunihiro. "Study of the Mechanism of Burn-Out in Boiling System of High Burn-Out Heat Flux". In: *Jsme International Journal Series B-fluids and Thermal Engineering* 16 (1973), pp. 1357–1366. URL: https://api.semanticscholar.org/CorpusID:120911156.

[89] D.B.R. Kenning and Victor H. Del Valle M. "Fully-developed nucleate boiling: Overlap of areas of influence and interference between bubble sites". In: *International Journal of Heat and Mass Transfer* 24.6 (1981), pp. 1025–1032. ISSN: 0017-9310. DOI: https://doi.org/10.1016/0017-9310(81)90133-2. URL: https://www.sciencedirect.com/science/article/pii/0017931081901332.

[90] Stothe Peter Kezios. "Heat transfer in the flow of a cylindrical air jet normal to an infinite plane". PhD thesis. Illinois Institute of Technology, 1956.

[91] Hyungdae Kim and Dong Eok Kim. "Effects of surface wettability on pool boiling process: Dynamic and thermal behaviors of dry spots and relevant critical heat flux triggering mechanism". In: *International Journal of Heat and Mass Transfer* 180 (2021), p. 121762. ISSN: 0017-9310. DOI: https://doi.org/10.1016/j.ijheatmasstransfer.2021.121762. URL: https://www.sciencedirect.com/science/article/pii/S001793102100867X.

[92] Jin S. Kim et al. "Effect of surface roughness on pool boiling heat transfer of water on hydrophobic surfaces". In: *International Journal of Heat and Mass Transfer* 118 (2018), pp. 802–811. ISSN: 0017-9310. DOI: https://doi.org/10.1016/j.ijheatmasstransfer.2017.10.124. URL: https://www.sciencedirect.com/science/article/pii/S0017931017323505.

[93] Jungho Kim. "Review of nucleate pool boiling bubble heat transfer mechanisms". In: *International Journal of Multiphase Flow* 35.12 (2009), pp. 1067–1076. ISSN: 0301-9322. DOI: https://doi.org/10.

1016/j.ijmultiphaseflow.2009.07.008. URL: https://www.sciencedirect.com/science/article/pii/S0301932209001311.

[94] Jungho Kim. "Review of nucleate pool boiling bubble heat transfer mechanisms". In: *International Journal of Multiphase Flow* 35.12 (2009), pp. 1067–1076. ISSN: 0301-9322. DOI: https://doi.org/10.1016/j.ijmultiphaseflow.2009.07.008. URL: https://www.sciencedirect.com/science/article/pii/S0301932209001311.

[95] Anthony J Kinloch. *Adhesion and adhesives: science and technology*. Springer Science & Business Media, 1986.

[96] Iu A Kirichenko et al. "The boiling of cryogenic liquids". In: *Heat and mass transfer-V, Volume 3* 3 (1976), pp. 137–146.

[97] Yu.A. Kirichenko, L.A. Slobozhanin, and N.S. Shcherbakova. "Analysis of quasi-static conditions of boiling onset and bubble departure". In: *Cryogenics* 23.2 (1983), pp. 110–112. ISSN: 0011-2275. DOI: https://doi.org/10.1016/0011-2275(83)90125-X. URL: https://www.sciencedirect.com/science/article/pii/001122758390125X.

[98] Yu.A. Kirichenko et al. "Study on cryogenic liquid boiling." In: *Heat and mass transfer - 5, (pp. v3(1)137-146). USSR* (1976). URL: https://inis.iaea.org/search/search.aspx?orig_q=RN:9391993.

[99] J.F. Klausner et al. "Vapor bubble departure in forced convection boiling". In: *International Journal of Heat and Mass Transfer* 36.3 (1993), pp. 651–662. ISSN: 0017-9310. DOI: https://doi.org/10.1016/0017-9310(93)80041-R. URL: https://www.sciencedirect.com/science/article/pii/001793109380041R.

[100] G Kocamustafaogullari and M Ishii. "Interfacial area and nucleation site density in boiling systems". In: *International Journal of Heat and Mass Transfer* 26.9 (1983), pp. 1377–1387.

[101] G. Kocamustafaogullari and M. Ishii. "Foundation of the interfacial area transport equation and its closure relations". In: *International Journal of Heat and Mass Transfer* 38.3 (1995), pp. 481–493. ISSN: 0017-9310. DOI: https://doi.org/10.1016/0017-9310(94)00183-V. URL: https://www.sciencedirect.com/science/article/pii/001793109400183V.

[102] C.P. Kothandaraman. *Fundamentals of Heat and Mass Transfer*. New Age International, 2006. ISBN: 9788122417722. URL: https://books.google.co.za/books?id=hIviT25WWIEC.

[103] Stephan Kotthoff and Dieter Gorenflo. "Heat transfer and bubble formation on horizontal copper tubes with different diameters and roughness structures". In: *Heat and mass transfer* 45 (2009), pp. 893–908.

[104] Andre Leclerc. "Déviation d'un jet liquide par une plaque normale à son axe". In: *La Houille Blanche* 6 (1950), pp. 816–821.

[105] D.H. Lee, Y.S. Chung, and D.S. Kim. "Turbulent flow and heat transfer measurements on a curved surface with a fully developed round impinging jet". In: *International Journal of Heat and Fluid Flow* 18.1 (1997). Selected Papers from the Engineering Foundation Turbulent Heat Transfer Conference, pp. 160–169. ISSN: 0142-727X. DOI: https://doi.org/10.1016/S0142-727X(96)00136-1. URL: https://www.sciencedirect.com/science/article/pii/S0142727X96001361.

[106] D.H. Lee, Y.S. Chung, and S.Y. Won. "Technical Note The effect of concave surface curvature on heat transfer from a fully developed round impinging jet". In: *International Journal of Heat and Mass Transfer* 42.13 (1999), pp. 2489–2497. ISSN: 0017-9310. DOI: https://doi.org/10.1016/S0017-9310(98)00318-4. URL: https://www.sciencedirect.com/science/article/pii/S0017931098003184.

[107] M Lemmert and JM Chawla. "Influence of flow velocity on surface boiling heat transfer coefficient". In: *Heat Transfer in Boiling* 237.247 (1977).

[108] Anatoliy Levin and Polina Khan. "Characteristics of nucleate boiling under conditions of pulsed heat release at the heater surface". In: *Applied Thermal Engineering* 149 (2019), pp. 1215–1222. ISSN: 1359-4311. DOI: https://doi.org/10.1016/j.applthermaleng.2018.12.126. URL: https://www.sciencedirect.com/science/article/pii/S1359431118354929.

[109] Xiangdong Li et al. "Numerical and experimental investigation of heat transfer on heating surface during subcooled boiling flow of liquid nitrogen". In: *International Journal of Heat and Mass Transfer* 52.5 (2009), pp. 1510–1516. ISSN: 0017-9310. DOI: https://doi.org/10.1016/j.ijheatmasstransfer.2008.08.012. URL: https://www.sciencedirect.com/science/article/pii/S0017931008004936.

[110] Huaqiang Liu et al. "Molecular dynamics study of the nanoscale boiling heat transfer process on nanostructured surfaces". In: *International Communications in Heat and Mass Transfer* 119 (2020), p. 104963. ISSN: 0735-1933. DOI: https://doi.org/10.1016/j.icheatmasstransfer.2020.104963. URL: https://www.sciencedirect.com/science/article/pii/S0735193320304917.

[111] Yang Liu and Nam Dinh. "Flow Boiling in Tubes". In: *Handbook of Thermal Science and Engineering*. Ed. by Francis A. Kulacki. Cham: Springer International Publishing, 2017, pp. 1–44. ISBN: 978-3-319-32003-8. DOI: 10.1007/978-3-319-32003-8_47-1. URL: https://doi.org/10.1007/978-3-319-32003-8_47-1.

[112] M Lopez de Bertodano. "Turbulent bubbly flow in a triangular duct". In: *Rensselaer Polytechnic Institute, Troy, New York* (1991).

[113] L Ludick. "Computational investigation into jet impingement boiling on pin-fin surfaces". MA thesis. University of Pretoria, 2023. DOI: DOI:https://doi.org/10.25403/UPresearchdata.23805636.v1. URL: http://hdl.handle.net/2263/91699.

[114] L. Ludick et al. "Influence of pin-fin patterns and geometry on the effectiveness of jet impingement boiling – A computational study". In: *Applied Thermal Engineering* 229 (2023), p. 120626. ISSN: 1359-4311. DOI: https://doi.org/10.1016/j.applthermaleng.2023.120626. URL: https://www.sciencedirect.com/science/article/pii/S1359431123006555.

[115] C.-F. Ma and A.E. Bergles. "Jet impingement nucleate boiling". In: *International Journal of Heat and Mass Transfer* 29.8 (1986). https://doi.org/10.1016/0017-9310(86)90140-7, pp. 1095–1101.

[116] D. S. Mackenzie. "History of quenching". In: *International Heat Treatment and Surface Engineering* 2.2 (2008), pp. 68–73. DOI: 10.1179/174951508X358437. eprint: https://doi.org/10.1179/174951508X358437. URL: https://doi.org/10.1179/174951508X358437.

[117] Majid H. Majeed. "Static Contact Angle and Large Water Droplet Thickness Measurements with the Change of Water Temperature". In: *Al-Nahrain Journal for Engineering Sciences* 17 (2014), pp. 114–128. URL: https://api.semanticscholar.org/CorpusID:104049703.

[118] Preeti Mani, Ruander Cardenas, and Vinod Narayanan. "Comparison of area-averaged and local boiling curves in pool and jet impingement boiling". In: *International Journal of Multiphase Flow* 42 (2012), pp. 115–127. ISSN: 0301-9322. DOI: https://doi.org/10.1016/j.ijmultiphaseflow.2012.02.002. URL: https://www.sciencedirect.com/science/article/pii/S0301932212000304.

[119] Lan Mao et al. "Pool boiling performance and bubble dynamics on graphene oxide nanocoating surface". In: *International Journal of Thermal Sciences* 147 (2020), p. 106154.

[120] P. J. Marto, J. A. Moulson, and M. D. Maynard. "Nucleate Pool Boiling of Nitrogen With Different Surface Conditions". In: *Journal of Heat Transfer* 90.4 (Nov. 1968), pp. 437–444. ISSN: 0022-1481. DOI: 10.1115/1.3597539. eprint: https://asmedigitalcollection.asme.org/heattransfer/article-pdf/90/4/437/5743816/437_1.pdf. URL: https://doi.org/10.1115/1.3597539.

[121] Shigeo Maruyama. "Molecular dynamics method for microscale heat transfer". In: *Advances in Numerical Heat Transfer, Volume 2*. CRC Press, 2018, pp. 189–226.

[122] Shigeo Maruyama, Tatsuto Kimura, and Y Yamaguchi. "A molecular dynamics simulation of a bubble nucleation on solid surface". In: *National Heat Transfer Symposium of Japan*. Vol. 34. 1997, pp. 675–676.

[123] John P. McHale and Suresh V. Garimella. "Bubble nucleation characteristics in pool boiling of a wetting liquid on smooth and rough surfaces". In: *International Journal of Multiphase Flow* 36.4 (2010), pp. 249–260. ISSN: 0301-9322. DOI: https://doi.org/10.1016/j.ijmultiphaseflow.2009.12.004. URL: https://www.sciencedirect.com/science/article/pii/S0301932209001967.

[124] T. Ménard, S. Tanguy, and A. Berlemont. "Coupling level set/VOF/ghost fluid methods: Validation and application to 3D simulation of the primary break-up of a liquid jet". In: *International Journal of Multiphase Flow* 33.5 (2007), pp. 510–524. ISSN: 0301-9322. DOI: https://doi.org/10.1016/j.ijmultiphaseflow.2006.11.001. URL: https://www.sciencedirect.com/science/article/pii/S0301932206001832.

[125] B. B. Mikic and W. M. Rohsenow. "A New Correlation of Pool-Boiling Data Including the Effect of Heating Surface Characteristics". In: *Journal of Heat Transfer* 91.2 (May 1969), pp. 245–250. ISSN: 0022-1481. DOI: 10.1115/1.3580136. eprint: https://asmedigitalcollection.asme.org/heattransfer/article-pdf/91/2/245/5743525/245_1.pdf. URL: https://doi.org/10.1115/1.3580136.

[126] B.B. Mikic and W.M. Rohsenow. "Bubble growth rates in non-uniform temperature field". In: *Prog. Heat Mass Transfer* 2 (1969). Cited by: 101, pp. 283–292. URL: https://www.scopus.com/inward/record.uri?eid=2-s2.0-0000148883&partnerID=40&md5=8a73a3f65a4ed40fd1ad2e6efe16ea4b.

[127] D. Mills. *Pneumatic Conveying Design Guide*. 3rd. Butterworth Heinemann, 2016. ISBN: 978-0-08-100649-8.

[128] Shuichiro Miwa and Takashi Hibiki. "Inverted annular two-phase flow in multiphase flow systems". In: *International Journal of Heat and Mass Transfer* 186 (2022), p. 122340. ISSN: 0017-9310. DOI: https://doi.org/10.1016/j.ijheatmasstransfer.2021.122340. URL: https://www.sciencedirect.com/science/article/pii/S0017931021014393.

[129] Saeed Moghaddam and Ken Kiger. "Physical mechanisms of heat transfer during single bubble nucleate boiling of FC-72 under saturation conditions-I. Experimental investigation". In: *International Journal of Heat and Mass Transfer* 52.5 (2009), pp. 1284–1294. ISSN: 0017-9310. DOI: https://doi.org/10.1016/j.ijheatmasstransfer.2008.08.018. URL: https://www.sciencedirect.com/science/article/pii/S0017931008005267.

[130] Hamid Reza Mohammadi, Hamed Taghvaei, and Ataollah Rabiee. "Experimental study of pool boiling on hydrophilic and hydrophobic thin films deposited on copper surfaces using atmospheric cold plasma". In: *International Journal of Thermal Sciences* 175 (2022), p. 107474.

[131] Maysam Molana and Salem Banooni. "Investigation of Heat Transfer Processes Involved Liquid Impingement Jets: A Review". In: *Brazilian Journal of Chemical Engineering* 30 (Sept. 2013), pp. 413–435. DOI: 10.1590/S0104-66322013000300001.

[132] M Monde and Y Katto. "Burnout in a high heat-flux boiling system with an impinging jet". In: *International Journal of Heat and Mass Transfer* 21.3 (1978), pp. 295–305.

[133] Gilbert Moreno, Jana Montgomery, and Sreekant Narumanchi. "Effects of Pressure and a Microporous Coating on HFC-245fa Pool Boiling Heat Transfer". In: *Journal of Heat Transfer* 136 (Oct. 2014), p. 101502. DOI: 10.1115/1.4027966.

[134] I Mudawar and DC Wadsworth. "Critical heat flux from a simulated chip to a confined rectangular impinging jet of dielectric liquid". In: *International Journal of Heat and Mass Transfer* 34.6 (1991), pp. 1465–1479.

[135] Youngsuk Nam and Y Sungtaek Ju. "Bubble nucleation on hydrophobic islands provides evidence to anomalously high contact angles of nanobubbles". In: *Applied Physics Letters* 93.10 (2008).

[136] Youngsuk Nam et al. "Experimental and Numerical Study of Single Bubble Dynamics on a Hydrophobic Surface". In: *Journal of Heat Transfer* 131.12 (Oct. 2009), p. 121004. ISSN: 0022-1481. DOI: 10.1115/1.3216038. eprint: https://asmedigitalcollection.asme.org/heattransfer/article-pdf/131/12/121004/5915983/121004_1.pdf. URL: https://doi.org/10.1115/1.3216038.

[137] Sreekant Narumanchi et al. "Numerical simulations of nucleate boiling in impinging jets: Applications in power electronics cooling". In: *International Journal of Heat and Mass Transfer* 51.1 (2008), pp. 1–12. ISSN: 0017-9310. DOI: https://doi.org/10.1016/j.ijheatmasstransfer.2007.05.026. URL: https://www.sciencedirect.com/science/article/pii/S0017931007004115.

[138] T Nonn, Z Dagan, and LM Jiji. "Boiling jet impingement cooling of simulated microelectronic heat sources". In: *ASME Paper* 88 (1988).

[139] Tadhg S. O'Donovan and Darina B. Murray. "Jet impingement heat transfer – Part I: Mean and root-mean-square heat transfer and velocity distributions". In: *International Journal of Heat and Mass Transfer* 50.17 (2007), pp. 3291–3301. ISSN: 0017-9310. DOI: https://doi.org/10.1016/j.ijheatmasstransfer.2007.01.044. URL: https://www.sciencedirect.com/science/article/pii/S001793100700138X.

[140] Paweł Ocłoń, Stanisław Łopata, and Marzena Nowak-Ocłoń. "A novel 1D/2D model for simulating conjugate heat transfer applied to flow boiling in tubes with external fins". In: *Heat and Mass Transfer* 51 (Mar. 2015), pp. 553–566. DOI: 10.1007/s00231-014-1434-x.

[141] B.N. Pamadi and I.A. Belov. "A note on the heat transfer characteristics of circular impinging jet". In: *International Journal of Heat and Mass Transfer* 23.6 (1980), pp. 783–787. ISSN: 0017-9310. DOI: https://doi.org/10.1016/0017-9310(80)90032-0. URL: https://www.sciencedirect.com/science/article/pii/0017931080900320.

[142] Haonan Peng et al. "Thermal pseudo-potential lattice Boltzmann method for simulating cavitation bubbles collapse near a rigid boundary". In: *Computers and Fluids* 217 (2021). Cited by: 26. DOI: 10.1016/j.compfluid.2020.104817. URL: https://www.scopus.com/inward/record.uri?eid=2-s2.0-85098620456&doi=10.1016%2fj.compfluid.2020.104817&partnerID=40&md5=54f308fde6d449b1e9c17caf88acdd98.

[143] X. F. Peng, H. Y. Hu, and J. M. Ochterbeck. "Interface shape and Marangoni effect around a bubble within the thermal boundary layer". In: *Journal of Thermal Science* 7.1 (Mar. 1998), pp. 54–60. DOI: 10.1007/s11630-998-0026-9.

[144] Sanja Petrovic, Tony Robinson, and Ross L. Judd. "Marangoni heat transfer in subcooled nucleate pool boiling". In: *International Journal of Heat and Mass Transfer* 47.23 (2004), pp. 5115–5128. ISSN: 0017-9310. DOI: https://doi.org/10.1016/j.ijheatmasstransfer.2004.05.031. URL: https://www.sciencedirect.com/science/article/pii/S0017931004002315.

[145] Robert D. Plant, Jacob Friedman, and M. Ziad Saghir. "A review of jet impingement cooling". In: *International Journal of Thermofluids* 17 (2023), p. 100312. ISSN: 2666-2027. DOI: https://doi.org/10.1016/j.ijft.2023.100312. URL: https://www.sciencedirect.com/science/article/pii/S2666202723000320.

[146] M So Plesset and So A Zwick. "The growth of vapor bubbles in superheated liquids". In: *Journal of applied physics* 25.4 (1954), pp. 493–500.

[147] C G Jothi Prakash and R. Prasanth. "Approaches to design a surface with tunable wettability: a review on surface properties". In: *Journal of Materials Science* 56 (Jan. 2021), pp. 1–28. DOI: 10.1007/s10853-020-05116-1.

[148] S.L. Qi et al. "Flow boiling of liquid nitrogen in micro-tubes: Part II – Heat transfer characteristics and critical heat flux". In: *International Journal of Heat and Mass Transfer* 50.25 (2007), pp. 5017–5030. ISSN: 0017-9310. DOI: https://doi.org/10.1016/j.ijheatmasstransfer.2007.08.017. URL: https://www.sciencedirect.com/science/article/pii/S001793100700542X.

[149] Shangtuo Qian, David Z. Zhu, and Hui Xu. "Splashing generation by water jet impinging on a horizontal plate". In: *Experimental Thermal and Fluid Science* 130 (2022), p. 110518. ISSN: 0894-1777. DOI: https:

//doi.org/10.1016/j.expthermflusci.2021.110518. URL: https://www.sciencedirect.com/science/article/pii/S0894177721001618.

[150] Lu Qiu et al. "Effect of conjugation on jet impingement boiling heat transfer". In: *International Journal of Heat and Mass Transfer* 91 (2015), pp. 584–593. ISSN: 0017-9310. DOI: https://doi.org/10.1016/j.ijheatmasstransfer.2015.07.121. URL: https://www.sciencedirect.com/science/article/pii/S001793101500839X.

[151] Lu Qiu et al. "Recent developments of jet impingement nucleate boiling". In: *International Journal of Heat and Mass Transfer* 89 (2015), pp. 42–58. ISSN: 0017-9310. DOI: https://doi.org/10.1016/j.ijheatmasstransfer.2015.05.025. URL: https://www.sciencedirect.com/science/article/pii/S0017931015005086.

[152] Md Mahamudur Rahman, Emre Ölçeroglu, and Matthew McCarthy. "Role of wickability on the critical heat flux of structured superhydrophilic surfaces". In: *Langmuir* 30.37 (2014). Cited by: 425, pp. 11225–11234. DOI: 10.1021/la5030923. URL: https://www.scopus.com/inward/record.uri?eid=2-s2.0-84928539998&doi=10.1021%2fla5030923&partnerID=40&md5=7e832adc495b43766aa6858a017110b9.

[153] Milad Rakhsha, Christopher E. Kees, and Dan Negrut. "Lagrangian vs. Eulerian: An Analysis of Two Solution Methods for Free-Surface Flows and Fluid Solid Interaction Problems". In: *Fluids* 6.12 (2021). ISSN: 2311-5521. DOI: 10.3390/fluids6120460. URL: https://www.mdpi.com/2311-5521/6/12/460.

[154] M.J. Rau and S.V. Garimella. *Two-phase jet impingement: liquid-vapor interactions and heat transfer mapping for multiscale surface enhancement design*. Vol. 2. Encyclopedia of Two-Phase Heat Transfer and Flow. 2018.

[155] Matthew J Rau and Suresh V Garimella. "Confined jet impingement with boiling on a variety of enhanced surfaces". In: *Journal of Heat Transfer* 136.10 (2014), p. 101503.

[156] Tingting Ren et al. "Experimental study on bubble sliding for upward subcooled flow boiling in a narrow rectangular channel". In: *International Journal of Heat and Mass Transfer* 152 (2020), p. 119489. ISSN: 0017-9310. DOI: https://doi.org/10.1016/j.ijheatmasstransfer.2020.119489. URL: https://www.sciencedirect.com/science/article/pii/S0017931019358399.

[157] Wilko Rohlfs et al. "Influence of Local Flow Acceleration on the Heat Transfer of Submerged and Free-surface Jet Impingement". In: Aug. 2014. DOI: 10.1615/IHTC15.fcv.008378.

[158] Warren M Rohsenow. "A method of correlating heat-transfer data for surface boiling of liquids". In: *Transactions of the American Society of Mechanical Engineers* 74.6 (1952), pp. 969–975.

[159] I.M. Ross. "The invention of the transistor". In: *Proceedings of the IEEE* 86.1 (1998), pp. 7–28. DOI: 10.1109/5.658752.

[160] Amgad Salama. "Velocity Profile Representation for Fully Developed Turbulent Flows in Pipes: A Modified Power Law". In: *Fluids* 6.10 (2021). ISSN: 2311-5521. DOI: 10.3390/fluids6100369. URL: https://www.mdpi.com/2311-5521/6/10/369.

[161] Lee Sang-Joon, Lee Jung-Ho, and Lee Dae-Hee. "Local heat transfer measurements from an elliptic jet impinging on a flat plate using liquid crystal". In: *International Journal of Heat and Mass Transfer* 37.6 (1994), pp. 967–976. ISSN: 0017-9310. DOI: https://doi.org/10.1016/0017-9310(94)90221-6. URL: https://www.sciencedirect.com/science/article/pii/0017931094902216.

[162] H Schlichting. *Boundary-Layer Theory, 7th ednMcGraw-Hill*. 1979.

[163] Horst Schrader. *Trocknung feuchter Oberflächen mittels Warmluftstrahlen: Strömungsvorgänge und Stoffübertragung*. VDI-Verlag, 1961.

[164] Hamed Setoodeh et al. "Modelling and simulation of flow boiling with an Eulerian-Eulerian approach and integrated models for bubble dynamics and temperature-dependent heat partitioning". In: *International Journal of Thermal Sciences* 161 (2021), p. 106709. ISSN: 1290-0729. DOI: https://doi.org/10.1016/j.ijthermalsci.2020.106709. URL: https://www.sciencedirect.com/science/article/pii/S1290072920311558.

[165] Xiaohui She et al. "Bubble formation on solid surface with a cavity based on molecular dynamics simulation". In: *International Journal of Heat and Mass Transfer* 95 (2016). Cited by: 59, pp. 278–287. DOI: 10.1016/j.ijheatmasstransfer.2015.11.082. URL: https://www.scopus.com/inward/record.uri?eid=2-s2.0-84951161313&doi=10.1016%2fj.ijheatmasstransfer.2015.11.082&partnerID=40&md5=ab95ed61e2be489a4d512af0331c7d84.

[166] Chang Hwan Shin et al. "Influences of nozzle-plate spacing on boiling heat transfer of confined planar dielectric liquid impinging jet". In: *International Journal of Heat and Mass Transfer* 52.23 (2009), pp. 5293–5301. ISSN: 0017-9310. DOI: https://doi.org/10.1016/j.ijheatmasstransfer.2009.08.002. URL: https://www.sciencedirect.com/science/article/pii/S0017931009004219.

[167] Anuj Shukla and Anupam Dewan. "Flow and thermal characteristics of jet impingement: Comprehensive review". In: *International Journal of Heat and Technology* 35 (Mar. 2017), pp. 153–166. DOI: 10.18280/ijht.350121.

[168] Dushyant Singh, B. Premachandran, and Sangeeta Kohli. "Effect of nozzle shape on jet impingement heat transfer from a circular cylinder". In: *International Journal of Thermal Sciences* 96 (2015), pp. 45–

69. ISSN: 1290-0729. DOI: https://doi.org/10.1016/j.ijthermalsci.2015.04.011. URL: https://www.sciencedirect.com/science/article/pii/S1290072915001398.

[169] Gulshan Kumar Sinha, Saylee Mahimkar, and Atul Srivastava. "Schlieren-based simultaneous mapping of bubble dynamics and temperature gradients in nucleate flow boiling regime: Effect of flow rates and degree of subcooling". In: *Experimental Thermal and Fluid Science* 104 (2019), pp. 238–257. ISSN: 0894-1777. DOI: https://doi.org/10.1016/j.expthermflusci.2019.02.018. URL: https://www.sciencedirect.com/science/article/pii/S0894177718314225.

[170] Gulshan Kumar Sinha, Surya Narayan, and Atul Srivastava. "Microlayer dynamics during the growth process of a single vapour bubble under subcooled flow boiling conditions". In: *Journal of Fluid Mechanics* 931 (2022), A23.

[171] National Institute of Standards and Technology. *Material Properties: OFHC Copper (UNS C10100/C10200)*. Tech. rep. URL: https://trc.nist.gov/cryogenics/materials/OFHC%20Copper/OFHC_Copper_rev1.htm.

[172] National Institute of Standards and Technology. *Thermophysical Properties of Fluid Systems*. Tech. rep. URL: https://webbook.nist.gov/chemistry/fluid/#.

[173] Dongke Sun et al. "Lattice Boltzmann modeling of bubble formation and dendritic growth in solidification of binary alloys". In: *International Journal of Heat and Mass Transfer* 94 (2016). Cited by: 59, pp. 474–487. DOI: 10.1016/j.ijheatmasstransfer.2015.11.079. URL: https://www.scopus.com/inward/record.uri?eid=2-s2.0-84949595525&doi=10.1016%2fj.ijheatmasstransfer.2015.11.079&partnerID=40&md5=07aa1b2da4fb872102f42e3464ee0a8a.

[174] Zhiguo Tang et al. "Numerical simulation of heat transfer characteristics of jet impingement with a novel single cone heat sink". In: *Applied Thermal Engineering* 127 (2017), pp. 906–914. ISSN: 1359-4311. DOI: https://doi.org/10.1016/j.applthermaleng.2017.08.099. URL: https://www.sciencedirect.com/science/article/pii/S1359431117341911.

[175] Tayfun E. Tezduyar. "Interface-tracking and interface-capturing techniques for finite element computation of moving boundaries and interfaces". In: *Computer Methods in Applied Mechanics and Engineering* 195.23 (2006). Incompressible CFD, pp. 2983–3000. ISSN: 0045-7825. DOI: https://doi.org/10.1016/j.cma.2004.09.018. URL: https://www.sciencedirect.com/science/article/pii/S0045782505002367.

[176] H Thomann. "Effect of streamwise wall curvature on heat transfer in a turbulent boundary layer". In: *Journal of Fluid Mechanics* 33.2 (1968), pp. 283–292.

[177] Cristiano Bigonha Tibiriçá and Gherhardt Ribatski. "Flow patterns and bubble departure fundamental characteristics during flow boiling in microscale channels". In: *Experimental Thermal and Fluid Science* 59 (2014), pp. 152–165. ISSN: 0894-1777. DOI: https://doi.org/10.1016/j.expthermflusci.2014.02.017. URL: https://www.sciencedirect.com/science/article/pii/S089417771400048X.

[178] VI Tolubinsky and DM Kostanchuk. "Vapour bubbles growth rate and heat transfer intensity at subcooled water boiling". In: *International Heat Transfer Conference 4*. Vol. 23. Begel House Inc. 1970.

[179] Akio Tomiyama. "Struggle with computational bubble dynamics". In: *Multiphase Science and Technology* 10.4 (1998), pp. 369–405.

[180] L.S. Tong and Y. S. Tang. *Boiling Heat Transfer And Two-Phase Flow*. CRS Press, 1997.

[181] Marcin Trojan. "Transient Heat Conduction in Semi-infinite Solid with Surface Convection". In: *Encyclopedia of Thermal Stresses*. Ed. by Richard B. Hetnarski. Dordrecht: Springer Netherlands, 2014, pp. 6181–6186. ISBN: 978-94-007-2739-7. DOI: 10.1007/978-94-007-2739-7_415. URL: https://doi.org/10.1007/978-94-007-2739-7_415.

[182] C.V. Tu and D.H. Wood. "Wall pressure and shear stress measurements beneath an impinging jet". In: *Experimental Thermal and Fluid Science* 13.4 (1996). Peter Bradshaw 60th Birthday Issue: Part II, pp. 364–373. ISSN: 0894-1777. DOI: https://doi.org/10.1016/S0894-1777(96)00093-3. URL: https://www.sciencedirect.com/science/article/pii/S0894177796000933.

[183] H. C. Ünal. "Maximum bubble diameter, maximum bubble-growth time and bubble-growth rate during the subcooled nucleate flow boiling of water up to 17.7 MN/m2". In: *International Journal of Heat and Mass Transfer* 19 (1976), pp. 643–649. URL: https://api.semanticscholar.org/CorpusID:123421751.

[184] D. T. Vader, F. P. Incropera, and R. Viskanta. "Convective Nucleate Boiling on a Heated Surface Cooled by an Impinging, Planar Jet of Water". In: *Journal of Heat Transfer* 114.1 (Feb. 1992), pp. 152–160. ISSN: 0022-1481. DOI: 10.1115/1.2911241. eprint: https://asmedigitalcollection.asme.org/heattransfer/article-pdf/114/1/152/5746043/152_1.pdf. URL: https://doi.org/10.1115/1.2911241.

[185] D.T. Vader et al. "Experimental investigation of subcooled liquid nitrogen impingement cooling of a silicon chip". In: *IEEE Transactions on Components, Packaging, and Manufacturing Technology: Part A* 18.4 (1995), pp. 788–794. DOI: 10.1109/95.477465.

[186] V. H. Del Valle. PhD thesis. Oxford University, 1980.

[187] W.G.J. Van Helden, C.W.M. Van Der Geld, and P.G.M. Boot. "Forces on bubbles growing and detaching in flow along a vertical wall". In: *International Journal of Heat and Mass Transfer* 38.11 (1995), pp. 2075–2088. ISSN: 0017-9310. DOI: https://doi.org/10.1016/0017-9310(94)00319-Q. URL: https://www.sciencedirect.com/science/article/pii/001793109400319Q.

[188] R Viskanta. "Heat transfer to impinging isothermal gas and flame jets". In: *Experimental thermal and fluid science* 6.2 (1993), pp. 111–134.

[189] Ya-Qiao Wang et al. "PTFE-modified porous surface: Eliminating boiling hysteresis". In: *International Communications in Heat and Mass Transfer* 111 (2020), p. 104441. ISSN: 0735-1933. DOI: https://doi.org/10.1016/j.icheatmasstransfer.2019.104441. URL: https://www.sciencedirect.com/science/article/pii/S0735193319303070.

[190] D.S Wen and B.X Wang. "Effects of surface wettability on nucleate pool boiling heat transfer for surfactant solutions". In: *International Journal of Heat and Mass Transfer* 45.8 (2002), pp. 1739–1747. ISSN: 0017-9310. DOI: https://doi.org/10.1016/S0017-9310(01)00251-4. URL: https://www.sciencedirect.com/science/article/pii/S0017931001002514.

[191] Rongfu Wen et al. "Enhanced bubble nucleation and liquid rewetting for highly efficient boiling heat transfer on two-level hierarchical surfaces with patterned copper nanowire arrays". In: *Nano Energy* 38 (2017), pp. 59–65.

[192] Frank M. White. *Fluid mechanics*. 7th ed. Mcgraw-Hill series in mechanical engineering. New York, NY: McGraw-Hill, 2011. ISBN: 978-0-07-352934-9.

[193] D.H. Wolf, F.P. Incropera, and R. Viskanta. "Jet Impingement Boiling". In: ed. by James P. Hartnett and Thomas F. Irvine. Vol. 23. Advances in Heat Transfer. Elsevier, 1993, pp. 1–132. DOI: https://doi.org/10.1016/S0065-2717(08)70005-4. URL: https://www.sciencedirect.com/science/article/pii/S0065271708700054.

[194] D Wright. "Investigation into simulation of phase-change jet impingement for electronics cooling". MA thesis. University of Pretoria, 2022. DOI: DOI:10.25403/UPresearchdata.20435856. URL: https://repository.up.ac.za/handle/2263/86719.

[195] D. Wright et al. "Computational investigation of single and multi-jet array impingement boiling". In: *Applied Thermal Engineering* 218 (2023), p. 119342. ISSN: 1359-4311. DOI: https://doi.org/10.1016/j.applthermaleng.2022.119342. URL: https://www.sciencedirect.com/science/article/pii/S1359431122012728.

[196] V. Yakhot et al. "Development of Turbulence Models for Shear Flows by a Double Expansion technique." In: *Physics of Fluids A Fluid Dynamics* 4 (Aug. 1992). DOI: 10.1063/1.858424.

[197] Takahiro Yamamoto and Mitsuhiro Matsumoto. "Initial stage of nucleate boiling: Molecular dynamics investigation". In: *Journal of Thermal Science and Technology* 7.1 (2012). Cited by: 73; All Open Access, Bronze Open Access, pp. 334–349. DOI: 10.1299/jtst.7.334. URL: https://www.scopus.com/inward/record.uri?eid=2-s2.0-84892161820&doi=10.1299%2fjtst.7.334&partnerID=40&md5=7cf39ab29abb9ecd8f25fd2e8b37b24f.

[198] Geunyoung Yang, Mansoo Choi, and Joon Sik Lee. "An experimental study of slot jet impingement cooling on concave surface: effects of nozzle configuration and curvature". In: *International Journal of Heat and Mass Transfer* 42.12 (1999), pp. 2199–2209. ISSN: 0017-9310. DOI: https://doi.org/10.1016/S0017-9310(98)00337-8. URL: https://www.sciencedirect.com/science/article/pii/S0017931098003378.

[199] Guang Yang et al. "Review on bubble dynamic of subcooled flow boiling-part a: Research methodologies". In: *International Journal of Thermal Sciences* 184 (2023), p. 108019. ISSN: 1290-0729. DOI: https://doi.org/10.1016/j.ijthermalsci.2022.108019. URL: https://www.sciencedirect.com/science/article/pii/S1290072922005476.

[200] Guang Yang et al. "Review on bubble dynamic of subcooled flow boiling-part b: Behavior and models". In: *International Journal of Thermal Sciences* 184 (2023), p. 108026. ISSN: 1290-0729. DOI: https://doi.org/10.1016/j.ijthermalsci.2022.108026. URL: https://www.sciencedirect.com/science/article/pii/S1290072922005543.

[201] Junsoo Yoo, Carlos E. Estrada-Perez, and Yassin A. Hassan. "Area of bubble influence due to sliding bubbles in subcooled boiling flow". In: *International Journal of Heat and Mass Transfer* 125 (2018), pp. 43–52. ISSN: 0017-9310. DOI: https://doi.org/10.1016/j.ijheatmasstransfer.2018.04.058. URL: https://www.sciencedirect.com/science/article/pii/S0017931017355722.

[202] Junsoo Yoo, Carlos E. Estrada-Perez, and Yassin A. Hassan. "Development of a mechanistic model for sliding bubbles growth prediction in subcooled boiling flow". In: *Applied Thermal Engineering* 138 (2018), pp. 657–667. ISSN: 1359-4311. DOI: https://doi.org/10.1016/j.applthermaleng.2018.04.096. URL: https://www.sciencedirect.com/science/article/pii/S1359431117369727.

[203] Zhao Yu, Hui Yang, and Liang-Shih Fan. "Numerical simulation of bubble interactions using an adaptive lattice Boltzmann method". In: *Chemical Engineering Science* 66.14 (2011). Cited by: 83, pp. 3441–3451. DOI: 10.1016/j.ces.2011.01.019. URL: https://www.scopus.com/inward/record.

uri?eid=2-s2.0-79958699225&doi=10.1016%2fj.ces.2011.01.019&partnerID=40&md5=76e6d8fe80159d3237122ae0ad51918e.

[204] Bo Yuan et al. "Experimental research on subcooled flow boiling heat transfer performance and associated bubble characteristics under pulsating flow". In: *Applied Thermal Engineering* 157 (2019), p. 113721.

[205] P. Zhang et al. "Confined jet impingement of liquid nitrogen onto different heat transfer surfaces". In: *Cryogenics* 51.6 (2011). Special Issue: ACASC 2009, pp. 300–308. ISSN: 0011-2275. DOI: https://doi.org/10.1016/j.cryogenics.2010.06.018. URL: https://www.sciencedirect.com/science/article/pii/S0011227510001402.

[206] Jianfu ZHAO et al. "Marangoni Effect in Subcooled Nucleate Pool Boiling". In: *Chinese Journal of Space Science* 28.2 (2008), p. 159. ISSN: 0254-6124. DOI: 10.11728/cjss2008.02.159. URL: http://dx.doi.org/10.11728/cjss2008.02.159.

[207] Zenghui Zhao, Yoav Peles, and Michael K Jensen. "Water jet impingement boiling from structured-porous surfaces". In: *International Journal of Heat and Mass Transfer* 63 (2013), pp. 445–453.

[208] DW Zhou and CF Ma. "Local jet impingement boiling heat transfer with R113". In: *Heat and Mass Transfer* 40 (2004), pp. 539–549.

[209] DW Zhou, CF Ma, and J Yu. "Boiling hysteresis of impinging circular submerged jets with highly wetting liquids". In: *International journal of heat and fluid flow* 25.1 (2004), pp. 81–90.

[210] DW Zhou, CF Ma, and J Yu. "Boiling hysteresis of impinging circular submerged jets with highly wetting liquids". In: *International journal of heat and fluid flow* 25.1 (2004), pp. 81–90.

[211] Pei Zhou et al. "Experimental investigation on bubble contact diameter and bubble departure diameter in horizontal subcooled flow boiling". In: *International Journal of Heat and Mass Transfer* 149 (2020), p. 119105. ISSN: 0017-9310. DOI: https://doi.org/10.1016/j.ijheatmasstransfer.2019.119105. URL: https://www.sciencedirect.com/science/article/pii/S0017931019348240.

[212] Neil Zuckerman and Noam Lior. "Jet Impingement Heat Transfer: Physics, Correlations, and Numerical Modeling". In: *Advances in heat transfer* 39 (2006), pp. 565–631. URL: https://api.semanticscholar.org/CorpusID:14810226.

Appendix A

The Multi-phase Eulerian Model

A.1 Overview

In the Multi-phase Eulerian model, phases are treated separately and are assumed to form interpenetrating continua (i.e. multiple phases can occupy the same region of space, each with their own respective properties continuous over that region[1]). However, in order to ensure that the total volume within every region of space remains constant, the concept of phasic volume fractions is introduced. Additionally, in order to account for the exchange of quantities between the phases, source and closing terms are introduced into the equations of the conservation of mass, linear momentum and energy for each phase. [127]

Below is a brief overview of the local instantaneous multi-phase (Eulerian-Eulerian) framework followed by an explanation of the Favre averaged model that necessitates the addition of a closing turbulence model and wall function selection. Where applicable, comments will be made concerning the sub-model choices and reasons for selection.

A.2 Governing Local Instant Partial Differential Equations

A.2.1 Volume Fraction

The volume fraction (α_q) is a dimensionless variable that forms a continuous function in both space and time and represents the fractional volume of phase q at every point in space [71].

$$\forbidden{V_q} = \int_{CV} \alpha_q \, d\forbidden{V} \tag{A.1}$$

The volume fraction is subject to the constraint:

$$\sum_{q=1}^{n} \alpha_q = 1 \tag{A.2}$$

Where n represents the total number of phases being considered.

An example distribution of the volume fraction along a surface is illustrated in *fig. A.1* for a three phase system. Note that *eq.* (A.2) holds throughout the domain as shown in the right of *fig. A.1*.

A.2.2 Conservation of Mass

Applying *eq.* (A.1) to the conservation of mass [40], for an infinitesimal control volume in Cartesian co-ordinates ($d\forbidden{V} = dx\ dy\ dz$) we obtain [71]:

$$\frac{\partial(\alpha_q \rho_q)}{\partial t} + \nabla(\alpha_q \rho_q \vec{\boldsymbol{V}}_{\boldsymbol{q}}^{\,T}) = \sum_{p=1}^{n} \left(\dot{m_{pq,q}} - \dot{m_{qp,q}} \right) \tag{A.3}$$

[1] The applicability of this statement is only strictly true when referring to the averaged governing equations

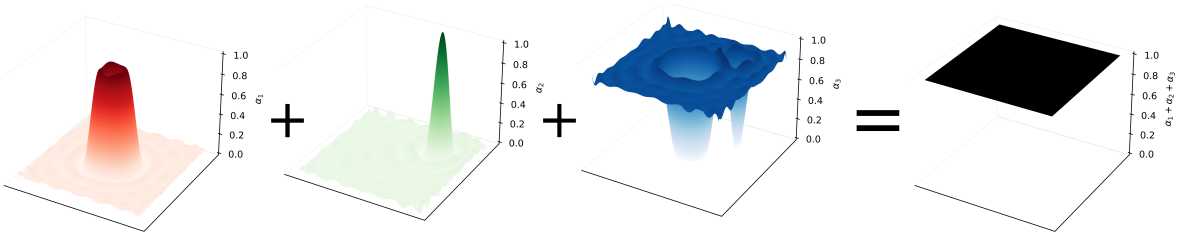

Figure A.1: Theoretical distribution of volume fractions for a 3 phase system along a single 2D surface with the resulting summation of the volume fractions displayed on the right

where ρ_q is the density of phase q. $\vec{\boldsymbol{V_q}} = [u_q, v_q, w_q]$ and $\nabla = [\frac{\partial}{\partial x}, \frac{\partial}{\partial y}, \frac{\partial}{\partial z}]$ are row vectors representing the velocity of phase q and the gradient operator, respectively. Furthermore when performing matrix multiplication of ∇ from the left, it is assumed that the operator acts on the term with which it is "multiplied". $\dot{m_{qp,q}}$ is the rate of mass transfer from phase q to phase p from the perspective of phase q and likewise, $\dot{m_{pq,q}}$ is the rate of mass transfer from phase p to phase q again from the perspective of phase q.

Furthermore, it is assumed that the total mass within the system remains constant ($\frac{dm_{syst}}{dt} = 0$) and thus the following relation is applied to ensure mass is neither lost nor generated when matter transitions between phases:

$$\dot{m_{pq,q}} = \dot{m_{pq,p}} \tag{A.4}$$

Mechanisms governing the transfer of mass are dependent on a number of factors including but not limited to: phase, material type and properties, operating conditions etc.. Thus a number of analytical and empirical equations have been proposed to provide a closed form solution to this term.

Mass Closing Models (two phase system)

For a two phase system this can be written as:

$$\dot{m_{pq}} = h_{ls}(T_l - T_i) \tag{A.5}$$

A_i is the interfacial area concentration computed from the ratio of spherical bubble surface area to volume [71]:

$$A_i = \frac{\pi d_b^2}{\frac{1}{6}\pi d_b^3} = \frac{6}{d_b} \tag{A.6}$$

where d_b is the bubble diameter.

A.2.3 Conservation of Momentum

Applying *eq.* (A.1) to the conservation of linear momentum [71], we obtain:

$$\begin{gathered}\frac{\partial(\alpha_q\rho_q\vec{\boldsymbol{V_q}})}{\partial t} + \nabla(\alpha_q\rho_q\vec{\boldsymbol{V_q}}^T\vec{\boldsymbol{V_q}}) = \\ -\alpha_q\nabla(P\bar{\bar{\boldsymbol{I}}}) + \nabla(\bar{\bar{\boldsymbol{\tau_q}}}) + \\ \alpha_q\rho_q\vec{\boldsymbol{g}} + \sum_{p=1}^{n}\Big(\vec{\boldsymbol{R_{pq}}} + \dot{m_{pq,q}}\vec{\boldsymbol{V_{pq}}} - \dot{m_{qp,q}}\vec{\boldsymbol{V_{qp}}}\Big) + \\ \vec{\boldsymbol{F_q}} + \vec{\boldsymbol{Flift_{,q}}} + \vec{\boldsymbol{Fwall_{,q}}} + \vec{\boldsymbol{Fvm_{,q}}} + \vec{\boldsymbol{Ftd_{,q}}}\end{gathered} \tag{A.7}$$

where $\bar{\bar{\boldsymbol{\tau_q}}}$ is the viscous stress tensor:

$$[\tau_q]_{ij} = \alpha_q\Big(\mu_q(\partial_i[V_q]_j + \partial_j[V_q]_i) + (\Lambda_q - \frac{2}{3}\mu_q)\partial_k[V_q]_k\delta_{ij}\Big) \tag{A.8}$$

where μ_q represents the shear viscosity and Λ_q the "bulk viscosity" of phase q. Note that this is an unconventional method of writing this equation as the actual bulk viscosity of the material that one would find in literature would be equated to this "bulk viscosity" by the formula:

$$\Lambda_{actual,q} = \Lambda_q + \frac{2}{3}\mu_q \tag{A.9}$$

From this point forth, Stokes's assumption will be invoked, implying $\Lambda_q = 0$.

$\vec{\boldsymbol{F_q}}$ represents the external body force (Note that gravitational forces have already been accounted for in the $\alpha_q \rho_q \vec{\boldsymbol{g}}$ term), $\vec{\boldsymbol{F_{lift,q}}}$ the lift force, $\vec{\boldsymbol{F_{wall,q}}}$ the wall lubrication force, $\vec{\boldsymbol{F_{vm,q}}}$ the virtual mass force and $\vec{\boldsymbol{F_{td,q}}}$ the turbulent dispersion force. P is the pressure term that is shared by all the phases. $\bar{\bar{\boldsymbol{I}}}$ is the identity matrix.

The summation term considers the exchange of momentum between the phases and consists of two parts. The first is the direct momentum exchange as mass in one phase carries its current momentum over to the other phase when it transitions phase. This is enforced with the terms:

$$\vec{\boldsymbol{V_{pq}}} = \begin{cases} \vec{\boldsymbol{V_p}} & \text{if } \dot{m_{pq,q}} > 0 \\ \vec{\boldsymbol{V_q}} & \text{if } \dot{m_{pq,q}} < 0 \end{cases} \quad \text{and} \quad \vec{\boldsymbol{V_{qp}}} = \begin{cases} \vec{\boldsymbol{V_q}} & \text{if } \dot{m_{qp,q}} > 0 \\ \vec{\boldsymbol{V_p}} & \text{if } \dot{m_{qp,q}} < 0 \end{cases} \tag{A.10}$$

which results in momentum being conserved as mass is transferred from one phase to another.

The second part is the term $\vec{\boldsymbol{R_{pq}}}$ (representing the mean interaction force between phases p and q [independent of turbulent effects]) which is subject to the following relations:

$$\vec{\boldsymbol{R_{pq}}} = -\vec{\boldsymbol{R_{qp}}} \quad \text{and} \quad \vec{\boldsymbol{R_{qq}}} = \vec{\boldsymbol{0}} \tag{A.11}$$

This term is dependent on a number of factors including: friction, pressure and cohesion. A closing relation is applied using the formula:

$$\vec{\boldsymbol{R_{pq}}} = K_{pq}\left(\vec{\boldsymbol{V_p}} - \vec{\boldsymbol{V_q}}\right) \tag{A.12}$$

where K_{pq} is the interphase momentum exchange coefficient:

$$K_{pq} = \frac{\rho_p f_{drag}}{6\tau_p} d_b A_i \tag{A.13}$$

$$\tau_p = \frac{\rho_p d_b^2}{18\mu_q} \tag{A.14}$$

f_{drag} is a drag function and A_i is the interfacial area concentration.

Momentum Closing Models (two phase system)

The following closing correlations have been proposed for the simulations used in this text:

External body force: $(\vec{\boldsymbol{F_q}})$

Neglected in this case due to the absence of magnetic or electrical fields that impact the fluid flow.

Lift force: $(\vec{\boldsymbol{F_{lift,q}}})$

$$\vec{\boldsymbol{F_{lift,q}}} = -C_{lift}\rho_q\alpha_q(\vec{\boldsymbol{V_q}} - \vec{\boldsymbol{V_p}}) \times (\nabla \times \vec{\boldsymbol{V_q}}) \tag{A.15}$$

where C_{lift} is the lift Coefficient. The *Tomiyama* lift Coefficient model is suitable for examining the lift force on larger-scale deformable bubbles within the ellipsoidal and spherical cap regimes [71]. The original model presented by Tomiyama 1998 [179] was modified by Frank, Shi, and Burns 2004 [50] and is presented below:

$$C_{lift} \begin{cases} \min\left[0.288\tanh\left(0.121Re_p\right), f(Eo^*)\right] & \text{if } Eo^* \leq 4 \\ f(Eo^*) & \text{if } 4 < Eo^* \leq 10 \\ -0.27 & \text{if } 10 < Eo^* \end{cases} \tag{A.16}$$

$$Re_p = \frac{\rho_q |\vec{\boldsymbol{V}}_{\boldsymbol{q}} - \vec{\boldsymbol{V}}_{\boldsymbol{p}}| d_b}{\mu_q} \tag{A.17}$$

$$f(Eo^*) = 0.00105Eo^{*3} - 0.0159Eo^{*2} - 0.0204Eo^* + 0.474 \tag{A.18}$$

$$Eo^* = \frac{g(\rho_q - \rho_v)d_h^2}{\sigma} \tag{A.19}$$

$$d_h = d_b(1 + 0.163Eo^{0.757})^{1/3} \tag{A.20}$$

where d_b is the bubble diameter and Eo is the Eötvös number:

$$Eo = \frac{g(\rho_q - \rho_v)d_b^2}{\sigma} \tag{A.21}$$

Wall lubrication force: $(\vec{\boldsymbol{F}}_{\boldsymbol{wall,p}})$

This force forces the vapour phase away from the wall.

$$\vec{\boldsymbol{F}}_{\boldsymbol{wall,p}} = C_{wall}\rho_q\alpha_p|\vec{\boldsymbol{V}}_{\boldsymbol{q}} - \vec{\boldsymbol{V}}_{\boldsymbol{p}}|^2\vec{\boldsymbol{n}}_{\boldsymbol{w}} \tag{A.22}$$

where C_{wall} is the wall lubrication coefficient and $\vec{\boldsymbol{n}}_{\boldsymbol{w}}$ is a normal vector to the wall.

The model proposed by Antal, Lahey Jr, and Flaherty 1991 [11] for C_{wall} is:

$$C_{wall} = \max\left(0, \frac{-0.01}{d_b}, \frac{0.05}{y_w}\right) \tag{A.23}$$

where y_w is the distance from the wall adjacent cell centre to the wall. $y_w < 5d_b$ for the model to be applicable [71].

Virtual mass force: $(\vec{\boldsymbol{F}}_{\boldsymbol{vm,q}})$

$$\vec{\boldsymbol{F}}_{\boldsymbol{vm,p}} = C_{vm}\alpha_p\rho_q\left(\frac{D\vec{\boldsymbol{V}}_{\boldsymbol{q}}}{Dt} - \frac{D\vec{\boldsymbol{V}}_{\boldsymbol{p}}}{Dt}\right) \tag{A.24}$$

where C_{vm} is the virtual mass coefficient. Due to the time dependent nature of this force, it was neglected and $C_{vm} = 0$ was selected.

Turbulent dispersion force: $(\vec{\boldsymbol{F}}_{\boldsymbol{td,q}})$

This force accounts for momentum transfer between phases. The turbulent dispersion force proposed by Lopez de Bertodano 1991 [112] is:

$$\vec{\boldsymbol{F}}_{\boldsymbol{td,q}} = -\vec{\boldsymbol{F}}_{\boldsymbol{td,p}} = C_{td}\rho_q k_q \nabla\alpha_p \tag{A.25}$$

with $C_{td} = 1$ and k_q the turbulent kinetic energy.

Drag function: (f_{drag})

$$f_{drag} = \frac{C_{drag}Re_p}{24} \tag{A.26}$$

with the drag coefficient (C_{drag}) determined from the model proposed by Ishii 1990 [76]:

$$C_{drag} = \min(C_{D,vis}, C_{D,dis}) \tag{A.27}$$

$$C_{D,vis} = \frac{24}{Re_p}(1 + 0.15Re_p^{0.75}) \tag{A.28}$$

$$C_{D,dis} = \frac{2}{3}\frac{d_b}{\sqrt{\frac{\sigma}{g(rho_q - rho_p)}}} \tag{A.29}$$

A.2.4 Conservation of Energy

Applying *eq.* (A.1) to the conservation of energy [71], we obtain:

$$\begin{gathered}\frac{\partial\left(\alpha_q\rho_q\left[e_q + \frac{\vec{\boldsymbol{V}}_{\boldsymbol{q}}\vec{\boldsymbol{V}}_{\boldsymbol{q}}{}^T}{2}\right]\right)}{\partial t} + \nabla\left(\alpha_q\rho_q\left[h_q + \frac{\vec{\boldsymbol{V}}_{\boldsymbol{q}}\vec{\boldsymbol{V}}_{\boldsymbol{q}}{}^T}{2}\right]\vec{\boldsymbol{V}}_{\boldsymbol{q}}{}^T\right) = \\ \nabla\left(\alpha_q k_{eff,q}(\nabla(T_q\bar{\bar{\boldsymbol{I}}}))^T + (\vec{\boldsymbol{V}}_{\boldsymbol{q}}\bar{\bar{\boldsymbol{\tau}}}_{\boldsymbol{eff,q}})^T\right) + \sum_{p=1}^{n}\left(Q_{pq} + \dot{m_{pq,q}}h_{pq} - \dot{m_{qp,q}}h_{qp}\right) + P\frac{\partial\alpha_q}{\partial t} + S_q\end{gathered} \tag{A.30}$$

Here, e_q is the internal energy, h_q is the enthalpy referenced to the enthalpy at a standard temperature. h_{pq} is the interphase enthalpy defined in a similar manner to *eq.* (A.10):

$$h_{pq} = \begin{cases} h_p & \text{if } \dot{m_{pq,q}} > 0 \\ h_q & \text{if } \dot{m_{pq,q}} < 0 \end{cases} \quad \text{and} \quad h_{qp} = \begin{cases} h_q & \text{if } \dot{m_{qp,q}} > 0 \\ h_p & \text{if } \dot{m_{qp,q}} < 0 \end{cases} \tag{A.31}$$

$k_{eff,q}$ is the effective thermal conductivity of phase q, calculated as:

$$k_{eff,q} = k_q + k_{t,q} \tag{A.32}$$

where $k_{t,q}$ is the turbulent contribution that enhances the thermal conductivity and is computed from the chosen turbulence model. $\bar{\bar{\boldsymbol{\tau}}}_{\boldsymbol{eff,q}}$ is the effective viscous stress tensor of phase q also calculated from the relevant turbulent model.

A.3 Reynolds and Favre Averaging

A.3.1 FANS Overview

As the applications of interest in this paper operates in the turbulent regime (so as to maximise heat transfer), a Favre averaging approach is applied to the governing partial differential equations (PDEs) *eq.* (A.3), *eq.* (A.7) and *eq.* (A.30) to form the Favre-Averaged Navier–Stokes (FANS) equations. This accounts for turbulent effects, whilst reducing the computational cost in comparison to more direct solvers such as Direct Numerical Simulation (DNS) solvers.

To begin with, let us discuss Reynolds decomposition. This approach is predicated on the assumption that all flow variables can be decomposed into their ensemble mean and a fluctuating components:

$$\phi_q = \hat{\phi_q} + \phi_q' \tag{A.33}$$

where ϕ_q is a function of space and time and can be substituted for any vector (such as $\vec{\boldsymbol{V}}_{\boldsymbol{q}}$) or scalar (such as P) quantity. $\hat{\phi_q}$ is the ensemble mean/average component defined as:

$$\hat{\phi_q} = \int_{-\infty}^{\infty}\int_{-\infty}^{\infty}\int_{-\infty}^{\infty}\int_{-\infty}^{\infty}\phi_q(\vec{\boldsymbol{X}},t)\Psi(\vec{\boldsymbol{X}},t)\,dx\,dy\,dz\,dt \tag{A.34}$$

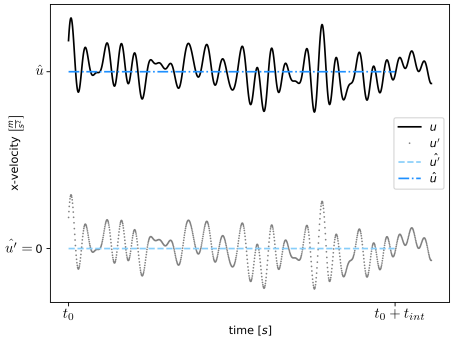

Figure A.2: Turbulent fluctuations of $\phi = u$ at a specific point in space over a finite time period

where $\vec{\boldsymbol{X}} = [x, y, z]$ and $\Psi(\vec{\boldsymbol{X}}, t)$ is the probability distribution function related to ϕ_q [18].

If one were to restrict themselves to averaging over time:

$$\hat{\phi}_q \approx \frac{1}{t_{int}} \int_{t_0}^{t_0+t_{int}} \phi_q \, dt \tag{A.35}$$

where t_{int} is the averaging period and is selected large enough to encapsulate a substantial number of fluctuations such that the average is representative of the true average [192]. This is illustrated in *fig. A.2* in order for one to visualise the concept, however, full ensemble averaging (over space and time) will be considered in this text from this point forth.

Applying this technique to calculate the ensemble average of the fluctuating component yields:

$$\hat{\phi}'_q = \widehat{(\phi_q - \hat{\phi}_q)} = \hat{\phi}_q - \hat{\phi}_q = 0 \tag{A.36}$$

However, the average of the product of two fluctuating components is in general not equivalent to zero:

$$\widehat{\phi'_q \gamma'_q} \neq 0 \tag{A.37}$$

where γ is yet another arbitrary flow variable (note: an argument of γ_q could be $\gamma_q = \phi_q$ in *eq.* (A.37)).

Applying Reynolds decomposition directly to all flow variables within the governing PDEs and then taking the ensemble average yields a large number of additional terms in all three equations. In order to reduce the number of additional terms (so as to reduce the number of closure models that need to be proposed) the concept of Favre averaging is introduced. Volume-weighted Favre averaged variables are defined as [25]:

$$\check{\phi}_q = \frac{\widehat{\alpha_q \phi_q}}{\hat{\alpha}_q} \tag{A.38}$$

whilst mass-weighted Favre averaged variables are defined as [25]:

$$\tilde{\phi}_q = \frac{\widehat{\alpha_q \rho_q \phi_q}}{\widehat{\alpha_q \rho_q}} \tag{A.39}$$

In an analogous manner to Reynolds decomposition, Favre decomposition can then be used to split variables into their mean and fluctuating components:

$$\text{Volume-averaged:} \qquad \phi_q = \check{\phi}_q + \phi''_q \tag{A.40}$$

$$\text{Mass-averaged:} \qquad \phi_q = \tilde{\phi}_q + \phi'''_q \tag{A.41}$$

Now, after applying Reynolds decomposition to each variable and ensemble averaging the PDEs, *eq.* (A.38)-*eq.* (A.41) together with the averaging rules in [25] can be used to re-arrange the resulting terms and express them in a more compact and elegant form. This yields the Favre-Averaged Navier–Stokes (FANS) equations:

Conservation of mass:

$$\frac{\partial \widehat{(\alpha_q \rho_q)}}{\partial t} + \nabla(\widehat{(\alpha_q \rho_q)} \tilde{\vec{\boldsymbol{V}}}_{\boldsymbol{q}}^{\,T}) = \sum_{p=1}^{n} \left(\overline{\dot{m}_{pq,q}} - \overline{\dot{m}_{qp,q}} \right) \tag{A.42}$$

where the $\overline{\phi}$ symbol has been utilised as a reminder that the terms for which there are still no closure models proposed (at this stage) must be based on the available Favre averaged values.

Conservation of momentum:

$$\begin{gathered}\frac{\partial(\widehat{(\alpha_q\rho_q)}\tilde{\vec{\boldsymbol{V}}}_{\boldsymbol{q}})}{\partial t}+\nabla(\widehat{(\alpha_q\rho_q)}\tilde{\vec{\boldsymbol{V}}}_{\boldsymbol{q}}{}^{T}\tilde{\vec{\boldsymbol{V}}}_{\boldsymbol{q}})= \\ -\hat{\alpha_q}\nabla(\check{P}\bar{\bar{\boldsymbol{I}}})+\nabla(\tilde{\bar{\bar{\boldsymbol{\tau}}}}_{\boldsymbol{q}})+ \\ \widehat{(\alpha_q\rho_q)}\vec{\boldsymbol{g}}+\sum_{p=1}^{n}\Big(\overline{\vec{\boldsymbol{R}}_{\boldsymbol{pq}}}+\overline{\dot{m}_{pq,q}\vec{\boldsymbol{V}}_{\boldsymbol{pq}}}-\overline{\dot{m}_{qp,q}\vec{\boldsymbol{V}}_{\boldsymbol{qp}}}\Big)+ \\ \overline{\vec{\boldsymbol{F}}_{\boldsymbol{q}}}+\overline{\vec{\boldsymbol{F}}_{\boldsymbol{lift,q}}}+\overline{\vec{\boldsymbol{F}}_{\boldsymbol{wall,q}}}+\overline{\vec{\boldsymbol{F}}_{\boldsymbol{vm,q}}}+\overline{\vec{\boldsymbol{F}}_{\boldsymbol{td,q}}}- \\ \widehat{(\alpha_q\rho_q\vec{\boldsymbol{V}}_{\boldsymbol{q}}{}'''^{T}\vec{\boldsymbol{V}}_{\boldsymbol{q}}{}''')}\end{gathered} \tag{A.43}$$

The last term in *eq.* (A.43) is called the *Reynolds stress* or *turbulent stress*. It has the same units as stress and is a result of turbulent fluctuations. A suitable closure model for this term can be found in [71].

If one assumes that $\mu_q \approx$ constant:

$$[\check{\tau}_q]_{ij}=\hat{\alpha_q}\Big(\mu_q(\partial_i[\check{V}_q]_j+\partial_j[\check{V}_q]_i)+(\frac{2}{3}\mu_q)\partial_k[\check{V}_q]_k\delta_{ij}\Big) \tag{A.44}$$

Unfortunately, *eq.* (A.44) is rather problematic as it contains a volume-averaged velocity ($\check{\vec{\boldsymbol{V}}}_{\boldsymbol{q}}$) whilst the the rest of the momentum equation contains the mass-averaged velocity ($\tilde{\vec{\boldsymbol{V}}}_{\boldsymbol{q}}$). This effectively introduces an additional variable which would necessitate the introduction of an additional equation to form a closed set of equations. However, if the following assumption is made:

$$\begin{gathered}\check{\vec{\boldsymbol{V}}}_{\boldsymbol{q}}=\frac{\widehat{\alpha_q\vec{\boldsymbol{V}}_{\boldsymbol{q}}}}{\hat{\alpha_q}}\approx\frac{\widehat{\alpha_q\rho_q\vec{\boldsymbol{V}}_{\boldsymbol{q}}}}{\widehat{\alpha_q\rho_q}}=\tilde{\vec{\boldsymbol{V}}}_{\boldsymbol{q}} \\ \therefore\rho_q\approx\text{constant w.r.t}\ \frac{d\widehat{\alpha_q}}{dt}\end{gathered} \tag{A.45}$$

This assumption can be justified considering that $\widehat{\alpha_q}$ is expected to vary over several orders of magnitude whilst ρ_q is expected to vary by far less than a single order of magnitude [196] (even with considerable pressure and temperature variations). An important distinction to make here is the fact that variable density is not strictly being omitted in the above formulation, its effects are just negligible in comparison to the volume fraction concentration. Therefore only minor errors will be made in the stress tensor term if one considers variable density.

Appendix B

Enhanced Quenching Coefficient

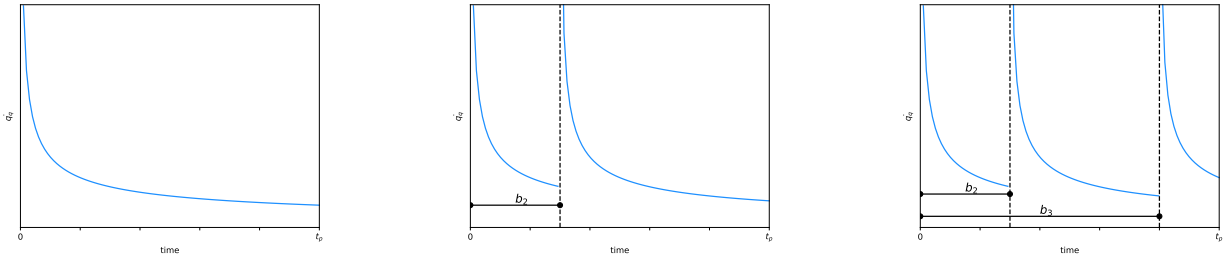

(a) Single area of influence *(b) Two overlapping areas of influence* *(c) Two overlapping areas of influence*

Figure B.1: Local instantaneous quenching heat flux for different overlapping scenarios for out of phase bubble departure

The instantaneous quenching heat transfer that occurs on an area of influence around a single isolated nucleation site is represented by *eq.* (3.10) and is repeated here for convenience:

$$\dot{q_q}(t) = \frac{k_l(T_w - T_l)}{\sqrt{\pi \lambda_l t}} \tag{B.1}$$

Let:

$$\Phi = \frac{k_l(T_w - T_l)}{\sqrt{\pi \lambda_l}} \tag{B.2}$$

Therefore the average of *eq.* (B.1) over a single bubble period is:

$$\dot{\bar{q}_1} = \Phi \frac{1}{t_p} \int_0^{t_p} t^{-\frac{1}{2}} dt = 2 t_p^{-\frac{1}{2}} \Phi \tag{B.3}$$

For two overlapping regions of the same frequencies but having phases that are independent of one another, the total average heat transfer becomes (where b_2 represents the offset between the initial and subsequent quenching event (*fig. B.1b*):

$$\dot{\bar{q}_2} = \Phi \frac{1}{t_p} \left[\frac{1}{t_p} \int_0^{t_p} \left(\int_0^{b_2} t^{-\frac{1}{2}} \, dt + \int_{b_2}^{t_p} (t - b_2)^{-\frac{1}{2}} \, dt \right) db_2 \right] = \frac{8}{3} t_p^{-\frac{1}{2}} \Phi \tag{B.4}$$

Likewise, for three overlapping areas of influence:

$$\dot{\bar{q}_3} = \Phi \frac{1}{t_p} \left[\frac{1}{t_p} \int_0^{t_p} \left(\frac{1}{t_p - b_2} \int_{b_2}^{t_p} \left(\int_0^{b_2} t^{-\frac{1}{2}} \, dt + \int_{b_2}^{b_3} (t - b_2)^{-\frac{1}{2}} \, dt + \int_{b_3}^{t_p} (t - b_3)^{-\frac{1}{2}} \, dt \right) db_3 \right) db_2 \right] = \frac{28}{9} t_p^{-\frac{1}{2}} \Phi \tag{B.5}$$

This same method can be extrapolated to n number of overlapping regions.

Normalising these results by computing $\dot{\bar{q}}_n/\dot{\bar{q}}_n$ yields the enhanced quenching coefficients shown in *table 3.5* and plotted in *fig. B.2*.

The maximum value that $\dot{\bar{q}}_n/\dot{\bar{q}}_n$ occurs when the quenching events are distributed evenly throughout the bubble period (i.e. $b_2 = \frac{1}{2}t_p$ for 2 overlapping areas of influence, $b_2 = b_3 = \frac{1}{3}t_p$ for 2 overlapping areas of influence etc...). This reduces to:

$$A_{n\ max} = \frac{\dot{\bar{q}}_{q-max}}{\dot{\bar{q}}_1} = \frac{\left(\Phi \frac{t_p}{n} \int_0^{t_p/n} t^{-\frac{1}{2}} dt\right)}{\left(2t_p^{-\frac{1}{2}}\Phi\right)} = \sqrt{n} \tag{B.6}$$

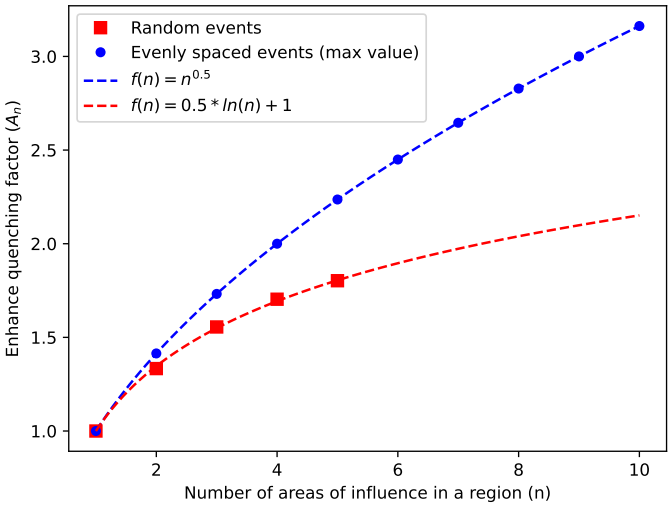

Figure B.2: Enhanced quenching coefficients as a function of number of areas of influence in a region

As can be seen, the randomly temporally distributed quenching events result in lower enhancement coefficients compared to the even temporal distribution of quenching events. The coefficients of the random events seem to follow the curve $f(n) = \frac{1}{2}\ln(n) + 1$ .This was used to approximate A_6.

Appendix C

Monte Carlo Simulation

A Monte Carlo simulation is proposed below in order to obtain a relationship for ζ as a function of wall superheat (ΔT_w) for nitrogen at $P_{sat=140\ \text{kPa}}$. Results are compared against existing correlations presented in *table 3.4*.

The simulation begins by defining a bounded square region of width $L = 1$ cm. The number of nucleation sites that are expected to appear in this region at a specified wall superheat (ΔT_w) is then computed using:

$$n_{sites} = \text{int}(N_w L^2) \tag{C.1}$$

where N_w is computed using either *eq.* (3.21), *eq.* (3.22) or *eq.* (3.23) form *table 3.2*.

The expected bubble departure diameter at this wall superheat is then computed from *eq.* (3.19) from *table 3.1*.

n_{sites} points are then randomly distributed in the square domain. Delaunay triangulation is then performed on the resulting collection of points in order to identify each point's nearest neighbours. The distance between neighbouring points A and B is then computed by:

$$d = \sqrt{(x_A - x_B)^2 + (y_A - y_B)^2} \tag{C.2}$$

If the neighbouring point B lies within a distance of $d_{suppression} = 0.75 D_i$ of a A, then a repulsion factor is computed by:

$$C_{repulsion} = C_{const}(d_{suppression} - d) \tag{C.3}$$

where C_{const} is a small constant relaxation factor. The normal vector is then computed as:

$$\boldsymbol{n}_{\vec{\boldsymbol{AB}}} = \langle n_{ABx}, n_{ABy} \rangle = \frac{\langle (x_B - x_A), (y_B - y_A) \rangle}{d} \tag{C.4}$$

An iterative process is conducted in which the each point is simultaneously moved in a direction opposite to every point within its suppression radius ($d_{suppression}$) by an amount of $C_{repulsion}$:

$$(x_{A\ new}, y_{A\ new}) = (x_A + C_{repulsion} n_{ABx}, y_A + C_{repulsion} n_{ABy}) \tag{C.5}$$

The resulting points are then plotted with a diameter of $D_i = \sqrt{K} D_w$ (where K is a constant) at a transparency of 0.2 so as to allow identification of up to 5 overlapping areas. The plot is saved as a "png" file using a dpi of 1500. Post processing is then done to identify the percentage of the domain covered by each region: no area of influence (a_0), single area of influence (a_1), 2 overlapping areas of influence (a_2), 3 overlapping areas of influence (a_3), 4 overlapping areas of influence (a_4), 5 overlapping areas of influence (a_5) and 6 overlapping areas of influence (a_6). This procedure is implemented in the following python code:

```
import numpy as np
from matplotlib import pyplot as plt
from matplotlib.patches import Circle, Rectangle
%matplotlib inline
import scipy
import time
import math
import itertools
from numba import njit, float64, float32, uint16, int64
from PIL import Image

Area_list=[]
Area1_list=[]
T_sup_list=[]
Area_placeholder=100

for t_increase in np.arange(0,21,2):
    @njit
    def np_unique(a):
        b = np.sort(a.flatten())
        unique = list(b[:1])
        counts = [1 for _ in unique]
        for x in b[1:]:
            if x != unique[-1]:
                unique.append(x)
                counts.append(1)
            else:
                counts[-1] += 1
        return np.array(unique), np.array(counts)

    @njit
    def np_any_axis1(a):
        b=[]
        for i in range(len(a[:,0])):
            b.append(np.any(a[i]))
        return np.array(b)

    def processLog(filename):
        im  = Image.open(filename).convert('RGBA').convert('RGB')
        imnp = np.array(im)
        h, w = imnp.shape[:2]
        colours, counts = np_unique(np.product(imnp.reshape(-1,3),axis=1))
        return np.round((100*counts)/(h*w),3)

    def flatten_list(xss):
        return [x for xs in xss for x in xs]

    @njit
    def speedup1(x,x_boundry_interp,y,y_boundry_interp):
        x_all=np.concatenate((x,x_boundry_interp),axis=0)
        y_all=np.concatenate((y,y_boundry_interp),axis=0)
```

```
    XY_all=np.empty((len(x_all),2),dtype=np.float64)
    for i in range(len(x_all)):
        XY_all[i,0]=x_all[i]
        XY_all[i,1]=y_all[i]
    return x_all,y_all, XY_all

@njit
def speedup2(x_all,y_all,Delaunay_simplices,tol,reduction,x,y,d_repulsion,STOP,n_boundry_interp):
    contain_points=np_isin(Delaunay_simplices,np.arange(0,n_sites,1))
    b=np_any_axis1(contain_points)
    Tri_contain_points=Delaunay_simplices[b]
    row_true_indexes,column_true_indexes=np.where(contain_points[b])

    vv=np.empty((len(column_true_indexes),3),dtype=np.int64)
    pop=np.empty((len(column_true_indexes),3),dtype=np.int64)
    s=np.shape(Tri_contain_points)[0]
    for v in range(len(column_true_indexes)):
        a1=column_true_indexes[v]%3
        a2=(column_true_indexes[v]+1)%3
        a3=(column_true_indexes[v]+2)%3
        vv[v,0]=a1
        vv[v,1]=a2
        vv[v,2]=a3
        pop[v,0]=row_true_indexes[v]+a1*s
        pop[v,1]=row_true_indexes[v]+a2*s
        pop[v,2]=row_true_indexes[v]+a3*s
    vv = Tri_contain_points.T.flatten()[pop.flatten()].reshape(np.shape(pop))
    vv =np.concatenate(( Tri_contain_points[:,0],Tri_contain_points[:,1],Tri_contain_points[:,2]))[pop.flatten()].reshape(np.shape(pop))
    vv=vv[vv[:, 0].argsort()]
    move_x=np.zeros(len(x_all))
    move_y=np.zeros(len(y_all))
    p=0
    for i in range(n_sites):
        list1=[]
        for j in range(p,np.shape(vv)[0],1):
            if vv[j,0]==i:
                list1.append(vv[j,1])
                list1.append(vv[j,2])
            elif vv[j,0]!=i:
                p=j
                break
        list1,forget=np_unique(np.array(list1))
        for m in range(len(list1)):
            dist=np.sqrt((x[i]-x_all[list1[m]])**2+(y[i]-y_all[list1[m]])**2)
            if d_repulsion>=dist:
                error2=(d_repulsion-dist)
            else:
                error2=0
            if error2>tol:
                fact=1
                if list1[m]>n_sites:
```

```
                fact=np.random.rand(1)[0]
            direction=(np.array([x_all[list1[m]]-x[i],y_all[list1[m]]-y[i]]))/dist
            move_x[list1[m]]=move_x[list1[m]]+direction[0]*(error2*reduction*fact+fact*1e-6)
            move_x[i]=-move_x[list1[m]]
            move_y[list1[m]]=move_y[list1[m]]+direction[1]*(error2*reduction*fact+fact*1e-6)
            move_y[i]=-move_y[list1[m]]
    x_new=np.clip(x+move_x[0:n_sites],-domain_L/2+domain_x0,domain_L/2+domain_x0)
    y_new=np.clip(y+move_y[0:n_sites],-domain_L/2+domain_y0,domain_L/2+domain_y0)
    for m in range(len(x_new)):
        if x_new[m]==-domain_L/2+domain_x0 or x_new[m]==domain_L/2+domain_x0 or y_new[m]==-domain_L/2+domain_y0 or y_new[m]==domain_L/2+domain_y0:
            x_new[m]=np.random.random()*domain_L-domain_L/2
            y_new[m]=np.random.random()*domain_L-domain_L/2
    if np.max(np.sqrt((x_new-x)**2+(y_new-y)**2))<1e-6:
        print('STOP')
        STOP=1
    else:
        x=x_new
        y=y_new
    return x, y, int(STOP)

@njit
def np_isin(a,b):
    shape=np.shape(a)
    a=a.flatten()
    b=b.flatten()
    return np.array([item in b for item in a]).reshape(shape)

@njit
def corner(x,y,domain_L):
    for i in range(len(x)):
        if x[i]==domain_L/2 or x[i]==-domain_L/2:
            if y[i]==domain_L/2 or y[i]==-domain_L/2:
                x[i]=np.random.random()*domain_L-domain_L/2
                y[i]=np.random.random()*domain_L-domain_L/2
    return x,y

def nucleation_sites(domain_L,domain_x0,domain_y0,n_boundry_interp,n_sites,d_repulsion,repulsion_iter,tol,reduction,d_influence):
    x=np.random.rand(n_sites)*domain_L-np.ones(n_sites)*(domain_L/2-domain_x0)
    y=np.random.rand(n_sites)*domain_L-np.ones(n_sites)*(domain_L/2-domain_y0)
    ##########################################################################
    x_boundry=np.array([-1,-1,1,1,-1])*domain_L/2+np.ones(5)*(domain_x0)
    y_boundry=np.array([-1,1,1,-1,-1])*domain_L/2+np.ones(5)*(domain_y0)
    bot_x_boundry_interp=(np.linspace(-1,1,n_boundry_interp)*domain_L/2+np.ones(n_boundry_interp)*(domain_x0))
    bot_y_boundry_interp=(np.ones(n_boundry_interp)*(domain_y0-domain_L/2))
    right_x_boundry_interp=(np.ones(n_boundry_interp)*(domain_x0+domain_L/2))[1:n_boundry_interp]
    right_y_boundry_interp=(np.linspace(-1,1,n_boundry_interp)*domain_L/2+np.ones(n_boundry_interp)*(domain_y0))[1:n_boundry_interp]
    top_x_boundry_interp=np.flip(np.linspace(-1,1,n_boundry_interp)*domain_L/2+np.ones(n_boundry_interp)*(domain_x0))[1:n_boundry_interp]
    top_y_boundry_interp=np.flip(np.ones(n_boundry_interp)*(domain_y0+domain_L/2))[1:n_boundry_interp]
    left_x_boundry_interp=np.flip(np.ones(n_boundry_interp)*(domain_x0-domain_L/2))[1:-1]
    left_y_boundry_interp=np.flip(np.linspace(-1,1,n_boundry_interp)*domain_L/2+np.ones(n_boundry_interp)*(domain_y0))[1:-1]
    x_boundry_interp=np.concatenate((bot_x_boundry_interp,right_x_boundry_interp,top_x_boundry_interp,left_x_boundry_interp),axis=0)
```

```
        y_boundry_interp=np.concatenate((bot_y_boundry_interp,right_y_boundry_interp,top_y_boundry_interp,left_y_boundry_interp),axis=0)
        ##########################################################################################
        ##########################################################################################
## Uncomment to show animation
#           plt.ion()
#           figure, ax = plt.subplots(figsize=(6,6))
#           line1, = ax.plot(x, y,'k.')
#           line2, = ax.plot(x_boundry,y_boundry,'k')
#           ax.set_xlim((-domain_L/2+domain_x0,domain_L/2+domain_x0))
#           ax.set_ylim((-domain_L/2+domain_y0, domain_L/2+domain_y0))
#           ax.axis('equal')
#           figure.canvas.draw()
        ##########################################################################################
        ##########################################################################################
        STOP=0
        for k in range(0,repulsion_iter,1):
            if STOP ==0:
                x_all,y_all, XY_all= speedup1(x,x_boundry_interp,y,y_boundry_interp)
                Delaunay=scipy.spatial.Delaunay(XY_all, furthest_site=False, incremental=False, qhull_options=None)
                x,y, STOP =speedup2(x_all,y_all,np.array(Delaunay.simplices),tol,reduction,x,y,d_repulsion,STOP,n_boundry_interp)
## Uncomment to show animation
#                   plt.ion()
#                   line1.set_xdata(x)
#                   line1.set_ydata(y)
#                   ax.set_xlim((-domain_L/2+domain_x0,domain_L/2+domain_x0))
#                   ax.set_ylim((-domain_L/2+domain_y0, domain_L/2+domain_y0))
#                   ax.axis('equal')
#                   figure.canvas.draw()
#                   figure.canvas.flush_events()
#                   time.sleep(0.1)
        return np.array([x,y]).T
    ##################################################################################################################
    ##################################################################################################################
    ##################################################################################################################
    for iind in range(1):
        # Variables
        T_wall=82.207+t_increase
        T_liquid=80.207-2
        d_repulsion_conatant=np.sqrt(2)*0.75
        d_influence_constant=np.sqrt(2)
        ##########################################################
        ##########################################################
        # Fluid Properties
        rho_l=792.98
        rho_v=6.2182
        mu=0.00014399
        sigma=0.0082383
        g=9.81
        hl=5868.9
        hv=2.0126e5
        hlv=hv-hl
```

```
cp_l= 2056.7
cp_v= 1146.7
k_l= 0.13918
lambda_l=k_l/(rho_l*cp_l)
T_sat=80.207

delta_T_w=T_wall-T_sat
delta_T_sub=T_sat-T_liquid
#################################################################
# Maximum departure diameter
tk_max_d=np.min([0.0006*np.exp(-delta_T_sub/45),0.0014])
Li=np.clip(2*(3/4*sigma/(g*(rho_l-rho_v))*(4*sigma*T_sat)/(hlv*rho_v*delta_T_w))**(1/3),0,1e-3)
tk_max_d=Li
#################################################################
# Nucleation site density
D_w3=Li
rho_star=(rho_l-rho_v)/rho_v
f_rho_star=2.157*10**(-7)*rho_star**(-3.2)*(1+0.0049*rho_star)**4.13
R_c=(2*sigma*T_sat)/(rho_v*hlv*delta_T_w)
R_c_star=2*R_c/D_w3
Kamustafaogullari_D_w_3=f_rho_star*R_c_star**-4.4/D_w3**2
N=Kamustafaogullari_D_w_3
#################################################################
import time
Total_time_start = time.time()

d_repulsion=d_repulsion_conatant*tk_max_d
print('d_repulsion:',d_repulsion)
d_influence=d_influence_constant*tk_max_d
print('d_influence:',d_influence)

#note: n_sites must be greater than 3
#x0 and y0 must be 0
domain_L=0.0075
domain_x0=0
domain_y0=0

n_sites=int(N*domain_L**2)
print('n_sites',n_sites)
n_boundry_interp=200
repulsion_iter=200
tol=1e-15
reduction=0.01
#################################################################################################################
start1 = time.time()
X=nucleation_sites(domain_L,domain_x0,domain_y0,n_boundry_interp,n_sites,d_repulsion,repulsion_iter,tol,reduction,d_influence)
end1 = time.time()
#################################################################
x=X[:,0]
y=X[:,1]
plt.figure(10)
```

```
ax1 = plt.gca()
ax1.cla()
ax1.set_axis_off()
# change default range so that new circles will work
ax1.set_xlim((-domain_L/2,domain_L/2))
ax1.set_ylim((-domain_L/2,domain_L/2))
for i in range(len(x)):
    circle = plt.Circle((x[i],y[i] ), d_influence/2, facecolor='r',alpha=0.2, edgecolor=None, fill=True ,clip_on=True)
    ax1.add_artist(circle)
plt.axis("tight")  # gets rid of white border
plt.axis('equal')
plt.axis("image")
plt.gca().set_axis_off()
plt.subplots_adjust(top = 1, bottom = 0, right = 1, left = 0,
            hspace = 0, wspace = 0)
plt.margins(0,0)
plt.gca().xaxis.set_major_locator(plt.NullLocator())
plt.gca().yaxis.set_major_locator(plt.NullLocator())
##########################################################
start2=time.time()
plt.savefig('fig1.png',bbox_inches = 'tight',pad_inches = 0,dpi=1500)
plt.savefig('fig1_pdf.pdf',bbox_inches = 'tight',pad_inches = 0,dpi=1500)
im = Image.open("fig1.png")
width, height = im.size
fact=0.05
end2=time.time()
##############################################################
start3 = time.time()
list1=processLog('fig1.png')
end3 = time.time()
##########################################################
from scipy.misc import electrocardiogram
from scipy.signal import find_peaks
plt.figure(12)
xp = np.concatenate((np.array([0]),np.array(list1),np.array([0])))
peaks, _ = find_peaks(xp, height=0.25)
for i in range(len(peaks)):
    plt.text(peaks[i], xp[peaks[i]],str(xp[peaks[i]])+'%')
plt.plot(peaks,xp[peaks],'o',color='black',markersize=5)
plt.plot(range(len(xp)),xp,'o',color='red',markersize=2)
plt.xlabel('colors')
plt.ylabel('')
plt.show()

Total_time_end = time.time()
print('nucleation time =',end1 - start1)
print('image saving time =',end2-start2)
print('image processing time =',end3 - start3)
print('Plotting time =', (Total_time_end-Total_time_start)-(end1-start1)-(end2-start2)-(end3-start3))
print('Total_time =',Total_time_end -Total_time_start)
```

```
Total_area=np.sum(np.flip(xp[peaks]))/100
Area={}
tap=0
for i in range(7):
    if i==0:
        if Area_placeholder<np.flip(xp[peaks])[i]/100/Total_area:
            Area['A_'+str(i)]=0
            tap=1
        else:
            Area['A_'+str(i)]=np.flip(xp[peaks])[i]/100/Total_area
            if (iind+1)%3==0:
                Area_placeholder=Area['A_'+str(i)]
    elif 0<i and i<6:
        if i<len(peaks):

            Area['A_'+str(i)]=np.flip(xp[peaks])[int(i-tap)]/100/Total_area
        else:
            Area['A_'+str(i)]=0

    else:
        if i<=len(peaks):
            Area['A_'+str(i)]=np.sum(np.flip(xp[peaks])[int(i-tap):])/100/Total_area
        else:
            Area['A_'+str(i)]=0

# Areas minus the maximum diameter
#########################################################################
x=X[:,0]
y=X[:,1]
plt.figure(13)
ax1 = plt.gca()
ax1.cla()
ax1.set_axis_off()
# change default range so that new circles will work
ax1.set_xlim((-domain_L/2,domain_L/2))
ax1.set_ylim((-domain_L/2,domain_L/2))
for i in range(len(x)):
    circle = plt.Circle((x[i],y[i] ), d_influence/2, facecolor='r',alpha=0.2, edgecolor=None, fill=True ,clip_on=True)
    ax1.add_artist(circle)
plt.axis("tight")  # gets rid of white border
plt.axis('equal')
plt.axis("image")
plt.gca().set_axis_off()
plt.subplots_adjust(top = 1, bottom = 0, right = 1, left = 0,
            hspace = 0, wspace = 0)
plt.margins(0,0)
plt.gca().xaxis.set_major_locator(plt.NullLocator())
plt.gca().yaxis.set_major_locator(plt.NullLocator())
#########################################################
for i in range(len(x)):
    circle = plt.Circle((x[i],y[i] ),tk_max_d/2, color='white',alpha=1, fill=True)
```

```
    ax1.add_artist(circle)
##########################################################
start2=time.time()
plt.savefig('fig2.png',bbox_inches = 'tight',pad_inches = 0,dpi=1500)
im = Image.open("fig2.png")
width, height = im.size
fact=0.05
end2=time.time()
##########################################################
start3 = time.time()
list1=processLog('fig2.png')
end3 = time.time()
##########################################################
from scipy.misc import electrocardiogram
from scipy.signal import find_peaks
plt.figure(14)
xp1 = np.concatenate((np.array([0]),np.array(list1),np.array([0])))
peaks1, _ = find_peaks(xp1, height=0.1)
for i in range(len(peaks1)):
    plt.text(peaks1[i], xp1[peaks1[i]],str(xp1[peaks1[i]])+'%')
plt.plot(peaks1,xp1[peaks1],'o',color='black',markersize=5)
plt.plot(range(len(xp1)),xp1,'o',color='red',markersize=2)

plt.show()

Total_time_end = time.time()

Total_area1=np.sum(np.flip(xp1[peaks1]))/100

Area1={}
for i in range(7):
    if i<6:
        if i<len(peaks1):
            Area1['A_'+str(i)]=np.flip(xp1[peaks1])[i]/100/Total_area1
        else:
            Area1['A_'+str(i)]=0
    else:
        if i<=len(peaks1):
            Area1['A_'+str(i)]=np.sum(np.flip(xp1[peaks1])[i:])/100/Total_area1
        else:
            Area1['A_'+str(i)]=0

Area_list.append(Area)
Area1_list.append(Area1)
T_sup_list.append(delta_T_w)
```

Appendix D

Simplified Empirical Model Equations

Below are the equations used to empirically solve the RPI wall boiling model based on the assumptions stated in *section 3.4*. The independent variables in these equations are the wall temperature (T_w), saturation pressure (P_{sat}) and liquid subcooling (ΔT_{sub}). T_w is typically left as a free parameter whilst P_{sat} and ΔT_{sub} are assumed to be constant. Then, by iterative inputting a different value for T_w, one can compute the bubble departure diameter, nucleation site density (N_w), bubble departure frequency (f), non-dimensional area of influence (A_b) and wall heat fluxes ($\dot{q}_E$ and $\dot{q}_C$) by following the steps detailed in *appendix D.1* or *appendix D.2*.

D.1 $N1$

Independent variable:

- T_w

Specified variables:

- P_{sat}
- ΔT_{sub} ($\Delta T_{sub} > 0$ K)

Known variables (based on specified variables):

- ρ_l (at specified saturation pressure [P_{sat}])
- ρ_v (at specified saturation pressure [P_{sat}])
- μ_l (at specified saturation pressure [P_{sat}])
- σ (at specified saturation pressure [P_{sat}])
- $g = 9.81$ m/s^2
- h_l (at specified saturation pressure [P_{sat}])
- h_v (at specified saturation pressure [P_{sat}])
- $c_{p,l}$ (at specified saturation pressure [P_{sat}])
- $c_{p,v}$ (at specified saturation pressure [P_{sat}])
- k_l (at specified saturation pressure [P_{sat}])
- T_{sat} (at specified saturation pressure [P_{sat}])
- $\theta = 7°$
- $C_{wt} = 3.142$

Compute the following variables in the following order based on a selected input value of T_w ($T_w \geq 0$) coupled with the specified and known variables stated above:

1. $D_w = \min\left[0.0014, 0.0006e^{\frac{-\Delta T_{sub}}{45}}\right]$ (*eq.* (3.17))
2. $\Delta T_W = T_w - T_{sat}$

3. $N_w = (210\Delta T_w)^{1.805}$ (*eq.* (3.21))
4. $f = \left[\frac{4g(\rho_l - \rho_v)}{3(1)\rho_l D_w}\right]^{1/2}$ (*eq.* (3.26) with $C_D = 1$)
5. $Ja = \frac{\rho_l c_{p,l} \Delta T_{sub}}{\rho_v h_{lv}}$
6. $K = 4.8e^{-Ja/80}$ (*eq.* (3.37))
7. $D_i = \sqrt{K} D_w$ (*eq.* (3.34))
8. $\beta = \frac{N_w \pi D_i^2}{4}$ (*eq.* (3.32))
9. A_b, where the default is computed as $A_b = \min(1, \beta)$ (*eq.* (3.33)). However, $A_b = 1 - e^{-1.5\beta^{1.2}}$ (*eq.* (3.44)) and $A_b = \frac{1-e^{-\beta}}{}$ (derived from *eq.* (3.36) and *eq.* (3.35)) have been used in *section 4.14* (*fig. 4.55c*)
10. $T_l = T_{sat} - \Delta T_{sub}$
11. $\lambda_l = \frac{k_l}{\rho_l c_{p,l}}$ (*eq.* (3.11))
12. $\dot{q_Q} = C_{wt} \frac{2k_l}{\sqrt{\frac{\pi \lambda_l}{f}}} (T_w - T_l) A_b$ (*eq.* (3.13))
13. $h_{lv} = h_v - h_l$
14. $V_d = \frac{\pi D_w^3}{6}$ (eq. (3.15))
15. $\dot{q_E} = V_d N_w \rho_v h_{lv} f$ (*eq.* (3.14))
16. Assume $\dot{q}_C = 0$
17. $\dot{q_W} = \dot{q_C} + \dot{q_E} + \dot{q_Q}$ (*eq.* (3.1))

D.2 *N2A* and *N2B*

The empirical solution for *N2A* and *N2B* are obtained in a similar fashion to appendix D.1. Below is the detailed solution method:

Independent variable:

- T_w

Specified variables:

- P_{sat}
- ΔT_{sub} ($\Delta T_{sub} > 0$ K)

Known variables (based on specified variables):

- ρ_l (at specified saturation pressure [P_{sat}])
- ρ_v (at specified saturation pressure [P_{sat}])
- μ_l (at specified saturation pressure [P_{sat}])
- σ (at specified saturation pressure [P_{sat}])
- $g = 9.81$ m/s^2
- h_l (at specified saturation pressure [P_{sat}])
- h_v (at specified saturation pressure [P_{sat}])
- $c_{p,l}$ (at specified saturation pressure [P_{sat}])
- $c_{p,v}$ (at specified saturation pressure [P_{sat}])
- k_l (at specified saturation pressure [P_{sat}])
- T_{sat} (at specified saturation pressure [P_{sat}])
- $\theta = 7°$
- $C_{wt} = 1.3$

Compute the following variables in the following order based on a selected input value of T_w ($T_w \geq 0$) coupled with the specified and known variables stated above:

1. $\Delta T_W = T_w - T_{sat}$
2. $h_{lv} = h_v - h_l$
3. $R_c = \frac{2\sigma T_{sat}}{\rho_v h_{lv} \Delta T_w}$ (*eq.* (3.20))
4. $D_w = 2\left[\frac{3}{4}\frac{\sigma}{g(\rho_l - \rho_v)}(2R_c)\right]^{1/3}$ (*eq.* (3.19))
5. For *N2A*: $N_w = 10^{-7}\left[\frac{h_{lv}\rho_v \Delta T_w}{\sigma T_{sat}}\right]^2$ (*eq.* (3.23) ($P/P_{cr} \geq 0.04$))

   For *N2B*:$\rho^* = \frac{\rho_l - \rho_v}{\rho_v}$ and $f(\rho^*) = 2.157 \times 10^{-7}\rho^{*-3.2}(1 + 0.0049\rho^*)^{4.13}$ and $R_c^* = \frac{2R_c}{D_w}$, $R_c = \frac{2\sigma T_{sat}}{\rho_v h_{lv} \Delta T_w}$ and $N_w = \frac{f(\rho^*)R_c^{*-4.4}}{D_w^2}$ (*eq.* (3.22))
6. $\lambda_l = \frac{k_l}{\rho_l c_{p,l}}$ (*eq.* (3.11))
7. $f = \frac{23\pi\lambda_l}{D_w^2}$ (*eq.* (3.28))
8. $K = 4$
9. $D_i = \sqrt{K} D_w$ (*eq.* (3.34))
10. $\beta = \frac{N_w \pi D_i^2}{4}$ (*eq.* (3.32))
11. A_b, where the default is computed as $A_b = 1 - e^{-1.5\beta^{1.2}}$ (*eq.* (3.44)). However, $A_b = \min(1, \beta)$ (*eq.* (3.33)) and $A_b = \frac{1 - e^{-\beta}}{}$ (derived from *eq.* (3.36) and *eq.* (3.35)) have been used in *section 4.14* (*fig. 4.54*)
12. $T_l = T_{sat} - \Delta T_{sub}$

13. $\dot{q_Q} = C_{wt}\frac{2k_l}{\sqrt{\frac{\pi\lambda_l}{f}}}(T_w - T_l)A_b$ *(eq. (3.13))*
14. $V_d = \frac{\pi D_w^3}{6}$ (eq. (3.15))
15. $\dot{q_E} = V_d N_w \rho_v h_{lv} f$ *(eq. (3.14))*
16. Assume $\dot{q}_C = 0$
17. $\dot{q_W} = \dot{q_C} + \dot{q_E} + \dot{q_Q}$ *(eq. (3.1))*

The code used to plot the above variables as a function of wall temperature is shown in *appendix E.*

Appendix E

Simplified Empirical Model Code

```
#Nitrogen
rho_l=792.98
rho_v=6.2182
mu=0.00014399
sigma=0.0082383
g=9.81
hl=5868.9
hv=2.0126e5
hlv=hv-hl
cp_l= 2056.7
cp_v= 1146.7
k_l= 0.13918
lambda_l=k_l/(rho_l*cp_l)
T_sat=80.207
theta=7
T_sub=2
T_sup=np.linspace(1,23,100)
######################################## DEPARTURE DIAMETER ################################
Fritz=(0.0146*theta*((2*sigma)/(g*(rho_l-rho_v)))**0.5)*np.ones(len(T_sup))
Tolubinsky=np.clip(0.0006*np.exp(-T_sub/45),None,0.0014)
Kocamustafaogullari=0.0012*((rho_l-rho_v)/(rho_v))**0.9*
                    (0.0208*theta*np.sqrt(sigma/(g*(rho_l-rho_v))))
Kirichenko=np.clip((2*(3/4*sigma/(g*(rho_l-rho_v))*
          (4*sigma*T_sat)/(hlv*rho_v*T_sup))**(1/3)),0,1e-3)
D_w=Kirichenko
############################## Nucleation site density ####################################
Lemmert=(210*T_sup)**1.85
rho_star=(rho_l-rho_v)/rho_v
f_rho_star=2.157*10**(-7)*rho_star**(-3.2)*(1+0.0049*rho_star)**4.13
R_c=(2*sigma*T_sat)/(rho_v*hlv*T_sup)
R_c_star=2*R_c/D_w
Kamustafaogullari_D_w=f_rho_star*R_c_star**-4.4/D_w**2
Kirichenko_greater=1e-7*((hlv*rho_v*T_sup)/(sigma*T_sat))**2
N_w=Kirichenko_greater
########################## Frequency ###############################################################
Cole=np.sqrt((4*g*(rho_l-rho_v))/(3*rho_l*D_w))
Jakob=0.078/D_w
Ivey=23*np.pi*lambda_l/D_w**2
Ja=(rho_l*cp_l*T_sub)/(rho_v*hlv)
Mickic=((0.83*Ja*(np.pi*lambda_l)**0.5)/D_w)**2
Tibirica=(0.003457/D_w)**2
R_c=(2*sigma*T_sat)/(rho_v*hlv*T_sup)
Hatton=3/(np.pi*lambda_l)*((8*k_l*sigma*T_sat)/((hlv*rho_v)**2*D_w*R_c))**2
F=Ivey
######################################## area of influence ################################
K=4
beta=K*N_w*np.pi*D_w**2/4
A_b=(1-np.exp(-1.5*beta**(1.2)))
```

```
K_eff=A_b/beta*K
################################################ C_wt ######################################
ERF=[]
for i in range(len(T_sup)):
    ERF.append(math.erf((K*N_w*np.pi*D_w**2/4)[i]**0.5))
ERF=np.array(ERF)
C_wt_constant=np.ones(len(T_sup))*1.3
C_wt=C_wt_constant
#############################################################################################
# QUENCH
q_Q=C_wt*(2*k_l)/(np.sqrt(np.pi*lambda_l/F))*(T_sup+T_sub)*K_eff*N_w*np.pi*D_w**2/4
q_E=np.pi*D_w**3/6*N_w*rho_v*hlv*F
q_W=q_Q+q_E
#############################################################################################
TEMP= #ENTER CFD RESULTS
QW=np.arange(0,len(TEMP)*5+1,5)[1:]
DW= #ENTER CFD RESULTS
NW= #ENTER CFD RESULTS
FREQ= #ENTER CFD RESULTS
AB= #ENTER CFD RESULTS
QQ= #ENTER CFD RESULTS
QE= #ENTER CFD RESULTS
QC= #ENTER CFD RESULTS
fig, ax = plt.subplots(3, 2, figsize=(10,12))
ax[0,0].plot(T_sup,q_W/1e4,label='Analytical solution')
exp=pd.read_csv(filepath_or_buffer='flat_original.csv',sep=',',names=['q','Delta_T_sat'])
ax[0,0].plot(exp['q'],exp['Delta_T_sat'],':',color='k',label='Experiment')
ax[0,0].fill_between(exp['q'], error_bar_generator(np.array(exp['Delta_T_sat']),7.37)[0],
error_bar_generator(np.array(exp['Delta_T_sat']),7.37)[1],color='black', alpha=0.2)
ax[0,0].plot(TEMP,QW,'o',color='dodgerblue', label='CFD')
ax[0,0].set_ylabel(r'Wall heat flux: $\dot{q_W}$ [W/$cm^2$]')
ax[0,0].set_xlabel(r'$\Delta T_{w}$ [K]')
ax[0,0].legend()
ax[0,1].plot(T_sup,D_w*1000)
ax[0,1].plot(TEMP,np.array(DW)*1000,'o', color='dodgerblue')
ax[0,1].set_ylabel(r'Departure diameter: $D_w$ [mm]')
ax[0,1].set_xlabel(r'$\Delta T_{w}$ [K]')
ax[1,0].plot(T_sup,q_Q/q_W,label=r'$\dot{q_x}=\dot{q_Q}$', color='dodgerblue')
ax[1,0].plot(T_sup,q_E/q_W,label=r'$\dot{q_x}=\dot{q_E}$', color='darkorange')
ax[1,0].plot(T_sup,np.zeros(len(T_sup)),label=r'$\dot{q_x}=\dot{q_C}$',color='limegreen')
ax[1,0].plot(TEMP,np.array(QQ)/(QW*10000),'o',color='dodgerblue')
ax[1,0].plot(TEMP,np.array(QE)/(QW*10000),'o',color='darkorange')
ax[1,0].plot(TEMP,np.array(QC)/(QW*10000),'o',color='limegreen')
ax[1,0].set_ylabel(r'Contribution of heat flux component: $\frac{\dot{q_x}}{\dot{q_W}}$')
ax[1,0].set_xlabel(r'$\Delta T_{w}$ [K]')
ax[1,0].legend()
ax[1,1].plot(T_sup,N_w)
ax[1,1].plot(TEMP,NW,'o', color='dodgerblue')
ax[1,1].set_yscale('log')
ax[1,1].set_ylabel(r'Nucleation site density: $N_w$ [sites/$m^2$]')
ax[1,1].set_xlabel(r'$\Delta T_{w}$ [K]')
ax[2,0].plot(T_sup,F)
ax[2,0].plot(TEMP,FREQ,'o', color='dodgerblue')
ax[2,0].set_ylabel(r'Frequency of bubble departure: $f$ [Hz]')
ax[2,0].set_xlabel(r'$\Delta T_{w}$ [K]')
ax[2,0].set_yscale('log')
ax[2,1].plot(T_sup,A_b)
ax[2,1].plot(TEMP,AB,'o', color='dodgerblue')
ax[2,1].set_ylabel(r'Area of influence: $A_b$')
ax[2,1].set_xlabel(r'$\Delta T_{w}$ [K]')
```

Appendix F

Material Properties

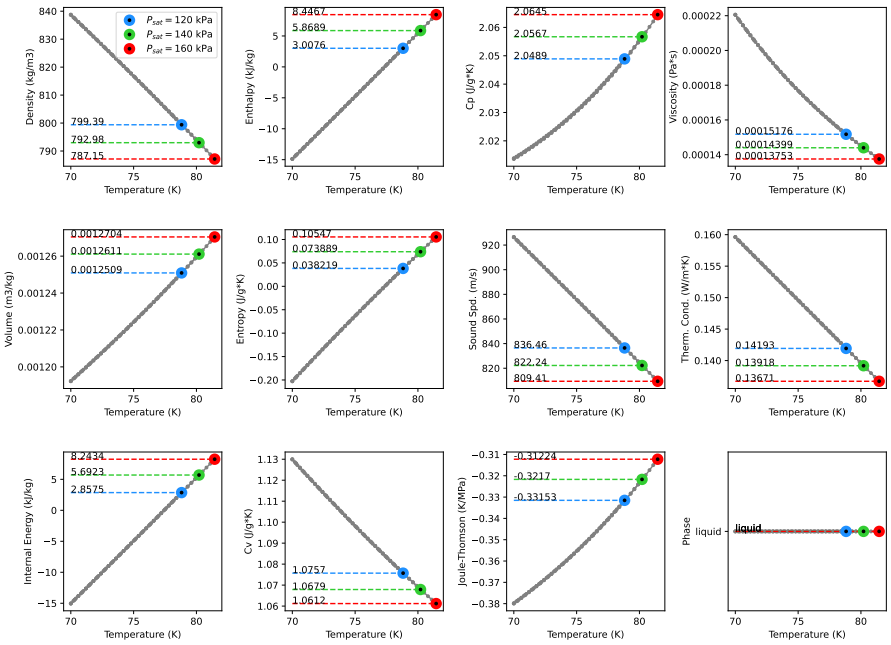

Figure F.1: Properties of liquid nitrogen for P= 120 kPa, 140 kPa, 160 kPa, data acquired from [172]

Table F.1: Properties of water at specified saturation pressures, data obtained from [172]

P_{sat} [Pa]	T_{sat} [K]	Phase	ρ [kg/m^3]	Enthalpy h [J/kg]	Entropy s [J/(kg · K)]	C_p [J/(kg · K)]	μ [Pa · s]	k [W/(m · K)]	σ [N/m]
140e3	382.44	liquid	951.49	39360	104.08	4227.4	2.564e-4	0.68017	0.057102
		vapour	0.80869	2.0978e3	5939.1	2121.0	1.256e-5	0.025506	

Appendix G

UDF for RPI Framework *N2A* and *N2B*

```
#include "udf.h"

#define g 9.81
#define sigma 8.238e-3
real D_w;
real N_w;

DEFINE_BOILING_PROPERTY(bubble_departure_diameter,f,t,c0,t0,from_index,from_species_index,to_index,to_species_index)
{/*Kirichenko Departure Diameter*/
  int liq_phase = from_index;
  int vap_phase = to_index;
  Thread **pt0 = THREAD_SUB_THREADS(t0);
  real rho_l = C_R(c0, pt0[liq_phase]);
  real rho_v = C_R(c0, pt0[vap_phase]);
  real T_wall = F_T(f,t);
  real T_sat = C_STORAGE_R(c0,t0,SV_SAT_TEMPERATURE);
  real h_v = C_H(c0, pt0[vap_phase]);
  real h_l = C_H(c0, pt0[liq_phase]);

  real delta_T_w = MAX(T_wall -T_sat,0.01);
  real h_lv = h_v-h_l;
  real numerator = (3.000*sigma*4.000*sigma*T_sat);
  real denomenator = (4.000*g*(rho_l-rho_v)*h_lv*rho_v*delta_T_w);
  double power = 0.33333333333333;
  D_w = MIN(2.000*pow(numerator/denomenator,power),0.001);
  return D_w;
}

/*Kirichenko*/

  DEFINE_BOILING_PROPERTY(nucleation_site_density,f,t,c0,t0,from_index,from_species_index,to_index,to_species_index)
{
  int liq_phase = from_index;
  int vap_phase = to_index;
```

```
  Thread **pt0 = THREAD_SUB_THREADS(t0);
  real rho_v = C_R(c0, pt0[vap_phase]);
  real T_wall = F_T(f,t);
  real T_sat = C_STORAGE_R(c0,t0,SV_SAT_TEMPERATURE);
  real h_v = C_H(c0, pt0[vap_phase]);
  real h_l = C_H(c0, pt0[liq_phase]);

  real delta_T_w = MAX(T_wall -T_sat,0.01);
  real h_lv = h_v-h_l;

  double power = 2.000000000;
  N_w = 1e-7*pow((h_lv*rho_v*delta_T_w)/(sigma*T_sat),power);
  return N_w;
 }

/*Kocamustafaogullari*/
/*
DEFINE_BOILING_PROPERTY(nucleation_site_density,f,t,c0,t0,from_index,from_species_index,to_index,to_species_index)
 {
  int liq_phase = from_index;
  int vap_phase = to_index;
  Thread **pt0 = THREAD_SUB_THREADS(t0);
  real rho_l = C_R(c0, pt0[liq_phase]);
  real rho_v = C_R(c0, pt0[vap_phase]);
  real T_wall = F_T(f,t);
  real T_sat = C_STORAGE_R(c0,t0,SV_SAT_TEMPERATURE);
  real h_v = C_H(c0, pt0[vap_phase]);
  real h_l = C_H(c0, pt0[liq_phase]);

  real h_lv = h_v-h_l;
  real delta_T_w = MAX(T_wall -T_sat,0.01);
  real rho_star = (rho_l-rho_v)/rho_v;
  double power2 = -3.2000;
  double power3 = 4.13000;
  real function_rho_star = 2.157e-7*pow(rho_star,power2)*pow((1.000+0.0049*rho_star),power3);
  real R_c = 2.000*sigma*T_sat/(rho_v*h_lv*delta_T_w);
  real R_c_star = 2.000*R_c/D_w;
  double power1 = -4.40000;
  N_w = function_rho_star*pow(R_c_star,power1)/(D_w*D_w);

  return N_w;
  }
 */

 DEFINE_BOILING_PROPERTY(frequency,f,t,c0,t0,from_index,from_species_index,to_index,to_species_index)
 {
  int liq_phase = from_index;
  int vap_phase = to_index;
  Thread **pt0 = THREAD_SUB_THREADS(t0);
  real rho_l = C_R(c0, pt0[liq_phase]);
  real cp_l = C_CP(c0, pt0[liq_phase]);
```

```
 real k_l = C_K_L(c0, pt0[liq_phase]);

 real lam_l = k_l/(rho_l*cp_l);
 real freq = 23.00*M_PI*lam_l/(D_w*D_w);
 return freq;
}

DEFINE_BOILING_PROPERTY(area_of_influence_constant,f,t,c0,t0,from_index,from_species_index,to_index,to_species_index)
{
 real K = 4.000;
 real beta = K*N_w*M_PI*D_w*D_w/4;
 double power = 1.20000;
 real A_b = 1-exp(-1.5*pow(beta,power));
 real K_eff = A_b/beta*K;
 return K_eff;
}
```